University of Alabama in Huntsville

LOUIS

Dissertations | UAH Electronic Theses and Dissertations

2016

Like-doublet injectors : the effects of varying the impingement distance and an analysis of the primary atomization zone

Brian A. Sweeney

Follow this and additional works at: https://louis.uah.edu/uah-dissertations

Recommended Citation

Sweeney, Brian A., "Like-doublet injectors : the effects of varying the impingement distance and an analysis of the primary atomization zone" (2016). *Dissertations*. 110.
https://louis.uah.edu/uah-dissertations/110

This Dissertation is brought to you for free and open access by the UAH Electronic Theses and Dissertations at LOUIS. It has been accepted for inclusion in Dissertations by an authorized administrator of LOUIS.

LIKE-DOUBLET INJECTORS: THE EFFECTS OF VARYING THE IMPINGEMENT DISTANCE AND AN ANALYSIS OF THE PRIMARY ATOMIZATION ZONE

by

BRIAN A. SWEENEY

A DISSERTATION

Submitted in partial fulfillment of the requirements
for the degree of Doctor of Philosophy
in
The Department of Mechanical and Aerospace Engineering
to
The School of Graduate Studies
of
The University of Alabama in Huntsville

HUNTSVILLE, ALABAMA

2016

In presenting this dissertation in partial fulfillment of the requirements for a doctoral degree from The University of Alabama in Huntsville, I agree that the Library of this University shall make it freely available for inspection. I further agree that permission for extensive copying for scholarly purposes may be granted by my advisor or, in his/her absence, by the Chair of the Department or the Dean of the School of Graduate Studies. It is also understood that due recognition shall be given to me and to The University of Alabama in Huntsville in any scholarly use which may be made of any material in this dissertation.

Brian Sweeney

Brian A. Sweeney

6/23/16

(date)

DISSERTATION APPROVAL FORM

Submitted by Brian A. Sweeney in partial fulfillment of the requirements for the degree of Doctor of Philosophy in Mechanical Engineering and accepted on behalf of the Faculty of the School of Graduate Studies by the dissertation committee.

We, the undersigned members of the Graduate Faculty of The University of Alabama in Huntsville, certify that we have advised and/or supervised the candidate of the work described in this dissertation. We further certify that we have reviewed the dissertation manuscript and approve it in partial fulfillment of the requirements for the degree of Doctor of Philosophy in Mechanical Engineering.

Robert C Frederick 6/23/16		
Dr. Robert Frederick Jr.	(Date)	Committee Chair
D. Keith Hollingsworth 6/23/16		
Dr. Keith Hollingsworth	(Date)	
6/23/16		
Dr. Kader Frendi	(Date)	
Jason T Cassibry 6/23/16		
Dr. Jason Cassibry	(Date)	
David Lineberry 6/23/16		
Dr. David Lineberry	(Date)	
D. Keith Hollingsworth 6/23/16		
Dr. Keith Hollingsworth	(Date)	Department Chair
Shankar Mahalingam 6-30-16		
Dr. Shankar Mahalingam	(Date)	College Dean
7/1/16		
Dr. David Berkowitz	(Date)	Graduate Dean

ABSTRACT

School of Graduate Studies
The University of Alabama in Huntsville

Degree Doctor of Philosophy College/Dept. Engineering/Mechanical and Aerospace Engineering

Name of Candidate Brian A. Sweeney

Title Like-Doublet Injectors: The Effects of Varying the Impingement Distance and an Analysis of the Primary Atomization Zone

This research explored how the jet breakup length to impingement distance ratio affects the spray characteristics of like-doublet injectors and consisted of cold-flow experiments using water at atmospheric pressure. A combination of three impingement angles, four jet velocities, and four jet breakup length to impingement distance ratios between one-half and two were tested. The breakup characteristics, sheet lengths and ligament wavelengths were determined from high-speed videos of the spray while droplet statistics were collected with a Phase Doppler Particle Analyzer. The sheet breakup characteristics were altered when the ratio transitioned from greater than one to equal to one and dramatically changed when the ratio became less than one. A robust impingement and 'steady' sheet formed when the ratio was greater than one. While an 'unsteady' sheet formed when the ratio equaled one due to intermittent jet breakup at the impingement point. Finally, no sheet was formed for ratios less than one. The flat sheet experienced two breakup modes separated by a transition Weber number. Empirical sheet breakup correlations based upon the Weber number and impingement angle were determined for both breakup modes. The mean wavelength between the shed ligaments was equal for

all jet velocities and impingement angles tested. This produced a mean atomization frequency that was near to and parallel with the Hewitt stability threshold for liquid rockets demonstrating the importance of injector primary atomization characteristics on combustion instability. In addition, the droplet diameter and droplet distribution width was found to be inversely proportional to Weber number and impingement angle and was described by a single empirical correlation. Finally, dynamic mode decomposition (DMD) was used to characterize the spray. The DMD analysis was able to extract modes and frequencies corresponding with both the impact waves on the surface of the sheet and the ligaments shed from the end of the sheet. The impact wave modal structure was also observed on the two jets suggesting that the disturbances present on the two impinging jets are the source of impact waves. This idea was solidified by observation of the high-speed videos that clearly showed that impact waves are formed by the local momentum imbalance between the two turbulent jets at the impingement point. Also, composite contour plots using all of the calculated dynamic modes produced a contour of the spray remarkably similar to what is seen in a high-speed photograph indicating the capability of DMD to extract the relevant modes that influence the complex impingement and breakup process.

Abstract Approval: Committee Chair

Dr. Robert Frederick Jr.

Department Chair

Dr. Keith Hollingsworth

Graduate Dean

Dr. David Berkowitz

ACKNOWLEDGMENTS

I would like to acknowledge the Alabama Space Grant Consortium, NASA Training Grant NNX10AJ80H for funding the first three years of my Ph.D. program as a Space Grant Graduate Fellow. Their support allowed me to complete my coursework, select a research topic, and finish the first part of the experimental test program.

I would also like to thank my advisor Dr. Robert Frederick for his continual guidance, insight and support of this research topic and myself as a graduate student. In addition, my committee members consisting of Dr. Keith Hollingsworth, Dr. Kader Frendi, Dr. David Lineberry, and Dr. Jason Cassibry have provided key advice and help in all aspects of this research including but not limited to experiment design, data analysis, and presentation of the results. Also, Mr. Tony Hall, the PRC Facility Engineer, provided his expertise and assistance in the modification of the test facility.

Finally, I would like to thank my family for their unwavering support as I embarked on this degree program. In particular, I would like to thank my wife Renae for her support and patience as I spent long hours finishing this research project and degree program.

TABLE OF CONTENTS

LIST OF FIGURES

LIST OF TABLES

TABLE PAGE

LIST OF SYMBOLS

SYMBOL	DEFINITION
A	Cross-Sectional Area
$\boldsymbol{A}$	Linear Operator
$\widetilde{\boldsymbol{A}}$	Approximate Linear Operator
b	Systematic Uncertainty
c	Speed of Sound or Scaling Coefficient (DMD)
C_c	Contraction Coefficient
d	Diameter
D	Damping
f	Friction Factor
F	Frequency or Acoustic Energy Flux (Ch. 1)
g	Gravitational Acceleration Constant
$\mathbb{I}$	Imaginary Part of Complex Number
K_c	Cavitation Number
k_L	Minor Loss Coefficient
l	Length
$\dot{m}$	Mass Flow Rate

$\hat{n}$	Unit Normal Vector
Oh	Ohnesorge Number
P	Pressure
$\dot{q}$	Heat Release Rate
$\mathbb{R}$	Real Part of Complex Number
Re	Reynolds Number
s	Random Uncertainty
Sp	Span
St	Strouhal Number
t	Time
T	Time Period of Oscillation
u	Standard Uncertainty
$\boldsymbol{U}$	Unitary Matrix with Left Singular Vectors
U_{95}	Total Uncertainty with 95% Confidence Interval
v	Velocity
V	Volume
$\boldsymbol{V}$	Unitary Matrix with Right Singular Vectors
We	Weber Number
x	Spacing or Data Vector 1 (DMD)

$\boldsymbol{X}$	Data Matrix 1
$\boldsymbol{Y}$	Data Matrix 2
y	Distance in y-direction or Data Vector 2 (DMD)
z	Data Vector

Greek Symbols

α	PDPA Receiver Off-Axis Angle
β	PDPA Transmitter Off-Axis Angle
γ	Specific Heat Ratio
δ	Small Difference
Δ	Difference Between Initial and Final States
λ	Wavelength or Eigenvalue (DMD)
θ	Impingement Half-Angle
ϑ	Cant Half-Angle
μ	Absolute Viscosity
ν	Kinematic Viscosity
ρ	Density
σ	Surface Tension
$\boldsymbol{\Sigma}$	Diagonal Matrix with Singular Values
τ	Shear Stress

ϕ	DMD Mode
φ	High-Speed Camera Off-Axis Angle or Phase Angle (Ch. 1)
ω	Natural Frequency
Γ	Injector Resistance
υ	Eigenvector (DMD)
Υ	Injector Inertance

Subscripts

0.5	Mass Median
10	Numerical Mean
32	Sauter Mean
10%	Droplet at 10^{th} Percentile of Distribution
50%	Droplet at 50^{th} Percentile of Distribution
90%	Droplet at 90^{th} Percentile of Distribution
atm	Atmospheric
atom	Atomization
avg	Average
ax	Axial
b	Breakup of the Liquid Jet
c	Vena Contracta

drop	Droplet
eff	Effective
ent	Entrance
gas	Gas
i	Impingement
inj	Injector
j	Jet
l	Ligament
lat	Lateral
liq	Liquid
max	Maximum
o	Orifice
p	Feedline Pipe
per	Perpendicular
s	Liquid Sheet
tp	Transition Point
tube	Tube
v	Vapor

Superscripts

$'$	Fluctuating Component
$\bar{}$	Mean Component
H	Complex Conjugate Transpose

CHAPTER 1

INTRODUCTION

Liquid rocket engines (LREs) are a versatile type of propulsion system used for a wide variety of flight applications. These range from booster engines used on the first stage of launch vehicles which require high thrust and large total impulse to spacecraft attitude control thrusters that require very small amounts of thrust and low total impulse. LREs offer several distinct advantages over other chemical rocket propulsion systems including the best performance, ease of control with the ability to be restarted and throttled, and component redundancy. Some disadvantages include greater system complexity and part count as well as safety concerns in handling the propellant prior to launch [1].

The liquid rocket propulsion system includes all of the components that are required for propulsive purposes. These include the propellant tanks, the feed system that provides the means and energy to transport the propellant from the tanks to the engine, the control devices to initiate and regulate propellant flow, the turbopumps (used in high thrust engines) which pressurize the propellant prior to injection into the thrust chamber, the thrust chamber which contains the chemical reactions and converts the chemical and thermal energy into kinetic energy and thrust, and finally

the structure that attaches the engine to the rocket and transmits the thrust force to the vehicle. Many different liquid rocket engine system designs and propellant combinations exist that are tailored to specific mission requirements [2].

The LRE can use either a monopropellant or a bipropellant combination. Monopropellant engines use a single propellant and can operate as either a cold gas or hot gas thruster. Hot gas thrusters function by exposing the liquid propellant to a catalyst that causes the propellant to undergo rapid thermal decomposition in an exothermic reaction. Bipropellant engines mix and combust a fuel and oxidizer mixture to release thermal energy. Liquid propellants can be either cryogenic or storable. Cryogenic propellants normally exist as a gas at Earth ambient conditions and are liquefied by cooling to very low temperatures e.g. liquid oxygen and liquid hydrogen. Storable propellants exist at a liquid state at Earth ambient conditions e.g. kerosene and hydrazine [2].

Liquid rocket engines have historically been classified by the type of feed system used. Two basic methods for delivering propellant from the tank(s) to the thrust chamber are tank-pressure fed and pump-pressure fed. Tank-pressure feed systems use pre-stored or generated ullage tank pressure to feed the propellants to the thrust chamber. Tank-pressure feed systems are a simpler design and have less parts but require heavier tanks to withstand the greater pressures. These systems are typically used for missions that require small total impulse. Pump-pressure feed systems use some of the chemical energy of the propellants to drive a turbopump that pressurizes the propellant before it is fed into the thrust chamber. Pump-fed systems are categorized according to the power cycle that drives the turbopump. The three

most common cycles are: gas generator, expander, and staged combustion. Pump-fed engines are more complex but are the superior system for high thrust applications or for vehicles/missions that require large propellant tanks [1].

The thrust chamber is the critical sub-assembly where the propellants undergo injection, mixing, and combustion and the resulting combustion products are accelerated to supersonic velocity out of the nozzle. A typical LRE thrust chamber consists of the fuel and oxidizer manifolds, injector, combustion chamber, and nozzle [2].

The injector can be considered the "heart of the thrust chamber [1]." The injector is responsible for controlling the atomization, vaporization, and mixing processes of the propellants to prepare a uniform combustible mixture. For these reasons, the injector is the core component that determines the performance of the rocket engine. Figure 1.1, shows a flow chart of the complexity of the injection and combustion processes that occur inside the thrust chamber of a liquid rocket engine, reproduced from the NASA SP-194 report.

The atomization process controls the transformation of liquid propellant jets or sheets into sprays of small droplets that are well dispersed within the combustion chamber. The vaporization process controls the evaporative phase change of the liquid droplets into a gas. Before combustion can take place, the fuel and oxidizer reactants must be adequately mixed. The design, number, and placement of the injectors will control the degree of liquid and gas phase mixing. The requirement that the injector control and/or set the boundary conditions for all of these physical processes

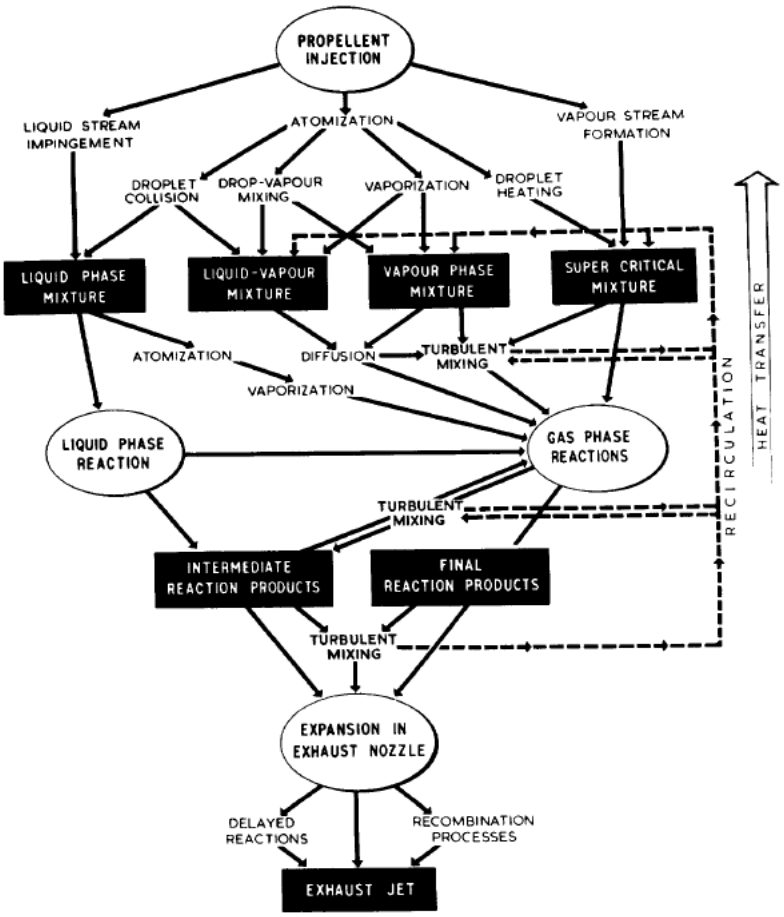

Figure 1.1: Liquid Rocket Injection and Combustion Process Diagram [3]

simultaneously for a range of operating conditions causes the injector development process to be extremely complex and difficult [1, 2].

Many injector designs have been used in operational liquid rocket engines. Several of the most common designs can be seen in Figure 1.2, reproduced from Humble [1]. The impinging-type injector injects the liquid propellant through angled orifices which cause the liquid jets to impact each other at the designed angle. The impingement forms a flat liquid sheet that disintegrates into a spray of small droplets downstream. The like-doublet injector, impinges and atomizes two streams

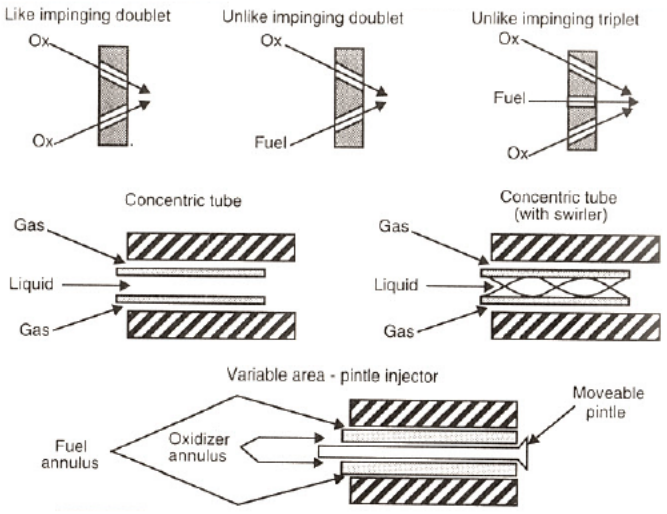

Figure 1.2: Common Liquid Rocket Injector Types [1]

of the same liquid propellant. Therefore, separate fuel and oxidizer doublets are canted towards each other to facilitate mixing. Unlike-doublets impinge, atomize, and mix the fuel and oxidizer streams directly [2]. Unlike-triplets operate in the same manner as the unlike-doublet except this type of element generally produces greater performance compared with the doublet designs [4]. Impinging jet injectors are typically used with LOX/hydrocarbon or hypergolic propellant combinations. Many historical liquid rocket engines have used impinging jet injectors including the F-1, LR-87, and Viking [5].

The concentric tube, also known as shear-coaxial, injector is typically used with a liquid oxygen and gaseous hydrogen propellant combination. This design features a low velocity, internal liquid oxygen jet core that is atomized by the shearing action of an outer, high velocity annular gaseous hydrogen jet. Propellant mixing occurs simultaneously with the atomization process. Engineers generally design the

injector to have a gas to liquid momentum flux ratio of around 10 in order to facilitate high atomization and mixing efficiencies. Two well known rocket engines that use shear-coaxial injectors are the RS-25 used as the main engine on the Space Shuttle and the RL-10. A variation upon this concept, swirls the liquid propellant which tends to enhance the atomization process for a wider range of operating conditions [2, 5, 6]. Russian engineers extensively utilize the gas-centered swirl-coaxial (GCSC) injector design for their LOX/kerosene rocket engines such as the RD-170 and NK-33. This design consists of an internal gaseous oxidizer core that is surrounded by the swirled liquid fuel [7].

The pintle injector is a variation of the coaxial element where the addition of an adjustable pintle inside the internal tube induces the first propellant to form a hollow conical spray sheet that impinges with the outer, annular cylindrical spray of the second propellant. This results in good atomization and mixing. The pintle also allows for the injection area to be changed during operation resulting in easy and reliable engine throttling without large reductions in efficiency and pressure drop across the injector [2]. This type of injector was used with great success in the Lunar Module Descent Engine (LMDE) during NASA's Apollo program [5] and is currently being used in the Merlin class of engines designed and built by SpaceX [8].

In addition, the injector and injection processes play an important role in the stability of the combustion process. A rocket engine can experience a phenomenon known as combustion instability. Combustion instability can be broadly defined as the coupling between the thermofluid parameters and the hardware of the engine. This coupling produces severe pressure oscillations, vibrations and heat release fluctuations

that can damage or destroy the engine. Combustion instability is maintained by complicated feedback mechanisms between the heat release, which is predominantly controlled by the injection process, and the acoustic pressure oscillations within the chamber [3]. The next sections in this chapter will give an overview of combustion instability as well as describe the design and spray characteristics of like-doublet injectors.

The research described in this dissertation focuses upon the changes in the spray atomization characteristics formed by like-doublet impinging injectors as the ratio between the liquid jet breakup length and impingement distance is varied and how the natural disturbances on the two impinging jets affects the primary atomization process of the like-doublet injectors. It has been suggested in the literature that the atomization frequency and the ratio between the breakup length of the jets versus the impingement distance is important in the combustion stability characteristics of liquid rocket engines that use like-doublet injectors.

1.1 Overview of Combustion Instability

Nearly every rocket engine development program has experienced and has had to overcome problems caused by combustion instability [3]. Combustion instability was first encountered in the late 1930s and 1940s when early rocket tests experienced anomalies that expressed themselves as structural vibrations, increased heat transfer to the chamber walls, variations in performance, and occasionally engine failure during extreme cases. Since the 1950s, combustion instability has and continues to appear and cause problems in all types of high-performance combustors and propulsion

systems including: rocket engines, gas turbines, afterburners/thrust augmenters, and ramjets. Therefore, careful design to prevent and eliminate combustion instabilities is an important part of all engine development programs [9].

Considerable effort was undertaken by both the United States and the Soviet Union during the space race between the late 1950s to mid 1970s to solve problems associated with combustion instability. These problems were particularly prevalent and destructive in large, high-performance rocket engines. The development process to counteract these instabilities during various engine programs was both long and expensive [9]. A brief historical overview of the development programs for the American F-1 and European Viking rocket engines will be given. Both engines used like-doublet impinging injector elements and both programs encountered and solved major combustion instability problems.

The F-1 rocket engine development program started in the mid 1950s and continued until the early 1970s. Five of these engines were clustered together to form the first stage of the Saturn V launch vehicle used to send astronauts to the Moon during the Apollo program. The F-1 engine utilized a gas generator power cycle and burned liquid oxygen (LOX) and Rocket Propellant 1 (RP-1), a derivative of kerosene, as the propellants. The engine operated at a chamber pressure of 7.76 MPa (1,125 psia) and produced a remarkable 6,672,000 N (1,500,000 lb_f) of thrust with a 93.8% characteristic velocity efficiency and a sea level specific impulse of 265 seconds [10].

From design inception until the fall of 1962, several engine failures due to combustion instability underscored that the knowledge and understanding of the

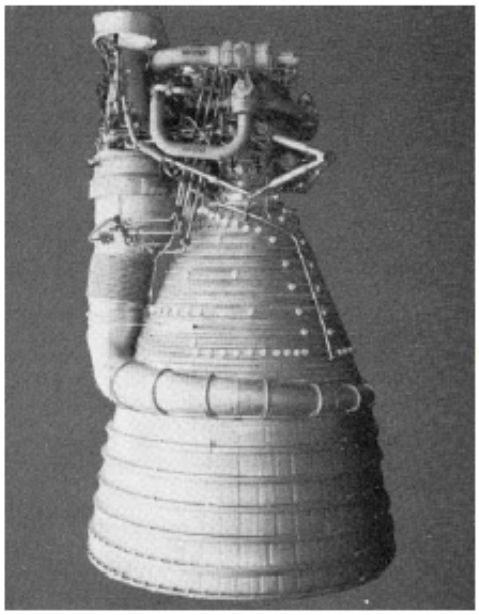

Figure 1.3: F-1 Rocket Engine [9]

phenomenon was not sufficient. This realization led to the initiation of the Project First program which was a concentrated effort to solve the combustion instability problems of the F-1 rocket engine at all costs. This program lasted until the fall of 1966 when the F-1 was qualified for human spaceflight. Approximately 3,200 full-scale engine tests of the F-1 were conducted during the development program of which about 2,000 were performed during Project First [10].

The F-1 engine was most vulnerable to the spinning first-tangential combustion instability mode at a frequency of about 500 *Hz*. The engine also sometimes experienced a resurging phenomenon and sinusoidal "buzzing" oscillations. A total of 14 injector designs/patterns in combination with 15 baffle configurations were experimentally tested. This test program also included several design modifications of the propellant manifolds and feed system and variations of the fuel film cooling

used for the chamber wall and baffles. Some designs were extremely unstable and produced chamber pressure oscillation amplitudes on the order of 400% of the mean chamber pressure. The final design incorporated the modified 5U injector plate with a 13 compartment baffle configuration. The modified 5U injector plate consisted of like-doublet impinging injector elements for both the fuel and oxidizer. The final iteration of the F-1 engine was able to suppress dynamically excited (bombed) combustion instability in about 13 milliseconds [10].

The Viking rocket engine development program started in the late 1960s and continued until the late 1980s. Viking engines were used in the first and second stages of the Ariane 1, 2, 3, and 4 launch vehicles. The first stage consisted of four Viking 5 rocket engines and the second stage consisted of one Viking 4 engine. All versions of the Viking engine used the same injector and turbopump. The difference occurred with the design of the nozzle, the Viking 4 engines contained a large expansion ratio nozzle optimized for high altitude flight [11].

The Viking engine utilized a gas generator power cycle and an earth-storable hypergolic propellant combination of nitrogen tetroxide (NTO) and unsymmetrical dimethylhydrazine (UDMH) as used in Ariane 1 and 2 and a combination of NTO and UH25, mixture of 75% UDMH and 25% hydrazine hydrate, as used in Ariane 3 and 4. The engine used a radial injection scheme where the fuel and oxidizer like-doublet impinging injector elements are arranged in rows placed circumferentially around the chamber wall as opposed to the conventional design of a flat injector plate at the head end of the combustion chamber. The earlier versions of the Viking engine operated at a chamber pressure of 5.45 MPa (790 psia) and produced about 623,700 N

Figure 1.4: Ariane Viking Engine [12]

(140,200 lb_f) of thrust and a vacuum specific impulse of 280 seconds. Chamber pressure and thrust of the Viking engine were improved slightly for the Ariane 3 and 4 [11].

The first launch of the Ariane 1 launch vehicle occurred on 24 December 1979 and was a complete success. The second launch on 23 May 1980 ended in failure when the Ariane rocket disintegrated 112 seconds after liftoff. Analysis of the wreckage found that the fourth Viking engine on the first stage developed high-frequency combustion instability which caused extensive damage to the injector and ruptured the combustion chamber 68 seconds into the flight. The destruction of the engine initiated a sequence of events that caused two of the remaining three engines to

malfunction. Leading to a loss of control authority over the rocket causing it to break apart at the 108 second mark [11].

After the failure, a considerable research and development effort went into finding a solution to the combustion instability problem. At its height, two engine tests were conducted per day. The re-designed engine included the following changes: larger injector orifice diameters, addition of acoustic absorbers, mechanically strengthened injector hardware and the addition of water to the UDMH fuel. These modifications stabilized the engine but resulted in a slight decrease in performance. Ariane was able to return to flight on 19 June 1981 [11].

Research in the field of combustion instability has been ongoing for the past 60 years. Incremental progress has been made during this time to understand the nature and triggers of these oscillations as well as the most effective control mechanisms. However, a complete theoretical framework that adequately describes the phenomena does not exist [13].

1.1.1 Characteristics of Combustion Instability

Combustion instability occurs when the fluid dynamics of the system couples with the combustion process and the acoustic modes of the engine. These instabilities are characterized by self-sustained, non-linear periodic oscillations of pressure, heat release, and velocity maintained by complicated feedback loops between the oscillations, the fluid dynamics of the system, the combustion energy and the resonant frequencies of the combustor [3, 13]. By design, the combustion chamber of a liquid rocket engine releases very large amounts of energy inside a relatively small

volume with minimal energy losses. Only slight interaction and feedback between the combustion and fluid dynamics of the system are necessary to excite undesirable oscillations. These conditions provide a favorable environment for the excitation and sustainment of combustion instability [9].

The most quoted theoretical principle by which combustion instabilities form is through the criterion developed by Lord Rayleigh in 1878. Rayleigh's criterion simply states that for a resonant interaction to occur between the acoustic field and the combustion process, the heat release rate fluctuations ($\dot{q}'$) due to the burning of propellant must be in-phase with the pressure oscillations (p$'$) in the chamber. On the other hand, damping of the unsteady motions will occur when the heat release rate and pressure oscillations are out-of-phase [14]. This criterion is mathematically described by Eq. (1.1) [15],

$$\int_V \int_t p'(V,t)\dot{q}'(V,t)dtdV > 0 \tag{1.1}$$

where p$'$ and $\dot{q}'$ are assumed to be harmonic perturbations of pressure and heat release rate. The harmonic oscillations can be denoted as [15]:

$$p'(t) = p'_{max} \sin(\omega t) \tag{1.2}$$

$$\dot{q}'(t) = \dot{q}'_{max} \sin(\omega t + \varphi) \tag{1.3}$$

The flame response to the acoustic pressure oscillations will be positive (excitation) when $0° < |\varphi| < 90°$, zero (neutral) when $|\varphi| = 90°$, and negative (damping) when $90° < |\varphi| < 180°$ [15]. Having the pressure and heat release oscillations in-phase is necessary but may not be sufficient to excite combustion instability in the engine. This is due to dissipation mechanisms present in the process. The energy dissipation includes the net energy flux $\left(\vec{F}\right)$ out of the domain control area and the characteristic damping (D) of the volume (combustion chamber). If the acoustic oscillation energy is greater than the combined dissipation mechanisms, then the oscillations will grow causing the system to become unstable. If however, the acoustic oscillation energy is less than the dissipation, net damping will occur and the engine will remain stable. A third scenario develops when the acoustic energy balances the dissipation of the system leading to a limit cycle where the oscillations neither grow nor decay. A more quantitative extension of the Rayleigh criterion that describes the conditions necessary to drive combustion instability in a rocket engine is given in Eq. (1.4), where γ is the specific heat ratio, c is the speed of sound, ρ is the density of the fluid, and T is the time period of the acoustic oscillation [16].

$$\frac{\gamma - 1}{\rho T c^2} \int_V \int_t p' \dot{q}' dt dV > \int_A \vec{F} \cdot \hat{n} dA + \int_V D dV \tag{1.4}$$

In actual combustors, the oscillations that form and comprise combustion instability are primarily the result of the vibrations produced by the flow and burning of propellant. These flow induced vibrations are formed in a complex process that includes but is not limited to turbulent atomization, vaporization, mixing, and

combustion of the propellants as well as pressure and mass flow oscillations induced from the feedlines, turbopumps and the injector [3].

Minor effects of combustion instability can decrease engine performance, cause variation in thrust output and lead to flight control problems. More importantly, this phenomenon can induce vibration levels greater than 1000 g's which can impair guidance components on the vehicle, damage the payload and can cause failure of the structural members of the rocket. The greatest concern of combustion instability however, is the increased heat transfer to the chamber walls, injector face and nozzle. This can lead to scarring, melting and even destruction of the chamber wall, injector face plate and nozzle of the rocket engine. These severe effects of combustion instability can ultimately destroy the rocket engine [3].

The majority of the progress and knowledge attained in the area of liquid rocket engine combustion instabilities took place prior to the mid-1970s. Important advances in the field have taken place since then but little in the fundamental understanding of this phenomenon has changed. This is a consequence of not having a large and sustained research program that utilizes theory, experiment, and numerical simulation. Some critical knowledge that is missing from the field includes a robust theory for nonlinear aspects of combustion instability and experimental data of linear excitation of combustion instability, whereas linear theory and nonlinear experimental data exists. Also, the coupling between the processes and the feedback mechanisms that excite, sustain and damp combustion instability are extremely complex and more work needs to be completed before a comprehensive understanding can be achieved [14]. The following sub-sections will describe some of the theory and

mechanisms known about combustion instability as well as some techniques used to control combustion instability.

1.1.2 Physical Manifestation of Combustion Instability

Researchers have determined three types of combustion instability that are defined by their respective frequency ranges: low-frequency, intermediate-frequency, and high-frequency. Low-frequency oscillations called "chugging" occur when the oscillation wavelength is much greater than the characteristic dimensions of both the combustion chamber and feed system. Frequencies are typically less than a few hundred Hertz and are usually caused by oscillations produced from the propellant feed system and pumps. Coupling between the combustion process and injector structural assembly has also been known to cause chugging. These types of instabilities are generally the easiest to model and mitigate during the development cycle. Several methods to eliminate chugging include an increase of pressure drop through the injector, decrease the volume of the combustion chamber and increase the length versus diameter ratio in the feed system [3].

High-frequency combustion instability known as "screaming" occurs when the injection and combustion processes interact and couple with one or more of the acoustic resonance modes of the combustion chamber. Screaming is the least understood and the most destructive form of combustion instability. The propellant feed systems generally have a negligible effect upon the excitation of high-frequency instabilities due to the much higher frequencies (typically $> 500\ Hz$) associated with acoustic resonance. Excitation of high-frequency combustion instability is dependent

upon a sustainable energy source and proper phasing between the energy release and pressure oscillations as per the Rayleigh criterion. Some of the mechanisms that contribute to the excitation of high-frequency combustion instability include the propellant injection process, ignition delay time, detonation of propellant droplets, pressure/temperature sensitive chemical kinetics, fluctuations or destruction of spray sheets and droplets due to combustion gas motion, etc. [3].

Screaming is physically manifested in the combustion chamber in the form of the following acoustic wave shapes: longitudinal, transverse and combined modes. Longitudinal (L) modes are standing wave patterns that form along the axial direction of the combustion chamber, where pressure waves reflect off the injector face and the converging section of the nozzle. This mode shape is similar to the common "organ pipe" mode seen in pipes with closed ends. The pressure anti-nodes/velocity nodes are present at the injector plate and throat.

Transverse modes are acoustic waves that form perpendicular to the chamber axis. In typical cylindrical combustion chambers, transverse modes can form as either radial or tangential wave shapes. Radial (R) modes are symmetrical standing wave patterns that form in the radial direction and oscillate from the center of the chamber to the chamber wall and back. Pressure anti-nodes are located at the center and the wall of the chamber. Tangential (T) modes are wave patterns that radiate across the chamber from one side of the wall to the other; in essence, it is similar to liquid sloshing back-and-forth in a cup. The pressure anti-nodes are localized at specific angular locations around the chamber wall. Tangential modes can form as either a standing or spinning mode. Spinning tangential modes often occur in large rocket

engines and cause the angular locations of the pressure anti-nodes to rotate about the chamber wall at some angular velocity. Transverse modes, particularly the tangential modes, are the most destructive and complex modes that can form in a rocket engine as the large pressure oscillations and heat release, up to five times greater than stable combustion, are transferred to localized areas along the chamber wall and engine hardware.

Combined modes are acoustic resonance modes that are excited in the combustion chamber that are any combination of the three wave shapes described above, e.g. the first-tangential first-radial (1T1R) combined mode. In addition, higher order harmonics of the fundamental acoustic mode can be excited in the engine by combustion instability, e.g. second-longitudinal (2L) mode or third-tangential (3T) mode. The pressure and velocity patterns of several transverse modes are shown in Figure 1.5, reproduced from Culick [9].

Sometimes chamber oscillations occur at an intermediate-frequency between a few hundred and one thousand hertz that does not have any of the characteristics of either low-frequency or high-frequency combustion instabilities. These oscillations are typically lumped into a catch-all term called "buzzing." This type of instability generally manifests from the growth of combustion noise at a specific frequency and can also be influenced by structural vibrations of the injector, manifold oscillations and propellant flowrate or mixture ratio fluctuations. In addition, buzzing can be caused by "entropy waves." This effect occurs when axial mixture ratio gradients pass through the sonic point at the throat of the nozzle and emit a pressure wave back upstream to the injector plate. This wave influences the mixture ratio of the burning

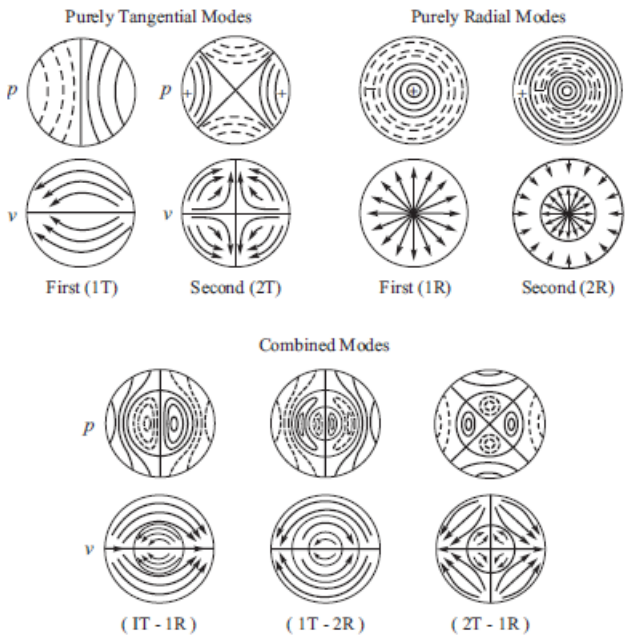

Figure 1.5: Transverse Combustion Instability Modes [9]

propellants near the injector and a new mixture ratio gradient travels downstream towards the nozzle. This feedback mechanism sustains an intermediate-frequency oscillation. Buzzing typically occurs in rocket engines that are designed with large throttling capability as the large changes in propellant injection velocity, atomization, combustion delay, etc. are likely to have an operating point that supports buzzing. If the oscillation amplitude is small, these types of instabilities are not particularly dangerous and tend to cause a decrease in performance and/or thrust oscillations. They can however, couple with the chamber acoustics and develop into high-frequency combustion instability [3].

1.1.3 Excitation Mechanisms

The initiation of combustion instability is generally a nonlinear process where a sustained instability will form if the amplitude of the perturbation is larger than some threshold value and damps out if the amplitude is below that value. Therefore, a single disturbance in the chamber can amplify to sustained combustion instability. The stability of a particular engine is determined by its ability to damp oscillations caused by the perturbation(s) and return to nominal operation [3]. Combustion instability can be initiated spontaneously out of the normal unsteadiness of the combustion process or through a discrete disturbance caused by some trigger mechanism [13].

Combustion instability initiated by spontaneous excitations, also known as soft excitations in the Russian literature [13], is defined as a smooth transition from random combustion noise to combustion instability characterized by organized, self-sustained pressure fluctuations with large amplitudes oscillating at a specific frequency or frequencies inside the combustion chamber. Linear analysis can be used to mathematically describe the growth of combustion instability due to spontaneous excitations as long as the pressure waves are roughly sinusoidal and the oscillation amplitude is below 10% of the mean chamber pressure [3]. Spontaneous/soft excitations typically occur in an engine when the chamber pressure and propellant flow rates are increased. This increases the amount of energy entering the combustion chamber and can cause any pressure oscillations that are present in the chamber to exceed the stability threshold of a particular engine. The possibility of

spontaneous/soft excitations make it difficult to theoretically determine the stability margin of an engine [13].

The majority of combustion instabilities encountered in liquid rocket engines are caused by discrete or hard excitations. The discrete disturbances and the ensuing excitation of combustion instability caused by them exhibit nonlinear behavior. If the amplitude of the disturbance is greater than the critical excitation amplitude and the damping of the engine is insufficient, then self-sustained combustion instability occurs. Discrete excitations are random in nature and may not occur every time the engine operates at the same operating condition. Examples of discrete excitation include "pops" or spontaneous pressure disturbances associated with the normal nonlinear behavior of the propellant mixing and combustion process during steady-state operation and the pressure spikes during engine start-up caused by a hard start [3,13].

The factors that excite combustion instability are probabilistic in nature. A rocket engine can operate at a steady state condition and combustion instability can unexpectedly develop inside the combustion chamber. Also, an identical engine may not experience combustion instability at the same conditions as another due to slight differences caused by manufacturing tolerances. This causes combustion instability as a whole to be extremely difficult to predict and reproduce under test conditions [13].

Therefore, new rocket engine designs undergo a series of tests during the development program to determine its stability rating. Two stability rating criteria exist, statistical stability and dynamic stability. A rocket engine is determined to be statistically stable if the engine never or rarely encountered combustion instability after a large number of test firings. This criterion does not rule out the possibility that

the engine can go unstable. However, the probability of the rocket engine experiencing combustion instability is low for the range of operating conditions tested. Dynamic stability rating determines the response of the rocket engine to transients as well as discrete perturbations for a wide range of system operating conditions. To determine this rating, high amplitude pressure spikes and/or oscillations are artificially excited in the engine and its response is observed. If the oscillations decay rapidly and damp back to the steady state operating condition, the engine is considered dynamically stable for that test condition. An engine that exhibits dynamic stability over a wide range of operating conditions should not experience nor sustain nonlinear combustion instability during flight even under anomalous circumstances [3].

1.1.4 Function of the Injector in Combustion Instability

Liquid rocket engines contain many sources of fluid and pressure fluctuations including but not limited to: turbulent fluid flow, cavitation and oscillations from the turbopumps, vibrations from the control valves, and unsteady acoustic oscillations in the combustion chamber and gas generator. Therefore, the process of propellant injection and the formation of a combustible mixture within the combustion chamber occurs in a regime of highly developed fluctuations that is subject to extensive feedback coupling between the dynamic processes of the combustion chamber, injector, and feed system that form a highly complex self-oscillating circuit [17]. See Figure 1.6, for a simplified diagram reproduced from Culick of the feedback mechanisms present in a liquid rocket engine [9].

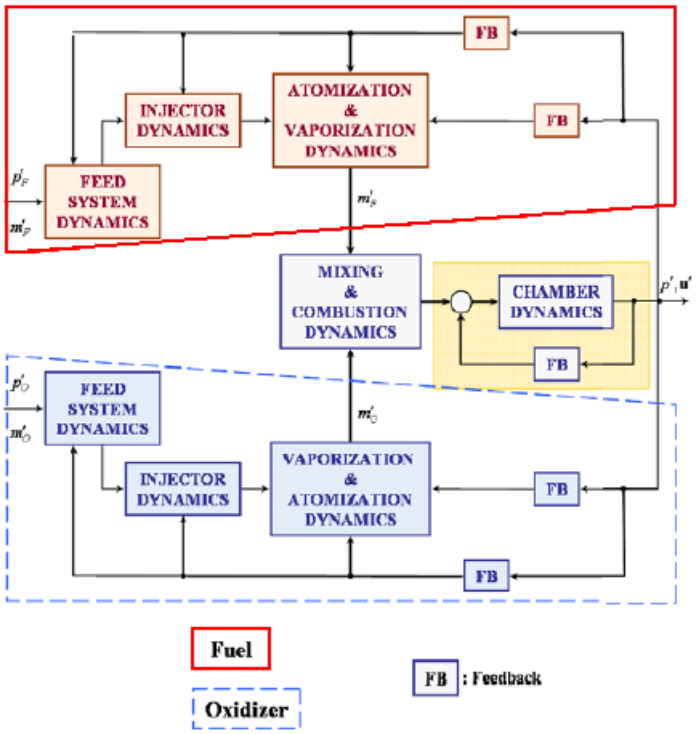

Figure 1.6: Injector Dynamics Diagram [9]

The injection process includes propellant atomization, vaporization, mixing and the initial combustion zone and is subject to all of the feedback couplings between the combustion chamber and other engine components making this the key process for the potential excitation and sustainment of combustion instability. This process is controlled by the injector which not only prepares a combustible mixture but acts as a sensitive element that can generate, modify and respond to flow fluctuations [17].

The fluid inside the combustion chamber of a liquid rocket engine is a mixture of gases and liquid spray. The liquid propellant spray region is confined to a small volume near the injector face while the rest of the chamber is filled with gaseous combustion products. This results in a significant density gradient along the axis

of the chamber. The acoustic pressure gradient is greater in the high-density region near the injector face. As a consequence, the amplitudes of the acoustic oscillations are much larger in the region near the injector face [18].

The injector serves as the dominant player for both intrinsic and injection-coupled feedback mechanisms of combustion instability. Intrinsic feedback mechanisms involve the variation and amplification of sub-processes that occur after the propellant is injected into the chamber which includes: atomization, vaporization, and mixing. The injector itself is only passively involved in the excitation of intrinsic combustion instability but does control the intrinsic mechanisms by determining the spray characteristics of the propellant [19]. The intrinsic mechanisms associated with the injector that are important for the excitation of combustion instability include propellant injection, primary and secondary atomization, liquid heating, droplet vaporization, gas phase mixing and heating, combustion and loss of some of the heat to the fresh propellant. One or several of these mechanisms can affect the onset of combustion instability by either becoming the rate controlling process, the process or mechanism that affects the characteristic time of the rate controlling process, or the mechanism that affects the spatial distribution of combustion which causes a variation in the local response to the pressure oscillations [20].

The rate controlling process has a characteristic time near the time period of the acoustic oscillations in the chamber causing the process to respond strongly to the pressure and velocity oscillations. Table 1.1 shows the characteristic time periods of the acoustic oscillations typically associated with combustion instability as well

as the injection, atomization, vaporization, mixing, and combustion characteristic times [20].

Table 1.1: Characteristic Time Periods of Relevant Processes [20]

Process	Characteristic Time (s)
Acoustic	$10^{-4} < t_{acous} < 10^{-3}$
Injection	$t_{inj} > 10^{-3}$
Atomization	$10^{-8} < t_{atom} < 10^{-5}$
Vaporization	$t_{vap} \approx 10^{-3}$
Mixing	$10^{-5} < t_{mix} < 10^{-3}$
Combustion	$10^{-4} < t_{comb} < 10^{-2}$

In rocket engines operating at subcritical pressure conditions, the liquid heating and vaporization of the droplets are considered the rate limiting process with characteristic times on the order of the resonant frequencies of the combustion chamber [20]. The primary atomization process provides the initial conditions for the combustion process by controlling the droplet size, distribution and velocity [21]. This directly influences the characteristic time of the rate controlling vaporization process [20]. Also, primary atomization process of impinging injectors shed ligaments and droplets in a periodic fashion that has a similar frequency range to combustion instability in rocket engines [21].

Large booster class liquid rocket engines however, typically operate at a pressure and temperature above the critical points of the main propellants. In this

supercritical regime, the surface tension of the propellants becomes very small, causing the characteristic times of both the propellant atomization and vaporization processes to become negligible. In this case, the mixing process of the fuel and oxidizer becomes the rate limiting process and is the dominant mechanism for the feedback between the acoustic chamber oscillations and the injection process [13].

Injection-coupled feedback mechanisms generally occur when the injector resonance frequency couples with one of the resonant frequencies of the combustion chamber. This feedback mechanism leads to fluctuations of propellant flow rate through the injector. Injection-coupled instability is not independent from the intrinsic processes because the phase relationship of the heat release with the pressure oscillations is determined by the intrinsic mechanisms. Coaxial type injectors seem to be more susceptible to injection-coupled feedback mechanisms because the LOX post resonance frequency is generally close to the frequency of one of the fundamental combustion instability modes for large liquid rocket engines [19].

Injector designs can be broadly classed into two groups that describe the primary mechanism by which the injection process couples with oscillations present in the combustion chamber. These groups are broadly split between pressure-sensitive and velocity-sensitive designs. Pressure-sensitive injector designs couple with chamber pressure oscillations and exhibit appreciable oscillations of heat release as a sole function of the local pressure fluctuations. This requires that the main processes that control the dynamic response of the injector to occur within the injector itself. Typical pressure-sensitive injectors have a large recess or a mixing cup below the injector face plate. This allows the critical injection and initial combustion processes

to occur inside the element so that it is shielded from the transverse gas motion present near the injector face plate [22]. Velocity-sensitive injector designs typically have very little or no recess within the face plate. The critical injection, mixing and combustion zone is located above the injector face and is exposed to the transverse "winds" or gas motion caused by acoustic oscillations within the chamber. The strength of the wind is defined by its velocity and is directly proportional to the strength of the acoustic oscillation. Like-doublet injectors have been found to be very sensitive to velocity coupling [3, 15, 23].

Injector impedance is another factor affecting injector sensitivity to oscillations and its ability to excite or sustain combustion instability. It is desirable to maintain a constant flow rate through the injector during steady state engine operation. The mean injection flow rate is dependent upon the chamber pressure, manifold pressure and injector impedance. The instantaneous flow rate varies due to the pressure fluctuations present in both the chamber and manifold. Engine stability is generally improved by increasing the injector impedance and decreasing the injector manifold volume. The impedance is proportional to both the orifice resistance and inertance. The inertance is the tendency for the flow rate through the injector to remain constant despite instantaneous pressure drop fluctuations. The resistance describes the pressure drop across the orifice required for a given mass flow rate. An equation that relates the pressure drop through the injector and the mass flow rate of propellant is expressed in Eq. (1.5), where Γ and Υ are the injector resistance and inertance respectively [3].

$$P_m(t) - P_c(t) = \Gamma \dot{m}^2(t) + \Upsilon \frac{d\dot{m}(t)}{dt} \tag{1.5}$$

$$\Gamma = \frac{\Delta \bar{P}_{inj}}{\dot{m}^2} \tag{1.6}$$

$$\Upsilon = \frac{l_{eff}}{gA_o} \tag{1.7}$$

1.1.5 Damping and Controlling Combustion Instability

Liquid rocket engine "chamber dynamics will become unstable if the rate of energy gains exceeds the rate of energy loss in the frequency range covering [a particular chamber] mode [9]." There are three possible techniques that can lessen or eliminate combustion instability. These techniques work by reducing the driving energy gains in the system, increasing the energy losses (damping) of the system, or shifting the frequency response of the thrust chamber so the acoustic response peaks are outside of the area where the rate of energy gain is greater than the rate of energy loss [9].

There are various devices and methods that can be used to damp or eliminate combustion instability oscillations that arise in liquid rocket engines. These methods can be broadly separated into two groups: passive control and active control. All past and present operational propulsion systems have utilized passive control methods and devices to control combustion instability. Active control methods are currently in development and have had some success in laboratory demonstrations but successful

implementations for operational liquid rocket engines have yet to be found. Current research is continuing to explore the fundamental mechanisms, design criteria and configurations of both passive and active control methods [9].

1.1.5.1 Passive Control

Passive control devices work by either reducing the coupling between the oscillations and the driving combustion processes or by increasing the damping of the system. The two most commonly used passive control designs for liquid rocket engines are injector plate baffles and resonance absorbers in the thrust chamber. Often, both devices are used concurrently in a liquid rocket engine. Baffles control combustion instability through increased damping and reduced coupling between the oscillations and driving processes. Resonators serve to increase damping of the combustion chamber [24]. Another method adjusts the geometry and design of the injectors themselves in the thrust chamber to naturally damp any oscillations that may occur. This can involve specific injector face plate patterns, injectors with varying lengths and diameters or even using different types of injectors in the chamber [13]. Figure 1.7 shows a cutaway drawing of a thrust chamber with both baffles and acoustic absorbers, reproduced from NASA report SP-194.

Baffles: Baffles are structures, often in the form of tuned blades, mounted to the surface of the injector face that extend axially into the combustion chamber to create multiple, small compartments near the injector face. Baffles are effective in providing a stabilizing effect upon transverse combustion instability modes and can

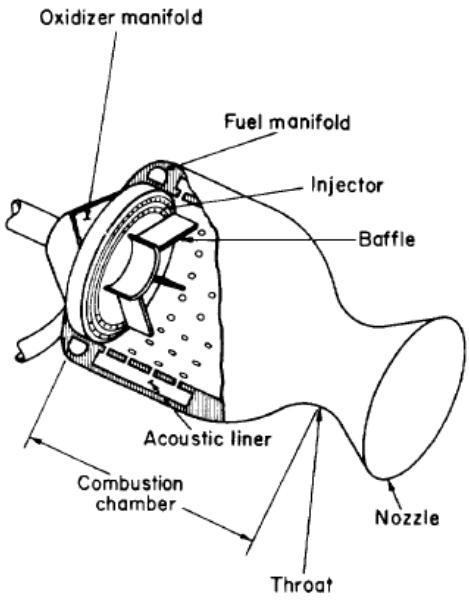

Figure 1.7: Cutaway of Thrust Chamber with Passive Control Devices Installed [3]

prevent hard or dynamic excitations from causing combustion instability and limit the magnitude of soft excitations [9, 13, 24, 25]. Injector face plate baffles have no effect on longitudinal modes nor feed-system coupled instabilities [24].

There is not a well-defined design criterion that allows the engineer to select an appropriate number of baffles, baffle configuration or baffle length that will guarantee stable operation. Most baffle designs for operational liquid rocket engines rely upon empirical data gathered from previous engines with similarly sized thrust chambers and propellant combinations [24]. The baffle configuration of operational liquid rocket engines have used either a number of radial baffle blades or a hub-and-spoke design which utilizes a combination of radial and circumferential (hub) baffle blades. Radial baffles consist of blades projected outward from the center of the injector face to the chamber wall in the radial direction and are used to distort the acoustic wave

by obstructing particle motion in the tangential direction and therefore are useful in the damping of tangential instabilities. Circumferential baffles are circular blades of constant radius that are used to restrict motion in the radial direction and hence damp radial instabilities [25].

Baffle orientation with respect to the acoustic field is important [25] and it has been recommended to place the radial and circumferential baffles at the acoustic pressure node(s) of the particular instability mode(s) of interest. This region corresponds with the acoustic velocity anti-nodes and maximum particle displacement. The presences of the baffle blade forces the region to become a velocity node [24, 25].

Unconventional baffle designs such as non-uniform spacing and non-radial configurations have been proposed as a method for achieving greater stability for a specified number of baffles. However, the limited hot-fire experimental studies of these designs have failed to find any advantages over the conventional radial or hub-and-spoke designs [24]. Figure 1.8 reproduced from the NASA SP-8113 report, illustrates some top-view sketches of various conventional and unconventional baffle designs.

Several proposed mechanisms of how baffles suppress combustion instability include: disruption of transverse gas particle motion, shielding the sensitive initial injection and combustion region from the transverse acoustic flow motion, increased damping caused by dissipation of acoustic energy due to vortex shedding from the blade tip and visco-acoustic interactions at the tips of the baffle blades, and modification of acoustic properties of the combustion chamber that reduces

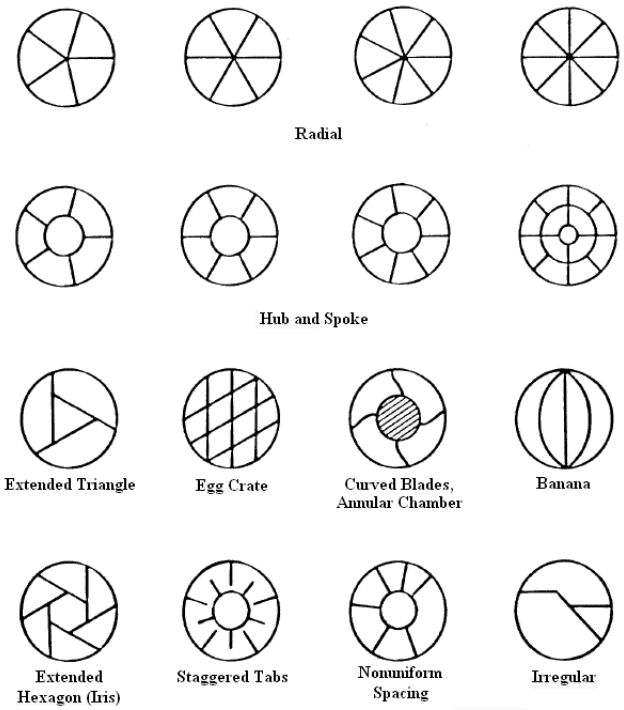

Figure 1.8: Various Baffle Designs [24]

coupling [24, 25]. Inside the baffle compartments, the transverse flow oscillations are turned so the flow oscillates in the longitudinal direction. This affects system stability by changing the local combustion response and acoustic frequency serving to uncouple the compartment from the bulk chamber oscillations. However, this effect causes high-amplitude pressure oscillations on the injector face which can be a problem if the injector or near-injector combustion process is pressure-sensitive [25].

The presence of baffles on the injector face has some drawbacks. Its placement on the injector plate requires discontinuities in the injection pattern which leads to irregularities in the propellant mixture and combustion flow field causing a reduction in combustion efficiency and engine performance. Baffle hardware also requires a suitable cooling strategy to survive the harsh environment inside the combustion

chamber. Finally, the addition of baffles increases the weight of the engine and causes greater design/manufacturing complexity and cost [3, 24].

Resonance Absorbers: Resonance absorbers, also known as resonators, are present as tuned cavities recessed inside acoustic liners attached to the inner surface of the chamber wall. The resonance absorber damps acoustic energy and oscillations by causing internal energy losses to the flow through fluid dynamic resistance caused by viscous jet losses at the throat of the cavity. The capability of the resonator to damp chamber oscillations is dependent upon the acoustic impedance of the absorber [13, 24].

The cavities are installed in arrays along and around the inside wall of the chamber and spaced appropriately to absorb the oscillation peaks. Resonators provide damping capability for both transverse and longitudinal modes. The most effective axial location to damp transverse combustion instability modes is near and adjacent to the injector face plate. Also, the size and shape of the cavities can be tuned to absorb specific frequencies. The most common designs include: Helmholtz resonators, quarter waves, variable quarter waves, and L-shaped resonators [3, 13, 24]. These designs are shown in Figure 1.9, reproduced from Cavitt. Past research, has found the Helmholtz resonator to possess the greatest damping capability compared with the other resonance absorber designs. This is due to the ability of Helmholtz resonators to absorb a wide range of acoustic frequencies while requiring the smallest number of resonators for optimal damping [26].

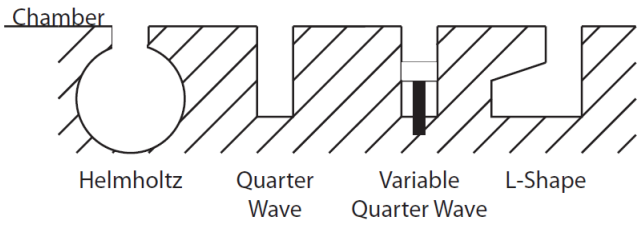

Figure 1.9: Various Resonance Absorber Designs [27]

Resonance absorbers can work effectively if they are optimally designed and fine-tuned to a specific frequency. However, they tend to have less reliability compared with baffles in controlling combustion instability. Some benefits of resonators compared with baffles include an established design criteria and the ability to install the devices without having to complete a major re-design of the injector/combustor [26]. Similar to baffles, resonance absorbers add weight and complexity to the thrust chamber [24].

1.1.5.2 Active Control

Active control devices utilize closed-loop control where current system operation is modulated in a manner that is dependent upon the recent state of the system. As opposed to active noise control or cancellation, active control of combustion processes does not attempt to remove combustion instability through destructive interference of the acoustic waves. Instead, the active control process attempts to cause favorable disruption of the primary energy sources. One method used, modulates the propellant injection and spray characteristics in ways that improve both combustion performance and stability [9].

Fast controllers seek to modulate propellant flow rates so that the burning rate of the propellant (heat release) is out of phase with the pressure oscillations in the combustion chamber. This serves to directly cut the main coupling process which helps damp the oscillations. Implementation of fast controllers has been hindered due to a decrease in actuator response as instability frequency increases which may limit its effectiveness against high-frequency combustion instability. Also, there are concerns that the actuator will fail when operating at high frequencies for extended periods of time [28].

An alternative approach is to use slow controllers which attempt to damp the instability oscillations through changing the feedback process by preventing the transfer of energy from the heat release of combustion to the acoustic oscillations. This can be accomplished by changing the spray characteristics of the liquid propellant stream to change the vaporization and hence combustion time scales which serves to decouple the process from the acoustic time scale reducing the chance of developing combustion instability. In addition, the slow controller can prevent combustion instability by increasing the stability margin of the engine through modulating the propellant injection characteristics. It has been experimentally demonstrated that an increase in the stability margin of the engine correlates with a decrease in pressure oscillation amplitude [28].

1.2 Characteristics of Liquids and Liquid Flow

1.2.1 Bulk Modulus and Density

Liquid propellants typically have a large bulk modulus value. The bulk modulus describes the differential change in pressure required to cause a differential change in volume of the fluid element and hence density of the fluid. The values are typically large enough to ignore the very slight change in volume and assume the density remains constant over a large pressure range. Liquids therefore are often modeled as incompressible fluids. An increase in fluid temperature however, tends to decrease fluid density. However, this density change is relatively small for large variations in liquid temperature [29].

Liquids with greater densities for a given volumetric flow rate have a higher kinetic energy. This will facilitate the disintegration process leading to the development of smaller droplets. However, the significance of liquid density on the overall atomization process is considered small because the density change of the liquid over a range of operating conditions is slight and also it is nearly impossible to significantly affect the density without changing some other physical property of the liquid [30, 31].

1.2.2 Viscosity

Fluids deform continuously when subjected to a shearing stress of any magnitude. The rate of shear strain of the fluid is proportional to the applied shear stress [29].

$$\tau \propto \frac{dv}{dy} \tag{1.8}$$

The actual strain rate for a given shear force is fluid dependent upon and is subject to frictional effects when motion occurs. This frictional effect is known as viscosity and is caused by the cohesion and momentum exchange between the molecules in the fluid. The shear stress proportion, Eq. (1.8), can then be modified to form an equation that calculates the amount of shear stress required to cause a particular strain rate for a given fluid by inserting a fluid specific proportionality constant into the equation (μ). μ is known as the absolute or dynamic viscosity of the fluid and has units of ${}^{N-s}/_{m^2}$ [29, 32].

$$\tau = \mu \frac{dv}{dy} \tag{1.9}$$

For most common fluids i.e. water, air, and oil, the required shear stress is linearly proportional to the shear strain rate. These fluids are known as Newtonian fluids. Fluids whose shear stress is not linearly proportional to the strain rate are known as non-Newtonian fluids. Non-Newtonian fluids can be either shear-thinning or shear-thickening. Shear-thinning fluids have apparent viscosities that decrease with increased strain rates. Shear-thickening fluids have apparent viscosities that increase with increased strain rates. The viscosity of a fluid is very sensitive to changes in temperature. For liquids, the viscosity decreases with an increase in temperature due to the reduction in the cohesive forces between the molecules. Often, problems in

fluid mechanics use the kinematic viscosity (ν) which is the ratio between the absolute viscosity to the density of the fluid and has units of $^{m^2}/_{s}$ [29].

Viscosity can be considered the most important physical property of the liquid. Even though the influence of viscosity on the atomization process is roughly equal to that of surface tension, it also affects the flow rate through the injector as well as the overall spray pattern. Viscosity inhibits the growth of instabilities on the surface of the liquid jet or sheet serving to delay the onset of breakup. Consequently, liquids with greater viscosities tend to generate larger droplets when atomized [30, 31].

1.2.3 Surface Tension

Apparent tensile forces form a thin "membrane" over the surface of a liquid when that liquid is in contact with a gas, another immiscible liquid, or a solid. This phenomenon is due to the unbalanced cohesive forces that act upon the molecules of the liquid at the interface. Interior liquid molecules away from the interface are surrounded by other liquid molecules which create a balance of cohesive forces in all directions. At the interface, the cohesive forces of the liquid layer just interior of the surface is not balanced by the layer just above the surface causing the surface molecules to be tightly bound to the interior molecules and to each other forming a "membrane." The strength of the cohesive force per unit length of the molecules at the surface of the liquid is known as surface tension (σ) [29, 32].

The surface tension can be defined as the differential change of surface energy required to cause a differential change in surface area of the liquid as seen with Eq. (1.10) [31].

$$\sigma = \frac{dE_A}{dA} \tag{1.10}$$

Equation (1.10) has units of $^{J}/_{m^2}$ which can be simplified to $^{N}/_{m}$. The magnitude of the surface tension is dependent upon the fluid or solid in contact with the liquid and the temperature of the liquid. An increase in temperature causes a decrease in surface tension due to reduced cohesion between the liquid molecules [29, 32].

Atomization is a method to disintegrate the bulk liquid into a spray of small droplets. Surface tension is a vital physical property for the atomization process because it provides the resisting force against the increase of surface area. All liquids attempt to form a state of minimum free energy at the surface which happens to be a spherical shape. Therefore, atomized liquid will tend to form spherical drops. The minimum energy required to atomize a liquid is equal to the surface tension multiplied by the change in surface area. Therefore liquids with high surface tension will form droplets with larger diameters for the same conditions compared with a low surface tension liquid [30,31]. In addition to atomization, surface tension is important in other fluid mechanics situations such as the movement of liquid through porous materials, formation of bubbles, and the flow of liquid films or sheets [29, 32].

1.2.4 Vapor Pressure and Cavitation

Liquids have a tendency to change phases from liquid to vapor when exposed to a gas such as air. This vaporization occurs because the liquid molecules at the surface

have sufficient momentum from their thermal vibrational energy to overcome the intermolecular cohesive forces and escape the surface. These vaporized gas molecules exert a partial pressure upon the liquid known as the vapor pressure. The vapor pressure is dependent upon and proportional with temperature. Boiling occurs when the external pressure is at or below the vapor pressure of the liquid causing vapor bubbles to be present throughout the liquid mass. Therefore, the boiling point is dependent upon both the temperature of the liquid and imposed pressure. Volatile liquids possess relatively high vapor pressures and hence vaporize easily [29, 32].

In many engineering situations, components such as valves, pumps, turbines, etc. can accelerate the liquid flow to the point where the local absolute static pressure is at or below the vapor pressure of the liquid. At this point, local boiling occurs resulting in the development of vapor filled bubbles or cavities that are convected downstream with the bulk flow. These vapor bubbles collapse suddenly when they reach a region of lower flow velocity and a local static pressure that is higher than the vapor pressure of the liquid. The formation and destruction of these vapor bubbles in a flowing liquid is known as cavitation. The dynamic effects of the implosion of vapor bubbles and the sudden rush of liquid to fill the void produces very large pressure spikes that can be as high as 690 MPa. Cavitation near a structural component can cause severe damage through pitting of the surface and repeatedly stressing the material beyond its elastic limit resulting in fatigue and eventual failure [29, 32].

1.2.5 Relevant Dimensionless Number Groups

Fluid mechanics makes use of a concept called similitude to extend or compare the results of one system to other similar systems. One method is to describe important results in the form of dimensionless parameters. Dimensionless parameters describe the underlying physics of the problem regardless of the geometry of the system, fluid properties, and external effects such as pressure, temperature and velocity. Several dimensionless number groups are useful for determining and comparing the flow characteristics seen with rocket injectors and include the: Reynolds, Weber, Ohnesorge, Strouhal, and cavitation numbers [29].

The Reynolds number (Re) is one of the most famous and important dimensionless numbers used in fluid dynamics. It is a relation that describes the magnitude of the fluid inertial forces to the viscous forces and is shown in Eq. (1.11).

$$Re = \frac{\rho v l}{\mu} \tag{1.11}$$

The Reynolds number is used to help determine whether the flow is laminar or turbulent. For $Re < 1$, the viscosity of the fluid is the dominant mechanism and the flow is described as creeping. For pipe flow, $Re <$ 2,100 is typically considered laminar and $Re >$ 4,000 considered turbulent. In between is considered the transition region. In contrast, flow over a flat plate transitions from laminar to turbulent when $Re \sim$ 500,000. These values are not exact and are subject to flow and design parameters such as surface roughness, entrance design and flow disturbances [29].

The Weber number (We) is important in fluid dynamics when there is an interface between two different fluids. Some typical examples where the Weber number is important for describing the phenomena of interest include the flow of thin liquid sheets, the formation of droplets, and the formation of vapor bubbles. For these types of problems, the surface tension of the liquid(s) plays a substantial role in the flow characteristics. The Weber number relates the magnitude of the fluid inertial forces to the surface tension forces and is shown in Eq. (1.12) [29, 32].

$$We = \frac{\rho v^2 l}{\sigma} \tag{1.12}$$

The Ohnesorge number (Oh) is an important relation that is used when describing the breakup characteristics of liquid jets and ligaments as well as the formation of small droplets. The number is a relation of the magnitude of the viscous forces to the surface tension forces of the liquid. It is found by dividing the square root of the Weber number by the Reynolds number as shown in Eq. (1.13) [33].

$$Oh = \frac{\sqrt{We}}{Re} = \frac{\mu}{\sqrt{\rho \sigma l}} \tag{1.13}$$

The Strouhal number (St) is a relation that becomes important for unsteady, oscillating fluid flow. It is a relation of the magnitude of the unsteady forces of the flow to the inertial forces due to flow convection. The Strouhal number is described in Eq. (1.14), where ω is the natural frequency of the oscillation [29].

$$St = \frac{\omega l}{v} \tag{1.14}$$

The cavitation number (K_c), described by Eq. (1.15), is used to characterize the cavitation potential of a particular flow. It is a ratio of the pressure differential between the absolute and vapor pressure of the liquid to the inertial forces (kinetic energy) of the flow [29, 32]. The probability and intensity of cavitation tends to increase with smaller cavitation numbers. $K_c < 1$ generally indicates the existence of fixed cavitation. Negative values of K_c generally indicate the presence of strong or supercavitation [34].

$$K_c = \frac{P - P_v}{{}^1\!/_2\ \rho V^2} \tag{1.15}$$

1.2.6 Laminar and Turbulent Flow Regimes

Real fluids (viscous) have flow characteristics with greater complexity compared with ideal (inviscid) fluids. Three flow regimes occur in real fluids that produce distinct differences in flow characteristics, velocity profiles, and other phenomena. Real flows can be laminar, transitional or turbulent. The transitional or semi-turbulent regime has characteristics of both the laminar and turbulent regimes. During transition, weak bursts of turbulence can randomly appear in the overall laminar flow that become stronger and more frequent as the flow transitions closer to the fully-turbulent regime. In addition, the semi-turbulent regime can consist of a turbulent core surrounded by a laminar envelope [29, 30].

The laminar flow regime consists of smooth streamlines where the fluid particles are constrained, due to viscosity, to travel in parallel paths with all of the other fluid particles. Agitation and diffusion is on the molecular scale only. Laminar

flow will quickly damp any disturbance that may appear and return to smooth flow through viscous dissipation [32]. Laminar flow is more likely to occur with fluids with high viscosity, low flow velocity, the absence of flow disturbances, and rounded or chamfered orifice entrances. An initially laminar flow will remain laminar if the Reynolds number remains below the critical value regardless of disturbances. In the absence of disturbances, it is possible for an initially laminar flow to remain laminar for Reynolds numbers much greater than the nominal critical value, however only a small disturbance is required to trip the flow into becoming turbulent [30].

In the turbulent flow regime, fluid particles travel along random paths that allow the particles to move past and collide with each other in a haphazard manner causing the velocity field to vary erratically in both position and time. Turbulent flow consists of eddies which can be defined as individual regions of coherent turbulent motion. Eddies can have a wide range of length scales with the largest being on the same order as the characteristic length scale of the boundary. Large eddies are unstable and tend to breakup into a number of smaller eddies. This breakup and energy transfer process continues until the smallest eddies eventually dissipate. Turbulent flows are sensitive to the unavoidable random fluctuations of fluid properties, initial conditions and boundary conditions. The turbulence intensity generally increases with an increase in average flow velocity. Also, the scale of turbulence generally increases with boundary dimensions. The characteristics of turbulence give the flow the ability to mix and transport fluids much more effectively than laminar flows [35]. Turbulent flow is more likely to occur with sharp orifice entrances, rapid changes in cross-sectional area, large tube size, high flow velocity, and

with the presence of disturbances. An initially turbulent flow will remain turbulent as long as the Reynolds number is greater than the critical value [30].

A solid boundary affects the flow phenomena near the surface. At the surface, the fluid molecules stick to the solid boundary causing the velocity to be equal to zero. This is known as the no-slip condition. Due to viscosity, the velocity of the fluid particles near the surface are slowed forming a region of some thickness where the fluid velocity is less than 99% of the freestream velocity. This region is known as the boundary layer. Surface roughness can affect turbulent flow near the boundary by introducing local unsteadiness into the fluid. Laminar flow is not affected by surface roughness and is characterized by a parabolic velocity profile. For smooth surfaces, the turbulent flow is separated from the boundary by a viscous sub-layer. Near the boundary, the available mixing length is close to zero which inhibits the turbulent mixing process (small Reynolds number) and extinguishes any turbulence that may be present causing the flow within the viscous sub-layer to be laminar. Surface roughness augments turbulence and reduces the thickness of the viscous sub-layer by introducing small eddies near the boundary. Whether or not the surface is considered smooth or rough depends upon the size of the protuberances on the surface with respect to the thickness of the sub-layer as well as the fluid Reynolds number. Large Reynolds numbers correlate with thinner viscous sub-layers. Outside of the viscous sub-layer, the mean velocity of the turbulent flow is uniform giving a flat velocity profile [29,32].

1.3 Liquid Jet Breakup

The design of like-doublet impinging injectors requires two liquid jets injected into a gaseous environment to impinge upon each other some distance downstream of the two orifices [5]. The resulting spray characteristics will be dependent on the condition of the liquid jets at the impingement point [36]. Therefore, the breakup lengths of the liquid jets, the breakup regimes, and the internal orifice flow characteristics are important in determining the spray pattern of like-doublet injectors.

The breakup of liquid jets injected into a stagnant gaseous environment has been extensively studied in the literature. Liquid jet breakup is commonly divided into breakup regimes that describe the changes in appearance and the dominant breakup mechanisms of the jet under various operating conditions. The breakup process is very complex due to the large quantity of variables and parameters including but not limited to the: operating conditions, physical and thermodynamic properties of the liquid jet and gaseous environment, turbulence, cavitation, and orifice design [37].

The initial condition of the liquid jet when it exits a round orifice is a continuous cylindrical body with a spray angle typically between 2° and 10°. At the jet surface, competition between the cohesive and destructive forces cause perturbations to form along the surface. If favorable conditions exist the aerodynamic and hydrodynamic forces amplify the perturbations leading to an increase of the liquid

jet surface area until the jet becomes unstable causing the liquid jet to disintegrate into droplets [30].

It is likely that no single mechanism is responsible for the breakup of liquid jets. Instead, a combination of factors and mechanisms are at play. Breakup is the end result of a complex interaction between the inertial, viscous and surface tension forces. The viscosity of the liquid tends to damp the growth of any disturbances. The aerodynamic and inertial forces will promote disturbance growth along the surface. Surface tension acts to pull the liquid molecules at the surface together. Pressure oscillations and liquid turbulence will influence the dynamics of and tend to promote breakup of the liquid jet [30, 31]. An increase in ambient gas pressure and density promotes jet breakup leading to shorter breakup lengths and an increase in the spray angle of the jet [30, 34].

The effects of aerodynamic forces increase exponentially as the Reynolds number is increased for a particular Ohnesorge number. However, liquid jets can breakup in the absence of aerodynamic forces through the effects of turbulence, cavitation, or abrupt velocity profile changes that occur when the liquid exits the injector [38]. Changes of the jet velocity profile after it exits the orifice can have a profound effect on the stability of the jet. Once the liquid leaves the orifice and the physical constraints of the walls are removed, the velocity profile tends to flatten in a process known as velocity profile relaxation. This occurs due to momentum transfer between the radial layers of the jet causing internal motions within the jet. Laminar flow with its initial parabolic velocity profile has a kinetic energy per unit mass of fluid equal to 2 while the kinetic energy per unit mass of ideal plug flow, which has a flat

velocity profile, is equal to 1 for the same average jet velocity. As the laminar parabolic profile flattens, the kinetic energy per unit mass of the jet reduces from 2 to 1 requiring considerable energy redistribution within the jet leading to substantial disturbances that promote jet breakup. Turbulent flow is thought to be less susceptible to the effects of velocity profile relaxation due to its velocity profile being nearly flat and having a kinetic energy per unit mass of fluid equal to approximately 1.1 or 1.2 [30]. The following sub-sections will describe the liquid jet breakup behavior in a stagnant gaseous environment and describe some of the effects that originate within the orifice that influence the jet breakup characteristics.

1.3.1 Breakup Regimes

Four main liquid jet breakup regimes exist for liquid injected into a stagnant gas environment based upon varying levels of liquid jet inertia. The regimes in order of increasing liquid inertia are known as:

- Rayleigh regime,
- 1^{st} wind-induced regime,
- 2^{nd} wind-induced regime,
- Atomization regime.

See Figure 1.10 for representative drawings of each of the four liquid jet breakup regimes as presented by Tseng et al. [39]. Sirignano and Mehring present a plot that shows the regions where each breakup regime likely appears as a function

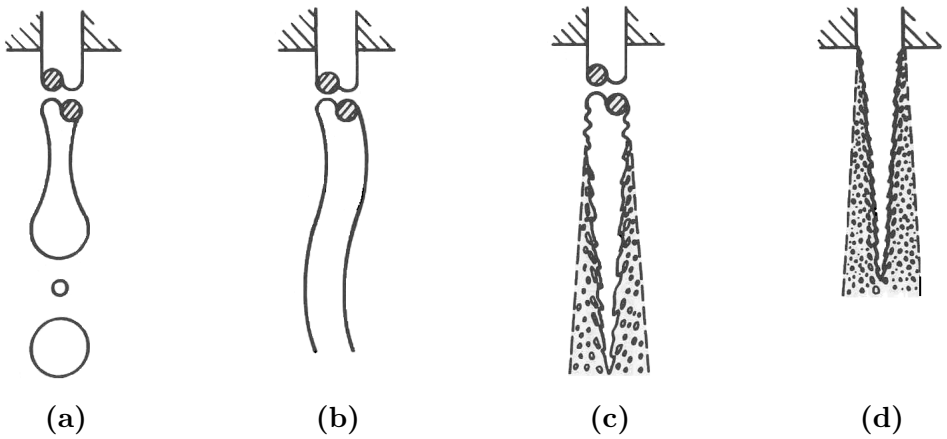

Figure 1.10: Jet Breakup Regimes: (a) Rayleigh, (b) 1^{st} Wind-Induced, (c) 2^{nd} Wind-Induced, and (d) Atomization [39]

of Weber number versus Reynolds number, see Figure 1.11 [40]. Of the four breakup regimes, only the Rayleigh breakup mechanism has a solid theoretical background and can be derived analytically [30].

The Rayleigh breakup regime occurs at the lowest values of liquid Reynolds and Weber numbers and corresponds with low-speed, laminar jets. For these flow conditions, the surface tension force is the dominant breakup mechanism. Dilatational disturbances with wavelengths greater than the jet circumference are able to be amplified and grow along the surface of the jet due to the surface tension forces of the liquid. In particular, dilatational oscillations with a wavelength equal to $4.51d_o$ have the fastest growth rate and will cause the jet to become unstable and breakup into large drops with a diameter equal to $1.89d_o$. All unsymmetric (sinuous) waves and axisymmetric waves with wavelengths less than the jet circumference are damped out. The large drops are formed and shed from the end of the jet many jet diameters

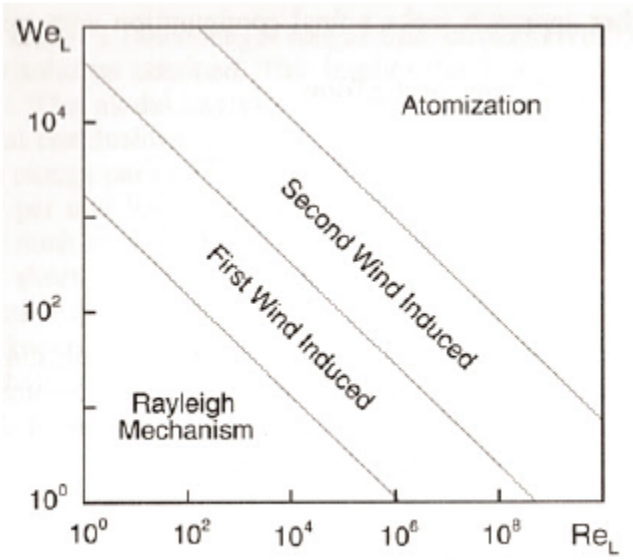

Figure 1.11: Jet Breakup Regimes as Functions of the Reynolds and Weber Numbers [40]

downstream of the orifice exit. This occurs when the amplitude of the dilatational oscillations grow to a point where the drop is connected to the intact jet only by a thin liquid cylinder forming a characteristic dumbbell shape. The drop breaks free from the jet when the ends of the connecting cylinder are pinched off. The connecting cylinder in turn becomes unstable shedding small droplets that coalesce into a single small satellite droplet that falls behind the large main droplet [30, 37, 38].

In the 1^{st} wind-induced regime, the aerodynamic force due to the presence of stagnant ambient gas becomes large enough to have an effect upon the breakup process of the liquid jet. Large unstable, sinusoidal oscillations with long wavelengths appear and grow along the surface of the jet. Droplets about the same diameter as the jet are pinched off the end of the jet many diameters downstream of the orifice exit [37, 38, 40].

The 2^{nd} wind-induced breakup regime appears at even greater jet Reynolds and Weber numbers. In this regime, the aerodynamic forces play a greater role in the breakup of the jet. Droplets are torn from the surface of the jet by the initiation and growth of unstable, short wavelength, sinuous surface waves. Droplet sizes tend to be smaller than the diameter of the liquid jet [37, 38, 40].

The atomization regime appears at the highest values of Reynolds and Weber numbers. This regime is characterized by the immediate breakup of the jet at the exit of the orifice. Instead of an intact liquid jet, the core can be described as a dense cloud of very small droplets. The mechanisms that produce the results observed with this regime are not completely understood [37, 38, 40].

The four regimes described above are general descriptions of the breakup process for liquid jets in a gaseous atmosphere. The breakup of a turbulent water jet exposed to air at standard temperature and pressure does not neatly fit into the one of the breakup regimes described. In this case, aerodynamic effects are very small ($\frac{\rho_{liq}}{\rho_{gas}} > 500$) and viscosity has a negligible effect on jet breakup due to the small Ohnesorge number. Exiting the orifice, the turbulent jet is covered by small, random protuberances caused by the motion of the turbulent eddies with characteristic dimensions proportional to the orifice diameter. Small scale turbulence within the jet decays. Some distance downstream of the exit, the liquid jet forms lateral kinks that are neither sinuous nor do they form as regular surface waves either in plane or as a helix but rather the kinks are random and unsymmetrical in nature which suggests their formation is due to the large scale turbulence distorting the jet [41–44].

The distortion and motion caused by the large eddies initiate the breakup process of the liquid jet and droplet formation on the surface of the jet. Droplets are formed when the kinetic energy of the turbulence is greater than the required surface energy and has sufficient time to deform the liquid surface enough to allow the surface tension forces to form a droplet of comparable size to the eddy and the diameter of the jet. The detailed breakup process is governed by the Weber number of the jet. For low to moderate Weber numbers ($We < 5{,}200$), the turbulent jet is destroyed when large droplets are formed and detached from the end of the liquid column by this axisymmetric disturbance. The breakup length of the jet increases with the Weber number. This process has been called Turbulent Primary Breakup and occurs for jet flow conditions (We & Re), typically associated with the 1^{st} Wind-Induced breakup regime but with the absence of significant aerodynamic excitation [41–44].

For higher Weber numbers ($5{,}200 < We < 17{,}000$), turbulence produces small scale surface roughness near the exit of the orifice. These disturbances grow until small droplets begin to be torn from the surface of the liquid column prior to the bulk breakup of the jet. These small droplets surround the jet core as a cloud. The core breaks up into large droplets far downstream similar to the 1^{st} Wind-Induced and Turbulent Primary breakup regimes. The stripping of small droplets from the surface of the turbulent jet is similar to the 2^{nd} Wind-Induced regime described previously. At high Weber numbers, the large scale turbulence can distort the core to such a degree that the kinks experience crossflow. Bag-like structures are formed along the surface of the distortion which eventually burst into small droplets. For Weber numbers above 17,000, surface breakup begins at the orifice exit [41–44].

1.3.2 Jet Breakup Length

The breakup of liquid jets is controlled not only by the surface instabilities and interfacial forces between the liquid and the environment but also by the internal flow characteristics originating within the orifice. These characteristics include the turbulence intensity of the flow, cavitation, and hydraulic flip. The presence and intensity of these three characteristics change the breakup behavior of the liquid jet and are strongly dependent upon the orifice geometry [34]. The effect of orifice length-to-diameter ratio, (l_o/d_o), on the jet breakup length is minimal and past experiments show no clear trend [30]. The transition from one jet breakup regime to the next as well as the breakup length of the jet for a given back pressure is governed by the velocity of the liquid jet and the internal flow conditions as demonstrated in the qualitative plot shown in Figure 1.12. The descriptions of the liquid jets were taken from Lefebvre and Hiroyasu [30, 34].

The region between points A and B seen in Figure 1.12 is characterized by a smooth jet with laminar flow. Jets in this region breakup due to the Rayleigh mechanism from axisymmetric disturbances driven by surface tension forces. The jet breakup length increases with velocity until the jet velocity reaches the critical velocity at point B [30]. The jet breakup length for the region between A and B can be predicted using the empirical correlation, Eq. (1.16), found by Grant and Middleman. This relation breaks down when the jet velocity approaches point B [45].

$$\frac{l_b}{d_o} = 19.5 \left(We_j^{0.5} + 3\frac{We_j}{Re_j} \right)^{0.85} \tag{1.16}$$

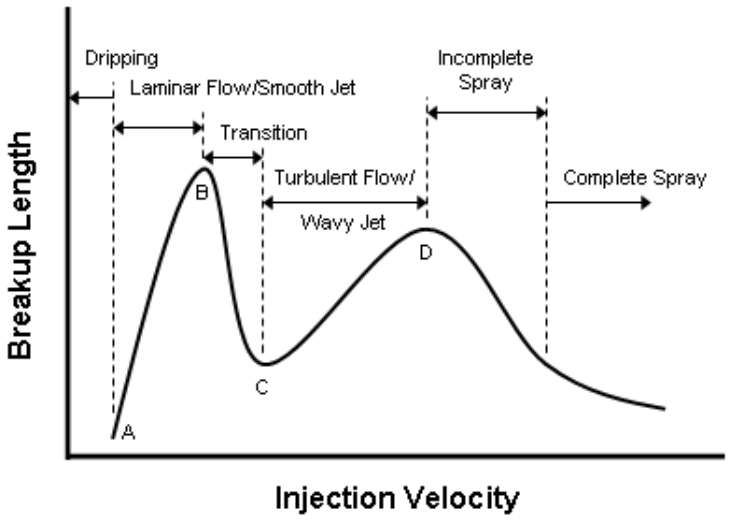

Figure 1.12: Qualitative Jet Breakup Length vs. Injection Velocity

Point B represents the longest breakup length for laminar liquid jets. The region beyond point B corresponds to the transition between laminar and turbulent jet flow as well as the region where aerodynamic forces begin to have an effect upon the breakup of the jet. The breakup length of the jet decreases rapidly beyond point B [30, 45]. The jet Reynolds number at transition point B, can be calculated with the empirical correlation by Grant and Middleman as seen in Eq. (1.17) [45].

$$Re_B = 325 Oh_j^{-0.28} \tag{1.17}$$

The jet transitions into fully-turbulent flow at point C in Figure 1.12. As the jet velocity is further increased the jet breakup length is seen to increase once again for the region between points C and D. It has been suggested by Eisenklam, Hooper and Rupe that the reduced effects of velocity profile relaxation for turbulent jets

would account for the increase of the breakup length as seen in this regime [30]. This interesting result can mislead one into thinking that turbulence enhances the stability of the jet. This is an incorrect assumption because the stability of the jet must be determined by the jet breakup time. Breakup time can be calculated by dividing the jet breakup length by the jet velocity (l_b/v_j). In this region, it has been experimentally found that the jet breakup time decreases, i.e. jet is less stable, with an increase of jet velocity [45]. The work of DeJuhasz and Schweitzer support the notion that the radial velocity components introduced by turbulence produce disturbances on the surface of the jet that promote disintegration [30]. Several empirical correlations have been developed to determine the breakup length of turbulent jets in the C-D region. The first, Eq. (1.18), is from the work of Grant and Middleman [45],

$$\frac{l_b}{d_o} = 8.51We_j^{0.32} \tag{1.18}$$

the second, Eq. (1.19), is Baron's correlation of the experimental data collected by Miesse on turbulent water jets [30],

$$\frac{l_b}{d_o} = 538We_j^{0.5}Re_j^{-0.625} \tag{1.19}$$

Eq. (1.20), is Wu and Faeth's correlation of the experimental data collected by Wu et al., Chen and Davis, as well as Grant and Middleman for turbulent jets [41],

$$\frac{l_b}{d_o} = 7.40We_j^{0.34} \tag{1.20}$$

the fourth and final correlation, Eq. (1.21), is from the work of Sallam, Dai and Faeth [42].

$$\frac{l_b}{d_o} = 2.1We_j^{0.5} \tag{1.21}$$

In addition, the lower part of the C-D region is characterized by an unsymmetrical, sinuous wave shape as expected with the 1^{st} Wind-Induced breakup regime. While the upper part of the C-D region is characterized by interactions between the liquid jet and the ambient gas. This leads to short wavelength sinuous disturbances that grow along the surface of the jet and strip small droplets from the surface. This is a characteristic of the 2^{nd} Wind-Induced breakup mechanism [30, 45].

The location of point D is not well defined. Point D describes the transition from an intact liquid jet exiting the orifice to the spray regime where the jet disintegrates immediately after it exits the orifice. There is considerable uncertainty as to the shape of the curve beyond point D as breakup length measurements become very difficult. This region corresponds with the atomization breakup regime [30].

Cavitation is probably the most important internal flow parameter that affects the turbulence intensity of the liquid jet and the resulting breakup length. The abrupt change in flow direction and velocity at the orifice entrance can reduce the local static pressure of the liquid to its vapor pressure forming cavitation bubbles. The presence and collapse of the vapor bubbles greatly enhances the turbulence intensity of the flow and may also cause a phenomenon known as hydraulic flip [46, 47].

Increasing the flow velocity tends to increase cavitation strength and thereby increases the turbulence intensity of the liquid leading to shorter breakup lengths. However, there are flow conditions that increase the strength of the cavitation to a point where the vapor bubbles do not collapse within the length of the orifice. This condition is called supercavitation. With supercavitation, the bubbles are so large that the liquid jet cannot reattach to the wall eliminating the influence of turbulence, wall friction, and surface disturbances upon the liquid jet. This results in a smooth, constricted jet with a very long breakup length [34]. Sharp-edged orifice entrances are more likely to cause cavitation within the injector compared with orifices with rounded inlets. The critical cavitation number is highly dependent on the entrance sharpness of the orifice with small deviations or imperfections having correspondingly large effects on the cavitation characteristics. Cavitation can also be enhanced by reducing the l_o/d_o ratio of the orifice [34, 46, 47].

Hydraulic flip occurs when the liquid flow separates from one or all sides of the orifice wall causing unpredictable flow characteristics [5]. The jet can adhere to one side of the wall arbitrarily and may experience precession along the circumference of the orifice [17]. This leads to misimpingement of the liquid jets in an impinging-jet type of injector causing performance losses. By reducing the flow area, hydraulic flip causes the mass flow rate of the propellant and discharge coefficient of the orifice to drop. In addition, the velocity of the liquid jet and therefore the breakup length will change as well [36,46]. Hydraulic flip phenomena are more prevalent with orifices with sharp-edge entrances and can be mitigated with the use of rounded entrances. Careful scaling of the l_o/d_o ratio of the injector can mitigate hydraulic flip from occurring by

taking into account the critical pressure drop that causes a full-flowing orifice to separate from the wall [5].

1.3.3 Acoustic Excitation of Liquid Jets

The breakup characteristics and lengths of liquid jets can also be affected by external forces such as acoustic oscillations. Pal et al. [48] conducted a series of experiments to explore the affect of acoustic oscillations at atmospheric conditions on both a single jet and like-on-like impinging jets. The results from the tests with the impinging jets are described in Section 1.4.2. The injector was placed into an optically accessible and instrumented steel cylindrical chamber that contained a speaker attached to the side wall. The speaker excited a variety of tangential, longitudinal, and combined tangential/longitudinal resonance modes inside the chamber. It was found that the jets shortened and deformed into a fan with an elliptical cross-section when excited with standing tangential and mixed tangential modes over a wide range of Reynolds and Weber numbers. The fan was aligned with the pressure node line. No jet distortion was observed when a standing longitudinal mode was excited in the chamber. The extent of deformation and shortening of the jet breakup length was proportional to the amplitude of the acoustic oscillations. This phenomenon was traced back to velocity coupling between the liquid jet and the standing acoustic field [48].

Carpentier et al. [49] conducted a series of experiments to investigate the behavior of low-speed, laminar cylindrical liquid jets exposed to transverse planar acoustic waves. For this research, a loudspeaker was attached to one end of a

horizontal Kundt tube and was used to excite standing longitudinal modes of various frequencies. The liquid jet entered the Kundt tube through a hole through the top of the side wall and exited through a similar hole on the bottom of the side wall. The experiment placed the injector at three locations with respect to the standing acoustic wave pattern: at the velocity node (pressure anti-node), between a velocity and pressure node, and at a pressure node (velocity anti-node) [49].

The results showed no effect on the length or breakup characteristics of the laminar jet while at the velocity node. When the injector was placed between the nodes, the jet was observed to deviate towards the nearest pressure node. This deviation was steady and further analysis demonstrated that this effect was caused by acoustic radiation forcing upon the cylindrical jet. When the jet is at a node, the radiation force is equal to zero and no deviation occurs. With the injector located at the pressure node, distinct changes occurred with the shape and breakup of the jet. For tests with acoustic velocities less than a critical value, the jet deformed into a regular series of flattened lobes. These lobes were oriented perpendicular to the acoustic velocity. Above the critical acoustic velocity value, the jet underwent a vivid and early breakup process. The jet flattened perpendicular to the acoustic velocity and developed rims around the edges that disintegrated into large droplets via the Rayleigh breakup process. In the middle region, the flattened liquid formed a square surface wave pattern that structured the disintegration of the sheet into small droplets. This surface instability was similar to the Faraday instability that develops on liquid films when exposed to perpendicular ultrasonic oscillations. The critical acoustic velocity was found to be associated with a critical gaseous Weber number

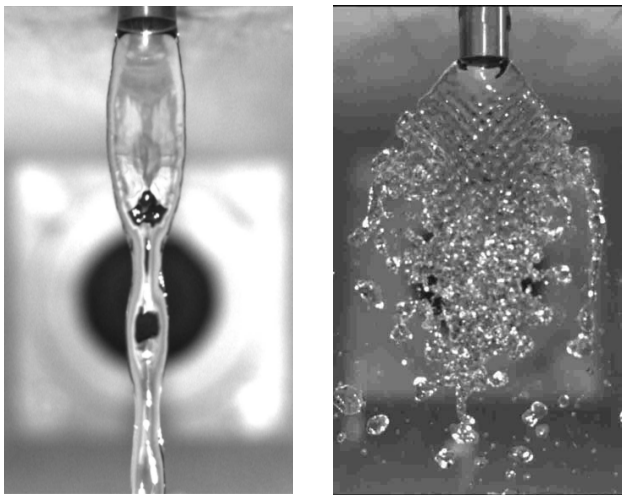

(a) **(b)**

Figure 1.13: Liquid Jet Located at Velocity Anti-Node of Standing Acoustic Wave: (a) $V_{ac}^{rms} < V_{ac}^{crit}$, (b) $V_{ac}^{rms} > V_{ac}^{crit}$ [49]

equal to 1.5, see Eq. (1.22). Figure 1.13 shows deformation of the liquid jet at the pressure node when (a) the acoustic velocity is below the critical value and (b) when the acoustic velocity is above the critical point [49].

$$We_{crit} = \frac{\rho_{gas} \left(V_{crit}^{rms}\right)^2 d_j}{\sigma} \tag{1.22}$$

In addition, the acoustic effects of coaxial air-assisted liquid jets were experimentally investigated by Baillot et al [50]. In this research, the injector was either placed at the pressure or velocity node. At the velocity node (pressure anti-node), the breakup of the liquid jet was only affected by the acoustic field when the jet was assisted by the coaxial air flow. At low acoustic levels the jet was stabilized while at higher acoustic levels, the breakup is accelerated due to the formation of

shear stress instabilities at the liquid-gas interface. When the injector is placed at the pressure node (velocity anti-node), the nonlinear radiation pressure flattens the jet to form a sheet and the spray becomes spatially organized leading to rapid breakup via intrinsic sheet instabilities, Faraday instabilities, membrane or cluster breakup. An exception occurred at very high coaxial air velocities that produced fiber-type breakup, these set points were unaffected by the acoustic waves possibly because the acoustic amplitude was not high enough to overcome the gas impulse [50].

1.4 Like-Doublet Impinging Injectors

Like-doublet impinging jet injectors have been widely used in liquid rocket engines. Several of these engines include the F-1 engine used in the first stage of the Saturn V rocket, the H-1 engine used in the first stage of the Saturn I and Saturn IB rockets, the LR-87 used in the Titan series of launch vehicles [5], and the Viking engine used on the first four versions of the Ariane launch vehicle [11]. Impinging jet injectors have been the preferred design for engines that use either liquid storable or LOX/hydrocarbon propellants. They are a better design than coaxial-type injectors when both propellants enter the combustion chamber in a liquid state due to greater propellant atomization and mixing efficiencies as well as reduced fabrication, inspection, and maintenance costs [51]. Other advantages of like-doublet injectors include the potential to support high mass flow rates, compatibility with the chamber wall, less susceptibility to reactive stream separation (blowapart), and proven dependability. Some disadvantages of these elements include increased axial distance required for proper mixing of the fuel and oxidizer, and increased sensitivity to design

and manufacturing tolerances [5]. Additionally, the injector design parameters that increase engine performance tend to increase the likelihood of combustion instability developing within the engine [51, 52].

Even with extensive use, there is a lack of fundamental knowledge about the atomization, mixing, and combustion processes of impinging injectors. This results in design criteria that is not as developed when compared with other injector types such as coaxial injectors. Therefore to mitigate risk, new impinging injector designs have been limited to reside within the existing empirical database [53].

1.4.1 Like-Doublet Injector Design

In a liquid rocket where propellants are injected with large dynamic pressures, the greatest source of inertia to destabilize a liquid jet is with another liquid jet. Having liquid jets impinge upon each other is therefore an effective method to atomize the propellant into small droplets. Like-doublet injectors are designed to impinge two geometrically and dynamically similar liquid jets composed of the same propellant at an oblique angle [51]. Propellant mixing with like-doublets, takes place downstream of the impingement point and requires interaction between the spray of a fuel doublet with the spray of an oxidizer doublet [5].

Typical liquid rocket engine designs that utilize like-doublet impinging injectors contain a faceplate at the head-end of the combustion chamber with alternating fuel and oxidizer injector rings. The injectors nearest to the chamber wall are typically composed of fuel elements for wall compatibility and cooling [5]. Two orifices angled towards each other are drilled through the injector faceplate to form a

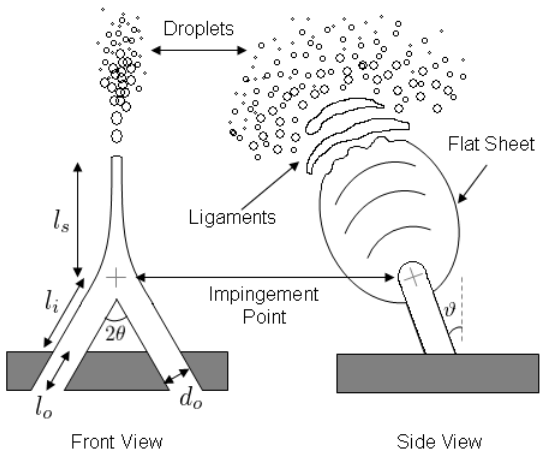

Figure 1.14: Schematic of a Typical Like-Doublet Injector

single like-doublet element. For typical operating conditions and orifice designs, the liquid Reynolds number is generally between 10^5 and 10^6 and the Weber number is around 10^5. Pressure drop through the element ranges between 5 to 30 atm [51].

Injector orifice length to diameter ratios (l_o/d_o) for like-doublet injectors are typically between 2 and 5 [51] with most practical injectors having a ratio of 3. Rounded or contoured orifice inlets have the advantage of increasing the discharge coefficient while avoiding flow cavitation, jet misdirection, and hydraulic flip especially for low l_o/d_o ratio orifices [5]. However, for fabrication and cost purposes the orifice entrances of most practical injectors have a sharp inlet. Discharge coefficients generally fall between 0.61 and 0.9 [51]. Smaller orifice diameters consistently produce higher performance due to smaller droplet sizes, increased vaporization rates and more uniform mixing. For like-doublets, the droplet size is approximately proportional to the square root of the orifice diameter [5]. Figure 1.14 shows the important design parameters and general spray formation of a typical like-doublet injector element.

The impingement angle (2θ) is defined as the angle between the centerlines of the two impinging jets. This angle affects the atomization efficiency and determines the amount of propellant backsplash that occurs. Atomization is enhanced with larger impingement angles. The resulting droplet size decreases linearly with the increase in impingement angle. Backsplash is proportional to the cosine of the impingement angle and results in some of the propellant flowing backwards and striking the injector faceplate. This can result in erosion or burnout of the injector face. Faceplate burnout is a more serious concern for unlike-doublet injectors and hypergolic propellant combinations. It has been recommended that like-doublet designs use an impingement angle of 60° to achieve a balance between good atomization characteristics with little propellant backsplash. However, impingement angles between 30° and 90° have been used in rocket engines [10, 11, 54].

The impingement point is described as the point where the centerlines of the two impinging jets intersect. The impingement point serves as a stagnation region where the static pressure is ideally equal to the total pressure of the propellant manifold [51]. The impingement distance (l_i) is the length of the freestream jet from the exit of the orifice to the impingement point. Long freestream jet breakup lengths can result in misimpingement due to partial disintegration of the jets, transverse chamber oscillations and amplification of alignment errors caused by manufacturing tolerances of the orifice geometry. Misimpingement can result in reduced performance, wall streaking, and sometimes combustion instability. The impingement distance can be described as a non-dimensional number by dividing the freestream jet length by the

orifice diameter (l_i/d_o) [5]. The l_i/d_o ratios of liquid rocket engines using like-doublet injectors range between 2 and 7 with the typical value being 5 [5, 51].

When two dynamically similar liquid jets impinge upon each other, the high pressure stagnation region at the impingement point causes the liquid to spread laterally forming a flat sheet (spray fan) whose broad side is perpendicular to the impinging jets. Beyond the impingement point, the liquid velocity of the fan is assumed to accelerate back to the initial jet velocity. At the edges of the sheet, the liquid is fragmented into ligaments and large droplets in a process known as primary atomization caused by the intertial, turbulence, tensile, aerodynamic, and viscous forces. The size and shape of these fragments are controlled by the liquid, injection and ambient characteristics as well as the orifice design. The ligaments and large droplets are then further disintegrated as a function of local flow and droplet conditions in a process called secondary atomization. The breakup length of the liquid sheet (l_s) can be defined as the length of the centerline from the impingement point to the point where the sheet disintegrates into ligaments and droplets [51].

Efficient mixing of like-doublet injectors depends upon the relative geometric arrangement of the fuel and oxidizer doublets. Propellant mass and mixture ratio distributions are a function of not only the orifice size but also the configuration of the fuel and oxidizer spray fans, the cant angle between the centerlines of the fuel and oxidizer doublets, and the spacing between the fuel and oxidizer injectors. Excellent mixing uniformity and high performance is achieved when the fuel and oxidizer doublets are oriented so the two sheets impinge edge-to-edge. This configuration also minimizes the risk of reactive stream separation when using hypergolic propellants.

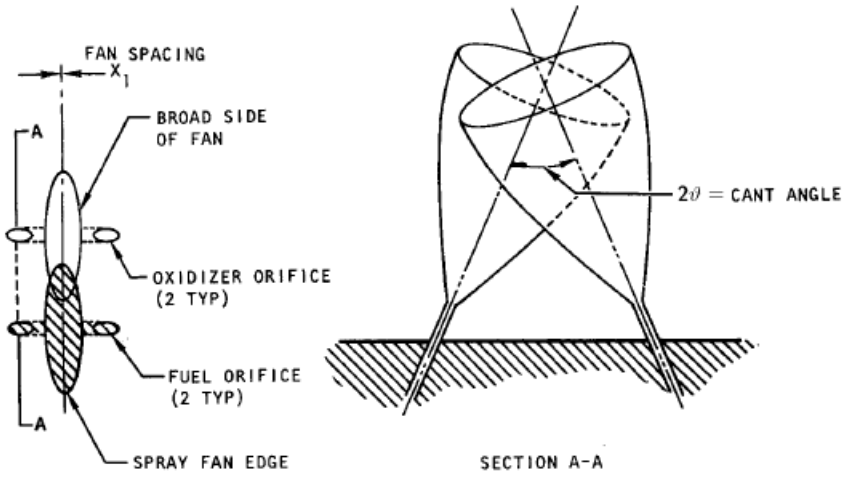

Figure 1.15: Spray Fan Impingement of Two Like-Doublets [5]

Propellant mixing is significantly affected by the cant angle (2ϑ). Mixing uniformity is improved by up to 40% by increasing the cant angle from 0° to 41°. Beyond 41°, mixing uniformity decreases [5]. Typical cant angles are designed between 20° and 41° [51]. See Figure 1.15, for a schematic of spray fan impingement for like-doublet injectors, reproduced from the NASA SP-8089 report. Since like-doublets depend solely upon inter-element mixing, the spacing of the fuel and oxidizer elements has a significant effect upon mixing efficiency and uniformity. The optimum spacing of the fuel and oxidizer doublet elements is dependent upon the particular engine design, operating characteristics, and propellant combination. The position of the fuel and oxidizer elements should be configured to attain uniform propellant mass distribution and the desired mixture ratio [5].

Work completed at Aerojet by Hewitt determined a strong empirical correlation between the combustion instability characteristics and the injection

parameters for liquid rockets using like-doublet injectors [55]. The Hewitt stability correlation, seen in Figure 1.16, relates the acoustic response frequency of the combustor with the ratio of the injector orifice diameter to the jet velocity of the least volatile propellant [4]. It suggests that the operating mode of a liquid rocket engine can be pushed from stable to unstable simply by decreasing the d_o/v_j ratio past the empirical threshold seen in Figure 1.16 [36].

The threshold line corresponds with the highest frequency of combustion instability that can be excited and sustained in engines using like-doublet injectors at a given design and operating condition. It also demonstrates that a high-frequency cutoff for combustion instability exists in liquid rocket engines [18]. The unstable points relate to the highest frequency of combustion instability that was excited in the engine while the stable points relate to the calculated frequency of the unexcited dominant acoustic chamber mode. This correlation demonstrates the importance of both injector design and the operating conditions in determining the stability characteristics of a rocket engine. It has been noted that this correlation only applies when combustion instability is primarily excited through intrinsic excitation mechanisms and not with injection coupled mechanisms [4]. Some proposed mechanisms to explain the plot and stability threshold have included atomization frequency, flamelet straining and extinction, fuel jet aerodynamic excitation, and the propellant vaporization and mixing processes [36, 55].

Anderson et al. conducted an effort to understand which component processes of like-doublet injectors contribute to combustion instability. It was calculated that the atomization process of impinging injectors has a characteristic time scale similar to

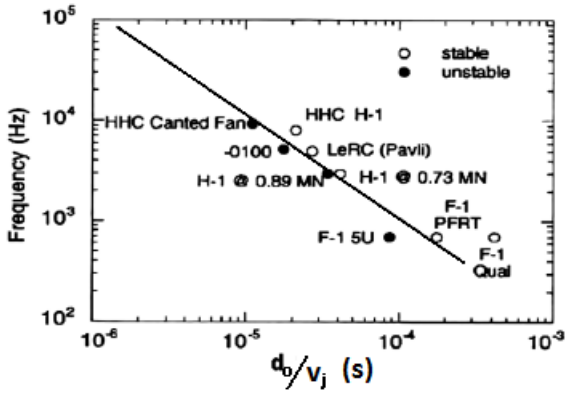

Figure 1.16: Hewitt Stability Correlation Plot [4]

the acoustic time scales of typical resonant combustion instability modes. A cold-flow experimental study at atmospheric conditions was undertaken to determine a link between the atomization process and combustion instability. The average frequency of the periodic impact waves and ligaments were very similar to the highest possible combustion instability frequency as determined by the Hewitt stability plot. Also, the Hewitt stability correlation ($^{d_o}/_{v_j}$) was changed by varying the injection flowrates and the orifice diameter. An increase of the Hewitt stability correlation resulted in an increase in both the mean droplet diameter and the polydispersity of the spray. Both of these observations are consistent with the known theory and practice of mitigating combustion instability in liquid rocket engines. These results support the notion that one of the key mechanisms of combustion instability includes the atomization process [53].

Kim and Williams [18] developed a counterflow flamelet response model with finite rate chemistry to study the interaction between flamelet response and acoustic instability phenomena. These counterflow flamelets are assumed to exist between

the fuel and oxidizer spray fans. Laminar diffusion flamelets near extinction have a characteristic diffusion time that is estimated to be equal to the extinction strain rate. This time scale is estimated to be on the order of the characteristic acoustic time scale for typical combustion instability modes [18].

Flamelets near extinction were shown to have high sensitivity to acoustic pressure oscillations when the acoustic time scale was larger than the flow time scale (reciprocal of strain rate) of the flamelet. This sensitivity to acoustic time scale supports the high-frequency cutoff of combustion instability excitation observed in liquid rocket engines. It is argued that the Hewitt stability correlation (d_o/v_j) is analogous to the reciprocal of the characteristic flamelet strain rate. As d_o/v_j is increased the strain rate is reduced thereby reducing the amplification rate and making the combustion process more stable. Also, the greatest acoustic oscillation amplitudes exist near the injector faceplate where these flamelets will be located thereby making flame response and acoustic coupling more likely to occur. However to date, there is not much experimental evidence to support the existence of strained laminar diffusion flamelets enveloping the spray of like-doublet impinging injectors [18].

Chehroudi [36] has presented an interesting idea that may explain the trend seen with the Hewitt stability correlation, described in the Section 1.4, for rocket engines that utilize like-doublet injector elements [36]. Prior research using shear-coaxial injectors have demonstrated that the cryogenic core is long under sub-critical conditions and shortens with increasing chamber pressure. At super-critical conditions the length of the cryogenic core is very short [23, 56, 57].

Extending this result to like-doublet impinging injectors, it is hypothesized that the relative lengths and dynamics of the fluctuating liquid jets play a crucial role in the sensitivity of the injector and spray to acoustic disturbances. Chehroudi hypothesizes what the implications are when the average breakup lengths of the liquid jets are on the order of the impingement distance ($l_b/l_i \sim 1$). He suggests that the impinging jets at this condition would have a dominating influence upon the dynamic behavior of the injector resulting in a spray that is very sensitive and responsive to chamber disturbances [36].

When the jet breakup length is longer than the impingement distance, ($l_b/l_i > 1$), a robust impingement is expected. This is the nominal design case and is expected to produce a stable liquid sheet that is insensitive to jet breakup length fluctuations [36]. Previous research by Pal, Rhys, and Mulmule has shown that this regime is susceptible to acoustic oscillations [48, 58, 59].

However, as the breakup length of the jets shorten; the impingement efficiency will decrease due to the smaller jet diameter near the tip and variations of the breakup length of the jet potentially causing increased levels of misimpingement. This effect will be most pronounced when the average jet core length is about the same as the impingement distance and in the presence of transverse acoustic disturbances. This operating regime may cause the liquid jets and subsequent impingement to be very sensitive to the acoustic and thermofluid parameters of the combustion environment which can strengthen the feedback mechanisms that lead to combustion instability. The injector under these conditions can be described as hypersensitive to acoustic disturbances [36].

When the operating conditions change to cause the average jet breakup lengths to become much shorter than the impingement distance, the impinging jets will be more like a spray of droplets. The jet breakup length fluctuations will also likely be smaller. This will lead to more robust injector dynamics that are less sensitive to chamber disturbances [36].

Chehroudi hypothesizes that the threshold that separates the stable and unstable operating regimes seen in the Hewitt stability plot for historical liquid rocket engines correspond with the condition where the impinging jets have an average jet breakup length about equal to the impingement distance. This critical regime can occur in a rocket engine for specific operating points e.g. supercritical conditions and/or during transient conditions such as throttling and during the start-up/shut-down sequence [36].

1.4.2 Atomization Process of Impinging Liquid Jets

Atomization is a stochastic process that transforms a bulk liquid (jet or sheet) into a disperse spray of droplets suspended in a gaseous medium. The liquid can be atomized in various ways including the exposure of the jet/sheet to a high-velocity gas, the addition of mechanical energy to the liquid e.g. vibration or rotation, or through the kinetic energy, if large enough, of the liquid jet/sheet itself [30]. The atomization process has a direct influence upon both engine performance and stability [20]. In turn, the fluid properties of the propellant, injector design characteristics, and operating conditions of the engine have a tremendous effect upon the atomization process and resultant spray quality [5].

The atomization process is generally described as occurring in two steps. The initial destruction of a liquid jet or sheet into ligaments and/or large drops is known as primary atomization. Secondary atomization is the process of breaking the ligaments and drops into smaller droplets until the cohesive forces acting on the liquid are equal to or greater than the atomization forces [33].

The like-doublet injector can be considered a variation of the common plain orifice pressure atomizer. Plain orifice pressure atomizers inject liquid through a small orifice, typically circular, under high pressures. The large upstream pressure is converted into kinetic energy leading to jet disintegration. Like-doublets accelerate the atomization process by colliding two high-speed liquid jets which form a flat sheet that promptly disintegrates into ligaments and droplets [30, 31]. The following sub-sections will describe in detail the primary and secondary atomization processes that occurs with like-doublet injectors.

1.4.2.1 Primary Atomization

The primary atomization process consists of the initial fragmentation of the liquid propellant into ligaments and large drops. For like-doublet impinging injectors, the primary atomization process consists of the collision of two liquid jets forming a liquid sheet or spray fan that subsequently disintegrates into ligaments and drops some distance downstream of the impingement point. The shape, size and distribution of the fan and drop field are dependent upon the propellant, injector geometry, injection conditions, and ambient conditions. The primary atomization process affects engine performance by determining to a significant degree the final drop size and propellant

distribution within the combustion chamber. This in turn affects the propellant vaporization rates, mixing uniformity and overall combustion efficiency. Also, the periodic nature of primary atomization may have an effect on the excitation and growth of combustion instability [51].

The formation of the liquid sheet is believed to be caused by the creation of a high-pressure stagnation region at the impingement point. At the stagnation region, the momentum of the two jets towards each other is canceled and the liquid is forced to spread outward in the lateral direction from the impingement point. This causes a thin, flat sheet to form in a plane perpendicular to the two impinging liquid jets [51].

Taylor developed an analytical model to predict the shape of the flat sheet formed by two impinging laminar jets at low Weber number ($We < 2{,}000$) conditions. The results showed that the shape of the sheet is determined by the impingement angle. With an impingement angle of 180°, a circular sheet is formed. For angles less than 180°, the sheet forms a cardiod/leaf-like shape. The width of the sheet decreases with decreasing impingement angle. For sprays with $We > 2{,}000$, Taylor's model breaks down. To date all attempts have been unsuccessful in the development of an accurate analytical model to describe the primary atomization process of two impinging jets at high Weber numbers especially when the flow is turbulent [51].

Experiments have identified four general spray patterns that describe the shape and characteristics of the liquid sheet formed by like-doublets. Heidmann et al. categorized the pattern regimes as [60]:

- Closed-rim,

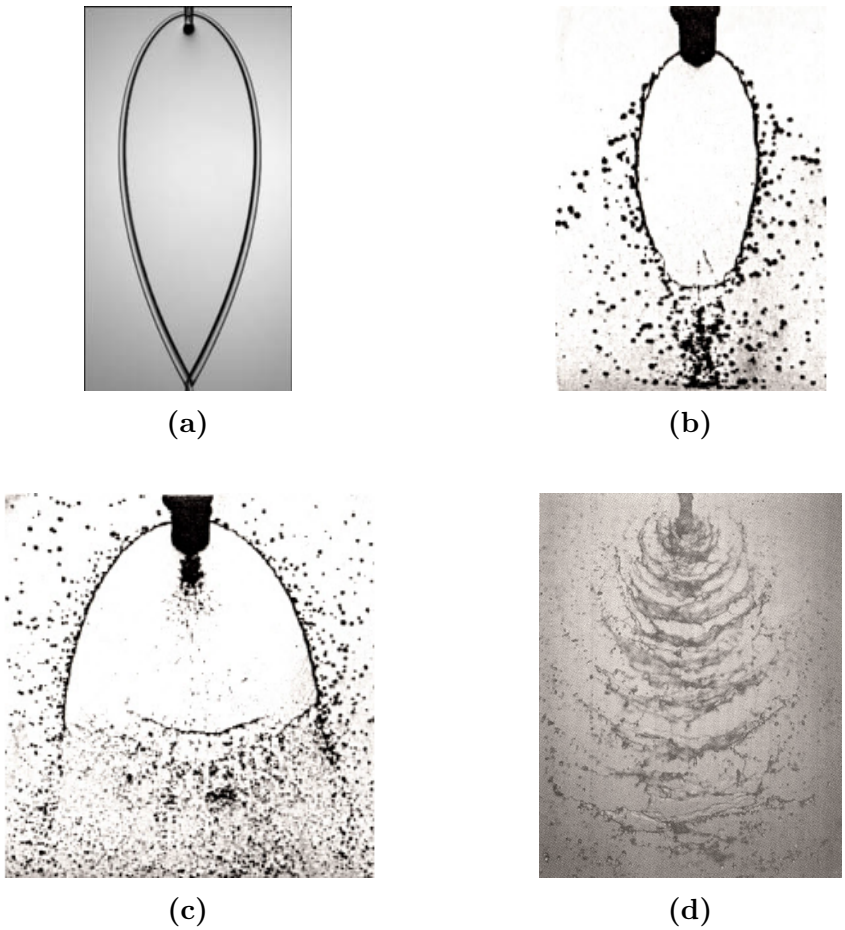

Figure 1.17: Like-Doublet Spray Fan Patterns: (a) Closed-Rim [61], (b) Periodic-Drop [62], (c) Opened-Rim [62],and (d) Fully-Developed [51]

- Periodic-drop,
- Opened-rim,
- Fully-developed.

See Figure 1.17 for photographs of the four spray fan patterns formed by like-doublet impinging injectors. These photographs are taken from the experimental results of Bremond et al., Dombrowski and Hooper, and Anderson et al.

A closed-rim spray pattern occurs at low jet velocities ($v_j < 4\ ^m/_s$) and forms a smooth sheet that is encompassed by a thick liquid rim that contains most of the liquid flow. The rim encloses the entire sheet with a laminar liquid stream forming at the downstream side of the sheet. This liquid stream breaks up into drops via the Rayleigh mechanism some distance downstream from the end of the sheet [51, 60].

The periodic-drop spray pattern occurred at jet velocities between 4 and 6 $^m/_s$ in the experiments conducted by Heidmann et al. This pattern can be considered a variation of the closed-rim regime. In this case, the rim becomes unstable and releases droplets tangentially from the rim of the liquid sheet in a regularly space pattern. The velocities of the drops have been found to be equal to the main flow within the sheet but the ejected mass is small in comparison. The main flow disintegrates into drops at the downstream end where the two rims meet [51, 60].

The opened-rim pattern is similar in structure as the closed-rim pattern except the sheet disintegrates before the rims of the sheet can impinge upon each other. The liquid sheet may have surface waves that affect the breakup of the sheet. The thickness of the liquid sheet reduces from the impingement point to the point of disintegration where the sheet breaks up into droplets. This spray pattern was observed to occur for jet velocities between 6 and 10 $^m/_s$ in the experiments conducted by Heidmann et al [51, 60].

A fully-developed spray pattern occurs at high velocities ($v_j > 10^m/_s$) and/or with the impingement of two turbulent jets and is characterized by waves of drops and ligaments that emanate from the impingement point. A small liquid sheet deformed

by large surface waves may or may not be present. The waves of ligaments and droplets are periodic in nature [51, 60].

Research conducted by Bailardi et al., identified seven distinct breakup regimes including those described above. Bailardi's experiment tested like-doublet impinging injectors with a fixed impingement angle of 90° with several different Newtonian fluids for a range of Reynolds and Weber numbers between 10 and 100,000 and Ohnesorge numbers from 0.0027 to 3.8. The additional breakup regimes identified are: rimless separation, smooth-sheet ligament, ruffled-sheet ligament, and aerodynamic instability breakup. Rimless separation occurs when distinct rims are not formed around the sheet. Droplets are shed from the edge of the sheet and parts of the sheet periodically separate and decay downstream. The smooth-sheet ligament regime incorporates a smooth sheet that periodically sheds bow shaped ligament structures. The aerodynamic instability regime occurs when the sheet generates a flapping motion that causes the sheet to disintegrate into droplets. The ruffled-sheet ligament regime shares many similarities with the definition of a fully-developed spray described by Heidmann and others. A small, wavy sheet, sheds waves of ligaments and droplets in this regime. Bailardi, describes the fully-developed regime as occurring when the impingement no longer produces a sheet or ligaments but directly disintegrates into droplets that are shed in bow-shaped clouds [63].

Liquid viscosity serves to damp the growth of surface waves on the sheet and delay sheet breakup. For a given jet velocity, high viscosity liquids generally formed longer liquid sheets and tended to form longer ligaments and larger droplets

during sheet breakup. Additionally, more pronounced spray patterns and periodic phenomena were observed for high viscosity liquids [51, 58, 60].

Surface tension serves to impede sheet breakup by opposing the creation of surface waves. This is due to the greater surface energy that must be overcome in high surface tension fluids before the liquid surface can be fragmented. Lower values of surface tension make it easier to atomize the liquid sheet and result in smaller ligaments and drops [58].

The breakup characteristics of liquid sheets are affected by several parameters including jet velocity, orifice geometry and diameter, impingement angle, and the flow conditions of the impinging liquid jets. Whether the impinging jets are laminar or turbulent has a major effect upon the resulting liquid sheet and the primary atomization process [46, 62]. For flow conditions where $We < 500$, sheet breakup is governed by the balance between the liquid inertial force forcing the fluid outward and the liquid cohesive force keeping the sheet intact [51]. At higher velocities/Weber numbers, the sheet disintegration process is caused by aerodynamic forces that cause waves to form and grow along the surface and/or by hydrodynamic forces that initiate waves from the impingement point a.k.a. impact waves. The breakup length decreases and breakup frequency increases for larger impingement angles. This is due to the greater impact force generated, which is proportional to the sine of the impingement half-angle ($\sin\theta$). Unlike aerodynamic waves, hydrodynamic waves have been observed when the spray discharges into a vacuum [46, 62]. The primary atomization of laminar impinging jets can be adequately described with linear aerodynamic instability theory. However, the theory breaks down with turbulent flow

due to the dominant affects of impact waves. No theory has been able to describe the breakup characteristics of sheets dominated by hydrodynamic instabilities [51].

For the opened-rim and fully-developed spray regimes, the sheet disintegrates into ligaments and large drops when the surface wave amplitudes reach a critical value that cause the sheet the thin to a point that the cohesive forces can no longer hold it together. Ligaments are generally torn away from the sheet in half-wavelengths of the surface waves. The breakup occurs at the crests and troughs of the waves where the magnitude of the vorticity within the fluid is greatest [62, 64].

The hydrodynamic breakup of liquid sheets is caused by the phenomenon known as impact waves. Impact waves are the controlling process and defining characteristic of the quick and violent breakup observed with fully-developed sprays. However, impact waves have been observed in other regimes specifically the opened-rim regime. The large flow rates, high injection velocities and sharp-edge orifice design of like-doublet injectors present in liquid rocket engines will in general cause a turbulent jet flow profile and fully-developed sprays ($We \sim 10^5$, $Re \sim 10^6$). This makes impact waves a crucial mechanism in the primary atomization of like-doublet injectors [64]. For turbulent flow profiles, Dombrowski and Hooper showed that impact waves appear above a critical Weber number and are independent of Reynolds number. The range for the critical Weber number was between 66 and 165 [62]. This is comparable to the critical Weber number range of 84 and 126 from the results of Heidmann et al. [60].

A full understanding of the source(s) of impact waves is still unknown and therefore the phenomenon has not been fully characterized [51]. This is exacerbated

by the fact that the formation and behavior of sinuous impact waves is both unstable and nonlinear and therefore cannot be described by linear stability analysis [64]. It has been reasoned that impact waves are formed as a consequence of the fluctuations of pressure and/or jet momentum at the impingement point. These fluctuations may arise from disturbances within the liquid jet that become accentuated at the impingement point, e.g. jet instabilities and turbulence, or from the jet impingement itself, e.g. periodic movement about the mean stagnation point [51]. The results of recent numerical simulations conducted by Chen, et al., have shown that impact waves could be formed by the interfacial shear stress between the two sides of the sheet forming dilatational waves near the impingement point. This causes nonlinear behavior that forces the sheet to resonate at its natural frequency and generate the unstable sinuous waves down the length of the sheet known as impact waves [64]. The numerical results found by Zheng, et al. [65] showed that impact waves could be formed by the velocity profile difference between the two impinging jets around the stagnation and impingement points. This difference also affects the stability and breakup of the flat sheet. The velocity difference is exacerbated by larger impingement angles leading to larger impact waves and enhanced sheet breakup.

Summary of Past Research: The experiments conducted by Dombrowski and Hooper [62] have shown that flow conditions play an important role in the breakup characteristics and process of liquid sheets formed by impinging jet injectors. The results of the experiments showed that laminar cases below a jet velocity of 10 $^{m}/_{s}$, displayed an intact liquid sheet that exhibited breakup with a

closed-rim or periodic-drop pattern. For laminar cases above 10 $^{m}/_{s}$, impact waves were formed from the impingement point that caused the sheet to disintegrate at about the midspan in an opened-rim pattern. Sheet breakup length was inversely proportional with jet velocity and impingement angle while the sheet width was directly proportional with velocity and angle. For all turbulent cases, large, robust impact waves were formed from the impingement point that caused near immediate disintegration of the liquid sheet. The spray pattern for all jet velocities and impingement angles were fully-developed with well defined periodic waves of ligaments and drops. The turbulent breakup process was entirely controlled by the hydrodynamic waves [62].

Ryan et al. [66] explored the atomization characteristics of like-doublet injectors as a function of impinging jet condition (laminar and turbulent), injector geometry (orifice diameter and impingement angle) and jet velocity. The cold-flow experiments showed distinct differences in the atomization characteristics between laminar and turbulent impinging jets consistent with the results of Heidmann et al. [60] and Dombrowski and Hooper [62] and lent further evidence of the importance of jet velocity profile and turbulence characteristics to sheet breakup. The wavelengths of the impact waves and shed ligaments were found to be directly proportional to orifice diameter and independent of both jet velocity and impingement angle. The experimental results of this study were then compared with theoretical predictions of breakup length and drop size using linear-stability based models. The model did not agree in either trend or magnitude with the experimental sheet breakup lengths. The model over-predicted the droplet size but did display a similar trend [66].

Anderson et al. [51] completed a series of experiments to help clarify the mechanisms of impinging jet atomization. His results showed spray patterns and characteristics consistent with those described by Heidmann et al. [60] and Dombrowski and Hooper [62]. Liquid sheet breakup characteristics were found to be dependent upon flow condition. Sheet breakup length for laminar flow was dependent upon the Weber number while turbulent flow was independent of the Weber number. The pre-impingement length of the jets had an affect upon the resultant breakup length of the sheet. Longer pre-impingement lengths caused shorter breakup lengths and allowed any disturbances or misalignment to become worse. Drop sizes were found to decrease with an increase in Weber number and impingement angle. The wavelength between the waves of ligaments and droplets were shown to be dependent upon orifice diameter and independent of jet velocity. The atomization frequencies of the shed ligaments were on the same order as the maximum combustion instability frequencies excited in liquid rocket engines using like-doublet impinging injectors. However, a definite link has not been found [51].

Anderson et al. [67] continued their work by studying the effects of like-doublet atomization upon combustion instability of liquid rocket engines. They developed a combustion response model incorporating periodic atomization and conducting hot-fire experiments in a sub-scale rocket engine using a like-doublet injector that electromechanically excited each jet at specific frequencies. The results from the combustion response model showed that periodic atomization caused large variations in the pressure response magnitude. The experimental results showed that atomization frequency can be controlled electromechanically and that longitudinal

instability modes can be excited in the sub-scaled engine. Greater instability amplitudes were excited with higher mass flow rates and when the two jets were oscillated in-phase [67].

Jung et al. conducted cold-flow experiments with like-doublet injectors under atmospheric pressure conditions using water and kerosene to determine the breakup characteristics of liquid sheets and ligaments. The experiments tested doublet injectors with both rounded and sharp-edge orifice entrances. The l_o/d_o ratio of the orifices was equal to 17. The experiments measured the breakup lengths and wavelengths of the liquid sheet and ligaments for a variety of test conditions that varied both the jet Weber number and impingement angle. From the data collected, Jung was able to obtain empirical equations for the breakup lengths (l) and wavelengths (λ) of the sheet and ligaments for turbulent flow using the sharp-edge injector. These relations are seen in Eqs. (1.23) through (1.26) [46].

$$\frac{l_s}{d_o} = 97.3We_j^{-0.27}\left(\sin\theta\right)^{-1.2} \tag{1.23}$$

$$\frac{\lambda_s}{d_o} = 45.2Oh_j^{0.096}We_j^{-0.24}\left(\sin\theta\right)^{-0.24} \tag{1.24}$$

$$\frac{l_{lig}}{d_o} = 69.8Oh_j^{0.094}We_j^{-0.14}\left(\sin\theta\right)^{-0.58} \tag{1.25}$$

$$\frac{\lambda_{lig}}{d_o} = 46.7Oh_j^{-0.078}We_j^{-0.23} \tag{1.26}$$

The results showed that an increase in both the turbulence strength and impact force shortens the breakup lengths and wavelengths of the liquid sheet and ligaments. The impact force of the jets is proportional to the impingement angle. Also, the lengths and wavelengths of the liquid sheet and ligaments were seen to be dependent upon the Weber number of the jet. The wavelengths of the ligaments were shown to be longer than those for the sheet for the same injection condition. This observation is thought to be caused by the elimination of the restrictive forces found within the sheet including surface tension and viscosity when the ligaments break free from the edge of the sheet [46].

Ramamurthi, et al. [68] conducted cold-flow experiments with like-doublet injectors for both non-cavitating and cavitating flows. Their results showed that the dominant frequencies within the spray as measured by a microphone in the vicinity of the impingement point originated with the two impinging jets. They determined that the frequencies of the spray were caused by a combination of the inertial dynamics of the injector and supply manifold as well as acoustic resonance of the feed system. In addition, they found that both the shape of the spray as well as the droplet size and distribution changed when the flow inside the injector cavitated.

The research conducted by Choo and Kang used a Laser Doppler Velocimetry (LDV) instrument to experimentally determine the velocity distribution of the liquid sheet formed by low-speed, impinging laminar jets. They found the common assumption that the liquid velocity of the sheet is constant and is equal to the mean jet velocity to be incorrect. Their results showed that the local sheet velocity changed everywhere and generally decreased as the azimuthal angle with respect to

the longitudinal axis of the sheet is increased. It was observed that the sheet velocity near the axis was higher than the mean jet velocity. This indicated that the high velocity core of the laminar jets, due to the parabolic velocity profile, flowed around the axis of the sheet. Whereas, the low speed region near the periphery of the jets tended to flow radially outward on the sheet. An increase in impingement angle tended to cause a more even distribution of sheet velocities [69].

In addition, the breakup characteristics of liquid sheets can be altered by the presence of an acoustic field. Rhys [58] conducted a cold-flow experiment where a single slit orifice produced a flat liquid sheet that was exposed to transverse acoustic waves of varying frequencies. This experiment aimed at determining the response of the spray to an acoustic field and positioned the injector at both the pressure and velocity anti-nodes. It was determined that the sheet is most sensitive to acoustic forcing when the injector was placed at the velocity anti-node. At this position, regular sinuous waves appeared and grew along the surface of the sheet leading to its destruction. It was also found that reducing the frequency of the acoustic oscillations caused the amplitude of the surface waves to grow, especially when the acoustic frequency approached the natural frequency of the liquid sheet leading to violent breakup of the sheet [58].

Pal et al. [48] conducted a series of experiments to explore the effect of acoustic oscillations at atmospheric conditions on both a single jet and like-on-like impinging jets. The results from the single jet tests were described in Section 1.3.3. The like-doublet injector was placed into an optically accessible and instrumented steel cylindrical chamber that contained a speaker attached to the side wall. The injector

was oriented so that the plane of the sheet was inline with the pressure nodal line of the excited 1560 Hz 1-T/3-L resonance mode. This allowed for the acoustic velocity to fluctuate normal to the sheet. The results showed that acoustic excitation can enhance breakup of the sheet. This was especially evident for the low injection velocity case. Droplet size measurements were conducted with a Phase Doppler Particle Analyzer (PDPA) and showed a similar shaped droplet size profile curve between the unexcited and excited experiments. However, there was a statistically significant jump in the number of drops between 250 and 750 μm and a decrease in the number of drops in the larger size range. Additionally, both the arithmetic mean and Sauter mean diameters decreased with acoustic excitation. Atomization frequency measurements did not yield a single shedding frequency but instead showed a mean frequency with a large standard deviation [48]. This is similar to previous results gathered by Heidmann [60] and Ryan et al [66]. The distribution did not show any energetic levels near the imposed 1560 Hz acoustic frequency. This suggested that the enhanced breakup and smaller droplets observed during acoustic excitation was due to the oscillating velocity field around the sheet excited by the standing acoustic wave and not because the sheet was responding to the imposed acoustic frequency [48].

Similarly, Mulmule et al. [59] conducted a cold-flow experiment to determine the effects of an transverse acoustic field upon the spray dynamics issuing from a 180° impinging injector. The experiment subjected the spray to a traveling acoustic wave which allowed for velocity coupling with the sheet. The results showed that the sheet was more susceptible to acoustic forcing at certain frequencies with lower frequencies being most effective. The effects of the acoustic field were observed to cause the intact

diameter of the sheet to become smaller and increase the number of droplets ejected from the rim of the sheet. Also, the mean droplet size decreased when the sheet was affected by transverse waves. Lower frequencies are argued to be more effective at influencing sheet breakup because the higher frequency waves are damped to a larger degree by the inertia of the sheet [59].

1.4.2.2 Secondary Atomization

Secondary atomization occurs when small drops form from larger liquid fragments. It is an important process because the large drops and fragments formed through the primary atomization process are naturally unstable and susceptible to further breakup. As such, final droplet size is determined by the secondary atomization process which affects performance of the rocket engine by influencing the rate of vaporization and mixing [33].

The liquid ligaments that are shed from the edge of the sheet are intrinsically unstable. The irregular shaped ligaments are contracted via surface tension into rough cylinders. At this point, the ligaments begin to disintegrate into drops via the Rayleigh mechanism. The surface of the ligament is deformed by dilatational waves that pinch off drops from the ends of the ligament until the ligament itself is reduced to a drop [51, 58].

Droplets can undergo secondary atomization by either the nonuniform pressure distribution of the ambient gas around the drop or by droplet collision. Several droplet secondary atomization regimes have been observed for droplets exposed to a gas flow. Simple drop division occurs when the drop is first flattened by the oncoming ambient

gas. The flattening process pushes the majority of the liquid to the rim of the drop causing the center of the drop to thin until it perforates leading to breakup of the rim. Up to four identical secondary droplets are formed with this mechanism. The bag breakup mechanism occurs at low velocities and is characterized by deformation of the droplet into a thin disk normal to the flow direction. The center of this disk is deformed into a parachute-like structure in the direction of the flowing gas. The parachute disintegrates into a cloud of small droplets and the rim disintegrates into a number of somewhat larger droplets. At relatively high velocities, drops are atomized by the shear breakup regime. The shear regime causes the drop to form into a thin fluid disk and deform the edges of the disk instead of the center. Small droplets are then stripped from the periphery of the deformed disk. A complex secondary atomization regime exists in the transition from the bag to the shear breakup regimes. This is called multi-mode breakup with portions of the atomization regime being described as burst, chaotic, bag-jet etc [31, 33].

The secondary atomization regime is largely dependent upon the gas Weber number and the Ohnesorge number. For aerodynamic breakup studies, the Weber number uses the density of the ambient gas [33]. The trend is to decrease droplet size until the Weber number nears unity [51]. At high Ohnesorge numbers, the viscous force of the liquid drop inhibits drop deformation and hence breakup. This requires larger aerodynamic disturbances i.e. larger Weber numbers, to deform and atomize the drop. This is an important consideration for the injector spray characteristics in liquid rocket engines. Thrust chambers typically operate at pressures and temperatures near or above the critical point for the propellant combination causing

the surface tension of the liquid propellants to approach zero, leading to a very high Ohnesorge number. One series of experiments determined that for $Oh > 10$, drop breakup was not possible with $\mathrm{We}_g < 1{,}000$. Likewise for $Oh > 1000$, deformation of the droplet was not possible with $\mathrm{We}_g < 1{,}000$. However, at small Ohnesorge numbers ($Oh \sim 0.006$) breakup was initiated with $We_g \sim 10$ [33].

1.4.2.3 Droplet Size

The various mechanisms that govern the disintegration of liquid jets and sheets cause the atomization process to be heterogeneous and chaotic in nature. As a result, injectors do not produce uniform drop sizes for a particular operating condition. The atomized spray can be described as a spectrum of droplet diameters distributed about an arbitrarily defined mean droplet diameter. A histogram or frequency distribution curve of the number of droplets or the percentage of the volume/mass of the droplets as a function of droplet diameter can be created to describe the spray. The most common drop size distribution in use is the Rosin-Rammler relationship. However, in many practical calculations it is more convenient to work with a defined mean droplet diameter of the spray instead of a spectrum [30].

Various mean diameters exist and each can be described by the generalized equation, Eq. (1.27). Where i is the diameter range under consideration, N_i is the number of droplets within the designated range and D_i is the middle diameter within range i [30].

$$D_{ab} = \left[\frac{\Sigma N_i D_i^a}{\Sigma N_i D_i^b}\right]^{\frac{1}{a-b}} \tag{1.27}$$

D_{10} would be equivalent to the arithmetic mean drop diameter for all of the drops within the spray. Whereas, D_{20} is the mean diameter of a droplet whose surface area when multiplied by the total number of drops within the spray is equal to the total surface area of the spray. For spray combustion research, the most valuable mean diameter is the Sauter mean diameter (D_{32}). The Sauter mean diameter is the diameter of a drop whose volume-to-surface area ratio is equal to that of the entire spray. Another diameter that has been used extensively in the atomization literature is the mass median diameter (MMD or $D_{0.5}$). The mass median diameter is the droplet diameter where 50% of the liquid volume is composed of droplets with smaller diameters. Figure 1.18 shows a representative droplet frequency distribution curve with the locations of various drop diameters. The q-relation describes the droplet uniformity of the spray. Higher values of q correlate with greater uniformity of droplet size with typical values ranging between 1.5 and 4. $D_{0.5}$ is equal to D_{peak} when $q = 3.2584$. $D_{0.5}$ is smaller than D_{peak} when q is greater than 3.2584 and vice versa. D_{32} on the other hand, is always smaller than D_{peak} and generally ranges between 80 and 84% of D_{peak} [30].

The results from the experiments conducted by Dombrowski and Hooper determined an empirical drop size correlation for a water spray emanating from a like-doublet impinging injector into air at atmospheric pressure. The tests varied both injection velocity and impingement angle. The correlation, Eq. (1.28), relates the Sauter mean diameter (D_{32}) in microns for like-doublet injectors and is valid for turbulent flow and water in an atmospheric air environment. The symbols in the equation are in c.g.s. units [62].

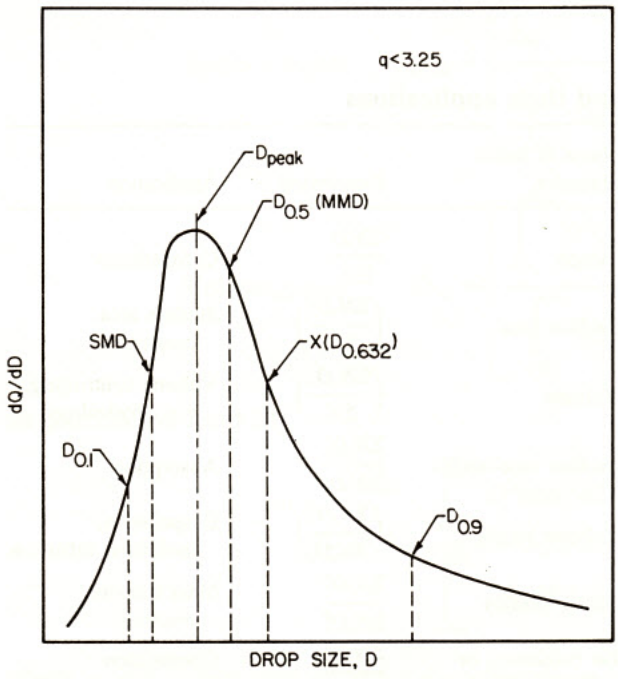

Figure 1.18: Representative Droplet Size Distribution with Locations of Several Mean Diameters [30]

$$D_{32} = \frac{4}{V^{0.79} \left(\sin\theta\right)^{1.16}} \tag{1.28}$$

Hautman conducted an experimental cold flow test program to determine the droplet size produced by a like-doublet impinging injector with an impingement angle of 60°. Water, Freon 113, and Jet A were used in the experiment. The injector was tested over a range of operating conditions and chamber pressures with each simulant to determine an empirical droplet size correlation. The resulting empirical correlation for the mass median diameter ($D_{0.5}$) of the droplets in microns is seen in Eq. (1.29). The variables in the equation require m.k.s. units [70].

$$D_{0.5} = 5.34 \times 10^6 \left(\rho_{liq} v_j^2\right)^{-0.62} \sigma_l^{0.43} \rho_{gas}^{-0.16} \tag{1.29}$$

Likewise, Lourme conducted a similar cold flow experiment using the like-doublet injectors found in the Ariane Viking rocket engine. The Viking injector used an impingement angle of 90°. The fluids used were water, UDMH, and N_2O_4. The injector was tested over a range of operating conditions and chamber pressures. The following empirical $D_{0.5}$ drop size correlation in microns was found. The variables require m.k.s units except for the length and diameter of the orifice which require dimensions in millimeters [54].

$$D_{0.5} = 150 \left(\frac{v_j}{30}\right)^{-0.95} \left(\frac{d_o}{2}\right)^{0.3} \left(\frac{l_o}{5}\right)^{-0.08} \left(\frac{\rho_{gas}}{5}\right)^{-0.2} \left(\frac{\sigma_l}{7.35 \times 10^{-2}}\right)^{0.5} \left(\frac{\mu_l}{1 \times 10^{-3}}\right)^{-0.04} \tag{1.30}$$

The values of the exponents for the empirical droplet size correlations given in Eq. (1.29) and Eq. (1.30) are in good agreement and several conclusions can be determined. The liquid velocity has the strongest affect upon the average droplet size. Increases in velocity/flow rate will decrease droplet diameter. Surface tension is an important variable that serves to increase the droplet size. Ambient gas density plays a moderate role in decreasing droplet size by exposing the droplet to greater aerodynamic forces. A larger orifice diameter promotes larger droplets. The results from Hautman include liquid density as a moderate contributor that reduces droplet

size. Finally, the contribution of viscosity and orifice length to the final droplet size is very weak or non-existent [54, 70].

CHAPTER 2

RESEARCH OBJECTIVE AND TEST PLAN

2.1 Research Objective

As described in more detail in Section 1.4, the results of Heidmann et al. [60] and Dombrowski and Hooper [62] showed that the atomization of two turbulent impinging jets forms a fully-developed spray pattern. This pattern is characterized by a small flat sheet distorted by impact waves that disintegrates into waves of ligaments and droplets. The work of Anderson et al. [51,53,67] demonstrated that the atomization frequencies of fully-developed like-doublet sprays are within the typical frequency range of combustion instability excited within liquid rocket engines as shown by the Hewitt stability correlation. This result demonstrated that primary atomization is likely a major player in exciting combustion instability. Chehroudi [36] has hypothesized that the empirical Hewitt stability threshold may occur at injection conditions that cause the average breakup length of the two impinging jets to approach the impingement distance.

Building upon the previous research described in the literature, the objective of this research program is to systematically determine how the ratio between the liquid jet breakup length and the impingement distance (l_b/l_i) affects and changes the

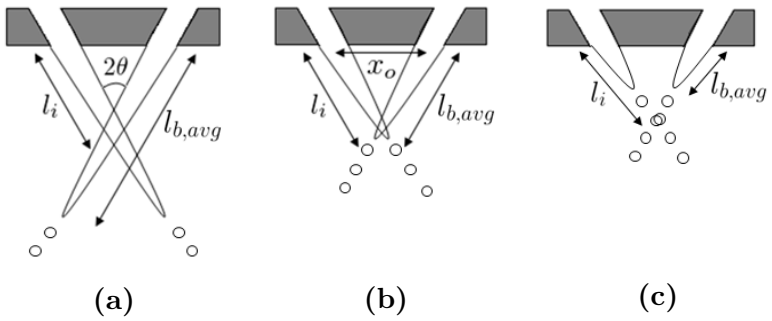

Figure 2.1: Liquid Jet Breakup Length to Impingement Distance Ratio: (a) $l_b/l_i > 1$**, (b)** $l_b/l_i \approx 1$**, (c)** $l_b/l_i < 1$

primary atomization characteristics of like-doublet impinging injectors using cold-flow experiments at atmospheric pressure. This study will observe the spray characteristics as well as measure the sheet breakup lengths, ligament wavelengths, and droplet diameter distributions of like-doublets when the l_b/l_i ratio is > 1, $= 1$, and < 1 using several impingement angles and a range of jet velocities. Figure 2.1 illustrates the three l_b/l_i regimes. From the collected data, empirical breakup length, ligament wavelength, and droplet diameter correlations will be developed. No previous research was found in the literature that systematically determined the effects of varying the (l_b/l_i) ratio for impinging jet injectors, especially when the breakup length of the impinging jets approach the impingement distance.

While the breakup lengths and characteristics of impinging jets that operate at atmospheric conditions will be different from the spray characteristics inside liquid rocket engines that operate at high, sometimes supercritical pressures and temperatures, the author believes it is important to establish a baseline data set at atmospheric conditions that systemically describes the changes in the atomization

characteristics of like-doublet injectors as the l_b/l_i ratio is varied. The purpose is not to determine whether or not the stable/unstable threshold seen in the Hewitt stability plot occurs when $l_b/l_i \sim 1$. This would require extensive experiments conducted with equivalent injector designs operating under similar conditions as the full-scale rocket engines studied. Instead, the results of this research are expected to quantify the differences in the primary atomization characteristics for like-doublet sprays over a range of l_b/l_i ratios.

Additionally, the second part of this research program will utilize visual observation in conjunction with Dynamic Mode Decomposition (DMD) to determine the physical characteristics and analyze the dynamic behavior that characterizes both the turbulent jets and resulting flat sheet. This part of the research program will investigate how the hydrodynamic impact waves form on the surface of the flat sheet and in turn how the atomization frequency of the shed ligaments is affected by the impingement process.

The unstable and nonlinear nature of impact wave formation and behavior is not fully characterized or understood. Several ideas have been put forth in the literature to describe impact wave formation including: fluctuations of pressure and momentum at the impingement point, periodic movement of the jets about the mean stagnation point, and interfacial shear stress within the liquid sheet [51, 64]. This research seeks to use cold-flow experiments with observation and DMD to characterize and correlate the instabilities seen on the two turbulent impinging jets with the surface waves on the flat sheet and periodic shedding of ligaments. This is the first time,

that the author is aware of, that the DMD technique has been used to study the impingement process of like-doublet injectors.

2.2 Test Plan

As a fundamental injector spray study, this research consists of a series of cold flow experiments conducted at atmospheric pressure. The liquid propellant simulant is water and the ambient environment is air. The two orifices that make up the like-doublet injector are designed to have a long l_o/d_o ratio to allow the flow to become fully-turbulent and minimize the formation of flow disturbances and hydraulic flip that could influence the resulting spray pattern and breakup characteristics. The research program consists of two parts. The first part systematically studies the effect of varying the l_b/l_i ratio on the atomization characteristics of like-doublet injectors. The second part of the program investigates the formation process of impact waves and the dominant dynamic modes within the spray.

2.2.1 The Jet Breakup Length to Impingement Distance Ratio for Like-Doublet Injectors

The first part of the research program will experimentally study the effects of the l_b/l_i ratio upon the primary atomization characteristics of like-doublet injectors. The gathered data will establish the natural spray pattern, sheet breakup length, ligament wavelength, atomization frequency, and droplet size distributions for each set point. The experiments are divided into two sets of test programs, single jet and like-doublet tests.

The single jet tests are used to determine the jet breakup lengths and breakup characteristics of the turbulent jet for the planned injection conditions. The single jet experiments are repeated with both orifices that make up the like-doublet injector. The injector is tested at four different jet velocities as shown in Table 2.1. The non-dimensional numbers are provided for reference and are calculated assuming a water temperature of $20°C$. The velocity range is selected to characterize the like-doublet spray from low velocities to jet velocities near the operating conditions of impinging injectors in liquid rocket engines. As a reference, the fuel injection velocity of the F-1 engine was 17 $^{m}/_{s}$ [10]. All four injection conditions form a fully-developed turbulent liquid jet.

Table 2.1: Planned Injection Conditions

Jet Velocity	Reynolds Number	Weber Number	Ohnesorge Number
5 $^{m}/_{s}$	5100	350	0.0037
10 $^{m}/_{s}$	10100	1400	0.0037
15 $^{m}/_{s}$	15200	3100	0.0037
20 $^{m}/_{s}$	20200	5500	0.0037

The like-doublet experiments test the injector at all of the operating conditions shown in Table 2.1 for four different $^{l_b}/_{l_i}$ ratio ranges: 2, 1.5, 1, and 0.5, refer to Figure 2.1. The $^{l_b}/_{l_i}$ ratio is varied for a given operating condition and impingement angle by changing the horizontal spacing (x_o) between the two orifices. Three impingement angles are used in the experiment: 30°, 60°, and 90°. These angles encompass the common design range of impingement angles used in past liquid

rocket engines. The most common impingement angle has been 60° [5]. However, the impingement angles for the F-1 injector were 30° for the fuel doublets and 40° for the oxidizer doublets [10]. While the Viking engine utilized 90° like-doublets for both the fuel and oxidizer [54]. These configurations result in a forty-eight point test matrix as seen in Table 2.2.

Table 2.2: Test Matrix

Impingement Angle	Jet Velocity	l_b/l_i Ratio			
30°	5 m/s	2	1.5	1	0.5
	10 m/s	2	1.5	1	0.5
	15 m/s	2	1.5	1	0.5
	20 m/s	2	1.5	1	0.5
60°	5 m/s	2	1.5	1	0.5
	10 m/s	2	1.5	1	0.5
	15 m/s	2	1.5	1	0.5
	20 m/s	2	1.5	1	0.5
90°	5 m/s	2	1.5	1	0.5
	10 m/s	2	1.5	1	0.5
	15 m/s	2	1.5	1	0.5
	20 m/s	2	1.5	1	0.5

2.2.2 Analysis of Like-Doublet Atomization using Visual Observation and Dynamic Mode Decomposition

The second part of the research program will investigate the primary atomization process of like-doublet injectors. Specifically, this research seeks to characterize the dynamic behavior of both the two turbulent jets and the flat

sheet. The results seek to determine the mechanism of impact wave formation and characterize the dominant dynamic modes in the primary atomization zone. The research will use visual observation and Dynamic Mode Decomposition (DMD) to analyze the high-speed videos of the experiments.

Similar to the l_b/l_i ratio study described above, the experiments are separated into two parts: single jet and like-doublet. The single jet tests will be used to determine the dynamic content of the turbulent jet for the planned operating conditions. Three jet velocities are tested: 5 m/s, 10 m/s, and 20 m/s. These velocities were selected to encompass a range of turbulence intensities and spray patterns. Approximately, 50 mm of the jet is captured by the camera frame with the exit of the injector tube centered at the top of the frame. Trying to capture the entire length of the jet for this part of the research program is impractical as a much smaller camera lens and/or an increase in the distance of the camera from the jet would be required and consequently very little surface detail of the jet would be captured by the video.

The like-doublet tests will test the injector for the same three jet velocities tested in the single jet configuration at a constant impingement angle and impingement distance. The impingement angle selected is 60° as it is the most common impingement angle used for the design of like-doublet injectors in liquid rocket engines. The impingement distance is selected so that $l_b/l_i = 2$.

Due to the unsymmetrical nature of impinging injector spray patterns, two sets of like-doublet experiments are conducted. The first set places the high-speed camera perpendicular to the face of the sheet capturing the side-view of the impingement

process. This allows a clear view of the entire surface of the flat sheet. The second set places the high-speed camera parallel with the face of the sheet capturing the front-view of the impingement process. This allows for an unobstructed view of both impinging jets and the edge of the flat sheet. Both video files will undergo DMD analysis to determine the characteristics and correlation between the dynamic behavior of the impinging jets and resulting spray.

CHAPTER 3

EXPERIMENTAL TECHNIQUE: TEST FACILITY, INSTRUMENTATION, AND DATA ANALYSIS

This chapter details the injector design, the test facility and equipment used during the experiments, the instrumentation used to collect data, as well as describe the techniques used to analyze the collected data.

3.1 Experimental Setup

The experiments described in Section 2.2 are conducted at the University of Alabama in Huntsville Atmospheric Spray Facility located at the Propulsion Research Center. The Atmospheric Spray Facility (ASF) uses a bench-top design that consists of two optics tables with a drain attached between them. The facility allows for unobstructed access to the flow field and can support custom setup for a wide variety of research topics and instrumentation setups.

The ASF is plumbed to use water and air as inert liquid and gas simulants for cold flow injector spray and atomization research. Water is supplied to the injector via a 0.23 m^3 run tank. A 141 m^3 air supply tank is used to supply inert gas flow to the injector (if needed) as well as pneumatic valve and dome regulator pressure

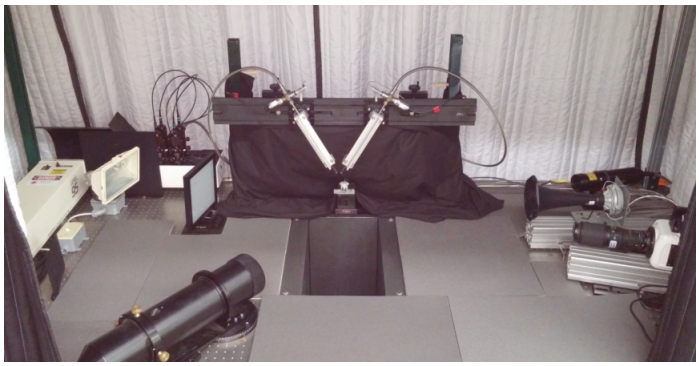

Figure 3.1: Atmospheric Spray Facility

to the facility. The liquid run tank pressure and air pressure is set by the operator and controlled by dome-regulated pressure regulators. Pneumatic ball valves control the flow of water and air to the experiment and also control the facility vents. Both the Atmospheric Spray Facility and the High Pressure Spray Facility share the same run and supply tanks. Therefore, the liquid and gas feedlines branch and the flow path is chosen by the opening/closing of isolation ball valves. The feedlines from the liquid run tank and air supply tanks are connected to the ASF through a bulkhead. All feedlines running from the either the liquid run tank and gas dome-regulators are 0.5 $in.$ diameter. For the like-doublet experiments described in this research, only the liquid feedline is used and the injector gas line is capped. From the bulkhead, additional experiment specific feed lines are constructed to finish the plumbing to the injector.

From the bulkhead, the liquid feedline reduces from 0.5 $in.$ diameter to 0.25 $in.$ diameter and remains constant up to the injector. After the reduction, the feedline is branched into two separate branches, each supplying one injector orifice. At the

branch point a thermocouple is installed to measure the water temperature. The two branches are of equal design and have identical lengths and contain the same type of instrumentation and fittings installed at the same locations downstream of the branch point. Beyond the branch point, an injector hand ball valve is used to open/close the flow path to the injector orifice allowing either orifice to be used in the single-jet tests. A 60 *in.* long stainless steel braided flex hose is used to connect the hand ball valve with a custom made instrumentation cross. The flex hoses enable the injector orifice to rotate and change position. The cross contains a static pressure transducer on one side and a high-frequency dynamic pressure transducer on the other side. These transducers are used to measure the injector pressure drop and flow oscillations respectively. The transducer cross is connected to the injector orifice via a 3.5 *in.* long, 0.25 *in.* diameter stainless steel line and a Swagelok UltraTorr fitting. The stainless steel line is mounted to the rotation platform so the glass injector tubes do not experience any bending stress. Additionally, a T-bar attaches from the rotation platform to 4 cm upstream of the exit of the glass orifice in order to increase the structural rigidity of the injector and reduce vibrations of the cantilevered injector tube. The T-bar is 21.75 cm long, with a width and height of 3.81 cm, and a thickness of 0.48 cm.

As stated previously, the Atmospheric Spray Facility test stand is composed of two 4 ft $\times$ 4 ft optics tables connected to each other by a drain. The overall surface dimensions of the test stand are 4 ft W $\times$ 9 ft L. The injector is oriented so that the centerline of the spray is located in middle of the drain and the normal vector from the face of the flat sheet points down the length of the test stand. The locations of

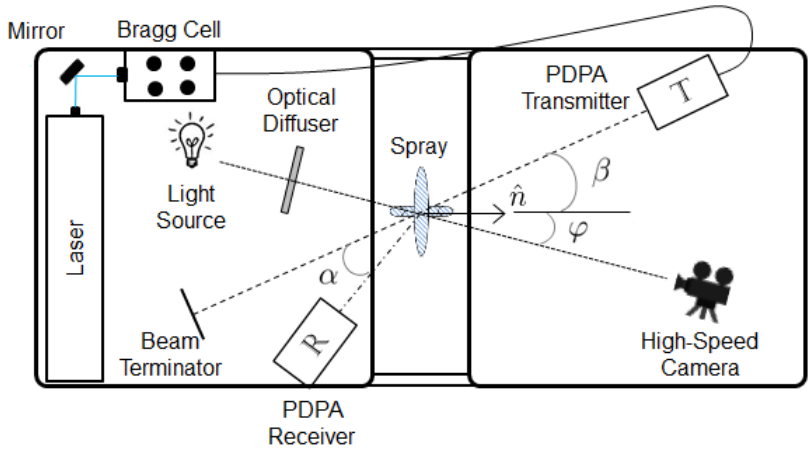

Figure 3.2: Spray Instrumentation Layout

the equipment and instrumentation on top of the surface of the test stand are shown in Figure 3.2.

The high-speed camera is mounted on a rail guide so that the camera can translate to capture the entire breakup length of the single-jet or primary atomization zone of the like-doublet spray. The camera is oriented at an angle, φ, from the normal vector of the flat sheet. The light source and optical diffuser is located directly in front of the camera on the opposite side of the spray. The light source is a 500 W halogen flood light. The light source is located behind a 200 mm $\times$ 200 mm size, 220 grit ground glass optical diffuser. This camera and light source orientation allows the spray to be backlit and captured with a shadowgraph imaging technique. The optical diffuser is used to create a light background that has an intensity level that is much more even compared with the light source alone.

The equipment for the Phase Doppler Particle Analyzer takes the greatest space on the test stand and is composed of the laser, Bragg cell, transmitter, and

receiver. The Lexel 95 laser is placed along the width of the test stand at opposite end from the camera. Using a mirror, the laser beam is directed into the Bragg cell. From there the split beams travel down a fiber optic cable to the transmitter. The transmitter is placed on the same side of the test stand as the camera and is oriented at an angle, β, from the normal vector of the flat sheet. The distance from the front of the transmitter to the spray is equal to the focus distance of the focus lens. On the opposite side of the spray, the receiver is setup in an off-axis forward scattering position with an off-axis angle, α, from the transmitted beams. The distance from the front of the receiver to the spray is equal to the focus length of the front receiver lens.

The experiment is monitored and controlled through two separate computers and three software programs. The first computer contains the LabView program that monitors and saves data for all of the instrumentation in the Atmospheric Spray Facility and injector feedline. The second computer contains the FlowSizer64 program used to control and record data from the PDPA as well as the Phantom Camera Control program used to control and record video from the high-speed camera. The data from each program is collected and saved at the same time during the experiment.

LabView is a graphical programming software developed by National Instruments that is used as a measurement and/or control system. LabView integrates with the wide selection of Data Acquisition (DAQ) cards and instrumentation modules developed by National Instruments allowing data to be measured and collected for all types of instrumentation. This capability allows LabView to be used to acquire data from experiments, used as embedded control systems, system prototyping,

etc [71]. For this research, LabView is used to monitor and record data from the static pressure transducers located throughout the Atmospheric Spray Facility and the instrumentation located in the feedline near the injector (static and dynamic pressure transducers and thermocouple). The static pressure and thermocouple data are routed through a NI BNC 2110 instrumentation module and into a NI PCI-6259 DAQ card that records the data at a sample rate of 100 Hz with 100 samples collected. The dynamic pressure transducers are routed through a NI 9215 instrumentation module connected into a portable NI cDAQ9188 chassis that records the data at a sample rate of 20,000 Hz with 10,000 samples collected.

The Phase Doppler Particle Analyzer (PDPA) is controlled with TSI's FlowSizer64 software. This program allows the user to control the settings of the PDPA, select the type of data that is to be recorded, and save the raw data and summary report of the statistics gathered from the spray. Some of the things that the PDPA can measure include: droplet diameter, 2-components of droplet velocity, and turbulence intensity. In addition, the software has a useful playback feature for saved data files that allows the user to replay that experiment and adjust various settings or save different data sets. Before the experiment, it is crucial that the user selects the correct hardware, lenses, and optical layout used in the PDPA setup as well as setting the right measurement technique and dominant light scattering method of the fluid under study in the FlowSizer64 program.

For this experiment, the PDPA is setup in a off-axis forward scattering position and the dominant light scattering method is refraction. The data in the form of histograms, plots and tables are shown on the front screen of the program which

updates in real time during an experiment allowing the user to see the results immediately. For these experiments, at least 10,000 droplets were measured to get good statistics of the injector spray for all set points. Additional information about the PDPA and the FlowSizer64 software can be found in the TSI PDPA/LDV manual [72].

The Phantom v711 high-speed camera is controlled with the Phantom Camera Control application (PCC 2.5). The PCC 2.5 program allows the user to adjust all of the camera settings during the experiment including: shutter speed, frame rate, trigger options, image tools, etc. In addition, it allows the user to view, save, and adjust the high-speed videos captured by the camera.

3.2 Injector Design

The objective of this research is to characterize the spray of like-doublet injectors as a function of the jet breakup length-to-impingement distance ratio (l_b/l_i). However, many parameters affect the spray atomization characteristics of like-doublet injectors including but not limited to: turbulence, cavitation, hydraulic flip, impingement angle, injection velocity etc. as was discussed in Section 1.4. Therefore to determine the effect of the l_b/l_i ratio on the spray characteristics of like-doublet injectors, it is necessary to isolate the other influences. This is done by changing the l_b/l_i in two ways, first by varying the injection condition and second by varying the injector geometry. The injection condition is varied by changing the jet velocity and the injector geometry is varied by changing both the impingement angle and orifice spacing, for a given jet velocity. Four jet velocities, three impingement

angles, and four l_b/l_i ratios were selected for this research program. The full 48 point injector test matrix can be seen in Table 2.2. In addition, careful design of the injector is required to minimize the likelihood of flow cavitation and hydraulic flip from developing within the injector.

The injector geometry is changed in two ways: impingement angle and orifice spacing. The two injector orifices are mounted to individual rotation platforms that allow for any impingement angle or impingement scheme to be set. In addition, the rotation platforms allow for both the like-doublet or single jet tests to be setup and performed with ease. The rotation platforms are attached to a horizontal rail guide that allows the spacing of the two injector orifices to be precisely controlled to match the l_b/l_i ratios given in the test matrix. The horizontal rail guide is mounted to vertical translating stages so that the impingement point and primary atomization zone can be centered in the frame of the camera. The injector is attached so that the spray travels vertically downward into the sink. Great care is taken to ensure that the orifice exits of each injector tube are aligned in the same horizontal and vertical planes so that robust impingement occurs and the flat sheet is oriented perpendicular to the impinging jets for all set points. Any misalignment of the impinging jets produces a flat sheet that is rotated at an angle from the perpendicular plane. The sheet rotation angle is proportional to the degree of misalignment. A large misalignment causes misimpingement of the two jets.

The injector consists of two thick-walled, smooth bore borosilicate glass capillary tubes. The glass tubes have a hole diameter of 1.016 mm $\pm$ 0.01 mm (0.04 $in.$), an outer diameter of 6.35 mm $\pm$ 0.25 mm (0.25 $in.$) and a length of

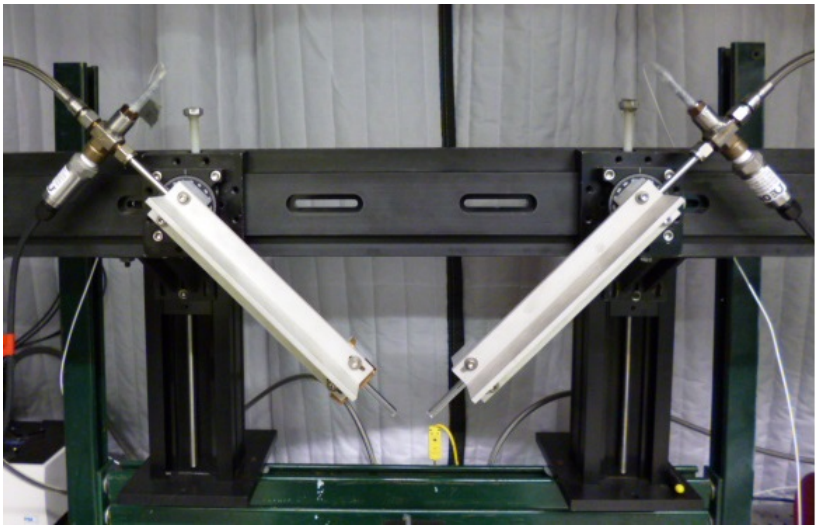

Figure 3.3: Injector Apparatus

203.2 $mm \pm 1\ mm$ (8 $in.$) resulting in a length-to-diameter (l_o/d_o) ratio equal to 200. The entrance of the orifice is sharp edged to initiate turbulent flow. The long (l_o/d_o) ratio is necessary to guarantee fully-developed turbulent pipe flow and minimize the likelihood of cavitation or hydraulic flip occurring for the flow rates being tested. The use of individual rotation platforms and a horizontal rail guide allows for the same two glass tubes to be used for all single jet and like-doublet test points in the experiment and greatly increases the repeatability of the flow conditions for all set points.

A flow calibration experiment of both glass tubes was conducted using water. The calibration method used a stopwatch and bucket to determine the mass flow rates as a function of injector pressure drop. Both tubes were tested independently for nine different pressure drops: 15, 25, 50, 75, 100, 125, 150, 175, and 200 psi. For each pressure drop, both tubes were tested three times resulting in a total of 54

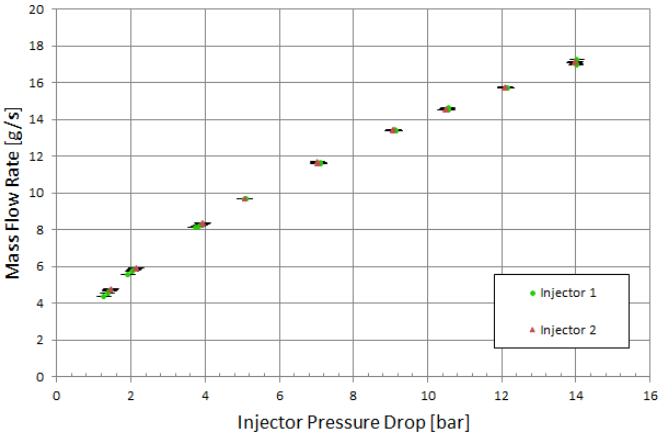

Figure 3.4: Injector Mass Flow Rate Calibration Data

calibration points. Each calibration test point lasted for approximately 60 seconds and the bucket was weighed with a digital scale before and after each point. This was done to reduce uncertainty in the calibration measurements. The average mass flow rate was calculated by dividing the mass of the water collected in the bucket by the elapsed time. Figure 3.4 shows the results of the calibration experiment, the circles represent injector tube 1 and the triangles represent injector tube 2. The horizontal and vertical bars represent the experimental uncertainty of the injector pressure drop and mass flow rate respectively. As can be seen, most of the test points are on top of one another indicating excellent repeatability and the very small vertical error bars indicate very small uncertainty in mass flow rate.

Since the glass tubes have a long (l_o/d_o) ratio, the injector is modeled as a pipe as opposed to an orifice. With the sharp edge entrance and long (l_o/d_o), fully-developed turbulent flow is assumed to exist within the injector tube. In addition, effects due to gravity are neglected as analysis showed that the relatively short vertical distance

between the entrance and the exit of the injector produces negligible pressure drop difference. The overall pressure drop through the injector tube (ΔP_{inj}) is described by Eq. (3.1), where ΔP_{ent} is the minor loss due to the entrance and ΔP_{tube} is the pressure drop down the length of the tube.

$$\Delta P_{inj} = \Delta P_{ent} + \Delta P_{tube} \tag{3.1}$$

The pressure drop associated with the minor loss due to the abrupt contraction at the entrance to the injector tube can be described by the following equation.

$$\Delta P_{minor} = K_L \frac{\rho v_2^2}{2} \tag{3.2}$$

Where K_L is the minor loss coefficient and is equal to 0.48 for a sharp edge entrance with an injector tube-to-feedline area ratio of 0.044 [32]. Inserting Eq. (3.2) into Bernoulli's equation, the total pressure drop caused by the sudden contraction at the entrance ΔP_{ent} can be found, see Eq. (3.3). Where v_2 is the velocity of the fluid downstream of the contraction and is assumed to be equal to the exit injection velocity, and v_1 is the fluid velocity within the feedline upstream of the entrance to the tube.

$$\Delta P_{ent} = \frac{\rho}{2} \left[\left(1 + K_L\right) v_2^2 - v_1^2 \right] \tag{3.3}$$

The Darcy-Weisbach equation is used with Bernoulli's equation to find the pressure drop down the length of the pipe ΔP_{tube}. The diameter of the injector

does not vary with axial distance and it is assumed that the turbulent flow is fully-developed and the flow velocity, equal to the exit injection velocity, does not vary down the length of the tube. ΔP_{tube} can be found with Eq. (3.4), where f is the friction factor.

$$\Delta P_{tube} = f\left(\frac{l_o}{d_o}\right)\frac{\rho v^2}{2} \tag{3.4}$$

For fully-developed turbulent pipe flow, the friction factor can be described by the Colebrook formula, Eq. (3.5). Where ε is the wall roughness. This equation is based upon empirical data for many pipes of varying diameter and wall roughness. It cannot be solved directly, so an iterative solution method is used instead [29].

$$\frac{1}{\sqrt{f}} = -2\log\left(\frac{\varepsilon/d}{3.7} + \frac{2.51}{Re\sqrt{f}}\right) \tag{3.5}$$

The wall roughness, ε, is neglected for the smooth-bore, glass injector tubes used in this research. However, when comparing the flow rate predictions using the above equations with the flow calibration data, it is seen that the Colebrook equation over-predicts the magnitude of the friction factor for the glass tubes causing a subsequent over-prediction of the required injector pressure drop for a given mass flow rate or jet velocity, refer to Figure 3.5. This is not surprising as the empirical Colebrook constant of 2.51 is a best fit for experimental data taken for a wide variety of pipes and wall roughness characteristics.

Therefore, the empirical constant was replaced with the constant X, the value of which was solved numerically using a least sum of squares approach with the

collected flow calibration data. The X value for the glass tubes was found to be equal to 1.83, see Figure 3.5. The modified form of the Colebrook equation, Eq. (3.6), is valid for the glass injector tubes used in this research. The pipe flow and modified Colebrook equations were incorporated into the LabView experiment control program to calculate in real-time the required pressure drop needed to match a required jet velocity per the test matrix and fluid properties.

$$\frac{1}{\sqrt{f}} = -2\log\left(\frac{1.83}{Re\sqrt{f}}\right) \tag{3.6}$$

The final analysis conducted on the injector design, calculated the cavitation number (K_c) over the range of operating conditions planned for the experiment. The cavitation number within a long $^{l_o}/_{d_o}$ orifice can be calculated using Eq. (3.7) as described by Hiroyasu, et al. [34]. Where l_c is the length of the vena contracta and C_c is the contraction coefficient which is approximately equal to 0.62 for a sharp-edge entrance [32].

$$K_c = C_c^2\left[\frac{P_{atm} - P_v}{\frac{1}{2}\rho v_j^2} + f\left(\frac{l_o - l_c}{d_o}\right) + 1\right] - 1 \tag{3.7}$$

Cavitation numbers smaller than 1.0 generally indicate the presence of fixed cavitation within the injector, while a negative value suggests possible supercavitation [34]. Table 3.1 contains the calculated cavitation numbers for the four jet velocities considered in this experiment. The water temperature is assumed to be $20°C$ which corresponds with a vapor pressure of $2,338\ Pa$ [32]. The length of the flow contraction (l_c) is assumed to be $4d_o$ which is equal to the observations of the

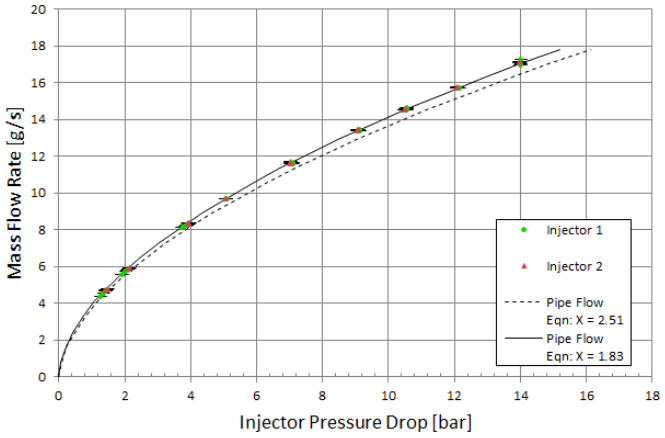

(a)

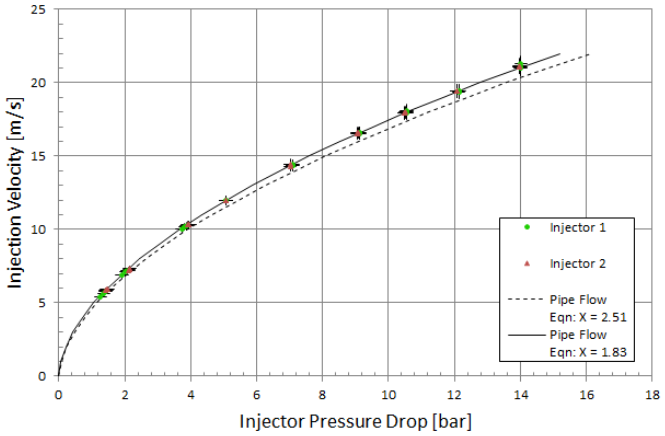

(b)

Figure 3.5: Calibration Data with Prediction Curves: (a) Mass Flow Rate per Orifice and (b) Injection Velocity

length of the separation region near the orifice entrance as described by Nurick [47]. From Table 3.1, all of the cavitation numbers are greater than 1.0 which indicates that cavitation should not be present within the injector tubes. Additionally, visual inspection of the glass tubes at each operating condition did not exhibit a "fuzzy" two-phase flow region near the entrance of the injector and the jets did not have

a "bushy" appearance after exiting the injector that would indicate the presence of cavitation as described by the results of Nurick [47].

Table 3.1: Calculated Cavitation Numbers

v_j	K_c
5 $^m/_s$	5.1
10 $^m/_s$	2.4
15 $^m/_s$	1.7
20 $^m/_s$	1.4

3.3 Instrumentation

The experimental setup contains two sets of instrumentation, one set located in the feedline and the other measuring the resulting spray properties downstream of the injector. The feedine instrumentation is located upstream of the orifices and are used to measure and determine the physical and flow properties of the liquid simulant. The instrumentation characterizing the spray is used to determine the atomization properties of the jet, sheet, ligaments, and droplets. The specific devices and locations used for each instrumentation set are described in the following subsections.

3.3.1 Feedline Instrumentation

Upstream of the orifices, there exists three types of instrumentation within the feedlines to measure the condition of the liquid simulant. A thermocouple is located at the branch point where the main feedline breaks into two equal branches that lead to the two orifices. The thermocouple measures the temperature of the

liquid which is used to determine the physical properties of the liquid, i.e. density, viscosity, and surface tension. Within each branch a static pressure transducer and a high-frequency dynamic pressure transducer are installed into a cross-type fitting with the centerlines approximately 13.5 cm (135 orifice diameters) upstream of the entrance to each orifice. The static pressure transducer measures the gauge pressure of the liquid which is used to calculate the mass flow rates and injection velocities of the liquid simulant. The high-frequency dynamic pressure transducer is used to measure any liquid pressure disturbances or oscillations within the feedline that can propagate through the injector and affect the breakup behavior of the spray.

The type of thermocouple used is an Omega $^1/_8$ $in.$ (3.2 mm) diameter K-type ungrounded thermocouple. K-type thermocouples have one lead made from chromel and the other from alumel which allows temperature measurements to be made up to 1,600 K. In water, the response time for the thermocouple is around 0.55 seconds. The total measurement uncertainty is 2.2°C or 0.75% of the reading, whichever is greater [73]. For the water temperatures considered in this research, the total uncertainty of the thermocouple is a constant 2.2°C.

The static pressure within the feedline is measured with Omega PX309-500G5V pressure transducers. These pressure transducers are designed to be rugged with high stability and low drift and incorporate solid state electronics and a case and diaphragm made from 316 stainless steel. The PX309-500G5V can measure gauge pressures between 0 and 500 psi with an output of 0 to 5 V_{dc}. They have a systematic measurement uncertainty of ± 0.25% of full-scale (± 1.25 psi) which includes the effects of linearity, hysteresis, and repeatability [74].

The PCB Piezotronics 106B integrated circuit piezoelectric (ICP) pressure sensor is used to measure dynamic pressure oscillations within the feedlines. These sensors are designed to measure small pressure perturbations either in gases or liquids and can be used in severe environments and at high static pressures. The 106B pressure sensor uses a "high-sensitivity, acceleration compensated quartz pressure element coupled to built-in integrated circuit impedance converting amplifiers [75]." This allows the sensor to have excellent linearity and a large usable frequency range that delivers outputs with strong signal-to-noise ratios and good resolution. The body and diaphragm of the sensor is made from stainless steel and is welded to form a hermetic seal. The sensitivity of the 106B sensor used in the feedline of Injector Tube 1 is 41.85 $^{mV}/_{kPa}$ and the sensor used in the feedline of Injector Tube 2 is 43.53 $^{mV}/_{kPa}$. Both sensors have a resolution of 0.69 Pa [75].

3.3.2 Spray Characterization

Two optical techniques are used to measure and characterize the atomization of the resulting injector spray. The first is a high-speed camera that is used to capture a sequence of images that are post processed to determine breakup lengths of the liquid jet and sheet, wavelengths between the ligaments, overall breakup characteristics, etc. The camera is oriented and focused to capture the primary atomization zone. The second optical technique is a phase doppler particle analyzer (PDPA) that is used to collect bulk statistics of the droplet field within the secondary atomization zone. The PDPA measures everything from droplet diameter to droplet velocity and turbulence

intensity in two dimensions. More information about the specifics of both optical instruments are given below.

3.3.2.1 High-Speed Camera

The Phantom v711 high-speed camera is used in this research to capture detailed images/video of the primary atomization process. The v711 is a 1 megapixel camera that contains a widescreen 1280 $\times$ 800 pixel CMOS image sensor. The image sensor has a 20 μm pixel size and a ISO Monochrome of 20,000T; 6,400D and a ISO Color of 2,500T; 2,000D. This camera can take 7,530 frames per second (fps) at the maximum resolution of 1280 $\times$ 800 pixels and up to 1,400,000 fps at the lowest resolution of 128 $\times$ 8 pixels with the 'FAST' option enabled. It also has an electronic shutter that can operate with a minimum exposure time of 1 μs [76]. This allows the sheet and droplets to be frozen for each frame and eliminates any blur associated with motion.

In addition, the v711 high-speed camera has the option of using the Extreme Dynamic Range (EDR) feature. By setting the EDR time between one-half to one-quarter of the global exposure time this feature reduces hot spots where certain pixels within an image are over-exposed. This allows for greater detail/data to be extracted from the previously saturated pixels. The resolution, frame rate, exposure time, EDR, etc. can be changed by the user on the fly with the camera control software. There are many other features and capabilities including but not limited to triggering, signaling and synchronization that will not be explained here and can be found in the manual and help files within the Phantom camera control software [76].

Different lenses were used with the Phantom v711 high-speed camera. During the single jet test cases, a Nikon Micro-Nikkor 105 mm f/2.8 lens was used. This lens is formatted for FX/35 mm sensors and has a maximum aperture of f/2.8, a minimum aperture of f/32 and a maximum viewing angle of $23°20'$ [77]. The 105 mm lens allows for a wide-view that captures the entire breakup length of the jet for all flow rates tested. During the like-doublet test cases, a Nikon AF Micro-Nikkor 200 mm f/4 IF-ED lens was used. This lens is also formatted for FX/35 mm sensors and has a maximum aperture of f/4, a minimum aperture of f/32 and a maximum viewing angle of $12°20'$ [78]. The 200 mm lens allows for close-up and detailed views of the whole flat sheet and primary atomization zone that captures the surface irregularities of the sheet and ligaments.

For the DMD experiments, smaller lenses were used. For the single jet and side view of the like-doublet spray, a Nikon AF Micro-Nikkor 60 mm f/2.8 lens was used. This lens is formatted for FX/35 mm sensors and has a maximum aperture of f/2.8, a minimum aperture of f/32 and a maximum viewing angle of $26°30'$ [79]. For the front view experiments of the like-doublet, a Nikon AF Nikkor 28 mm lens was used. This lens is also formatted for FX/35 mm sensors and has an aperture range of f/2.8 to f/22 and a maximum viewing angle of 74° [80].

3.3.2.2 Phase Doppler Particle Analyzer

The Phase Doppler Particle Analyzer (PDPA) is a laser optical technique and instrument based upon the Laser Doppler Velocimetry (LDV) method to simultaneously measure the velocity and diameter of spherical particles. It can also

be used to determine species concentration and mass flux. This enables particle measurements to be collected with high accuracy and spatial resolution without interfering with the flow. Also, since the PDPA method is based on an absolute physical effect, no calibration is necessary [81]. Unlike the LDV technique which has the transmitting and receiving optics in one unit called a transceiver, a PDPA uses a separate transmitter and receiver. This allows the PDPA to be setup to detect light scattering caused by refraction in addition to reflection [72].

To measure the droplet velocity, the PDPA uses the principle of light scattering caused by light interacting with the surface of the droplet. For a PDPA system, a set of two laser beams, one set for each velocity component, intersect to form a measurement volume composed of a fringe pattern. When a droplet passes through the measurement volume, it scatters light when it passes a bright fringe and doesn't scatter light when it passes a dark fringe. The result is a fluctuating intensity pattern of scattered light that has a frequency directly proportional to droplet velocity. This measured Doppler frequency (F_d) can be converted to droplet velocity (v) by multiplying the Doppler frequency by the known fringe spacing (δ_f), see Eq. (3.8) below [72].

$$v = \delta_f F_d \tag{3.8}$$

However, if both laser beams in the set have an equal frequency, the intersection will create a measurement volume that contains a stationary fringe pattern. This is not a problem for measuring the speed of the droplet but the

instrument will not be able to determine the direction of droplet motion. Therefore, one of the two laser beams in each set is frequency shifted by a Bragg cell to a suitably high frequency, approximately 40 MHz for the PDPA used in this experiment. The result is a fringe pattern that moves at a rate equal to the Bragg frequency within the measurement volume. When a droplet passes through the measurement volume, the measured frequencies will be either greater than the Bragg frequency when the droplet moves in a direction opposite the fringe motion or smaller than the Bragg frequency when the droplet moves with the fringe motion. The difference between the measured frequency and the Bragg frequency is equal to the Doppler frequency that can be then converted to droplet velocity, see Eq. (3.8) [72].

To measure droplet diameter, the PDPA measures the droplet's radius of curvature by measuring the relative phase shift of light scattered by the droplet. As a droplet passes through the measurement volume, it causes the fringes themselves to be scattered resulting in spatial variation of the fringes detected by the receiver. The spatial frequency can be related to droplet size by comparing the phase shift of the scattered light signal between at least two detectors. Several factors can effect the resulting size measurement and include: effective spacing between the detectors, particle shape, index of refraction, scattering process, and droplet number density. The greatest limitation to this method is the requirement that the measured droplets be spherical. The theory behind the calculations made by the PDPA assume spherical particles. Therefore, nonspherical particles, such as ligaments, or oscillating droplets will be sized based upon how the light is scattered from the surface and can result in large measurement errors. Techniques exist to minimize measurement uncertainty

and include utilizing a correct optical layout for the type of spray in question, knowing the properties of the fluid, having multiple independent size measurements that can be compared and discard those measurements that have large disagreement between the detectors, intensity validation schemes and having the measurement volume located in a region of the spray where the vast majority of droplets can be assumed to be spherical [72, 82].

In order to collect valid measurements, the transmitter and receiver of the PDPA system must be oriented at correct angles that depend on the optical properties of the fluid(s) under study. The off-axis angle between the receiver and transmitter can vary between 0° and 180°. Angles between 0° and 90° correspond with forward scattering (refraction) and angles between 90° and 180° correspond with back scattering (reflection). For water droplets in air, the relative refractive index is 1.33 and the attenuation coefficient is 0. This makes refraction the dominant light scattering method of the droplets. In order to minimize reflections from interfering with the droplet measurements, an off-axis forward scattering setup is applied with valid off-axis angles between $30° < \alpha < 75°$ for the receiver. Strongest light intensity is received at an off-axis angle of 30° [72].

The PDPA system used in this research is the TSI 2-component PDPA with a TLN05-250 transmitter and a TLN10-500 receiver. The transmitter is installed with a 0.5:1 internal beam contractor and a 1000 mm focus lens. The receiver has a 150 μm slit aperture and is installed with a 368 mm back focus lens and a 500 mm front focus lens. The receiver is oriented with an off-axis angle (α) of 42° in relation to the transmitter. This setup results in a measurable droplet diameter range of 6 μm

to 2066 μm and a measurable droplet velocity range of -154 $^{m}/_{s}$ to 308 $^{m}/_{s}$ in the axial direction and -146 $^{m}/_{s}$ to 292 $^{m}/_{s}$ in the lateral direction across the face of the sheet. The measurement volume of the PDPA is placed about 75 mm downstream of the impingement point within the secondary atomization zone centered on the axial centerline from the impingement point for each test condition. The droplets passing through the measurement volume should be approximately spherical as this location is between two to five times the breakup length of the flat sheet.

The transmitter is oriented at an angle (β) of 9° in relation to the normal vector from the face of the sheet. Therefore, a transformation matrix must be applied to the velocity calculations to find the correct values of the lateral velocity across the face of the sheet. v_1 is the vertical velocity component measured by the PDPA and is equal to the axial velocity of the fluid (v_{ax}), see Eq. (3.9). v_2 is the horizontal velocity component measured by the PDPA and is equal to Eq. (3.10).

$$v_1 = v_{ax} \tag{3.9}$$

$$v_2 = v_{lat}\,(cos\beta) + v_{per}\,(sin\beta) \tag{3.10}$$

Where v_{lat} is the lateral velocity across the face of the sheet, v_{per} is the velocity perpendicular to the face of the sheet and β is the transmitter angle in relation to the normal vector from the sheet. Due to the formation of a flat sheet when two jets impinge, the spray can be approximated as two dimensional with the velocity

component normal to the surface of the flat sheet equal to zero. Therefore the equation for v_2 simplifies to Eq. (3.11).

$$v_2 = v_{lat}\,(cos\beta) \tag{3.11}$$

The v_1 and v_2 equations are then put into matrix form and entered into the PDPA FlowSizer64 control program. The matrix must be entered into the program in the form seen in Eq. (3.12) because the FlowSizer64 program automatically calculates the inverse of the matrix and solves for v_{ax} and v_{lat}. The resulting velocity outputs from the PDPA are the corrected orthogonal velocity components.

$$\begin{bmatrix} v_1 \\ \\ v_2 \end{bmatrix} = \begin{bmatrix} 1 & 0 \\ \\ 0 & cos\beta \end{bmatrix} \cdot \begin{bmatrix} v_{ax} \\ \\ v_{lat} \end{bmatrix} \tag{3.12}$$

3.4 Data Analysis

After the data is collected from the instrumentation and saved into separate files, it is processed to garner results that are useful for characterizing the injection conditions and spray. The following subsections detail the various analysis techniques used in this research. Section 3.4.1 describes the two Matlab programs written to calculate flow parameters such as mass flow rate and feedline oscillations. Section 3.5 describes the method and calculations used to determine the uncertainty of the calculated results. Section 3.4.2 describes the image analysis technique used to measure and characterize the spray from the high speed video files. Section 3.4.3, describes the method to calculate the bulk statistics of the spray field collected by

the PDPA. Finally, Section 3.4.4 describes the dynamic mode decomposition (DMD) technique.

3.4.1 Matlab Analysis

The pressure and temperature data collected from the LabView experiment control program is processed using Matlab. The data is analyzed with two Matlab programs, a low-speed data analysis program and a high-speed data analysis program. These two programs are used to calculate useful results that fully characterize the flow conditions for a given set point.

3.4.1.1 Low-Speed Data Analysis

The low-speed data analysis program is used to process the data collected by the static pressure transducers located upstream of the injector as well as the temperature data collected by the thermocouple. These instruments are sampled at a relatively low sample rate of 100 Hz for 100 samples. In addition, the friction factor for that set point and other user specified set point constants such as impingement angle are saved in the data file. Various equations are used to calculate meaningful results that characterize the flow condition for each set point based upon the collected pressure and temperature data.

The first step in the analysis, calculates the mean and standard deviation of the static pressure and temperature measurements. Then the density, surface tension, and viscosity of the water is calculated using the mean temperature and curve-fit equations interpolated from tabular water property data found in Vennard [32]. Using the

known injector dimensions, the following equations are used to calculate the injection velocity and mass flow rate per injector orifice respectively.

$$v_j = \sqrt{\frac{\Delta P_{inj}}{\frac{1}{2}\rho\left[1 + k_L + f\left({}^{l_o}/_{d_o}\right) - \left({}^{d_o}/_{d_p}\right)^4\right]}} \tag{3.13}$$

$$\dot{m}_{inj} = \left(\frac{\pi d_o^4}{4}\right)\rho v_j \tag{3.14}$$

Finally, the Reynolds number, Weber number, and Ohnesorge number are calculated to fully characterize the flow condition. The equations used are the same as shown in Eq. (1.11) for the Reynolds number, Eq. (1.12) for the Weber number, and Eq. (1.13) for the Ohnesorge number. The data analysis program then saves all of the results and set point information into an Excel spreadsheet. This spreadsheet contains the results for all set points tested.

3.4.1.2 High-Speed Data Analysis

The high-speed data analysis program is used to process the data collected by the high-frequency dynamic pressure transducers located in the feed system. These instruments are used to capture the oscillating pressure fields due to feed line disturbances. Therefore they are sampled at the high rate of 20,000 *Hz* for 10,000 samples, much greater than the instrumentation analyzed by the low-speed data program.

This program outputs two plots for each sensor. The first plot is the waveform of the oscillating pressure signal with respect to time. The second plot is a Fast Fourier

Transform (FFT) of the data. The FFT technique transforms the time-dependent data into frequency space and plots the relative peak amplitude(s) of all of the frequency modes that comprise the oscillating signal. Where the amplitude of each frequency component of the signal is on the y-axis and the frequency is on the x-axis. For the dynamic pressure transducers, the peak pressure amplitude is in units of millibars.

3.4.2 Image Analysis

The high-speed video taken with the Phantom v711 camera is processed using the ImageJ image analysis program. ImageJ is used to measure the breakup length of the jet and sheet, the wavelengths between the shed ligaments, and the diameter of the large droplets pinched off the end of the single jet. One out of every four frames from each video (at least 50 frames) are analyzed and the results are entered into an Excel spreadsheet. From the compiled results, the mean and standard deviation are calculated which describe the breakup characteristics of the single jet and flat sheet.

Before an experiment, the camera position and settings are adjusted so that a clear, detailed view can be seen of the entire jet for the single jet experiments or the primary atomization zone for the like-doublet experiments. Once the camera is set, a ruler is placed in front of the camera at the location of the jet or sheet and a snapshot is taken. This snapshot is used as a calibration image that gives the ratio of pixels per millimeter for that camera setting. The pixel size of the high-speed video varied depending on camera settings and location requirements to allow the entire spray to be captured by the camera frame. For Part 1 of the research program (l_b/l_i

study), the pixel size is 3.43 $^{pix}/_{mm}$ with a resolution of 48 x 696 pixels for the single jet experiments. While the pixel size varied between 8.28 and 14.16 $^{pix}/_{mm}$ with a resolution of 800 x 800 pixels for the like-doublet experiments. For Part 2 of the research program (DMD study), the pixel size is 3.225 $^{pix}/_{mm}$ with a resolution of 80 x 160 pixels for the single jet and the side view of the like-doublet experiments while the pixel size is 3.667 $^{pix}/_{mm}$ with a resolution of 80 x 160 pixels for the front view of the like-doublet experiments.

The breakup length measurements are straightforward. For the single jet experiments, the breakup length is found by measuring the axial distance from the exit of the orifice to the point where the liquid column disintegrates into drops or the first point where the liquid column becomes segmented. For the like-doublet experiments, the breakup length is found by measuring the axial distance from the impingement point to the point where the sheet disintegrates into droplets and/or ligaments. Figure 3.6 shows examples of the measurement technique for finding the breakup length for both a single jet and a flat sheet.

The wavelength of the ligaments formed from the disintegration of a flat sheet with a like-doublet injector is determined by measuring the axial distance between two consecutive ligaments. The atomization frequency is calculated by dividing the measured wavelength by the mean axial velocity of the droplet measured by the PDPA system. Figure 3.7 shows an example of the measurement technique used for determining the ligament wavelength for like-doublet injectors.

For the single jet tests, the jet disintegrates into large droplets with diameters much larger than those formed from impinging jets. For the single jet case, the

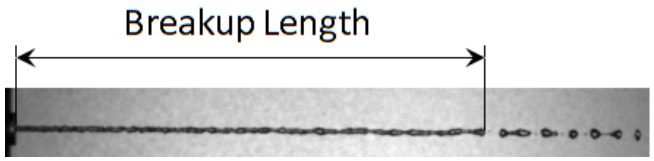

(a)

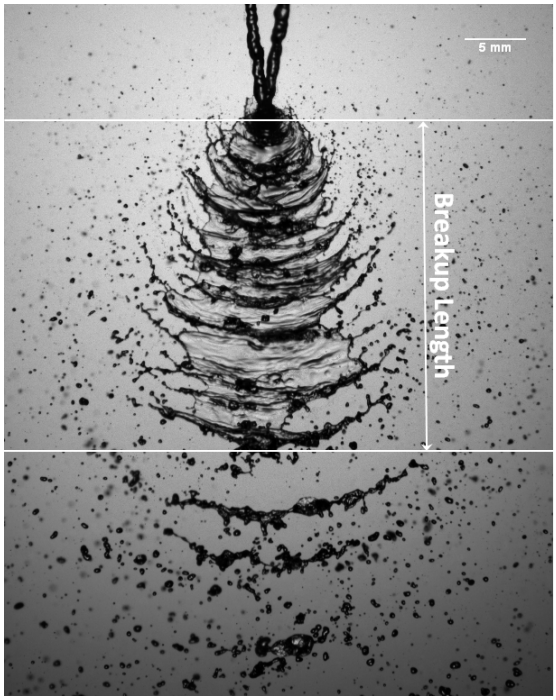

(b)

Figure 3.6: Breakup Length Measurements: (a) Jet and (b) Flat Sheet

droplet diameter is too large to be measured by the PDPA. Therefore, they are measured using image analysis. The droplets are roughly spherical well downstream of the jet. However, the shape of the droplets captured by the camera near the end of jet approximate ellipsoids whose shape fluctuates with time.

Therefore the droplet diameter is determined in two ways, the Waddel disk and equivalent sphere techniques. The Waddel disk diameter technique calculates

Figure 3.7: Atomization Frequency Measurements

the diameter of a circular disk with the same area as the two dimensional image of a non-spherical particle [83]. The area of each droplet is measured using the Analyze Particles function of the ImageJ image processing program.

The equivalent sphere method measures each droplet twice, once across the length and once across the width of the droplet. These measurements give two dimensions of an ellipsoid, one long and one short dimension. It is then assumed that the two short dimensions of the ellipsoid, m and n, are equal. The equivalent spherical diameter of the drop is calculated by setting the volume of the sphere equal to the volume of the measured ellipsoid and solving for the spherical diameter.

$$V_{sphere} = \frac{\pi}{6} d^3 \tag{3.15}$$

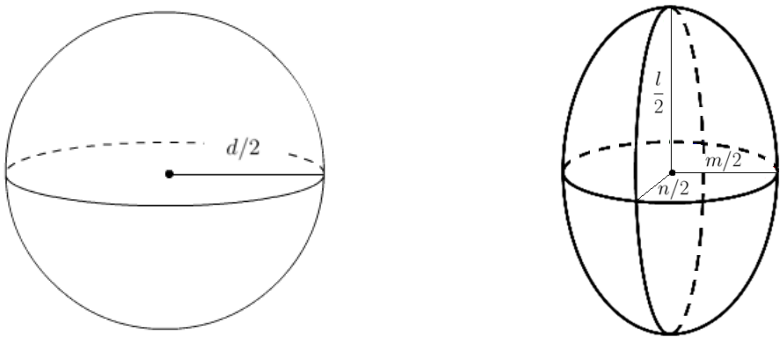

(a) **(b)**

Figure 3.8: Geometry of: (a) Sphere and (b) Ellipsoid

$$V_{ellipsoid} = \frac{\pi}{6} lmn$$
$$= \frac{\pi}{6} lm^2 \quad (m = n) \tag{3.16}$$

After equating the volume of the equivalent sphere with the volume of the ellipsoid and solving for the diameter of the equivalent sphere which is equal to the diameter of the droplet (d_{drop}). The final equation is displayed in Eq. (3.17).

$$d_{drop} = \sqrt[3]{lm^2} \tag{3.17}$$

3.4.3 PDPA Analysis

For each set point, five types of files are saved from the Phase Doppler Particle Analyzer (PDPA). The first three types are a set of files that contain all of the information needed for the FlowSizer64 software to replay the data set and contains

the following filetypes: *.d64, *.dat, *.set. The fourth file type saved is a *.csv file of the raw data collected for the droplet diameter as well as the axial and lateral droplet velocities. The final file type saved is a *.txt file that is a summary report of the statistics collected by the PDPA for that set point. The summary report contains the droplet diameter measurement statistics which includes the number mean diameter, Sauter mean diameter, number of samples, sample rate, etc. In addition, it contains the velocity statistics including mean and rms velocities, turbulence intensity, number of samples, etc. It also shows the transformation matrix used to correct the velocity magnitudes caused by the transmitter being oriented at an angle α from the normal vector of the sheet.

The *.csv file containing the raw data is used to create histograms to visualize the droplet diameter and velocity distributions. Occasionally within the data set, some outliers are present in the velocity data. An example being velocity measurements of -40 $^{m}/_{s}$ when the rest of the measurements agree with the jet velocity of approximately 5 $^{m}/_{s}$. No obvious reason for this discrepancy can be found. Therefore, Chauvenet's criterion is used as an objective statistical procedure to identify these outliers in the data set so that they can be discarded from the analysis. Chauvenet's criterion defines, from the standpoint of probability, the acceptable amount of scatter within a given data set of sample size N from the Gaussian parent population. It specifies that the data points within a probability band of $1 - \frac{1}{2N}$ around the mean should be retained. Points falling outside of this probability band can be rejected [84].

Three types of histogram plots of the droplet distribution are created for each data set: droplet diameter, axial velocity, and lateral velocity. The two velocity histograms are plotted with velocity on the x-axis and number fraction on the y-axis. The number fraction is found by dividing the number of droplets in each bin by the total number of droplets sampled by the PDPA. The droplet diameter distribution plot contains two histograms. The first is the distribution of number fraction versus droplet diameter and the second histogram is the distribution of mass fraction versus droplet diameter. The mass contained in each droplet bin is found by multiplying the density of water for that set point by the volume of the droplet and the number of droplets in that bin. Each droplet is assumed to be spherical. See Eq. (3.18) for the equation used. The mass fraction is calculated by dividing the bin mass by the total mass sampled by the PDPA. It can be argued that the mass fraction distribution is more important from a combustion standpoint because of the greater chemical energy available with the droplet diameters associated with a large mass fraction.

$$m_{drop} = \frac{\pi}{6}\rho d_{drop}^3 \tag{3.18}$$

Additionally, values of the numerical mean and Sauter mean diameters are calculated. Also, a table containing the mean velocities, median velocities, rms fluctuation velocity, and turbulence intensity is made for the axial and lateral components. v_{rms} is calculated by taking the standard deviation of the velocity measurements. Turbulence intensity is calculated by dividing v_{rms} by v_{mean}.

3.4.4 Dynamic Mode Decomposition

Turbulent fluid flow is of great scientific interest due to its importance and commonality in nature and technological devices such as rocket engines. Yet turbulence remains one of the least understood subjects in physics. This seems contradictory as the basic physical laws governing fluid mechanics have been established for over a century and can be described mathematically by the Navier-Stokes equations. The difficulty begins by realizing that the governing equations are nonlinear and comparatively little is known about their solutions at high Reynolds numbers even in simple geometries and boundary conditions. Additionally, the results from experiments and the available mathematical evidence suggests that turbulence operates over many degrees of freedom with wide spatial and time scales [85].

Fully-developed turbulent flows tend to form coherent structures that manifest themselves as organized spatial features which have a characteristic temporal life-cycle that repeatedly form and decay. As such, the behavior of turbulent flows which are governed by infinite-dimensional partial differential equations can be reduced to a lower-order dynamic model which captures the dominant features. One widely accepted approach that has been developed to extract these coherent features from experimental data is called proper orthogonal decomposition (POD). The same technique as been independently rediscovered several times and applied to different fields of study. As such, this approach is called by several names including Karhunen-Loeve decomposition and principal component analysis. POD is a statistics

based approach that permits the extraction of systematically hidden but dominant dynamic spatial and temporal features from a turbulent flow field as described by experimental or numerical data. Its mathematical foundation provides a clear understanding of the method's limitations and capabilities as well as providing a rigorous analytical description of the extracted modes [85].

The POD technique using the method of snapshots, generates a set of basis functions that spans the collected data. This basis set is optimal in that it captures the maximum amount of energy with respect to the ensemble average of all possible truncations with the same order. It determines the most energetic coherent features of the flowfield by diagonalizing the spatial correlation matrix computed from the snapshots. However, two limitations of this method include: the ranking by energy of the coherent features may not in all cases be the correct measure of rank for the dynamic structures and the phase information about the dynamic features is lost because the method utilizes second-order statistics as the basis for the decomposition. The loss of phase information is due to a averaging procedure where the temporal structures represent the eigenvectors of the spatially averaged temporal correlation matrix and the spatial structures represent the eigenvectors of the temporally averaged spatial correlation matrix [86,87]. More detailed information about the POD technique can be found in Berkooz, et al. [85].

In order to solve some of the limitations of the POD technique a new decomposition method called dynamic mode decomposition (DMD) was developed by Peter Schmid in 2008 [88]. DMD is based upon snapshots of the flowfield (data based), yet retains all phase information of the dynamic modes yielding coherent

structures that accurately describe the dynamics and motion of the flowfield. DMD is applicable for fluid flows that are governed by either linear or nonlinear dynamics. For linearized flows, the extracted dynamic modes and eigenvalues are exact solutions and are equivalent to the results of a global stability analysis. For a nonlinear flowfield, the extracted dynamic modes and eigenvalues describe the best-fit linear tangent approximation of the dominant coherent structures that control the dynamic behavior of the flowfield as captured by the data [87, 89].

It has been mathematically shown that the dynamics of a nonlinear system can be accurately described by the eigenvalues and modes found by DMD. This results from DMD being closely related to Koopman analysis. The Koopman operator is a linear, infinite-dimensional operator whose eigenvalues and modes capture the evolution of a set of 'observables' that describe any dynamic system (linear or nonlinear). In this sense, DMD is considered a least-squares numerical approximation of the Koopman operator for a finite set of data describing the motion of a nonlinear system. Confidence of the connections between DMD and Koopman analysis is held when the set of observables is sufficiently large to span the space that contains the relevant Koopman eigenfunctions and the collected data is sufficiently rich to capture the dynamic behavior of the system [89].

The original DMD algorithm ('Standard' DMD) developed by Schmid [87] is formulated using a companion matrix. This approach emphasizes the connection of DMD to the Arnoldi method and Koopman operator theory. The 'Standard' DMD algorithm is based off of a singular value decomposition (SVD) of the collected data matrix. The data matrix is required to be made up of a sequential set of n data

vectors $\{z_0, ..., z_n\}$ collected by n number of snapshots taken with a uniform sampling rate (constant Δt). Each data vector z_i makes up a column in the data matrix and each row corresponds with a separate measurement, e.g. instrument, pixel, etc. The data in each entry of the data matrix is a real number. It is assumed that a linear operator $\boldsymbol{A}$ maps the flowfield measurement z_i to the next flowfield measurement z_{i+1}. So that $z_{i+1} = \boldsymbol{A} z_i$. This mapping is approximately the same over the full sample interval. For a flowfield governed by linear dynamics the mapping is exact. When this is applied to a nonlinear dynamical system, the assumption is a linear tangent approximation of the dynamics. Therefore, the computed DMD modes and eigenvalues approximate the eigenvectors and eigenvalues of $\boldsymbol{A}$ respectively [87, 89]. Greater detail about the theoretical framework of the 'Standard' DMD method can be found in the papers published by Schmid [87, 88].

The 'Standard' DMD algorithm is outlined below [87, 89]:

1. Arrange the uniform sampled, sequential data matrix of n snapshots $\{z_0, ..., z_n\}$ into two matrices, $\boldsymbol{X}$ and $\boldsymbol{Y}$, where

$$\boldsymbol{X} = [z_0, ..., z_{n-1}], \quad \boldsymbol{Y} = [z_1, ..., z_n]. \tag{3.19}$$

   Each column vector in the data matrix (z_i) contains m measurements.

2. Compute the reduced SVD of $\boldsymbol{X}$, where

$$\boldsymbol{X} = \boldsymbol{U}\boldsymbol{\Sigma}\boldsymbol{V}^H \tag{3.20}$$

$\boldsymbol{X}$ is the $[m \times p]$ data matrix, $\boldsymbol{U}$ is a $[m \times r]$ unitary matrix containing the left singular vectors, $\boldsymbol{\Sigma}$ is a $[r \times r]$ diagonal matrix containing the singular values, and $\boldsymbol{V}$ is a $[p \times r]$ unitary matrix containing the right singular vectors of the decomposition. The superscript H refers to the conjugate transpose of a matrix and r is the rank of data matrix $\boldsymbol{X}$.

3. The matrix $\widetilde{\boldsymbol{A}}$ is defined as:

$$\widetilde{\boldsymbol{A}} = \boldsymbol{U}^H \boldsymbol{Y} \boldsymbol{V} \boldsymbol{\Sigma}^{-1} \tag{3.21}$$

4. Calculate the eigenvalues and eigenvectors of $\widetilde{\boldsymbol{A}}$ so that

$$\widetilde{\boldsymbol{A}} v = \lambda v \tag{3.22}$$

Where λ is the eigenvalue and v is the right eigenvector. The eigenvalues are used to determine the frequency (f) and the temporal growth/decay rate constant (ψ) of the modes. The frequency is calculated by:

$$f = \frac{\mathbb{I}\left(\ln \lambda_i\right)}{2\pi \Delta t} \tag{3.23}$$

The temporal growth/decay rate constant is calculated by:

$$\psi = \frac{\mathbb{R}\left(\ln \lambda_i\right)}{\Delta t} \tag{3.24}$$

5. Calculate the dynamic modes (ϕ) corresponding to eigenvalue λ.

$$\phi = \boldsymbol{U}\upsilon \tag{3.25}$$

6. Scale the DMD modes (ϕ) to determine the hierarchy of the dynamic modes.

Interestingly, the DMD modes found by the 'Standard' DMD method are not eigenvectors of the linear operator $\boldsymbol{A}$. This is due to $\boldsymbol{U}$ containing the left singular vectors of $\boldsymbol{X}$. Therefore, the calculated DMD modes (ϕ) happen to be the modes found from the right singular vectors contained in $\boldsymbol{V}$ projected to lie in the image of $\boldsymbol{X}$ [89].

The 'Standard' DMD technique is limited to a data set containing measurements collected in a sequential time series with uniform sampling where the measurement dimension is much greater than the number of measurements taken (method of snapshots). A new theoretical framework was recently developed by Jonathan Tu [90] that generalizes the DMD technique to a larger range of data sets. This framework results in a slight modification to the SVD-based 'Standard' DMD algorithm but strengthens the relationship between DMD and Koopman analysis theory and allows for the data set to be collected by nonsequential sampling techniques and does not require the columns of $\boldsymbol{X}$ and $\boldsymbol{Y}$ to overlap opening up the potential for processing techniques that result in greater computing efficiency and a reduction of noise in the data set. This new framework and algorithm has been termed 'Exact' DMD [89].

In developing the theoretical framework to generalize the DMD method, Tu defined DMD as an analysis of a set of data pairs of m-dimensional data vectors $\{(x_0, y_0), ..., (x_n, y_n)\}$ instead of a sequential time series of data vectors. 'Exact' DMD is then defined in terms of two $(m \times n)$ data matrices, $\boldsymbol{X} = [x_0, ..., x_n]$ and $\boldsymbol{Y} = [y_0, ..., y_n]$. With this definition, the standard method using sequential time series is merely a special case of the exact definition [89, 90].

Similar to the standard method, a linear operator, $\boldsymbol{A}$, is constructed to approximate the Koopman operator where $y_i = \hat{\boldsymbol{A}} x_i$ and $\boldsymbol{A} = \boldsymbol{Y}\boldsymbol{X}^+$. $\boldsymbol{X}^+$ is the pseudoinverse of $\boldsymbol{X}$. The linear operator $\boldsymbol{A}$ is the least-squares/minimum norm solution to the potentially over- or under-constrained equation $\boldsymbol{A}\boldsymbol{X} = \boldsymbol{Y}$. If the data vectors x_i are linearly independent, then there exists an operator $\boldsymbol{A}$ that exactly satisfies $\boldsymbol{A}\boldsymbol{X} = \boldsymbol{Y}$ and the choice of $\boldsymbol{A} = \boldsymbol{Y}\boldsymbol{X}^+$ minimizes the Frobenius norm of $\boldsymbol{A}$. If there does not exist an operator $\boldsymbol{A}$ that exactly satisfies $\boldsymbol{A}\boldsymbol{X} = \boldsymbol{Y}$, then the choice of $\boldsymbol{A} = \boldsymbol{Y}\boldsymbol{X}^+$ minimizes the Frobenius norm of $(\boldsymbol{A}\boldsymbol{X} - \boldsymbol{Y})$ [89, 90].

The 'Exact' DMD of the data pair $(\boldsymbol{X}, \boldsymbol{Y})$ ends up being the eigendecomposition of $\boldsymbol{A}$ where the computed DMD modes and eigenvalues are the eigenvectors and eigenvalues of the operator $\boldsymbol{A}$ respectively. For this condition to hold in practice, the two data matrices $\boldsymbol{X}$ and $\boldsymbol{Y}$ must be linearly consistent. $\boldsymbol{X}$ and $\boldsymbol{Y}$ are linearly consistent only when the nullspace of $\boldsymbol{Y}$ contains the nullspace of $\boldsymbol{X}$. This is satisfied whenever $\boldsymbol{X}c = 0$ and $\boldsymbol{Y}c = 0$. Linear consistency is always satisfied when the data vectors x_i are linearly independent [89, 90].

The general algorithm for the 'Exact' DMD method is outlined below [89].

1. Arrange the n number of data vector pairs, $\{(x_0, y_0), ..., (x_n, y_n)\}$, into two matrices, $\boldsymbol{X}$ and $\boldsymbol{Y}$, where

$$\boldsymbol{X} = [x_0, ..., x_n], \quad \boldsymbol{Y} = [y_0, ..., y_n]. \tag{3.26}$$

   Each column vector in the data matrix (x_i, y_i) contains m measurements.

2. Compute the reduced SVD of $\boldsymbol{X}$, where

$$\boldsymbol{X} = \boldsymbol{U}\boldsymbol{\Sigma}\boldsymbol{V}^H \tag{3.27}$$

   $\boldsymbol{X}$ is a $[m \times n]$ matrix, $\boldsymbol{U}$ is a $[m \times r]$ unitary matrix containing the left singular vectors, $\boldsymbol{\Sigma}$ is a $[r \times r]$ diagonal matrix containing the singular values, and $\boldsymbol{V}$ is a $[n \times r]$ unitary matrix containing the right singular vectors of the decomposition. The superscript H refers to the conjugate transpose of a matrix and r is the rank of data matrix $\boldsymbol{X}$.

3. The matrix $\widetilde{\boldsymbol{A}}$ is defined as:

$$\widetilde{\boldsymbol{A}} = \boldsymbol{U}^H\boldsymbol{Y}\boldsymbol{V}\boldsymbol{\Sigma}^{-1} \tag{3.28}$$

4. Calculate the eigenvalues and eigenvectors of $\widetilde{\boldsymbol{A}}$ so that

$$\widetilde{\boldsymbol{A}}\upsilon = \lambda\upsilon \tag{3.29}$$

Where λ is the eigenvalue and υ is the right eigenvector. The eigenvalues are used to determine the frequency (f) and the temporal growth/decay rate constant (ψ) of the modes. The frequency is calculated by:

$$f = \frac{\mathbb{I}\left(\ln \lambda_i\right)}{2\pi\Delta t} \tag{3.30}$$

The temporal growth/decay rate constant is calculated by:

$$\psi = \frac{\mathbb{R}\left(\ln \lambda_i\right)}{\Delta t} \tag{3.31}$$

5. Calculate the dynamic modes (ϕ) corresponding to eigenvalue λ.

$$\phi = \frac{1}{\lambda}\boldsymbol{Y}\boldsymbol{V}\boldsymbol{\Sigma}^{-1}\upsilon \tag{3.32}$$

6. Scale the DMD modes (ϕ) to determine the hierarchy of the dynamic modes.

The 'Exact' DMD method is perhaps more natural and accurate than the 'Standard' DMD method since it uses all of the data vectors in its decomposition rather than leaving out the last data vector. The calculated eigenvalues are the same for both the 'Exact' and 'Standard' methods but the values of the dynamic modes are different. More detail about the theory and applications of the 'Exact' DMD technique can be found in the published papers and dissertaion of Tu [89, 90].

The above discussion and algorithms of both the 'standard' and 'exact' DMD techniques assumed a temporal analysis of the collected data. In turbulent

fluid dynamics, coherent features evolve both temporally and spatially. Therefore, temporal and spatial analysis of the coherent features are distinguished in fluid dynamic stability theory. Temporal analysis deals with the growth and decay in time of wave-like spatial features. In contrast, spatial analysis deals with the evolution in space of time-dependent perturbations up- and downstream of their origin [87].

Since the theoretical framework of DMD does not assume nor form a system matrix that maps one snapshot to the next, a spatial analysis of the data is just as feasible as the temporal analysis. The algorithms for both methods are identical to those described above except the original data matrix is transposed so that the data matrix contains m columns equal to the number of measurements and n rows which contain the time history from the n number of data snapshots taken at each measurement location [87]. The eigenvalues of the spatial analysis provides the spatial frequency and the growth/decay rate constant of each mode. These values are calculated with similar equations as Eq. (3.23) and Eq. (3.24) with the spatial frequency equation seen below.

$$f_s = \frac{\mathbb{I}\left(\ln \lambda_i\right)}{2\pi\Delta x} \tag{3.33}$$

The spatial growth/decay rate constant is calculated with the following equation.

$$\gamma = \frac{\mathbb{R}\left(\ln \lambda_i\right)}{\Delta x} \tag{3.34}$$

Scaling the computed dynamic modes is necessary to find the dominant modes and determine the associated hierarchy of the those modes. Dominant DMD modes are often identified by calculating their norms. It is generally assumed that modes with large norms are more dynamically important. Sometimes however, modes with large norms have only a limited effect on the overall dynamics of the flowfield due to the modes having a rapid decay rate. Therefore, the modes are weighted by a scaling value that determines which dynamic modes have the greatest effect on the underlying dynamics of the system [89].

The choice of a scaling parameter is somewhat arbitrary, however Tu [89] suggests to scale the modes to have unit norm where the data vector of interest (v) is equal to $v = \sum_{i=1}^{n} c_i \phi_i$. c_i is the scaling coefficient for the i^{th} dynamic mode and represents the contribution of each mode to the underlying system dynamics. Tu demonstrates that c_i can be computed efficiently without having to calculate all of the DMD modes by applying the scaling to the eigenvectors of the linear operator $\widetilde{\boldsymbol{A}}$. DMD modes are orthogonal to the adjoint DMD modes corresponding with different eigenvalues. The adjoint eigenvectors (z) are scaled so that $z^H v = 1$ with $\|v\| = 1$. This leads to the following equation, $\frac{1}{\lambda} z_i^H \widetilde{\boldsymbol{A}} v_i = 1$. A biorthogonal set is formed between the exact DMD modes and the adjoint DMD modes with this scaling. The scaling coefficient can then be calculated from $c = \boldsymbol{Z}^H \boldsymbol{\Sigma} v_i$ where $\boldsymbol{Z}^H = \left[z_0^H, ..., z_n^H\right]$ and v_i is the i^{th} column vector of $\boldsymbol{V}^H$. The choice of v_i allows the researcher to capture the mode contributions for a specific part of the dataset (beginning, end, etc.). For this research, the average scaling amplitude for each mode over the entire dataset considered was calculated. The scaling coefficient c_i is multiplied by two for

oscillating modes in order to calculate the correct relative scaling between oscillating and steady modes. Refer to Tu for a more detailed explanation about the scaling method [89].

3.5 Uncertainty Analysis

Since no experimentally determined result is 100% accurate, an objective statistical method of determining the uncertainty or degree of goodness of the measurement/result is required. Experimental uncertainty can be described as an estimate of what the error would be if it was measured or if it was possible to measure by calibration. In this respect, uncertainty analysis calculates the statistical range where the unknown error resides about the measured value or calculated result. Uncertainty analysis is a very powerful tool that is not only useful for determining the error range of results after an experiment is complete but can be used to great effect in the planning and design process [84].

In general there are two types of uncertainties to any measurement, systematic and random. Systematic or bias errors (b) are inherent to the particular device in use or the experimental setup and do not vary during the measurement period. Random errors (s) fluctuate during the measurement period and is responsible for the scatter seen with measurements. The standard uncertainty (u) of the result is described by Eq. (3.35) [84].

$$u = \sqrt{b^2 + s^2} \tag{3.35}$$

The Monte Carlo method is a powerful tool for determining the uncertainty of the measurement and/or calculated result made practical through the use of computers. The method is not limited to relatively simple expressions like the Taylor Series method but can be used to determine the uncertainty of calculated results based upon complicated data reduction equations. The Monte Carlo method generates simulated data in a numerical experiment. It starts by inputting the "true" values (measured or specified) of the variables as well as the standard uncertainty of each variable based upon the known systematic and random uncertainty of the measurement or manufacturing tolerance. Next, the analyst must assume a representative probability distribution about which the uncertainty of the variable is spread about the "true" value. Several common distributions include: Gaussian (normal), uniform (rectangular), and triangular. Random values of the variables are generated based upon the known true value and given uncertainty magnitude and distribution. Also, any results from data reduction equations that use one or more of the variables are calculated. This process is iterated until the standard deviation of the Monte Carlo results converges to some value within 1-5%, typically 1,000 or more points are required. The converged standard deviation of the Monte Carlo simulation for each variable and calculated result is a good approximation of the standard uncertainty of that variable/result [84].

Confidence intervals are used to calculate the uncertainty range about the mean value that will encompass a certain percentage of the measurements/results. Common confidence interval percentages include: 90%, 95%, and 99%. For this research, the uncertainty range is calculated with the standard 95% confidence interval

(U_{95}). To determine the uncertainty of the variable with 95% level of confidence, the standard uncertainty, Eq. (3.35), found from the standard deviation of the Monte Carlo analysis is multiplied by two [84].

For the orifice flow calibration experiment, the mass flow rate of water was found as a function of injector pressure drop using the stopwatch and catch bucket method. The uncertainty of each calibration point was calculated using the Monte Carlo method with 5,000 points. From the data files, the mean temperature as well as the mean and standard deviation of the static pressure upstream of the injector is calculated. For the thermocouple, the systematic uncertainty of the measurement is considered a constant 1.1 K or half the total uncertainty. For the pressure transducers, the systematic uncertainty of the transducer is 0.25% of full-scale or 1.25 psi. The uncertainty of the temperature and pressure measurements are considered to have a Gaussian probability distribution. The mean value and uncertainty of the injector diameter and length, is known and is considered constant with a uniform probability distribution. The uncertainty of the injector diameter is 0.01 mm and the uncertainty of the injector length is 1 mm. The uncertainty of the weight scale used for measuring the weight of the bucket before and after the calibration test is 0.1 grams and is considered to have a Gaussian probability distribution. Finally, the uncertainty of the combined stopwatch and user is considered to be 0.25 sec with a uniform probability distribution.

Using the mean and uncertainty information described in the previous paragraph, 5,000 randomly generated points are generated for the temperature, pressure, injector geometry, mass of the water, and calibration time for that set point.

Using the interpolated water property data, 5,000 values of density, surface tension, and viscosity are calculated. Finally, the mass flow rate and injection velocity for the calibration point is calculated with Eq. (3.36) and Eq. (3.37) respectively.

$$\dot{m}_{cal} = \frac{m}{t} \tag{3.36}$$

$$v_{cal} = \left(\frac{4}{\pi}\right) \frac{\dot{m}}{\rho d_o^2} \tag{3.37}$$

The results from the Monte Carlo simulation are output into a table that contains the mean values of the temperature, pressure, mass flow rate and injection velocity as well as the total uncertainty with a 95% confidence level in both magnitude and percent of the mean. The 95% uncertainty range of a variable is calculated by taking the standard deviation of the Monte Carlo simulation and multiplying the result by two. This 95% uncertainty of the mass flow rate, velocity and pressure are used to create error bars for the calibration plots, see Figure 3.5.

The procedure to determine the uncertainty of the results from the single-jet and like-doublet experiments is very similar to the one outlined above for the flow calibration experiment. It utilizes a 5,000 point Monte Carlo method and uses the same uncertainty values and probability distributions for the thermocouple, pressure transducers, and injector geometry described above. A total of 5,000 randomly generated values for the temperature, pressure measurements, and injector geometry each are used to calculate the mean and uncertainty values for each variable. The physical properties of the water for each point are calculated using the temperature

value and interpolated curve-fit equations. At this point, the uncertainty procedure for the experiments changes from the calibration procedure due to not collecting the water in a bucket.

The friction factor for each set point is calculated using Eq. (3.6) and is assumed constant for each of the 5,000 points in the Monte Carlo simulation. The injection velocity is calculated with Eq. (3.13) and the mass flow rate through each tube is calculated by Eq. (3.14). The last three values calculated in the Monte Carlo simulation are the Reynolds number, Weber number, and Ohnesorge number for both tubes. The total uncertainty of the measured and calculated parameters with 95% confidence is calculated by multiplying the standard deviation of each variable within the Monte Carlo simulation by two.

The Weber number uncertainty starts at 18% for $We \approx 350$ and decreases exponentially to just under 3% for $We \approx 5,500$. Likewise, the uncertainty of the jet velocity and mass flowrate follows a similar exponentially decreasing trend. For jet velocity, the uncertainty starts at 10% for $v_j = 5$ $^m/_s$ and decreases exponentially to about 1% for $v_j = 20$ $^m/_s$. Uncertainty of the mass flowrate starts at 10% and decreases exponentially to 3% at the highest flowrates. Appendix D contains all of the results of the detailed uncertainty analysis for the experiments. Section D.1 contains tables of the uncertainty results for each set point tested and Section D.2 contains the uncertainty plots.

CHAPTER 4

RESULTS – PART 1: THE JET BREAKUP LENGTH TO IMPINGEMENT DISTANCE RATIO FOR LIKE-DOUBLET INJECTORS

This chapter presents and explains the results gathered from the first part of the research program studying the effects of the jet breakup length to impingement distance (l_b/l_i) ratio for like-doublet injectors. The chapter is split into separate sections that detail the single jet and like-doublet experimental results. Additionally, the like-doublet section is split into four subsections that describe the overall spray characteristics, sheet breakup length, ligament wavelengths, and droplet size distributions.

4.1 Single Jet

The single jet experiments determined the breakup characteristics and average breakup length of the liquid jets for each operating condition. Each 1.016 mm i.d. orifice was tested individually for the four operating conditions described in Table 2.1 at atmospheric pressure using water as the inert propellant simulant. The actual test conditions for the single jet experiments can be found in Appendix A. The jets were

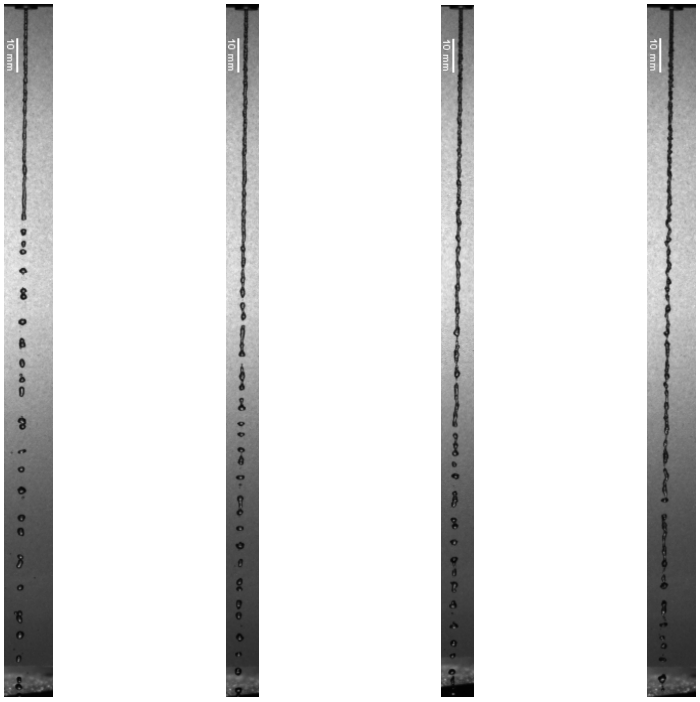

Figure 4.1: Single Jet Snapshots: (a) $v_j = 5$ $^m/_s$, (b) $v_j = 10$ $^m/_s$, (c) $v_j = 15$ $^m/_s$, and (d) $v_j = 20$ $^m/_s$

oriented to travel vertically downwards, $\pm 1^\circ$. Figure 4.1, shows example still frames of the single jet at each velocity condition to illustrate the breakup process of the turbulent jets. The jets were observed to follow a breakup process called turbulent primary breakup [41,42] for each operating condition tested. Cavitation was ruled out as a factor through the use of calculated cavitation numbers and visual inspection of the liquid within the glass injector tubes for each operating condition, see Section 3.2.

Turbulent primary breakup tends to occur for jet Weber numbers below 5,200 when the aerodynamic effects of the gaseous medium are very small ($^{\rho_{liq}}/_{\rho_{gas}} > 500$), and viscosity has a negligible effect upon the breakup process due to small Ohnesorge

numbers. This regime occurs for jet flow conditions (We & Re), typically associated with the 1^{st} Wind-Induced breakup regime. The issuing jet is characterized by small, random protuberances with characteristic dimensions on the order of the orifice diameter caused by the motion of the turbulent eddies. The large-scale eddies eventually cause unsymmetrical lateral kinks which distort the liquid column. The distortion and motion caused by the large eddies initiate the breakup process of the liquid column and droplet formation on the surface of the jet. Droplets are formed when the turbulence energy has sufficient time to deform the liquid surface enough to allow the surface tension forces to form a droplet of comparable size to the eddy and jet diameter. The turbulent jet is destroyed when droplets are formed and detached from the end of the jet by this axisymmetrical disturbance. The breakup length of the turbulent jet tends to increase with jet Weber number under this process [41–45].

The breakup length of the liquid jet was measured from the orifice exit to the first point the jet is broken or segmented. A total of 150 sequential frames from the high speed video were analyzed for each test condition. The jet breakup length was consistent for both orifices and was found to increase with jet velocity and fluctuate randomly with time. The standard deviation of the fluctuations was approximately 12–13% of the mean breakup length for each operating condition. The breakup length results are tabulated in Table 4.1 located below where the ± variations correspond with the standard deviation of the breakup length measurements.

Table 4.1: Single Jet Breakup Length Results

v_j (m/s)	$(l_b/d_o)_{tube\ 1}$	$(l_b/d_o)_{tube\ 2}$
5	62.0 ± 8.3	62.5 ± 8.4
10	90.2 ± 10.9	89.3 ± 11.2
15	111.5 ± 14.5	109.4 ± 14.3
20	130.3 ± 17.1	128.7 ± 15.2

The breakup length results were compared with existing empirical breakup length correlations for turbulent liquid jets discharging into atmospheric air. The four empirical correlations considered are those found by Grant and Middleman, Wu and Faeth, Sallam, et al., and Baron. Refer to Eqs. (1.18), (1.19), (1.20), and (1.21) for the empirical correlations.

Figure 4.2 is a plot of non-dimensionalized jet breakup length (l_b/d_o) as a function of jet Weber number and contains the results of the single jet experiments as well as the predicted breakup lengths from the empirical correlations described above. The points for each orifice represent the mean breakup length measured for each operating condition and the vertical error bars represent one standard deviation of the jet breakup length fluctuations while the horizontal error bars represent the uncertainty of the jet Weber number. From Figure 4.2, it is observed that the test data match very well with the correlations found by Grant and Middleman as well as Wu and Faeth. The correlation found by Sallam, et al. has a different trend and the correlation found by Baron under-predicts the observed breakup length.

The average droplet diameter formed by the breakup of the liquid jet was measured from still images of the high speed video. The diameters of a set of droplets

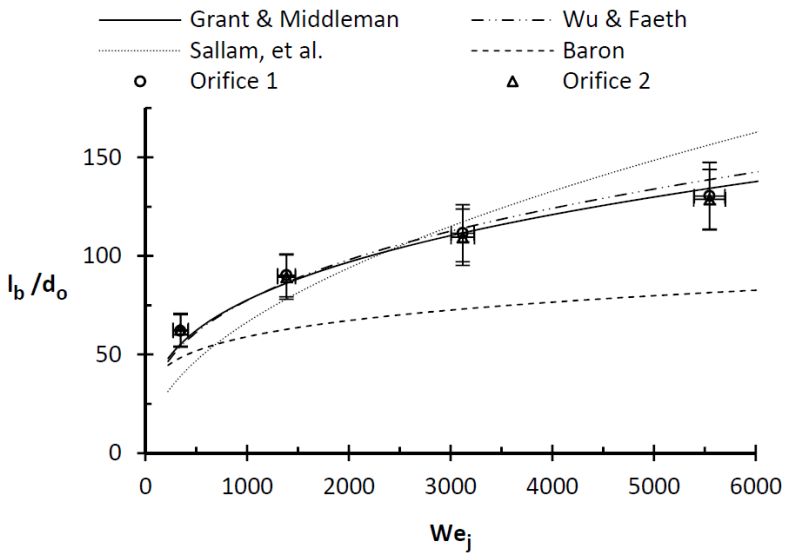

Figure 4.2: Single Turbulent Jet Breakup Length

were measured from the first frame of the video. Then the video was advanced 25 frames so that a new set of droplets could be measured from the end of the jet. This process was repeated for the length of the video file. At least 50 unique droplets were sampled from each orifice and operating condition tested. The PDPA could not be used for the droplet measurements because the average droplet diameter was near the limit of the PDPA measurement range and the measurement volume was near the end of the jet where the detached droplets could not be assumed spherical.

From the high-speed video, the droplets shed from the end of the jet did not exhibit an ideal spherical shape. Instead, the shape of the droplets fluctuated with time and approximated ellipsoids at any given time. Therefore, the droplet diameter was equated to the Waddel disk diameter. The Waddel disk diameter technique calculates the diameter of a circular disk with the same area as the two dimensional

image of a non-spherical particle [83]. The area of each droplet was measured using the "Analyze Particles" function of the ImageJ image processing program. The numerical average diameter of the large droplets shed from the end of the turbulent jet for all flow conditions was found to be 1.81 mm with a standard deviation of 0.25 mm. The average measured droplet diameter was consistent for all operating conditions and is very close to the predicted droplet diameter for the surface tension dominated Rayleigh jet breakup mechanism where $d_{drop} \sim 1.89 d_o$ [30] and $d_o \approx 1\ mm$.

The second technique utilized the equivalent sphere technique. Each droplet was measured twice, one across the length and the other across the width of the droplet. The equivalent spherical diameter was then calculated using Eq. (3.17). The numerical mean droplet diameter for all operating conditions was found to be 1.80 mm with a standard deviation of 0.26 mm. Both techniques calculated near identical mean droplet diameters increasing confidence in the result. The mean measured droplet diameter was consistent for all operating conditions and is very close to the predicted droplet diameter for the surface tension dominated Rayleigh breakup mechanism for liquid jets where $d_{drop} \sim 1.89 d_o$ [30] with $d_o \approx 1\ mm$.

The average axial spacing between the large droplets formed from the end of the liquid jet was measured from still images of the high-speed video using a similar process outlined above for the droplet diameter. The average spacing was calculated by measuring the axial distance spanned by a set of droplets and dividing that distance by the number of large droplets seen in the set. The video was advanced about 25 frames and the process was repeated. The average droplet spacing for all operating conditions tested equaled $4.52 \pm 0.22\ mm$. This distance is close to the predicted

wavelength of the dilatational oscillations with the fastest growth rate on the surface of the jet described by the Rayleigh mechanism. These disturbances are amplified by surface tension and have a characteristic wavelength of $\lambda \sim 4.51 d_o$ [30]. This result further suggests that turbulence distorts and initiates breakup of the liquid column but surface tension dominates the formation of droplets that shed from the end of the turbulent jet in this operating regime.

4.2 Like-Doublet

The like-doublet experiments tested the injector at atmospheric pressure using water as the propellant simulant for three different impingement angles, four jet velocities, and four l_b/l_i ratios as described in the test plan, Section 2.2.1. The actual test conditions of each set point of the like-doublet experiments can be found in Appendix A. The breakup characteristics, breakup lengths of the sheet, spatial wavelengths between the ligaments and droplet size distributions are discussed in the subsections below. The sheet breakup lengths and ligament wavelengths were measured using the ImageJ image processing program.

4.2.1 Spray Characteristics

Still frame images from the high-speed videos recorded for each operating condition are presented in Figure 4.3, Figure 4.4, and Figure 4.5. Figure 4.3, presents the images of the spray formed by the like-doublet injector with a 30° impingement angle. For jet breakup lengths greater than the impingement distance, $l_b/l_i \geq 1.5$, a long, narrow flat sheet is formed. When $v_j = 5\ m/s$, the flat sheet has a ruffled

appearance with small wave structure apparent on the surface while large ligaments and droplets are formed and detached from the end of the sheet. Very few droplets are shed from the edge of the sheet. When the jet velocity is increased to $v_j = 10\ ^m/_s$, impact waves are seen on the surface of the sheet while small droplets are ejected from the edges of the sheet. Waves of ligaments are shed from the end of the sheet which subsequently disintegrate into small droplets. The impact waves seen on the surface of the sheet become very strong and cause significant distortion of the flat sheet as the jet velocity increases to 15 and 20 $^m/_s$. Likewise, the number of small droplets ejected from the edge of the sheet increases and the ligaments disintegrate into a greater number of small droplets.

Similar overall characteristics are seen when the impingement distance is increased to equal the average breakup length of the jets, $^{l_b}/_{l_i} = 1$. However at this condition, the flat sheet has a tendency to segment with time at multiple places down the length of the sheet when one or both of the impinging jets disintegrates into droplets prior to reaching the impingement point. At $v_j = 5\ ^m/_s$, the sheet has a tendency to collapse/disappear briefly when the impinging jets disintegrate prior to impinging. Watching the high-speed video shows a flat sheet that appears unsteady.

When the impingement distance is increased beyond the breakup length of the impinging jets, $^{l_b}/_{l_i} = 0.5$, no flat sheet is formed. Instead, intermittent droplet collisions occur at the impingement point. At $v_j = 5\ ^m/_s$, the collision causes the coalescence of the two droplets forming an unsteady ligament which subsequently disintegrates into smaller droplets with a broad diameter spectrum that travel down the centerline from the impingement point. At higher jet velocities, the collision

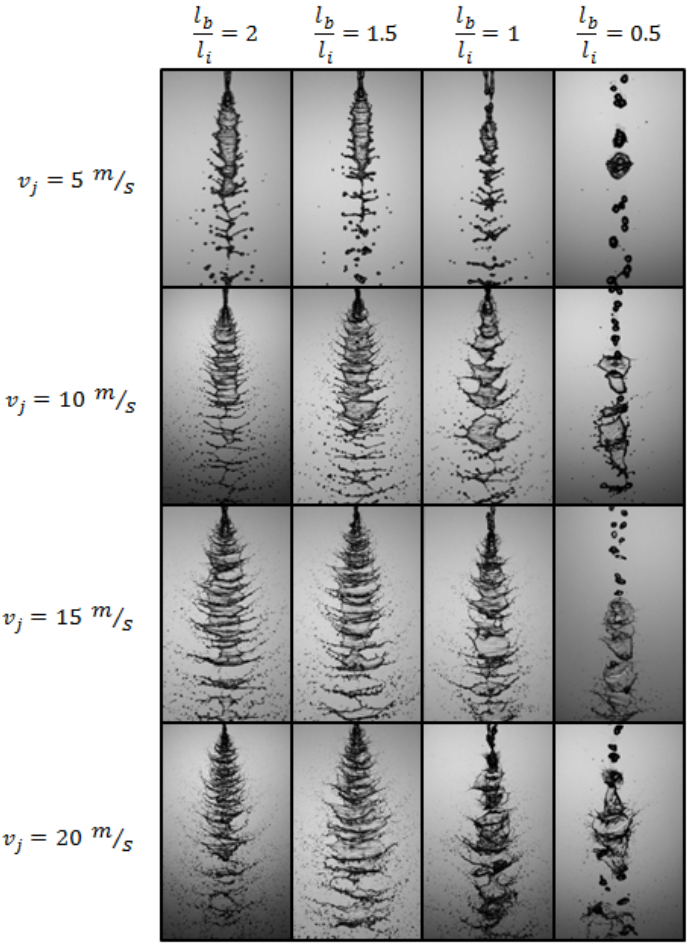

Figure 4.3: Spray Snapshots: 30° Impingement Angle

causes the two large droplets to disintegrate into a cloud of small droplets that travel axially from the impingement point. Most of the large droplets detached from the end of the turbulent jet travel through the impingement point untouched by the droplets shed from the opposing jet and continue on their straight line paths.

Figure 4.4 presents the images of the spray formed by the 60° like-doublet configuration. The breakup characteristics follow the same trend as the 30° impingement case described previously. However, the flat sheet is both broader and shorter and the spray field is wider as numerous droplets are released from the edges

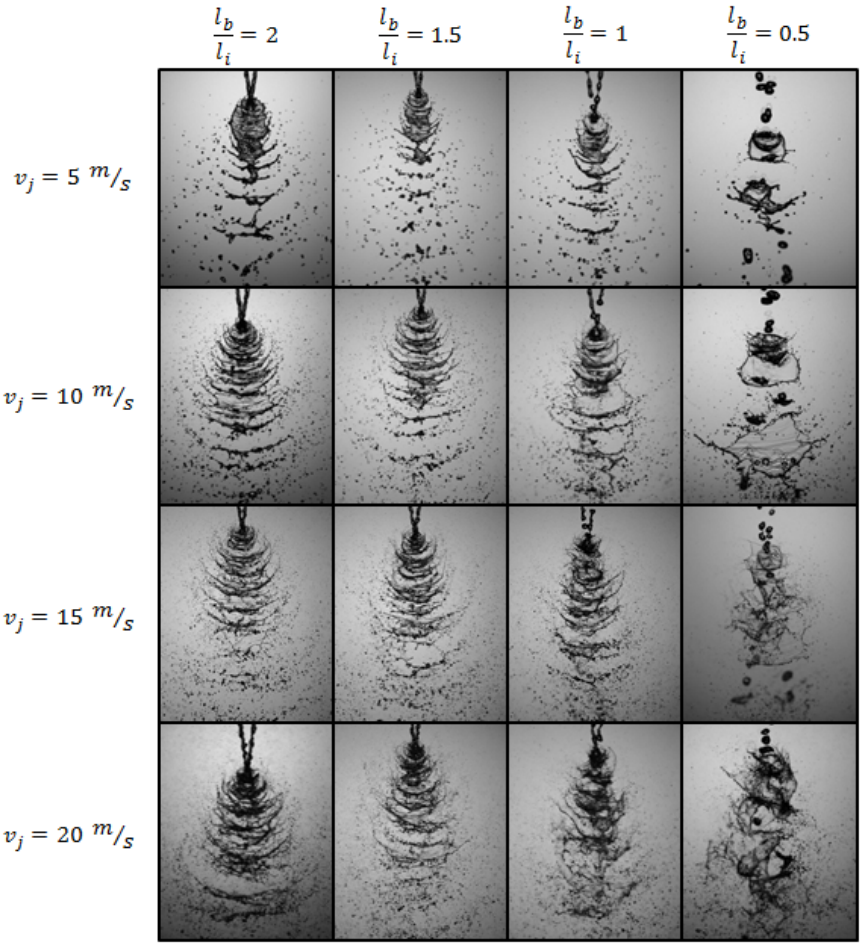

Figure 4.4: Spray Snapshots: 60° Impingement Angle

of the sheet. This is due to the larger impingement angle producing a greater impact force. The impact waves on the surface of the sheet and the waves of ligaments shed from the end of the sheet are more distinct compared with the 30° configuration for a given jet velocity. For the $l_b/l_i = 0.5$ configurations, the droplet collision is much more destructive at each operating condition resulting in a cloud of very small droplets.

Figure 4.5 presents the still frame images of the spray when the like-doublet injector is in the 90° impingement angle configuration. Similar general descriptions apply to the spray pattern trends for this configuration as described above with the

previous two impingement angles. However, at $v_j = 5$ $^m/_s$ and 10 $^m/_s$, the flat sheet displays a much rounder shape. Many small droplets are shed from the edge of sheet producing a cloud of mist around the sheet and impingement point. For $v_j = 20$ $^m/_s$, the impact force is so great that it is difficult to distinguish the surface of the flat sheet from the surrounding droplet field. It is assumed that the sheet is intact within the contiguous dark region immediately downstream from the impingement point. At $^{l_b}/_{l_i} = 0.5$, the droplet collision becomes more and more catastrophic as jet velocity increases resulting in a dense cloud of tiny droplets. However, most of the large droplets pass through the impingement point without colliding with another droplet.

Figure 4.6 shows a representative front-view photograph of the spray when $^{l_b}/_{l_i} = 0.5$. The operating condition is $v_j = 10$ $^m/_s$ and $2\theta = 60°$. This image clearly shows that the majority of the large droplets shed from the ends of the two impinging jets pass through the impingement point untouched by the droplets issuing from the other jet. As a result, the spray takes on a characteristic X-pattern as the unaffected droplets continue on their straight line paths and the intermittent collisions form the fine spray below the impingement point.

4.2.2 Sheet Breakup Length

The breakup length of the sheet is defined as the axial distance from the impingement point to the location where the intact sheet disintegrates into ligaments and droplets. Every fourth still frame was analyzed in the 200 frame high-speed video file allowing a total of 50 sheet breakup lengths to be measured for every set point. This was enough frames for the mean breakup length to converge. A comparison

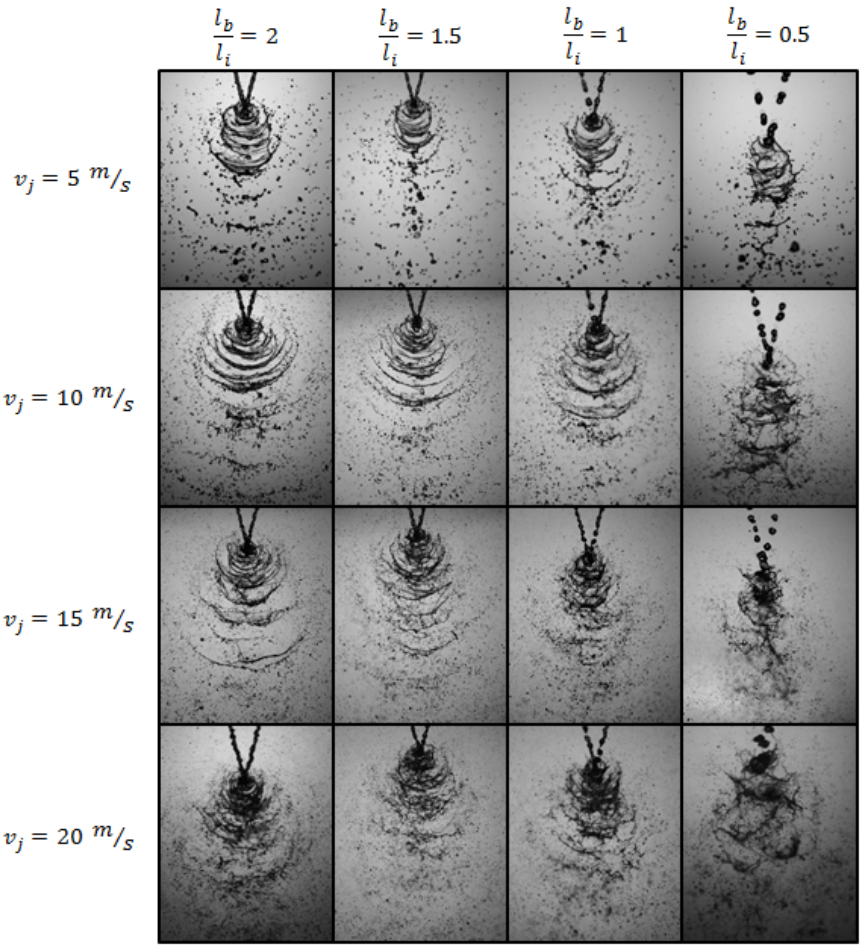

Figure 4.5: Spray Snapshots: 90° Impingement Angle

Figure 4.6: Front View of Impingement, $l_b/l_i = 0.5$

of the results was made between the analysis of 50 frames and all 200 frames of the high-speed video. The comparison demonstrated negligible differences of less than 0.5 mm between the two results for both the mean sheet breakup length and standard deviation. See Table B.1, Table B.2, and Table B.3 in Appendix B for the sheet breakup length results. Where v_j is the jet velocity determined from Eq. (3.13) and the recorded injector pressure drop and v_{ax} is the measured axial velocity of the droplets using the PDPA. The $\pm$ variations seen in the tables correspond with the standard deviation of the measurements

Figure 4.7, is a plot of the mean non-dimensionalized sheet breakup lengths for each impingement angle as a function of jet Weber number for the $l_b/l_i \geq 1.5$ operating conditions. The vertical error bars of each set point are the standard deviation of the measured sheet breakup length and the horizontal error bars are the uncertainty of the jet Weber number. The lines correspond with the empirical sheet breakup length correlations and will be described later. For each set point, the breakup length of the sheet was observed to fluctuate randomly with time similar to the breakup length fluctuations of a single liquid jet.

At each set point and impingement angle, the average sheet breakup length of the $l_b/l_i = 2$ and $l_b/l_i = 1.5$ cases are about equal. The breakup length of the sheet shortens with an increase of impingement angle for all jet Weber numbers. This is expected due to the greater impact force experienced with larger impingement angles. For the 30° impingement angle configurations, the breakup length of the sheet continuously increases with an increase of Weber number. The sheet breakup length for the 60° and 90° impingement angle configurations is more complicated. At

low Weber numbers, the breakup length of the sheet increases with Weber number up to some transition point where the breakup length begins to shorten with further increases of the Weber number. This may be indicative of the sheet transitioning to a different breakup mode.

From Figure 4.3, Figure 4.4, and Figure 4.5, it is observed that the operating conditions that are associated with an increase of sheet breakup length with jet Weber number are characterized in general by a flat sheet that has a wavy or impact wave structure on the surface of the sheet and bow-shaped ligaments are shed from the end of the sheet. This breakup regime is similar to the characteristics of the "ruffled-sheet ligaments" breakup mode described by Bailardi, et al [63]. Likewise, the operating conditions associated with a shortening of the breakup length as a function of jet Weber number are characterized by a flat sheet that is distorted by large impact waves on the surface while waves of ligaments or clouds of droplets are shed from the sheet. At the $v_j = 20\ ^m/_s$ set points for the 60° and 90° impingement configurations, the sheet becomes difficult to detect from the surrounding droplet field. These characteristics fit the "fully-developed" breakup mode described by Heidmann [60], Dombrowski and Hooper [62], and Anderson [51].

Therefore, two new empirical non-dimensional sheet breakup length correlations are developed to describe the two breakup modes captured in this experiment. Both correlations are functions of the jet Weber number and the injector impingement half-angle (θ). The empirical correlations have the form described by Eq. (4.1).

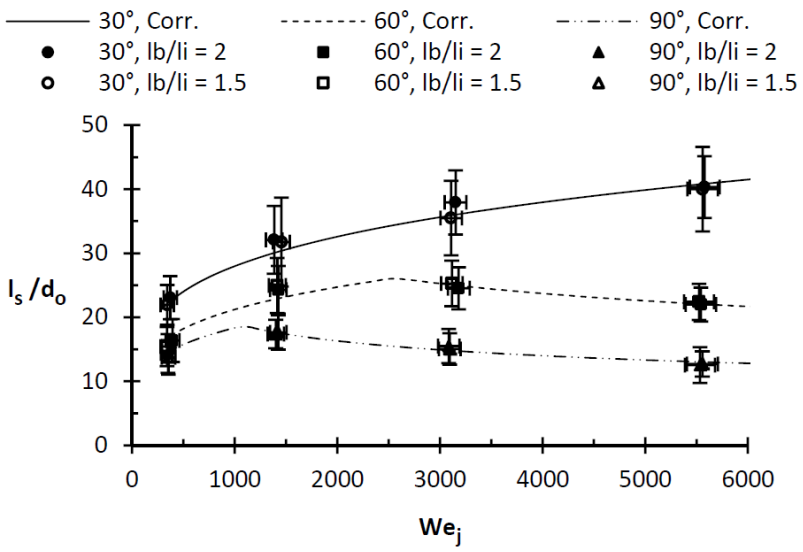

Figure 4.7: Flat Sheet Breakup Length with Empirical Correlation, $l_b/l_i \geq 1.5$

$$\frac{l_s}{d_o} = C\ We_j^a\ (\sin\theta)^b \tag{4.1}$$

The constant (C) and exponents (a & b) of the correlation are determined through the least squares method using the mean sheet breakup length data. The ruffled-sheet (RS) breakup mode correlation uses the mean results from all four operating conditions of the 30° impingement configuration, the 5 and 10 $^m/_s$ results of the 60° impingement configuration and the 5 $^m/_s$ operating condition of the 90° impingement configuration to determine the empirical correlation. The resulting empirical correlation, Eq. (4.2), has an $R^2 = 0.984$. The fully-developed (FD) breakup mode correlation uses the results from the 15 and 20 $^m/_s$ results of the 60° impingement configuration and the 10, 15, and 20 $^m/_s$ results of the 90° impingement configuration.

The empirical correlation, Eq. (4.3), has an $R^2 = 0.994$. Figure 4.8 shows that both breakup length correlations fit their respective experimental data extremely well.

$$\frac{l_s}{d_o} = 3.47\ We_j^{0.22}\,(\sin\theta)^{-0.42} \quad [RS,\ {}^{l_b}/_{l_i} \geq 1.5] \tag{4.2}$$

$$\frac{l_s}{d_o} = 51.28\ We_j^{-0.22}\,(\sin\theta)^{-1.52} \quad [FD,\ {}^{l_b}/_{l_i} \geq 1.5] \tag{4.3}$$

It is remarkable that the magnitude of the Weber number exponent is equal, but have opposite algebraic signs, for both breakup modes. The jet Weber number that defines the transition point between the ruffled-sheet and fully-developed breakup modes, seen in Eq. (4.4), was derived by equating the two breakup length correlations (Eqs. (4.2) and (4.3)). The transition Weber number is solely a function of the impingement half-angle.

$$We_{j,tp} = 455\,(\sin\theta)^{-2.5} \quad [{}^{l_b}/_{l_i} \geq 1.5] \tag{4.4}$$

The "Corr." lines seen in Figure 4.7 are the empirical correlations for each impingement angle described by Eqs. (4.2) and (4.3). While the transition point is determined from Eq. (4.4). The empirical sheet length correlations and transition points fit the experimental data very well and capture both breakup modes of the flat sheet.

A comparison is made between the derived empirical correlations and the sheet breakup length results gathered from past studies by separate researchers. The

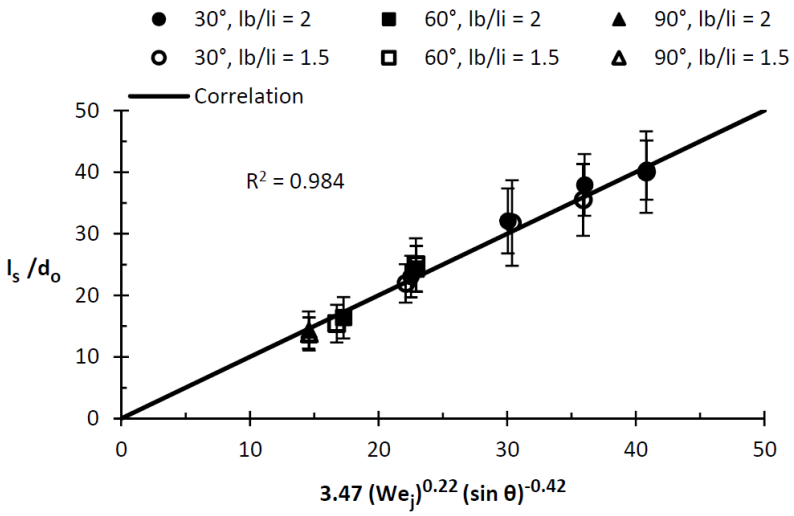

(a) Ruffled-Sheet Correlation

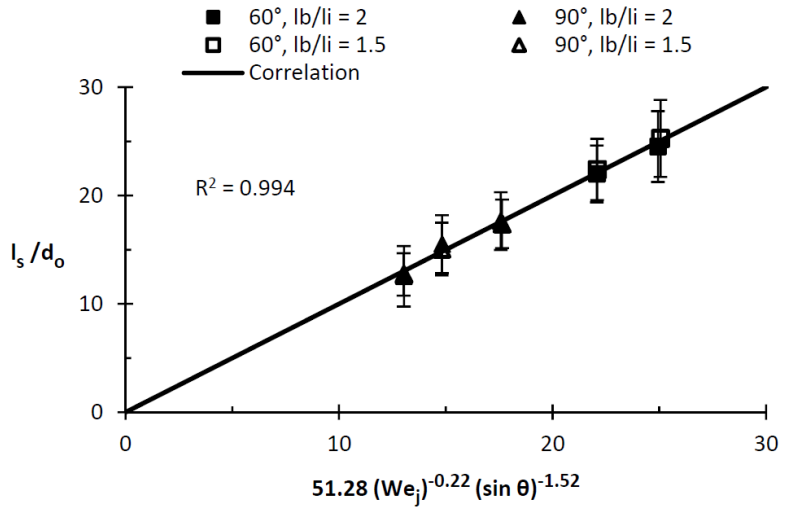

(b) Fully-Developed Correlation

Figure 4.8: Sheet Breakup Length Correlations, $l_b/l_i \geq 1.5$

three studies considered, all tested 60° like-doublet injectors at atmospheric conditions using water as the simulant. Strakey and Talley [52] tested a 60° like-doublet with a sharp-edge entrance that had the following design characteristics: $d_o = 1.194\ mm$, $l_o/d_o = 18.4$, and $l_i/d_o = 5$. Jung, et al. [46] also tested 60° like-doublets with both sharp and rounded entrances. Only the sharp-edge results are considered. Their injector design consisted of: $d_o = 1.1\ mm$, $l_o/d_o = 17$, and $l_i/d_o = 5$. The final comparison was made with the results from Anderson, et al. [51]. The data considered utilized like-doublets with a sharp-edge entrance and the following characteristics: $d_o = 0.64$, 1.02, and 1.45 mm, l_o/d_o between 80 and 35, and l_i/d_o between 2 and 4.

The data from these three studies provide breakup length results for a variety of orifice diameters, orifice length-to-diameter ratios, and impingement distances that are much shorter than those considered with the current experiments. Figure 4.9 is a plot of the 60° sheet breakup length results from this study for $l_b/l_i \geq 1.5$ and the results from the past studies compared to the empirical correlation line found for a 60° impingement angle. The results from Anderson, et al. and Jung, et al. did not provide standard deviation values for their breakup length results.

The sheet breakup lengths recorded by Jung, et al. [46] are a close match to both the trend and the predicted breakup lengths by the empirical correlation for the fully-developed breakup mode, Eq. (4.3). The breakup lengths recorded by Anderson, et al. [51] for jet Weber numbers below 2,000 match the trend for the ruffled-sheet breakup mode, Eq. (4.2). The sheet breakup lengths at these conditions are slightly greater than the predicted values, however. For Weber numbers greater than 2,000, Anderson, et al. reported that the breakup length of the sheet was

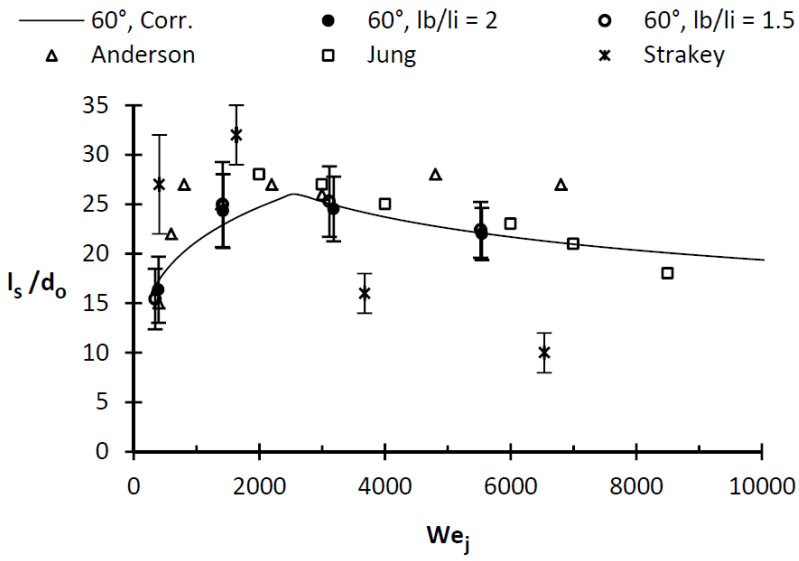

Figure 4.9: Sheet Breakup Length Comparison with Results of Previous Studies

nearly independent of Weber number. This doesn't follow the trend seen with the results of this research nor the results reported by Jung and Strakey. This leads to measured breakup lengths up to 5 orifice diameters greater than the predicted breakup length by the fully-developed correlation. The breakup lengths reported by Strakey and Talley [52] are greater than the correlation for the low speed (ruffled-sheet) set points and less than the correlation for the higher speed (fully-developed) set points. It should be noted that cavitation was reported by Strakey for the higher velocity set points. Cavitation is known to enhance breakup and could be responsible for the shorter breakup lengths seen at these conditions. Remarkably, the breakup length trend of Strakey's results match the trend of the empirical correlations and the transition region between the two breakup modes.

The range of sheet breakup lengths and breakup trends are similar for the five sets of results. The differences can be attributed to the presence of cavitation within the injector and perhaps the difference of the jet condition when it exits a short l_o/d_o orifice compared with a fully-developed jet exiting a long l_o/d_o orifice. From this analysis it appears that in the absence of cavitation and hydraulic flip, the average breakup length of the flat sheet is not greatly affected by the l_b/l_i ratio when $l_b/l_i \geq 1.5$.

For $l_b/l_i = 1$, the average breakup length of the sheet is generally shorter with a larger standard deviation when compared with the $l_b/l_i \geq 1.5$ for the 30° impingement configuration and 5 and 10 m/s jet velocities for the 60° configuration. This is due to the nature of the sheet to segment when one or both of the impinging jets break up prior to reaching the impingement point. On the other hand, the 90° impingement angle configurations and the higher jet velocity cases for the 60° impingement angle configuration displayed mean sheet breakup lengths that are about equal between the $l_b/l_i \geq 1.5$ and $l_b/l_i = 1$ cases.

The $l_b/l_i = 1$ condition displays two distinct breakup modes similar to the $l_b/l_i \geq 1.5$ cases. Two empirical correlations are found for the non-dimensional sheet breakup length for the $l_b/l_i = 1$ condition using the least squares regression technique. The two empirical correlations use the experimental results from the same set of operating conditions described for the $l_b/l_i \geq 1.5$ correlations. Equation (4.5) is the correlation for the ruffled-sheet mode and Eq. (4.6) is the correlation for the fully-developed breakup mode when $l_b/l_i = 1$. The transition Weber number correlation is found in Eq. (4.7). Figure 4.10 displays the mean non-dimensional sheet breakup length results with the empirical curves described by Eqs. (4.5), (4.6), and (4.7). Figure 4.11 shows

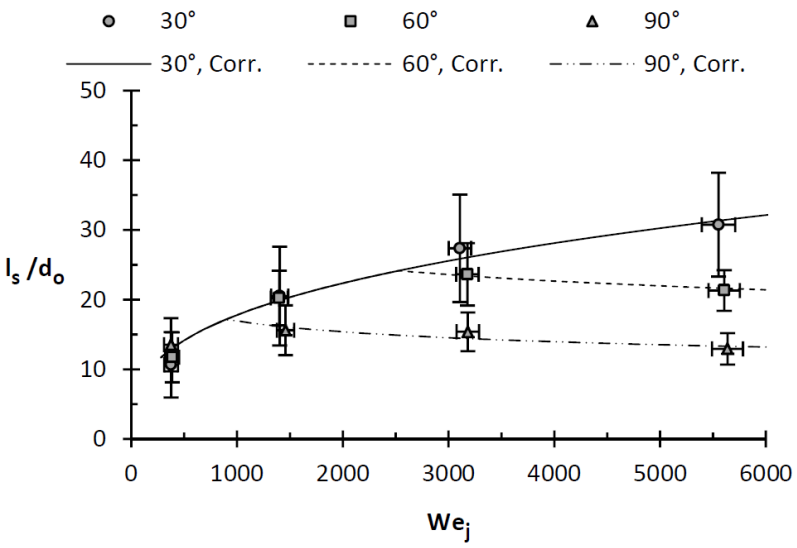

Figure 4.10: Flat Sheet Breakup Lengths with Empirical Correlation, $l_b/l_i = 1$

that the two correlations fit the respective experimental breakup length data very well.

$$\frac{l_s}{d_o} = 1.82\ We_j^{0.33} \quad [RS,\ l_b/l_i = 1] \tag{4.5}$$

$$\frac{l_s}{d_o} = 27.42\ We_j^{-0.14}\,(\sin\theta)^{-1.4} \quad [FD,\ l_b/l_i = 1] \tag{4.6}$$

$$We_{j,tp} = 321\,(\sin\theta)^{-2.98} \quad [l_b/l_i = 1] \tag{4.7}$$

No sheet breakup length measurements were made for the $l_b/l_i = 0.5$ set points because no flat sheet was formed, as seen in Figure 4.3, Figure 4.4, and Figure 4.5. The spray consists of intermittent droplet collisions at the impingement point producing

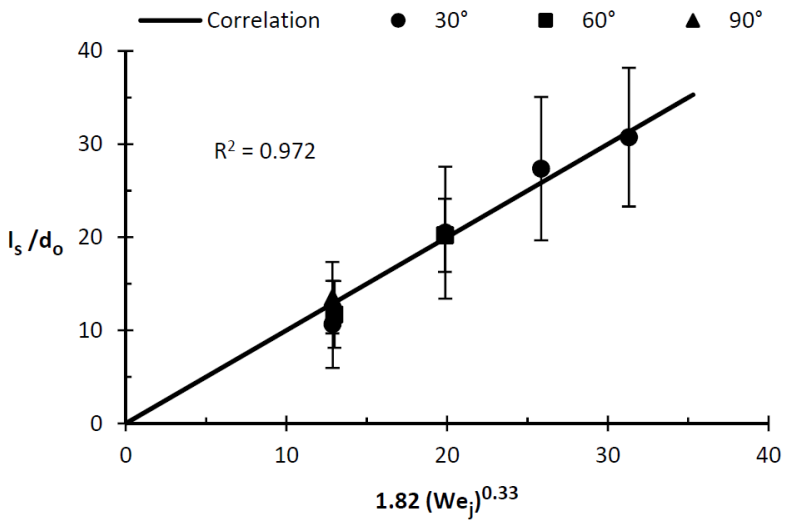

(a) Ruffled-Sheet Correlation

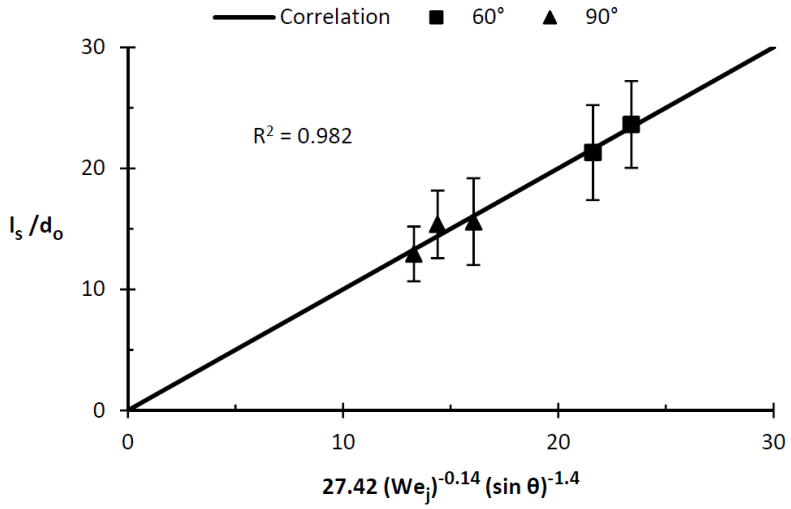

(b) Fully-Developed Correlation

Figure 4.11: Sheet Breakup Length Correlations, $l_b/l_i = 1$

small droplets that travel axially down the centerline of the spray while the majority of the large droplets formed from the breakup of the two jets pass through the impingement point following a straight line path forming a distinct X-pattern.

4.2.3 Ligament Wavelength

The spatial ligament wavelength is determined by measuring the axial distance between two distinct ligaments. Between 20 and 50 wavelengths were measured for each set point depending on the number of unique and distinct ligaments that were shed from the end of the sheet during the duration of the high-speed video. The atomization frequency is determined by dividing the axial droplet velocity measured by the PDPA with the wavelength of the shed ligaments. See Table B.1, Table B.2, and Table B.3 in Appendix B for a tabulated list of ligament wavelength and atomization frequency results.

After analyzing the high-speed videos, it was determined that the flat sheet does not shed ligaments in regular intervals for $l_b/l_i \geq 1.5$. Instead, ligaments are shed at a variety of frequencies about a mean value. The average spatial wavelength of the shed ligaments are similar for all three impingement angles and jet Weber numbers when $l_b/l_i \geq 1.5$ with the mean $\lambda_l/d_o \approx 6.0 \pm 1.5$, see Figure 4.12(a). The large standard deviation of the measured ligament wavelengths is indicative of the wide range of ligament shedding frequencies that are formed from the end of the flat sheet. The constant mean wavelength for all test conditions suggest that the formation and shedding of ligaments from the end of the flat sheet is not influenced by the jet Weber number nor the impingement angle. However due to the nearly constant mean

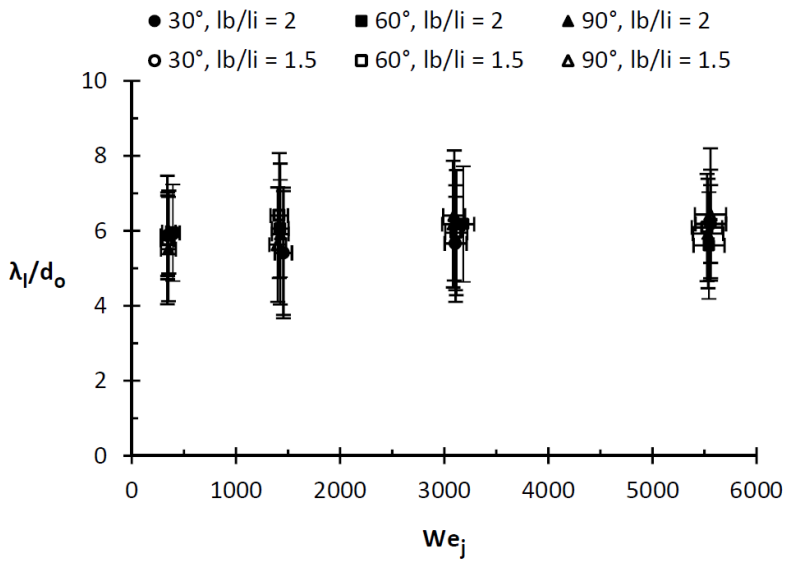

(a) $l_b/l_i \geq 1.5$

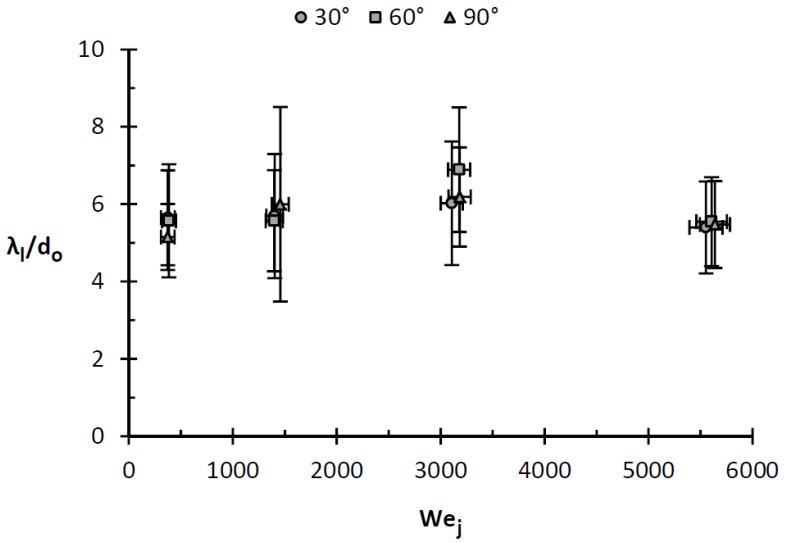

(b) $l_b/l_i = 1$

Figure 4.12: Ligament Wavelength

wavelengths, the resulting mean atomization frequency is proportional to jet velocity and Weber number.

For $l_b/l_i = 1$, an analysis of the wavelengths of the shed ligaments showed similar results when compared with the results from the cases when $l_b/l_i \geq 1.5$, see Figure 4.12(b). The average spatial wavelength between the shed ligaments are similar for all three impingement angles and jet Weber numbers when $l_b/l_i = 1$ with the mean $\lambda_l/d_o \approx 5.8 \pm 1.4$. Likewise, a large standard deviation exists for the wavelength of the shed ligaments. The similarities of the results between the two cases suggest that the ligament spatial wavelength and atomization frequency are independent of the l_b/l_i ratio when a flat sheet is formed.

Histograms of the measurements were created to determine the probability distribution of the ligament wavelengths. Since the mean and standard deviation of the measured wavelengths were very similar for all impingement angles and jet velocities tested, all of the measurements were considered in the creation of the histograms for the $l_b/l_i \geq 1.5$ and $l_b/l_i = 1$ configurations. These histograms are shown in Figure 4.13. The measured ligament wavelengths for both l_b/l_i ratios display a nearly symmetric Gaussian probability distribution with the peak nondimensional ligament wavelength between 5.5 and 6. The distributions are quite broad with a standard deviation of about 1.5. The histograms show the ligament wavelength obeys the central-limit theorem with a well-defined mean value and variance.

The results reported by Anderson, et al. [51] showed that the mean ligament wavelength was independent of jet velocity with mean wavelengths between four and five orifice diameters. There was a large spread in the wavelength data, leading

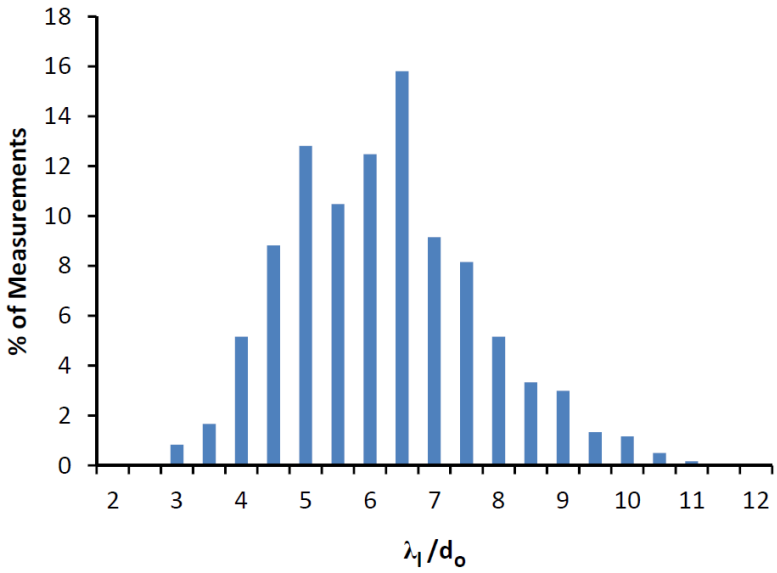

(a) $l_b/l_i \geq 1.5$

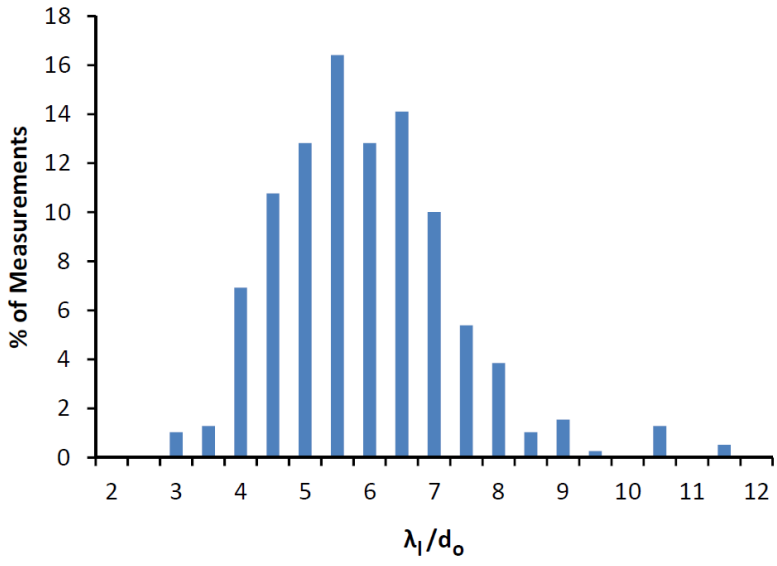

(b) $l_b/l_i = 1$

Figure 4.13: Histogram of the Ligament Wavelength Measurements

to a standard deviation about 35% of the mean value. Likewise, the experiments conducted by Jung, et al. [46] resulted in a mean λ_l/d_o between 5 and 6.5 for jet Weber numbers up to 6,000. The mean wavelength then decreased to about four orifice diameters when the Weber number was increased to a maximum value of 9,000.

Next, the mean ligament shedding frequencies are calculated by dividing the axial droplet velocity measured by the PDPA with the mean ligament wavelength for each set point. These ligament shedding frequencies are then compared with the Hewitt stability correlation for liquid rocket engines using like-doublet impinging injectors. The Hewitt correlation [4, 55] describes the high-frequency cutoff value for combustion instability based on the design parameter, (d_o/v_j). Since the measured atomization frequency of the ligaments was determined to be independent of the l_b/l_i ratio, a single average frequency point for each impingement angle and operating condition is plotted as a function of the Hewitt stability correlation, see Figure 4.14. The Hewitt threshold seen in the plot, is valid for LOX/RP-1 propellant combinations.

From the plot, the ligament atomization frequencies for each operating condition are within the frequency range of the dominant combustion instability modes typically excited in liquid rocket engines. Also, the measured ligament frequencies form a log-linear trend as a function of the d_o/v_j ratio with a slope nearly parallel with the log-linear Hewitt stability threshold. The measured frequencies are about 1.5 times greater than the threshold frequency predicted by the Hewitt threshold. This frequency difference may be due to differences between the characteristic mean ligament wavelength of water versus kerosene (RP-1). The

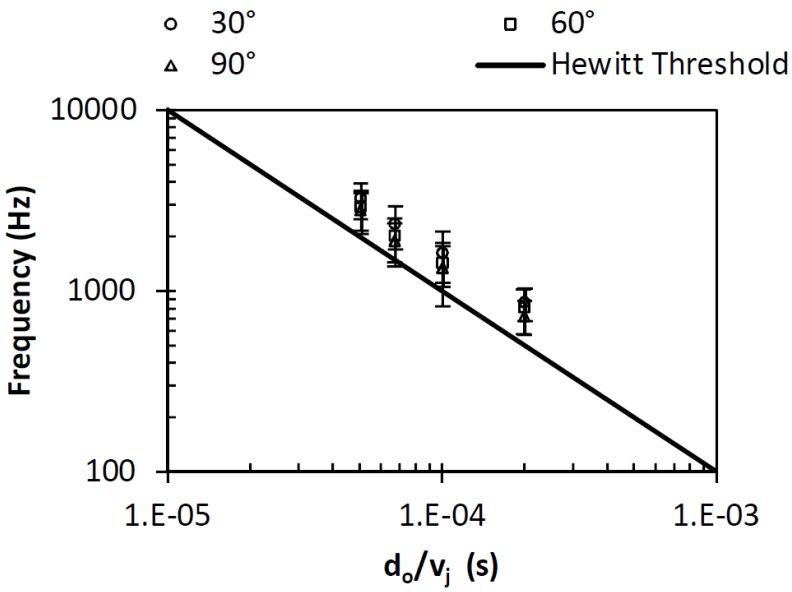

Figure 4.14: Avg. Ligament Atomization Frequency as Function of the Hewitt Stability Parameter

similarity of both the trend and frequency magnitude between the empirical Hewitt threshold line and the ligament shedding frequencies suggest that the primary atomization process of like-doublet injectors may be a major element in determining the stability of a liquid rocket engine. These results are similar with the trend found by Anderson, et al [53].

The Rayleigh criterion for combustion instability can be helpful in explaining the excitation mechanism assuming the link between the ligament shedding frequency and combustion instability is valid. The Rayleigh criterion broadly states that coupling between the periodic heat release of the combustion process and the pressure oscillations within the chamber promote combustion instability. The collected data demonstrate that the atomization process of like-doublets cause ligaments and droplets to be shed in a periodic fashion which can lead to an oscillating burn rate

and heat release that can couple with the pressure oscillations in the chamber. Both the atomization frequency and resulting heat release oscillations are tied to the $^{d_o}/_{v_j}$ ratio. For a given combustion chamber design, the frequency of the dominant acoustic resonant mode will be constant. If the injector design ratio ($^{d_o}/_{v_j}$) is small, then the characteristic ligament shedding frequency will be greater than the frequency of the dominant acoustic chamber mode. This allows the heat release fluctuations to have ample opportunity to couple with the resonant pressure oscillations in the chamber leading to the excitation of combustion instability. Conversely, if the $^{d_o}/_{v_j}$ ratio is large enough so that the characteristic ligament shedding frequency is below the dominant acoustic frequency of the chamber then the resulting heat release fluctuations will be too slow to couple with the resonant chamber pressure oscillations inhibiting the development of combustion instability.

No ligament wavelength measurements were possible for the $^{l_b}/_{l_i} = 0.5$ set points because neither a flat sheet was formed nor were waves of ligaments/droplets were shed from the impingement point, as seen in Figure 4.3, Figure 4.4, and Figure 4.5. The impingement of the two jets at this $^{l_b}/_{l_i}$ ratio consists of random droplet collisions producing a cloud of small droplets.

4.2.4 Droplet Size

A Phase Doppler Particle Analyzer (PDPA) was used to collect bulk statistics of the spray (droplet velocity and diameter) within a measurement volume located 75 mm below the impingement point at the centerline of the spray within the secondary atomization zone. Approximately 10,000 droplets were sampled by the

PDPA for each set point. From the collected data, average droplet diameters as well as droplet diameter histograms displaying the number fraction and mass fraction of the spray were calculated.

The number fraction corresponds with the fraction of the total number of droplets sampled by the PDPA that droplets of a given diameter bin passed through the measurement volume. Likewise, the mass fraction is equal to the mass of water contained in each diameter bin divided by the total mass of water sampled from the measured droplets. The mass of each droplet is calculated by multiplying the spherical volume of the droplet by the density of water. For an individual droplet, a larger diameter corresponds with a greater amount of propellant mass that is proportional with the quantity of stored chemical energy. Therefore, the shape of the mass fraction curve can be assumed to be similar to the fraction of potential combustion energy stored by droplets of a given diameter.

Figure 4.15(a) presents a droplet distribution that is representative of the results collected for all three impingement angles when the jet velocity is equal to 5 $^{m}/_{s}$. At these conditions, the like-doublet injector produces a spray that contains a wide spectrum of droplet diameters. The mass fraction increases with droplet diameter. The spray produces large numerical mean diameters (d_{10}) and Sauter mean diameters (d_{32}).

Figure 4.15(b) contains a droplet spectrum that is more representative of the droplet distributions produced by the like-doublet operating at $v_j \geq 15$ $^{m}/_{s}$ for the 30° impingement angle configuration and $v_j \geq 10$ $^{m}/_{s}$ for the 60° and 90° configurations. These set points produce a more uniform spray with a droplet diameter spectrum that

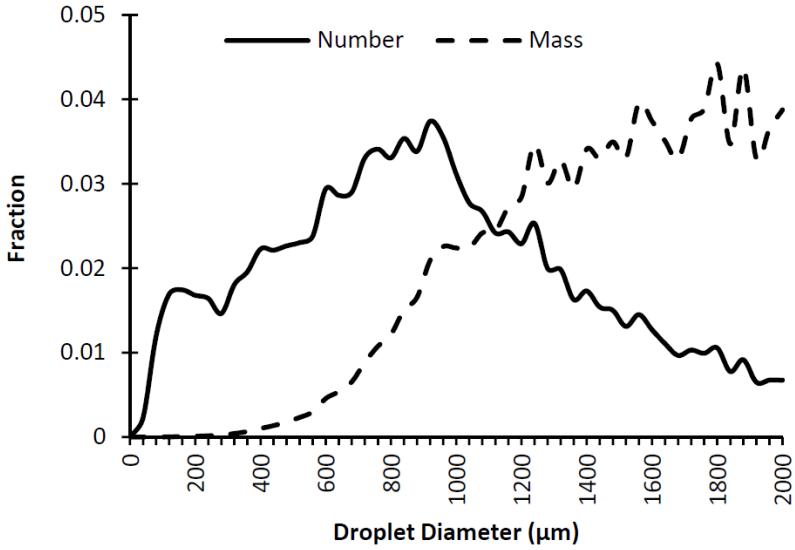

(a) $2\theta = 30°$, $v_j = 5\ ^m/_s$, $^{l_b}/_{l_i} = 2$: $(d_{10} = 908\ \mu m, d_{32} = 1327\ \mu m)$

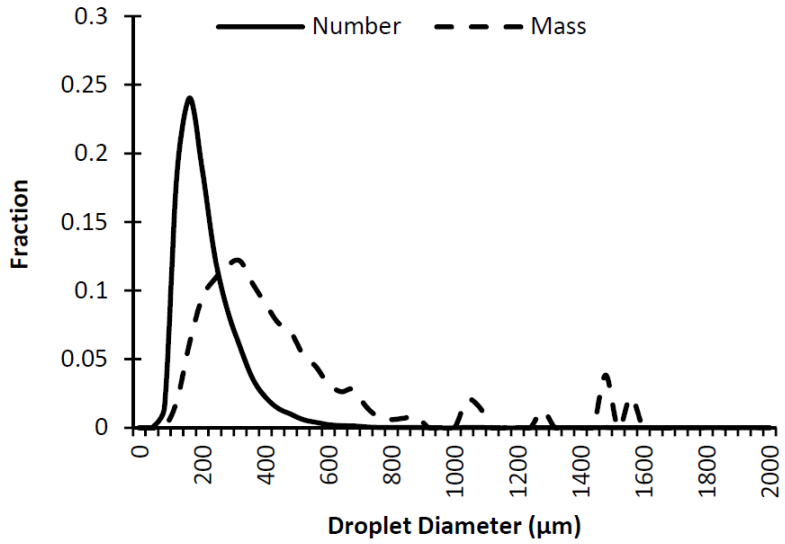

(b) $2\theta = 90°$, $v_j = 20\ ^m/_s$, $^{l_b}/_{l_i} = 2$: $(d_{10} = 197\ \mu m, d_{32} = 327\ \mu m)$

Figure 4.15: Droplet Diameter Histograms

approaches a positively skewed normal distribution with the longer tail towards the larger droplet diameters. The spray is also composed of droplets with much smaller diameters. The mass fraction curve has a similar positively skewed normal shape as the number fraction curve but is shifted towards the larger diameter droplets. The peak of the mass fraction curve is close to the calculated Sauter mean diameter in these cases. The small peaks near the 1000 and 1500 μm diameters in the mass fraction distribution correspond with the large amount of mass that is contained in the relatively tiny number of large diameter droplets that do happen to form.

Figure 4.16 is a plot of the numerical mean droplet diameter (d_{10}) as a function of jet Weber number for all three impingement angles and l_b/l_i ratios of 2, 1.5, and 1. In general, as the jet Weber number is increased and/or the impingement angle is increased, the mean droplet diameter decreases. Also for each impingement angle and Weber number, the results for the three l_b/l_i ratios cluster around the same mean droplet diameter. This suggests that the mean droplet diameter is independent of l_b/l_i for ratios ≥ 1. The uncertainty of the measured mean diameter is on the order of 10 μm for each set point. This is too small to plot error bars on the graph. The uncertainty of the jet Weber number is equal to that seen in Figure 4.7.

An empirical droplet size correlation was found using the same least squares technique described previously for the sheet breakup length. Similar to the sheet breakup length correlations, the droplet size correlation is a function of jet Weber number and impingement half-angle. All of the numerical mean droplet results for $l_b/l_i \geq 1$ were used to determine the correlation. The resulting numerical mean droplet diameter correlation, Eq. (4.8), has an $R^2 = 0.956$. This empirical correlation is seen

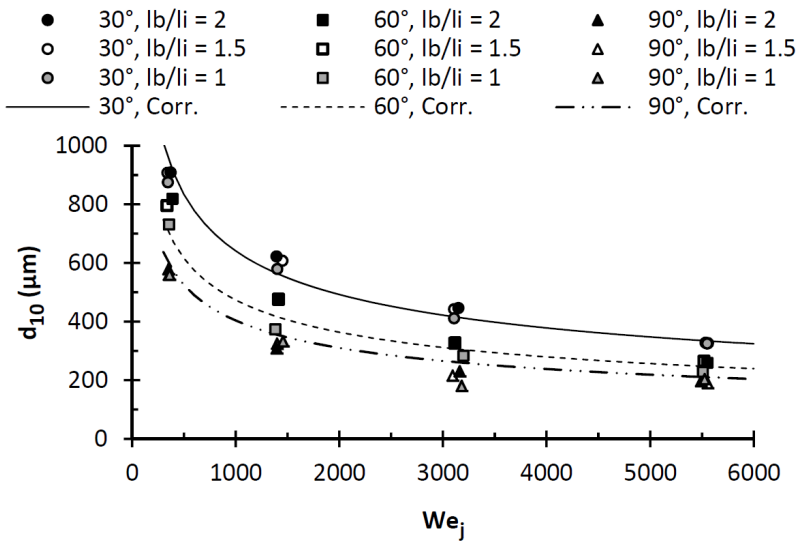

Figure 4.16: Numerical Mean Droplet Diameter, $l_b/l_i \geq 1$

in Figure 4.16 as the "Corr." lines for each impingement angle. Figure 4.17 shows that the derived numerical mean droplet diameter correlation fits the experimental data very well for all impingement angles and jet velocities tested for l_b/l_i ratios ≥ 1.

$$d_{10}\,(\mu m) = 4751\ We_j^{-0.38}\,(\sin\theta)^{-0.46} \quad [l_b/l_i \geq 1] \tag{4.8}$$

An accurate correlation describing the Sauter mean diameter could not be determined with the collected data. This is due to the relatively small number of large droplets within each data set causing the Sauter mean diameter distribution to be dramatically skewed toward the larger diameters. Also, the mass fraction curve does not peak within the measurement range for the polydisperse droplet distributions formed by the low velocity set points, see Figure 4.15(a). This leads to a calculated Sauter mean diameter that is not representative of the entire droplet

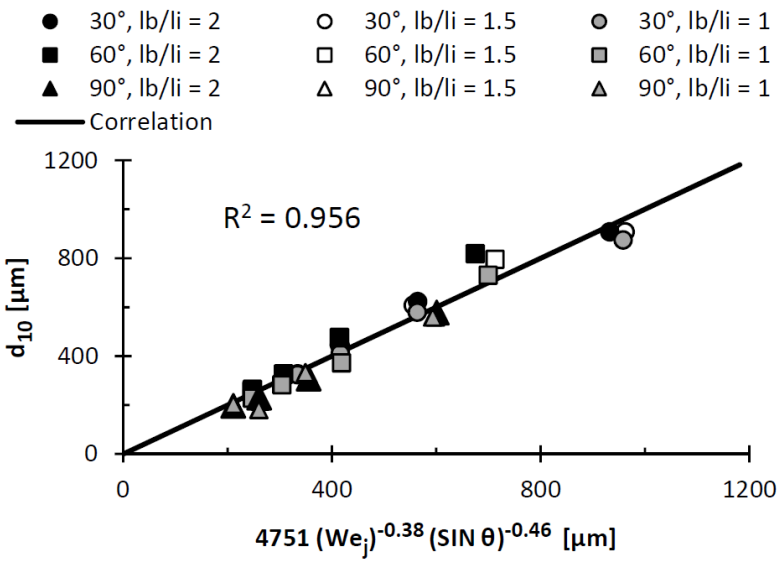

Figure 4.17: Numerical Mean Droplet Diameter Correlation, $l_b/l_i \geq 1$

distribution. However for completeness, the calculated Sauter mean diameters based on the collected data for each set point are contained in Table C.1, Table C.2, and Table C.3 located in the Appendix C.

A qualitative observation of the droplet distributions shows that the polydispersity of the spray decreases with an increase in jet velocity and/or impingement angle. To better quantify the polydispersity of the spray and account for the positively skewed distributions observed at each condition, the spread of the numerical droplet diameter distribution as opposed to the standard deviation is calculated for each condition [91]. The spread of the numerical distribution is defined here as the difference between $d_{90\%}$ and $d_{10\%}$. Where $d_{90\%}$ is the diameter at the 90^{th} percentile of the droplet distribution and $d_{10\%}$ is the diameter at the 10^{th} percentile of the measured droplets. Figure 4.18, is a plot of the average spread of the numerical droplet distributions for each impingement angle versus jet Weber

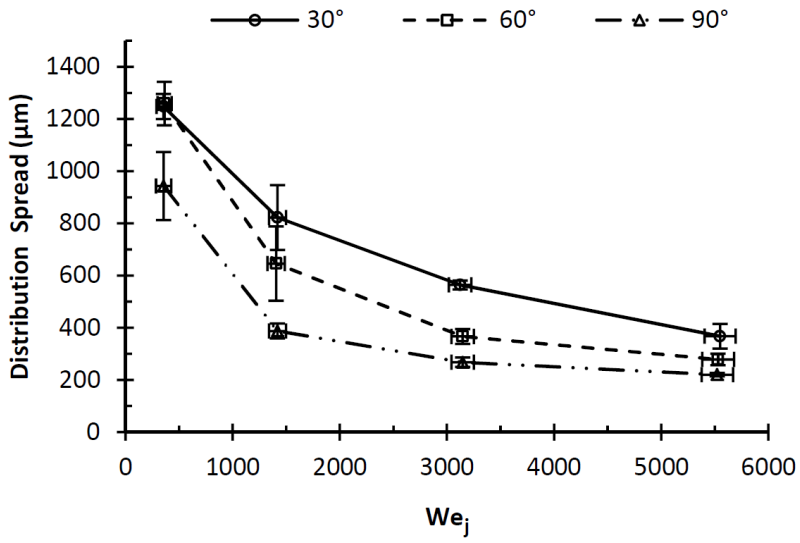

Figure 4.18: Avg. Droplet Distribution Spread, $l_b/l_i \geq 1$

number. The vertical error bars represent the standard deviation between the droplet distribution spreads for data collected when $l_b/l_i \geq 1$ while the horizontal error bars represent the uncertainty of the jet Weber number.

From this plot, it is clear that the polydispersity of the spray reduces with an increase of both Weber number and impingement angle. A comparison of Figure 4.18 with Figure 4.16, shows that the behavior of the droplet spread is qualitatively similar with the mean droplet diameter curves. The operating conditions that produced larger mean droplet diameters also produced a droplet distribution with greater polydispersity and vice versa. In a liquid rocket engine, a spray distribution with a large spread and mean droplet diameter alludes to greater axial distribution of the combustion energy release within the combustion chamber. Likewise, the combination of a smaller mean droplet diameter and a more uniform droplet spectrum can lead to the majority of the combustion energy to be released near the injector faceplate.

Another method to characterize the droplet distribution is with the span. The span of each distribution is calculated using Eq. (4.9). Where $d_{50\%}$ is the median diameter [92]. For this research, the span of the numerical distribution is calculated. The numerical span and droplet diameter results of each set point are presented in Table C.1, Table C.2, and Table C.3 located in the Appendix C for $l_b/l_i = 2$, $l_b/l_i = 1.5$, & $l_b/l_i = 1$ respectively.

$$Sp = \frac{d_{90\%} - d_{10\%}}{d_{50\%}} \tag{4.9}$$

No droplet statistics were collected for the $l_b/l_i = 0.5$ case since most of the droplets formed from the disintegration of the liquid jets passed through the impingement point. Only the cloud of small droplets formed by occasional drop collisions at the impingement point would be sampled by the PDPA. This would lead to erroneous droplet statistics as the bulk of the spray would not be sampled. However, it can be assumed that the average diameter of the large drops that pass through the impingement point is equal to 1.81 mm. This was the mean droplet diameter formed during the single jet experiments. The overall number and mass fraction of the spray at this condition could not be determined.

CHAPTER 5

RESULTS – PART 2: ANALYSIS OF LIKE-DOUBLET ATOMIZATION USING VISUAL OBSERVATION AND DYNAMIC MODE DECOMPOSITION

This chapter presents and explains the results gathered from the second part of the research program characterizing the turbulent jet and the primary atomization region of like-doublet injectors using visual observation and Dynamic Mode Decomposition (DMD). The chapter is split into two sections that describe the qualitative observations and the results from the DMD analysis of both the single jet and the like-doublet spray. The DMD analysis was conducted with Matlab.

5.1 Single Jet Analysis

A single injector tube was tested for three jet velocities, $v_j = 5$, 10, and 20 $^m/_s$, at atmospheric pressure using water as inert propellant simulant. Section 2.2.2 describes the test plan in greater detail. The actual test conditions for the single jet experiment can be found in Appendix A. The jet was oriented to travel vertically downwards, $\pm 1°$. The following subsections will describe the breakup characteristics observed in the video files and detail the results of the DMD analysis on the jet.

(a) $v_j = 5\ m/s$ **(b)** $v_j = 10\ m/s$ **(c)** $v_j = 20\ m/s$

Figure 5.1: Snapshots of the Turbulent Jet

5.1.1 Physical Characteristics of the Single Jet

As described in Section 4.1, the jet is fully-turbulent when exiting the injector tube and was not subjected to cavitation nor hydraulic flip within the orifice. For all three set points, the jet was observed to breakup in the turbulent primary breakup process [41, 42]. Figure 5.1 are still frame images of the single jet for all three jet velocity conditions.

Turbulent primary breakup tends to occur for turbulent jets with Weber numbers below 5,200 when the aerodynamic effects of the gaseous medium are very small ($\rho_{liq}/\rho_{gas} > 500$), and viscosity has a negligible effect upon the breakup process due to small Ohnesorge numbers. This regime occurs for jet flow conditions (We & Re), typically associated with the 1^{st} Wind-Induced breakup regime. As can be observed in Figure 5.1, the issuing jet is characterized by random protuberances with characteristic dimensions on the order of the orifice diameter caused by the motion of the turbulent eddies. The large-scale eddies cause unsymmetrical lateral

kinks to distort the liquid column. The distortion and motion caused by the large eddies initiate the breakup process of the liquid column and droplet formation on the surface of the jet. Droplets are formed when the turbulence energy has sufficient time to deform the liquid surface enough to allow the surface tension forces to form a droplet of comparable size to the eddy and jet diameter. The turbulent jet is destroyed when droplets are formed and detached from the end of the jet by this axisymmetrical disturbance. The breakup length of the turbulent jet tends to increase with jet Weber number under this process [41–45].

As was reported in Section 4.1, large diameter droplets are shed for the end of the jet by the axisymmetrical surface tension forces. The mean droplet diameter was 1.81 mm which is very close to the predicted droplet diameter of $1.89d_o$ for the Rayleigh breakup mechanism associated with laminar jets [30] where d_o in this experiment is 1.016 mm. Also, the average spacing between the large droplets was found to be 4.52 mm. This result agrees well with the predicted wavelength of the most unstable axisymmetrical disturbance for the Rayleigh mechanism which is equal to $4.51d_o$ [30]. These observations show that turbulence distorts and initiates the breakup of the jet but surface tension is the dominant mechanism for the formation and shedding of the droplets.

5.1.2 DMD Analysis of the Single Jet

During the single jet experiments, the high-speed camera was sampled at 20,000 frames per second with an exposure time of 8 μs. The exit of the injector tube was centered at the top edge of the video frame. The image size was set to

80 x 160 pixels which allowed for the first 49 mm of the jet to be captured by the camera for each set point. A total of 2,500 frames were analyzed using a temporal DMD analysis for each set point.

A temporal Dynamic Mode Decomposition (DMD) analysis of the high-speed video is able to extract the specific modes and frequencies that contribute greatly to the overall dynamics of the turbulent jet. The scaled amplitude of each mode represents the degree to which an individual mode contributes to the overall dynamics of the jet for the video frames analyzed. From the complex eigenvalues, the frequency and temporal growth rate can be directly calculated for each dynamic mode. Contour plots of the dynamic modes present a visual depiction of how each mode forms and evolves spatially. In addition, all of the calculated DMD modes weighted according to their scaled amplitudes can be combined into a single composite contour plot producing a representation that should be similar to a still image of the actual jet.

Figure 5.2 displays the results of this analysis with plots of the scaled mode amplitude as a function of frequency for all three jet velocities tested. The plots 'zoom in' on the dynamic modes. Therefore, the amplitude of the mean flow (0 Hz) mode is not shown as the amplitude is too large and is off the scale. Each set point exhibits a large mode at 120 Hz. This has been determined to be caused by slight flickering of the light source consistent with the harmonic of the 60 Hz AC electrical grid frequency and not a dynamic mode of the jet. This was verified with the FFT of several pixels outside of the jet region which displayed only one frequency peak at 120 Hz.

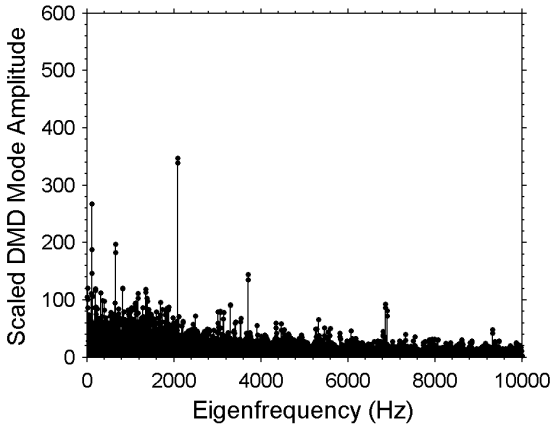

(a) $v_j = 5\ ^m/_s$

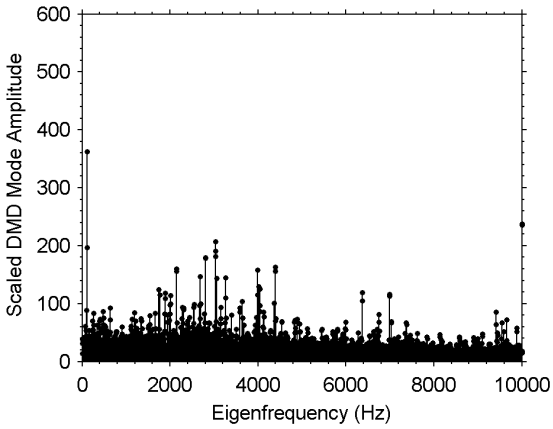

(b) $v_j = 10\ ^m/_s$

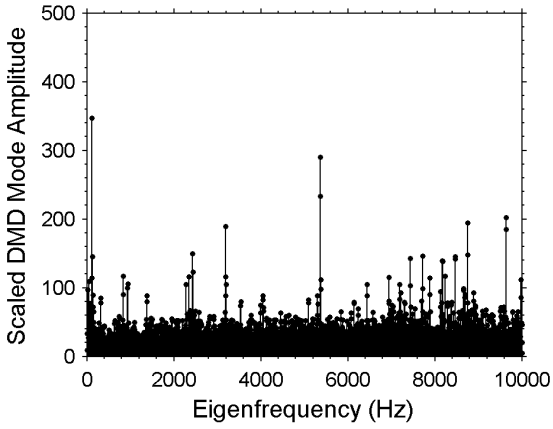

(c) $v_j = 20\ ^m/_s$

Figure 5.2: Scaled Mode Amplitude vs. Frequency

From Figure 5.2, it is seen that hundreds of modes with relatively low amplitudes span the frequency range from 0 Hz to the Nyquist frequency of 10 kHz and represent the broadband nature of turbulent jet dynamics. Embedded within the broadband turbulence, a relatively small number of high amplitude modes are apparent as large spikes on the plot.

Starting with the 5 $^{m}/_{s}$ jet velocity case, Figure 5.3 displays the DMD mode contour plots for the mean flow mode, four of the largest dynamic modes, and a composite of all DMD modes calculated in the analysis where the contribution of each mode is weighted by its scaled amplitude. The four dynamic modes selected are: 2,092 Hz, 664 Hz, 3,704 Hz, and 823 Hz. Table 5.1 displays the scaled amplitude, frequency, and temporal growth rate of each of the individual dynamic modes plotted in Figure 5.3. A negative growth rate indicates that the mode decays with time.

Table 5.1: Temporal DMD Results: Single Jet, $v_j = 5$ $^{m}/_{s}$

Mode Number	Scaled Amplitude	Frequency (Hz)	Growth Rate ($^{1}/_{s}$)
1	16,863	0	-0.01
2	347	2,092	-21.70
3	197	664	-7.56
4	144	3,704	-68.23
5	121	823	-22.05

The mean flow mode (0 Hz) displays a smooth jet of constant diameter without surface irregularities nor distortions. This is expected as the mean shape of the jet is unchanging. Both the 2,092 Hz and the 3,704 Hz modes display axisymmetrical

disturbances observed by the locations of the alternating dark and light regions on the left side of the jet being in phase with the dark and light regions on the right side of the jet. In contrast, the 823 *Hz* and 664 *Hz* modes start as unsymmetrical (sinuous) disturbances on the upper half of the jet that is identified by the modal wave pattern on one side of the jet being out of phase with the pattern on the other side. These unsymmetrical disturbances gradually become more axisymmetrical down the length of the jet. This transition is supported by the description of the turbulent primary breakup process where lateral distortions of the jet initiated by turbulence are transformed into axisymmetrical bulges as surface tension forms droplets from these distortions. Finally, the composite mode plot looks remarkably similar to a still image of the jet. The surface irregularities and distortions of the jet are captured in the contour plot along with the transition to the axisymmetrical bulges near the bottom of the image as surface tension begins to form droplets on the surface of the jet. These results demonstrate the capability that DMD has in being able to accurately extract a finite number of modes that characterize the dynamics of a turbulent jet.

Figure 5.4 displays the DMD mode contour plots for the 10 $^{m}/_{s}$ jet velocity condition. In addition to both the mean flow mode plot and the composite plot that shows the scaled combination of all the calculated DMD modes, four individual dynamic modes with frequencies of: 3,038 *Hz*, 4,399 *Hz*, 2,147 *Hz*, and 3,997 *Hz* are plotted. The 0 *Hz* mean flow mode shows the expected smooth jet of constant diameter. The 3,038 *Hz*, 4,399 *Hz*, and 3,997 *Hz* dynamic modes are characterized by axisymmetrical disturbances that travel down the length of the jet. While the 2,147 *Hz* dynamic mode is an unsymmetrical disturbance causing the jet to distort

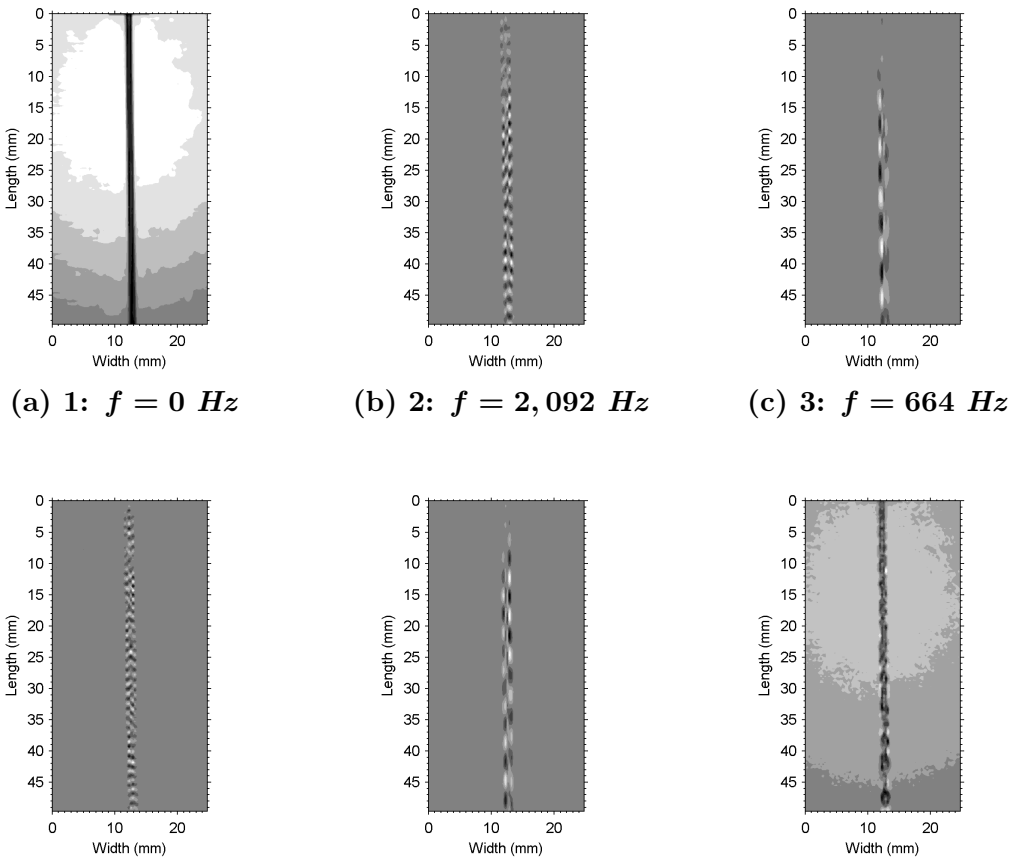

(a) 1: $f = 0$ *Hz* **(b) 2: $f = 2,092$ *Hz*** **(c) 3: $f = 664$ *Hz***

(d) 4: $f = 3,704$ *Hz* **(e) 5: $f = 823$ *Hz*** **(f) Composite**

Figure 5.3: Single Jet DMD Modes: $v_j = 5$ $^m/_s$

laterally in a sinuous fashion. The mode composite plot once again displays an image of the jet that is very similar to any given snapshot of the jet. Table 5.2 shows the results of the temporal DMD analysis on the 10 $^m/_s$ jet for the individual modes seen in Figure 5.4.

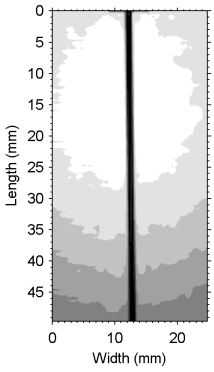

(a) 1: $f = 0$ Hz

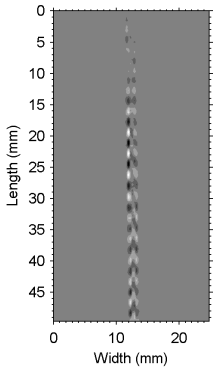

(b) 2: $f = 3,038$ Hz

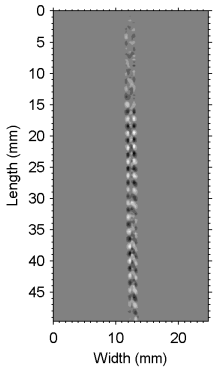

(c) 3: $f = 4,399$ Hz

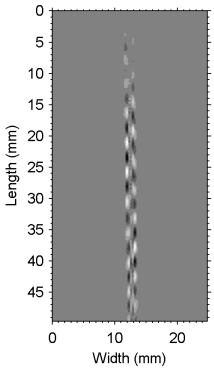

(d) 4: $f = 2,147$ Hz

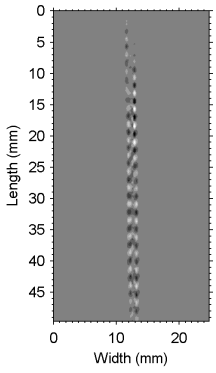

(e) 5: $f = 3,997$ Hz

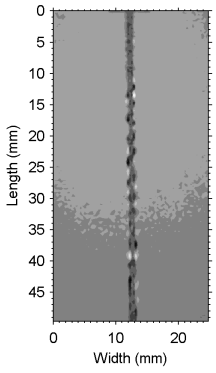

(f) Composite

Figure 5.4: Single Jet DMD Modes: $v_j = 10$ $^m/_s$

Table 5.2: Temporal DMD Results: Single Jet, $v_j = 10$ $^m/_s$

Mode Number	Scaled Amplitude	Frequency (Hz)	Growth Rate ($^1/_s$)
1	16,753	0	-0.03
2	207	3,038	-23.76
3	163	4,399	-137.44
4	160	2,147	-11.49
5	158	3,997	-57.12

Likewise, Figure 5.5 displays the DMD mode contour plots for the 0 Hz mean flow mode, a composite of all the DMD modes, and four individual dynamic modes with frequencies of: 5,368 Hz, 9,636 Hz, 3,190 Hz, and 2,430 Hz. As expected the mean flow mode shows a smooth jet while the mode composite plot displays a jet that is very similar to the actual image of the jet. Of the four dominant dynamic modes plotted, three are axisymmetrical modes. While the 9,636 Hz dynamic mode shows an unsymmetrical sinuous configuration. See Table 5.3 for a summary of the characteristics of the five dynamic modes plotted in Figure 5.5.

Table 5.3: Temporal DMD Results: Single Jet, $v_j = 20\ ^m/_s$

Mode Number	Scaled Amplitude	Frequency (Hz)	Growth Rate ($^1/_s$)
1	16,754	0	-0.03
2	290	5,368	-31.84
3	202	9,636	-67.02
4	189	3,190	-58.77
5	150	2,430	-103.39

5.1.3 Feed System Coupling

Feedline pressure oscillation data of each feedline branch was collected by PCB 106B high-frequency dynamic pressure transducers with a sample rate of 20,000 Hz for 10,000 samples. The transducers are placed in a cross with the centerline of the transducers located approximately 13.5 cm (135 orifice diameters) upstream of the injector tube entrances. A Fast Fourier Transform (FFT) of the collected data,

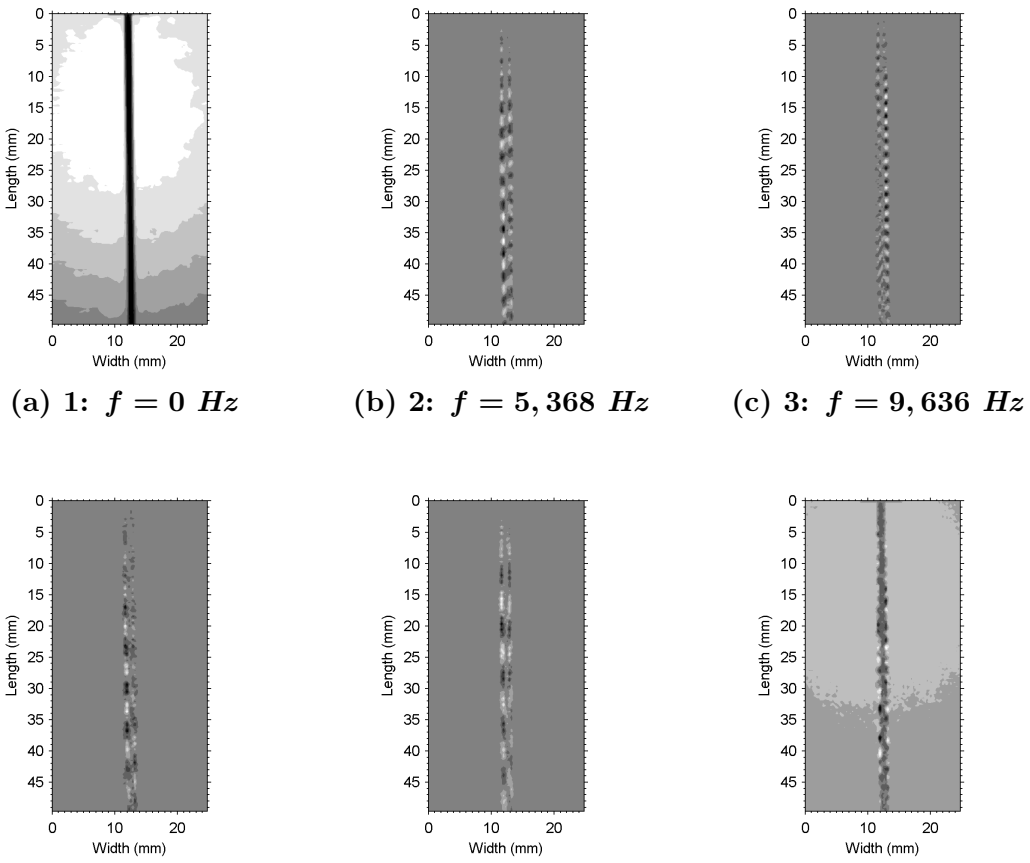

(a) 1: $f = 0$ Hz **(b) 2: $f = 5,368$ Hz** **(c) 3: $f = 9,636$ Hz**

(d) 4: $f = 3,190$ Hz **(e) 5: $f = 2,430$ Hz** **(f) Composite**

Figure 5.5: Single Jet DMD Modes: $v_j = 20$ $^m/_s$

revealed consistent frequency content over the range of operating conditions tested. Figure 5.6 shows the FFTs for each jet velocity tested. Figure 5.6(a), (b), and (c) show the full frequency spectrum while Figure 5.6(d), (e), and (f) focuses on the frequency range of interest.

Examining Figure 5.6(a), (b), and (c) shows that the dynamic content illustrated by the FFT is very similar for all three jet velocity conditions. There are a few large amplitude spikes near 0 Hz and a second region between 3,000 and 4,000 Hz

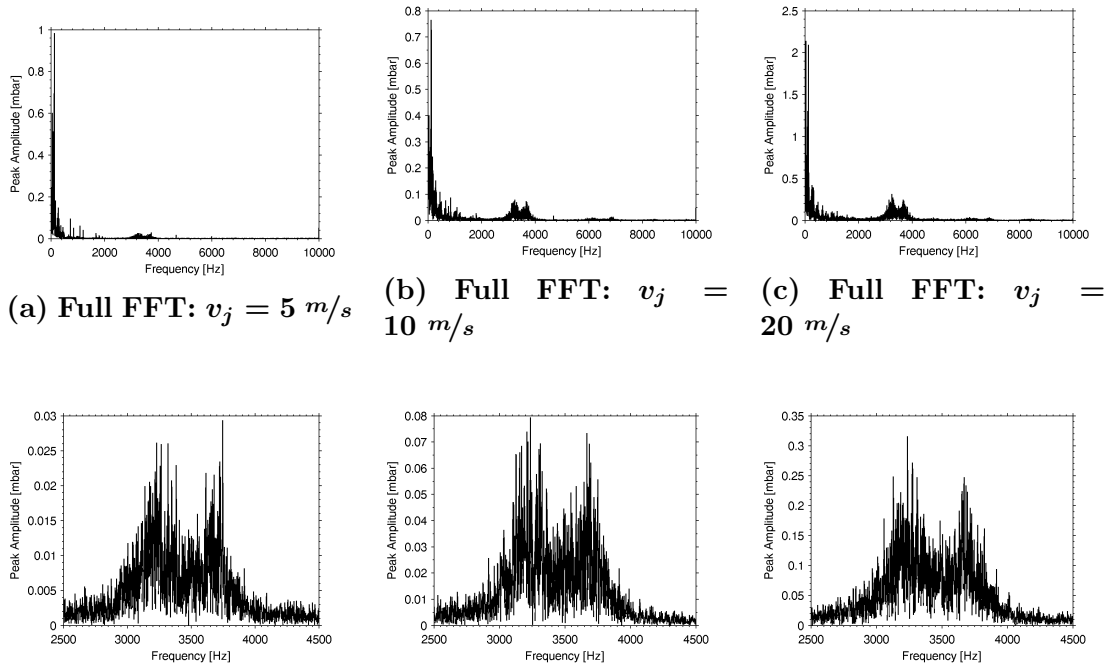

(a) Full FFT: $v_j = 5\ m/s$ **(b) Full FFT: $v_j = 10\ m/s$** **(c) Full FFT: $v_j = 20\ m/s$**

(d) Cropped FFT: $v_j = 5\ m/s$ **(e) Cropped FFT: $v_j = 10\ m/s$** **(f) Cropped FFT: $v_j = 20\ m/s$**

Figure 5.6: Feedline Oscillations

that contains two peak frequencies with lower amplitudes. The low frequency spikes have been determined to be electrical interference with frequencies at the subharmonic and harmonics of the 60 *Hz* AC frequency. Therefore, the only frequency region of interest on the FFT is the dynamic content with peak frequencies between 3,000 and 4,000 *Hz*.

Figure 5.6(d), (e), and (f) display remarkably similar frequency content. Two distinct pressure oscillations were detected with peak frequencies approximately equal to 3,200 *Hz* and 3,700 *Hz*. The amplitudes of both peaks are about equal. This bi-modal dynamic content and peak frequency values are consistent for all jet velocities and were detected in both feedline branches. The peak amplitudes of

these oscillations increases proportional with the increase in jet velocity. This result suggests that the source of these oscillations are fluid dynamic in nature.

An analysis of the feed system and injector demonstrated that resonant standing waves is the most likely source of these pressure oscillations. The glass injector tubes are 8 $in.$ (203.2 mm) long with a hole diameter of 0.04 $in.$ (1.016 mm). A tube with such a large l_o/d_o ratio is susceptible to developing a standing longitudinal resonance mode. Therefore, the frequency of the fundamental mode for the injector tube is calculated by Eq. (5.1). Where c is the speed of sound of water which is equal to 1,481 m/s at $20°C$ [93] and l is the length of the injector tube. The mean velocity of the liquid is neglected due to $v/c \ll 1$. Both the entrance and exit of the injector tube are modeled as open boundary conditions. The resonant frequency is calculated to be 3,650 Hz. This result matches the second peak frequency around 3,700 Hz and demonstrates that resonant standing waves within the injector tube is the source of this pressure oscillation.

$$f = \frac{c}{\lambda} = \frac{c}{2l} \tag{5.1}$$

The source of the 3,200 Hz peak was traced to the part of the feed system just upstream of the injector tube entrance. The glass injector tubes are connected to the feed system with Swagelok Ultra-Torr fittings. A 3.5 $in.$ (89 mm) long stainless steel tube with an inner diameter of 0.19 $in.$ (4.8 mm) connects the injector fitting with the transducer cross and itself is clamped to the rotation platform. See Figure 5.7 for a photograph of the feed system.

Figure 5.7: Picture of the Feed System

Inside the transducer cross, the internal diameter expands to allow placement of the transducers causing an opened boundary condition at the interface. However, at the injector tube entrance the diameter reduces from 0.19 *in.* (4.8 *mm*) to 0.04 *in.* (1.016 *mm*) forming a closed boundary condition due to the area ratio of the orifice and pipe being very small ($A_o/A_p = 0.044$). Therefore, the feedline between the expansion of the transducer cross and the entrance of the injector tube forms a closed-opened pipe with a length of around 120 *mm* and a diameter of 4.8 *mm*. The frequency of the fundamental longitudinal resonance mode of this system can be found from Eq. (5.2). The calculated resonant frequency of the feedline is approximately 3,100 *Hz*. This frequency is very similar with the first peak frequency near 3,200 *Hz* and provides compelling evidence that a resonant standing wave of the feedline is the source of this second pressure oscillation.

$$f = \frac{c}{\lambda} = \frac{c}{4l} \tag{5.2}$$

The presence of resonant standing waves within both the feedline and injector tube presents the possibility of coupling between these oscillations and the liquid jets. Feed system coupling occurs when vibrations and/or resonances in the feed system and injector propagate into the fluid causing mass flowrate oscillations or disturbances within the fluid with similar frequencies as the upstream fluctuations. Therefore, evidence of feed system coupling within the liquid jets should present itself in the DMD analysis.

Referring back to Figure 5.2, it is seen that higher amplitude dynamic modes exist within the jets at frequencies between 3,000 and 3,800 *Hz*. The modes consistent with feed system coupling are dominant in the $v_j = 10\ {}^{m}/_{s}$ jet and are some of the main dynamic modes affecting the $v_j = 20\ {}^{m}/_{s}$ jet. Feed system coupling does not dominate the dynamics of the $v_j = 5\ {}^{m}/_{s}$ jet, but the cluster of modes in the frequency range of interest shows that feed system coupling is present. This result is not surprising as the amplitudes of the fluctuations increase with an increase of jet velocity.

5.2 Like-Doublet Analysis

The like-doublet experiments tested the injector at atmospheric pressure using water as the propellant simulant with a 60° impingement angle, jet velocities of 5, 10, and 20 ${}^{m}/_{s}$, and a ${}^{l_b}/_{l_i}$ ratio equal to two as described in the test plan, Section 2.2.2. A table of the actual test conditions for each set point of the like-doublet experiments

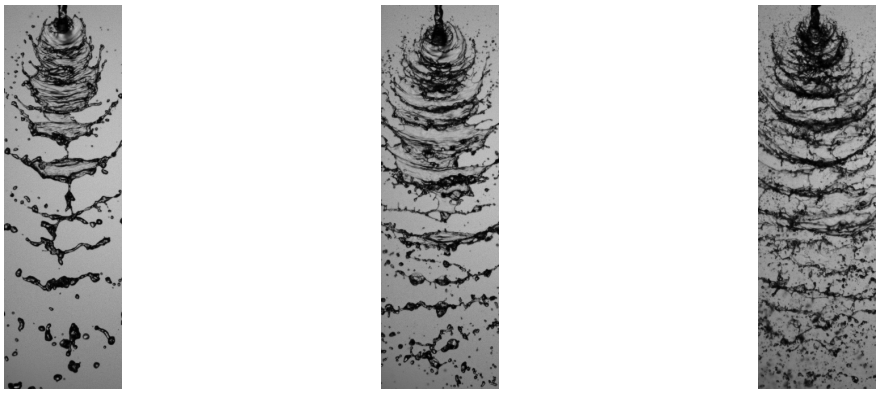

(a) $v_j = 5\ m/s$ **(b)** $v_j = 10\ m/s$ **(c)** $v_j = 20\ m/s$

Figure 5.8: Snapshots of the Spray, Side-View

can be found in Appendix A. The subsections below will describe the characteristics of the primary atomization process and impact wave formation as well as detail the results of the DMD analysis on the spray.

5.2.1 Physical Characteristics of the Like-Doublet Spray

Watching the high-speed videos offers insight into the impingement process and resulting primary atomization characteristics of like-doublet injectors. As previously described in Section 1.4, two impinging jets of the same same fluid and similar injection conditions will produce a flat sheet whose orientation is perpendicular to the plane of the two impinging jets. This flat sheet is unstable and quickly disintegrates into ligaments and droplets. The unsymmetrical nature of the spray requires two views, a side-view and a front-view, to get a full understanding of the impingement and primary atomization process.

The primary atomization process of like-doublet impinging injectors will first be described using the observations of the spray from a side-view, see Figure 5.8. To collect the side-view video, the high-speed camera is pointed directly at the face of the sheet, $\varphi = 0°$ in Figure 3.2. When $v_j = 5\ {}^{m}/_{s}$, the flat sheet has a ruffled appearance with small wave structure apparent on the surface while large ligaments are detached from the end of the sheet. The ligaments themselves are unstable and quickly disintegrate into droplets. A relatively small number of large droplets are shed from the edge of the sheet.

When the jet velocity is increased to $v_j = 10\ {}^{m}/_{s}$, robust impact waves are seen on the surface of the sheet while a greater number of small droplets are ejected from the edge of the sheet. Waves of ligaments are shed from the end of the sheet which subsequently disintegrate into small droplets. As jet velocity is increased, the strength of the impact waves seen on the surface of the sheet become very strong and cause significant distortion of the flat sheet. For $v_j = 20\ {}^{m}/_{s}$, the impact force is so great that it is difficult to distinguish the surface of the flat sheet from the surrounding droplet field. A large number of small droplets are ejected from the edge of the sheet and waves of ligaments are shed from the end of the sheet which quickly disintegrate into a large number of small droplets.

From Chapter 4, the mean ligament wavelength was found by operator analysis of the videos to be constant for ${}^{l_b}/_{l_i}$ ratios ≥ 1 and was equal to about six orifice diameters. This mean wavelength was independent of both the impingement angle and jet velocity. However, the sheet did not shed ligaments at a specific frequency. Instead, a range of wavelengths were measured for the ligaments as demonstrated

(a) $v_j = 5\ m/s$ **(b)** $v_j = 10\ m/s$ **(c)** $v_j = 20\ m/s$

Figure 5.9: Snapshots of the Spray, Front-View

by the large standard deviation between measurements. Since the mean wavelength remained constant, the average atomization frequency increased with jet velocity and was found to be parallel and near to the empirical Hewitt stability threshold for liquid rocket engines that use like-doublet injectors, refer to Figure 4.14. These results demonstrate that the primary atomization process has a large effect on the stability rating of a rocket engine.

To record video of the primary atomization process in a front-view orientation, the high-speed camera is pointed parallel to the face of the flat sheet, $\varphi = 90°$ in Figure 3.2. See Figure 5.9 for still images of the front-view of the like-doublet primary atomization zone for the three jet velocities tested. The front-view orientation provides an unobstructed view of the two impinging jets which allows for direct observation of the condition of the two jets at the impingement point. This view also shows the edge of the flat sheet which clearly displays the wave-like distortion

from the impact waves. In addition, the ligaments detached from the end of the sheet can also be observed.

As the jet velocity is increased from $v_j = 5\ {}^{m}/_{s}$ to $v_j = 20\ {}^{m}/_{s}$, the amplitude of the impact waves increases and is proportional with the increase in the collision force of the two jets. The amount of droplets shed from the edge of the sheet also increases with jet velocity. At $v_j = 20\ {}^{m}/_{s}$ the violent collision causes a large amount of tiny droplets to surround the sheet obscuring the view. The crests and troughs of the impact waves seen in the front-view images correspond with the periodic dark wave regions seen on the sheet in the side-view images.

Impact waves are a hydrodynamic phenomena and are the controlling process and defining characteristic of the quick and violent breakup observed with fully-developed sprays. Typically, impact waves are formed with the impingement of two turbulent jets. However, small impact waves have been observed for high-speed laminar conditions that form an opened-rim spray pattern [64]. A full understanding of the source(s) of impact waves is still unknown due to the unstable and nonlinear nature of process and therefore the phenomenon has not been fully characterized [51, 64].

Several ideas have been put forth to describe the formation and source(s) of impact waves. One idea states that impact waves form as a consequence of the fluctuations of pressure and/or jet momentum at the impingement point. These fluctuations may arise from disturbances within the liquid jet that become accentuated at the impingement point, e.g. jet instabilities and turbulence, or from the jet impingement itself, e.g. periodic movement about the mean stagnation

point [51]. Another idea extending from the results of numerical simulations conducted by Chen, et al., have shown that impact waves could be formed by the interfacial shear stress between the two sides of the sheet forming dilatational waves near the impingement point. This causes nonlinear behavior that forces the sheet to resonate at its natural frequency and generate the unstable sinuous waves down the length of the sheet known as impact waves [64]. The numerical results found by Zheng, et al. [65] showed that impact waves could be formed by the velocity profile difference between the two impinging jets around the stagnation and impingement points. This difference also affects the stability and breakup of the flat sheet. The velocity difference is exacerbated by larger impingement angles leading to larger impact waves and enhanced sheet breakup.

A direct observation of the formation of impact waves on the flat sheet was possible with the high-speed videos recorded in this experiment when the like-doublet injector was oriented in the front-view orientation. A qualitative understanding of the sources of impact waves was possible through watching the high-speed videos for each set point. The sources and formation of impact waves are discussed in conjunction with Figure 5.10. Figure 5.10 is a sequence of still images from the 60° like-doublet for $v_j = 5\ {}^{m}/_{s}$. This set point was chosen as the impingement point and flat sheet is unobstructed by numerous small droplets which occurs for the higher jet velocity conditions. The sources and formation process of impact waves were observed to be identical for all set points tested.

It is typically assumed for an impinging jet injector that the momentum of the two jets towards each other is destroyed and this collision forces the liquid to spread in

the lateral direction in the shape of a flat sheet. For the impingement of two laminar jets at the same velocity, the jet momentum would be constant down the length of both jets and be equal at the impingement point. Therefore the impingement process would form a smooth, flat sheet as is observed in experiments.

However, fully-developed turbulent jets are characterized by random protuberances and distortions of the jet column caused by the shape and motion of the large turbulent eddies, see Figure 5.1. This causes local regions in the jet to contain greater amounts of fluid mass which are identified by the small protuberances and bulges on the jet. These bulges travel at the same speed as the mean flow of the jet and therefore cause local variations of the jet momentum.

Applying the description of turbulent jets to the case of impinging jets, it is reasoned that the slight differences of the local momentum between the two jets at the impingement point can cause the flat sheet to distort in the direction of travel as the jet with the greater momentum i.e. toward the jet with less momentum, forming the characteristic impact waves on the flat sheet. This process is a purely hydrodynamic source for impact waves.

The momentum imbalance mechanism dictates that the formation of impact waves is governed by the relative alignment between the bulges of the two impinging jets and as the size and locations of these protuberances vary down the length of the two jets, the periodicity and strength of the resulting impact waves change with time. This explains why the impact waves observed on a flat sheet do not exhibit a constant wavelength and ligaments are shed from the end of the sheet over a wide range of frequencies.

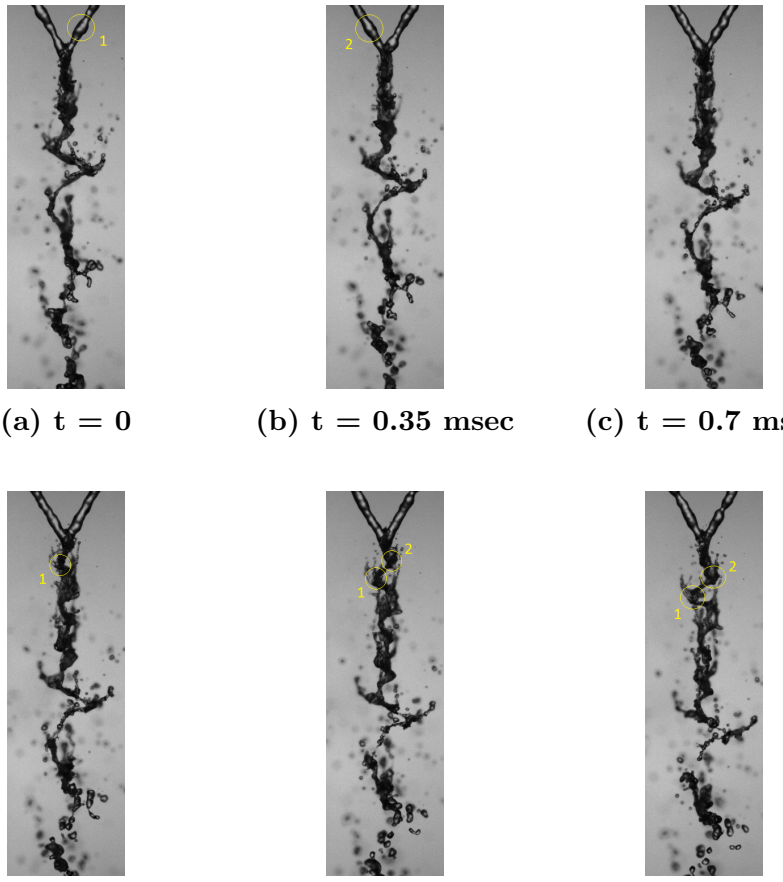

(a) t = 0 **(b) t = 0.35 msec** **(c) t = 0.7 msec**

(d) t = 1.05 msec **(e) t = 1.4 msec** **(f) t = 1.75 msec**

Figure 5.10: Formation of Impact Waves from Impinging Jets

Momentum imbalance can also explain the small impact waves sometimes observed for the opened-rim spray pattern. Previous studies have shown that the opened-rim pattern is formed by high-speed laminar jets [60, 62]. However, it is possible at these conditions that the jets are actually semi-turbulent with a weak turbulent core surrounded by a laminar envelope. The local momentum differences between the two turbulent cores at the impingement point can cause small impact waves to form on the sheet.

Observational evidence for the momentum imbalance mechanism is displayed in the sequence of images seen in Figure 5.10. Starting with Figure 5.10(a), a local bulge of the right jet is identified and marked with the number 1. The same region on the left jet does not have a similar bulge. Therefore, a momentum imbalance will exist when these two regions reach the impingement point. 0.35 msec later in Figure 5.10(b), a different bulge is identified on the left jet and is marked with the number 2. A similar momentum imbalance will exist between the left and right jets when these local regions reach the impingement point. Figure 5.10(c) and Figure 5.10(d) each advance the time by 0.35 msec and display the impingement of both bulges. In Figure 5.10(d), the flat sheet is distorted towards the left jet just below the impingement point. This shows the initial formation of the impact wave caused by the momentum imbalance from the bulge 1 region. Advancing the video another 0.35 msec, Figure 5.10(e), shows a new distortion of the flat sheet this time towards the right jet. This corresponds with the impact wave caused by the momentum imbalance of the bulge 2 region. The final frame shown in Figure 5.10(f), shows the two impact waves traveling down the length of the sheet with the identifying numbers corresponding with the bulges that formed the respective distortions of the sheet (impact waves).

From Figure 5.10, the formation of the impact waves on the flat sheet can be clearly attributed to the local momentum imbalances between the two jets at the impingement point. The momentum imbalance causes the flat sheet to distort in the direction of travel of the jet with locally higher momentum, i.e. towards the jet with less momentum. The degree of distortion (amplitude of the impact wave) is

proportional to the local momentum imbalance of the two jets. The surface tension of the liquid is responsible for holding the sheet together as the impact waves travel down the length of the sheet. The size and shape of the impact wave changes as it travels down the length of the sheet due to competition between the inertial, surface tension, and viscous forces. The unstable nature of the flat sheet leads to disintegration of the sheet and the formation of ligaments. Ligaments are formed when the sheet is broken at the crests of the impact waves and the segmented portion of the sheet contracts into a bowed cylindrical-like shape via surface tension. However, it should be noted that the sheet does not necessarily breakup at every wave crest. Oftentimes a ligament will form from a sheet segment that contains two or more impact waves. This is the reason why the mean ligament shedding frequency is lower than the mean impact wave frequency on the sheet and why the measured ligament wavelengths of a large standard deviation.

In addition, the protuberances and distortion present on the two turbulent jets causes the stagnation point of the impinging jets to move randomly about the mean (designed) impingement point. This slight movement can be observed in the high-speed videos. It is possible this movement can have a secondary influence in the formation of the flat sheet and resulting impact waves.

These experimental results did not support the idea of interfacial shear stress between the top and bottom of the flat sheet as the source of impact waves as suggested by the numerical results of Chen, et al. [64]. Instead, the impact waves were observed to originate with the disturbances of the two jets. The idea presented by Zheng, et al. [65] that the velocity profile differences at the stagnation and

impingement points are the cause of impact waves is interesting. Velocity differences at the impingement point is similar in concept to the observed momentum imbalance mechanism described above. The main difference is that this research showed the momentum imbalance is caused by the local mass variations due to the protuberances and distortions along the lengths of the two jets. However, slight velocity differences between the two jets at the impingement point could not be verified nor ruled out in this experiment.

5.2.2 DMD Analysis of the Like-Doublet Spray

During the like-doublet experiments, the high-speed camera was sampled at 20,000 frames per second with an exposure time of 8 μs for the side-view and 5 μs for the front-view. The injector was oriented so that the impingement point is visible and centered approximately 3 to 5 mm below the top of the frame allowing for part of the impinging jets to be visible. The image size was set to 80 x 160 pixels which allowed for the entire primary atomization zone to be viewed including the impingement point, full length of the sheet and the ligament zone for each set point.

From the temporal DMD analysis of the high-speed video, specific modes and frequencies that greatly contribute to the overall dynamics of the spray are extracted. The scaled amplitude of each mode represents the degree to which an individual mode contributes to the dynamics of the sheet and spray for the 2,500 video frames analyzed. From the complex eigenvalues, the frequency and temporal growth rate can be directly calculated for each dynamic mode. Contour plots of the dynamic modes present a visual representation of how each mode forms and behaves spatially. In addition,

all of the calculated DMD modes weighted according to their scaled amplitudes can be combined into a single composite contour plot producing a representation that is similar to a still image of the actual spray.

In addition, Fast Fourier Transforms (FFT) of the variations in pixel intensity with respect to time for two pixel locations of the side-view video files are compared with the results of the side-view DMD analysis to see if similar dynamic content is detected between the two techniques. Prior to calculating the FFT, the pixel intensity vectors are windowed using the Hann function. The side-view videos were chosen because the pixel intensity values fluctuate periodically as the impact waves and ligaments pass through the respective measurement regions. The first pixel location corresponds with the sheet and is located halfway down the mean breakup length of the sheet along the centerline. The second pixel location resides in the ligament zone and is located at an axial distance of 1.5 times the mean sheet breakup length along the centerline of the spray. The following subsections detail the results of the DMD and FFT analysis for the like-doublet injector for the three jet velocities tested.

5.2.2.1 Like-Doublet: $v_j = 5\ ^m/_s$

The results of the temporal Dynamic Mode Decomposition analysis of the $v_j = 5\ ^m/_s$ test condition is discussed utilizing both the front-view and side-view data. Figure 5.11 displays plots of the scaled DMD mode amplitude as a function of the mode frequency. Figure 5.11(a) contains the scaled amplitudes of the extracted modes from the front-view test while Figure 5.11(b) contains the scaled mode amplitudes

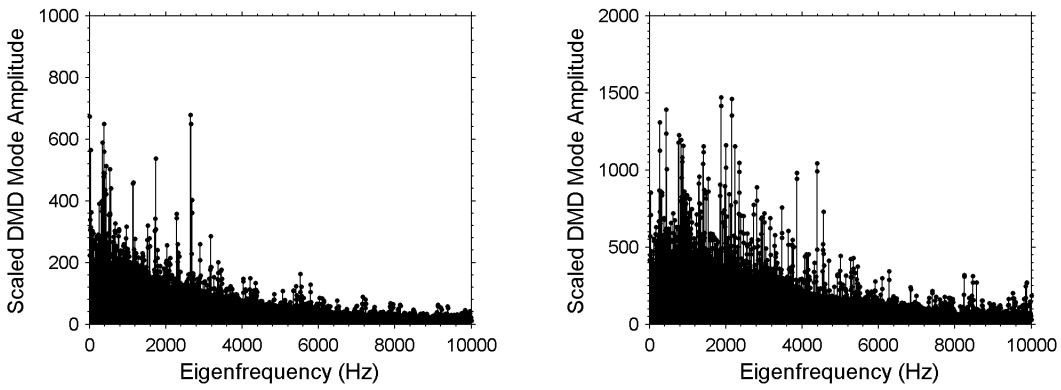

(a) Front View **(b) Side View**

Figure 5.11: Scaled Amplitude Plots: Like-Doublet, $v_j = 5\ ^m/_s$

from the side-view test. These plots 'zoom in' on the dynamic modes causing the amplitude of the 0 *Hz* mean flow mode to be off the scale.

Similar to the single jet experiments, relatively few large amplitude dynamic modes exist among hundreds of relatively low amplitudes dynamic modes that span the entire frequency range, from 0 *Hz* to the Nyquist frequency of 10,000 *Hz*. Additionally, it can be observed that the modes around and below 3,000 *Hz* have greater amplitudes than the modes with higher frequencies forming a 'hill' on the plot. This suggests that the spray at this velocity is dominated by these lower frequency dynamics while the higher frequency modes have a limited effect. Also, the frequencies of the high-amplitude modes present within the like-doublet spray have similar frequencies with the high-amplitude modes within the single jet, refer to Figure 5.2(a). This suggests that the dynamic modes originate with or are influenced by the dynamic modes present in the two impinging jets.

Both the front-view and side-view plots display high amplitude modes over a wide range of frequencies. After studying the contour plots of these high amplitude dynamic modes, it became apparent that the modes above approximately 1,500 Hz have spatial structure that emanates from the impingement point and is dominant in the region where the flat sheet is located. These modes would represent the myriad of impact wave frequencies that are formed from the collision of two turbulent jets. Likewise, the modes with frequencies below 1,500 Hz have a spatial structure that is strong in the region from the bottom of the sheet through the ligament zone. These modes represent the ligaments shed from the sheet and the variation of ligament shedding frequency.

From the results discussed in Chapter 4, it was found that the mean wavelength of the shed ligaments was equal to about six orifice diameters for all impingement angles and jet velocities. Also, ligaments were not shed in regular intervals leading to a large standard deviation between measurements. Due to a constant mean ligament wavelength, the shedding frequency increased proportional with jet velocity. For $v_j = 5\ {}^{m}/_{s}$, the mean ligament shedding frequency was about 820 Hz with a standard deviation of about 190 Hz.

For brevity, a discussion of the largest mode within the ligament shedding frequency range is selected from both the front-view and side-view results to represent the group of high amplitude modes within this range. Likewise, the largest mode above 1,500 Hz is selected from both views to represent the impact waves on the surface of the sheet. Also, the 0 Hz mean flow mode is discussed. Refer to Table 5.4 for the scaled amplitude, frequency, and growth rate of the three selected dynamic

modes from the results of each camera view. As stated previously, a negative growth rate indicates a mode that decays with time.

Table 5.4: Temporal DMD Results: Like-Doublet, $v_j = 5\ ^m/_s$

Camera View	Mode Type	Scaled Amplitude	Frequency (Hz)	Growth Rate ($^1/_s$)
Front	Mean Flow	16091	0	0.08
	Sheet	679	2653	-622.24
	Ligaments	327	680	-8.64
Side	Mean Flow	24244	0	-0.03
	Sheet	1470	1878	-35.24
	Ligaments	1194	835	-36.64

Figure 5.12 contains contour plots of the three selected individual dynamic modes plus a composite of all the calculated DMD modes where each individual mode is weighted by its scaled amplitude for both camera views. The contour plots show how each mode forms and evolves spatially. This gives the spatial information for each mode to complement the temporal information given in Table 5.4.

The mean flow modes are seen in Figure 5.12(a) and Figure 5.12(d). The front-view displays two smooth jets of constant diameter impinging at a 60° angle producing a flat sheet oriented perpendicular to the impinging jets. The edge of the flat sheet can be detected as the dark region extending from the impingement point to about the 25 mm marker. The ligament zone resides in the region below 25 mm. From the side-view, the mean shape of the sheet is leaf-like. The shape of the sheet is remarkably similar to the sheet produced with the closed-rim spray pattern when

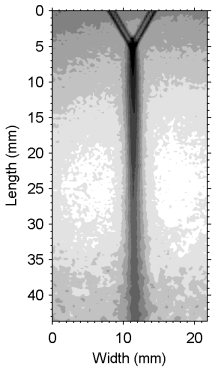

(a) Front Mean Flow: $f = 0$ Hz

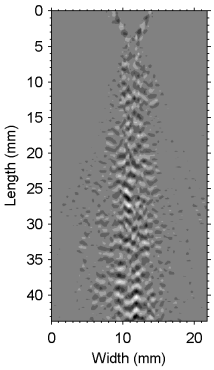

(b) Front Sheet Waves: $f = 2653$ Hz

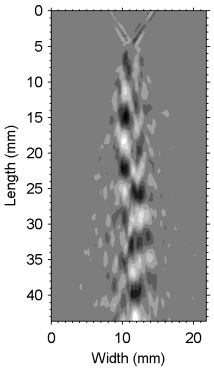

(c) Front Ligaments: $f = 680$ Hz

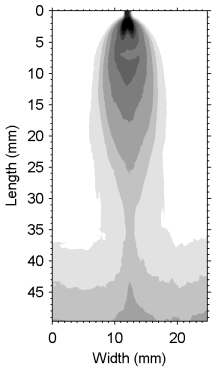

(d) Side Mean Flow: $f = 0$ Hz

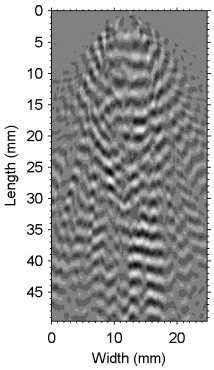

(e) Side Sheet Waves: $f = 1878$ Hz

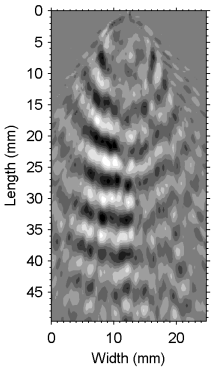

(f) Side Ligaments: $f = 835$ Hz

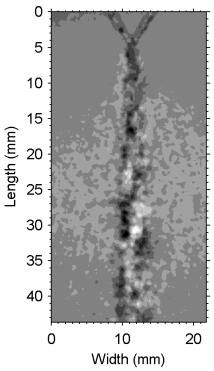

(g) Front Composite

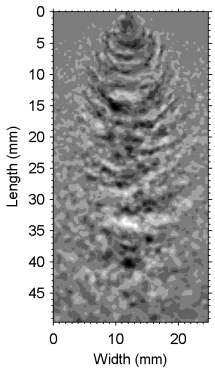

(h) Side Composite

Figure 5.12: Like-Doublet DMD Modes: $v_j = 5$ $^m/_s$

two laminar jets impinge. This suggests that the average shape of the flat sheet is similar to the shape predicted by Taylor's model. However at any instant in time, the flat sheet will not assume this leaf shape due to the violent impingement of two turbulent jets and the distorting and destructive nature of impact waves.

Moving to Figure 5.12(b) and (e), the modal shape of the sheet modes are displayed. In Figure 5.12(e), bowed wave structure is apparent from the impingement point and down the length of the sheet into the ligament zone. The spacing between consecutive dark regions is equal to the wavelength of this mode. The color differences between the dark and light regions are stronger on the sheet and weaken downstream indicating that this mode is predominatly present on the surface of the sheet. Likewise, Figure 5.12(b) displays the wave structure looking at the edge of the sheet. It is interesting to note the wave structure on the two impinging jets. This suggests that the sheet modes originate with the impinging jets and lends further evidence to the theory that the formation of impact waves is due to disturbances on the jets.

Figure 5.12(c) and (f) show the shapes of the dynamic modes representing the ligaments shed from the end of the sheet. In Figure 5.12(c), the front-view mode shape shows wave structure on one side of the sheet that is out of phase with the structure on the other side of the sheet. This represents a sinuous distortion of the flat sheet. Downstream of the sheet the mode structure consolidates into a single column representing the waves of ligaments formed and shed from the sheet. Figure 5.12(f) shows the side-view mode shape. While the mode extends from the sheet to the bottom of the frame, it is apparent that the strength of the mode is strongest in the

ligament region starting around 20 mm mark. This mode was not present in the jets suggesting the ligaments are dependent formed from the waves on the sheet.

The composite plots seen in Figure 5.12(g) and (h) are very similar to a still image of the spray in both the front and side views. The front view shows two jets with disturbances characteristics of turbulence impinging and forming a sheet that has a sinuous appearance. Distinct dark and light regions below the sheet represent the ligaments. The side view shows a flat sheet distorted by impact waves of varying wavelengths. Downstream of the sheet bowed and separated dark regions represent the ligaments shed from the sheet. The composite plots were able to construct an image that faithfully captures the complexity of the impingement and breakup process.

Now a comparison is made between the temporal DMD analysis of the side-view video file with the FFT of the pixel intensity fluctuations for two pixel locations. The two pixel locations corresponds with the flat sheet and ligament zone. Figure 5.13(a) shows the locations of the two pixels analyzed, where pixel 1 is the sheet pixel and pixel 2 is the ligament pixel. Figure 5.13(b) and (c) display the FFTs of the sheet and ligament zones respectively. The amplitude of the FFT corresponds with the power spectrum and is equal to the root mean square (rms) value of the pixel intensity fluctuations squared.

The FFT of the sheet pixel, Figure 5.13(b), shows a cluster of high amplitude frequency content between roughly 1,200 Hz and 2,000 Hz. These frequencies are near to the cluster of sheet impact wave frequencies captured in the DMD analysis, see Figure 5.11(b). Smaller peaks are seen in the higher frequency ranges above 2,000 Hz

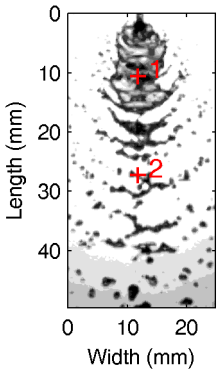

(a) Pixel Locations

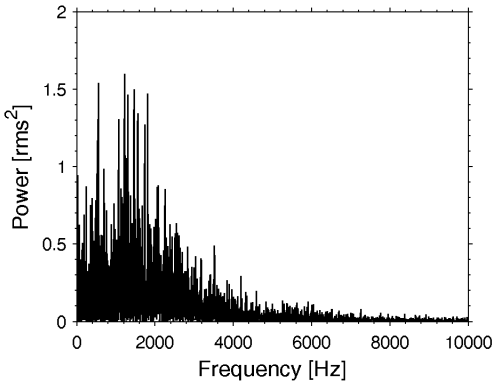

(b) Pixel 1: Sheet Region

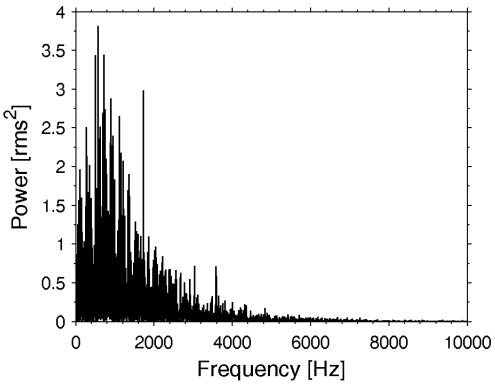

(c) Pixel 2: Ligament Region

Figure 5.13: Pixel FFT: $v_j = 5$ $^m/_s$

representing the variety of surface wave frequencies. Additionally, a large amplitude fluctuation occurs at about 550 *Hz*. This is close to the lower limit of the ligament shedding frequency range found by the DMD analysis.

The FFT of the ligament pixel, Figure 5.13(c), shows the bulk of the fluctuations occur at frequencies below 2,000 *Hz*. The largest amplitudes are in a frequency range between 500 and 1,200 *Hz*. This is in the same range as the cluster of ligament frequencies determined by the DMD analysis. The average frequency of this

cluster is about 750 Hz which is near to the 800 Hz mean ligament shedding frequency determined from the ligament wavelength measurements described in Chapter 4. There is an additional large amplitude peak at 1,725 Hz that is in the range of the impact wave frequencies seen on the surface of the sheet.

The commonality between the DMD and FFT results demonstrates that both analysis techniques were able to extract similar frequency ranges for the impact waves on the surface of the sheet and the shed ligaments downstream of the sheet. Additionally, the ligament shedding frequency range determined by both the DMD and FFT analysis are within the frequency range calculated by the ligament wavelength measurements. This similarity provides additional confidence in the dynamic mode results.

5.2.2.2 Like-Doublet: $v_j = 10\ ^m/_s$

The results of the temporal Dynamic Mode Decomposition analysis of the $v_j = 10\ ^m/_s$ test condition is now discussed using both the front-view and side-view data. Figure 5.14 displays plots all of the scaled DMD mode amplitudes as a function of the mode frequency for both the front-view and side-view data sets. Similar with the $v_j = 5\ ^m/_s$ plots discussed in the previous subsection, these plots 'zoom in' on the dynamic modes causing the amplitude of the 0 Hz mean flow mode to be off scale.

Once again, a relatively few large amplitude dynamic modes exist among hundreds of low amplitudes dynamic modes that span the entire frequency range, from 0 Hz to the Nyquist frequency of 10,000 Hz. Both the front-view and side-view plots display high amplitude modes over a wide range of frequencies. From studying

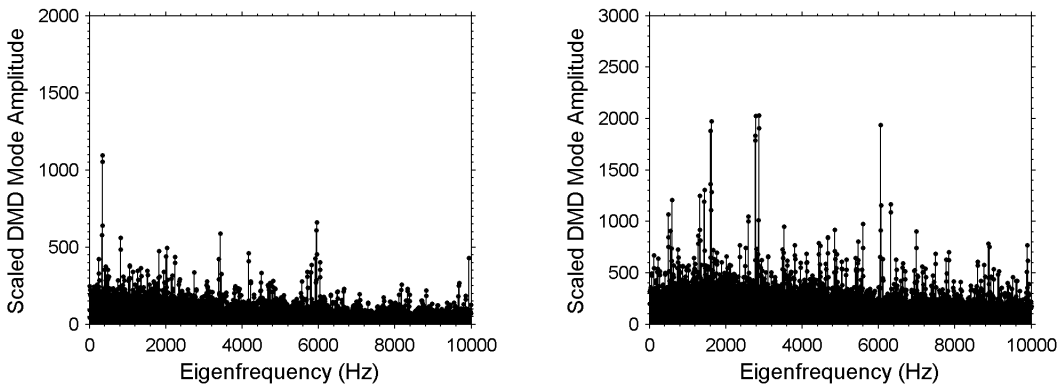

(a) Front View **(b) Side View**

Figure 5.14: Scaled Amplitude Plots: Like-Doublet, $v_j = 10$ $^m/_s$

the contour plots of the high amplitude dynamic modes, it was found that the modes above approximately 2,000 *Hz* represent the variety of impact wave frequencies that are formed from the impingement of two turbulent jets. Referring back to the single jet analysis, Figure 5.2(b) shows that the single jet contained the majority of its high-amplitude dynamic modes between 2,000 and 4,000 *Hz* with the rest at higher frequencies. This corresponds well with the sheet mode frequencies found for the like-doublet spray suggesting that the impact waves depend upon the dynamic content of the two impinging jets. Likewise, the modes with frequencies below 2,000 *Hz* represent the ligaments shed from the sheet and the variation of ligament shedding frequency.

From the results discussed in Chapter 4, it was found that the mean ligament shedding frequency for $v_j = 10$ $^m/_s$, was about 1,350 *Hz* with a standard deviation of about 380 *Hz*. The largest mode within the ligament shedding frequency range is selected from both the front-view and side-view results to represent the ligament

modes. Likewise, the largest mode above 2,500 Hz is selected from both views to represent the impact waves on the surface of the sheet along with the 0 Hz mean flow mode. See Table 5.5 for the scaled amplitude, frequency, and growth rate of the selected dynamic modes for each camera view.

Table 5.5: Temporal DMD Results: Like-Doublet, $v_j = 10$ $^m/_s$

Camera View	Mode Type	Scaled Amplitude	Frequency (Hz)	Growth Rate ($^1/_s$)
Front	Mean Flow	14799	0	-0.04
	Sheet	662	5953	-34.59
	Ligaments	364	1352	-14.33
Side	Mean Flow	22888	0	-0.20
	Sheet	2029	2866	-19.78
	Ligaments	1974	1625	-62.49

Figure 5.15 contains the contour plots for both camera views of the three selected individual dynamic modes plus a composite of all the modes where each individual mode is weighted by its scaled amplitude. The contour plots give spatial information for each mode to complement the temporal information given in Table 5.5. Each plot shows how each mode forms and evolves downstream of the impingement point.

Figure 5.15(a) and (d) contain the mean flow mode for the front and side view data sets. The front-view displays two smooth jets of constant diameter impinging at a 60° angle producing a flat sheet with the edge of the sheet facing the camera. The ligament zone resides in the medium gray region below 30 mm. From the side-view,

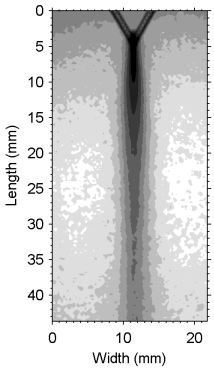

(a) Front Mean Flow: $f = 0$ Hz

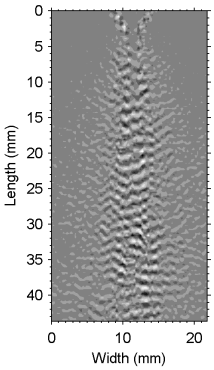

(b) Front Sheet Waves: $f = 5953$ Hz

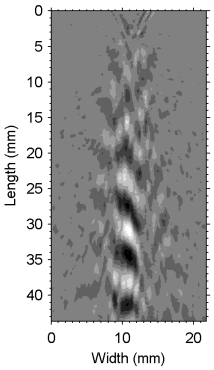

(c) Front Ligaments: $f = 1352$ Hz

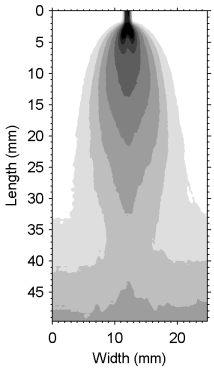

(d) Side Mean Flow: $f = 0$ Hz

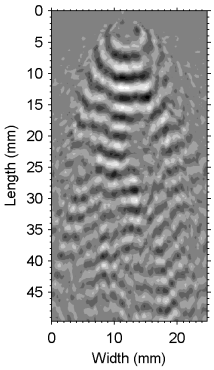

(e) Side Sheet Waves: $f = 2866$ Hz

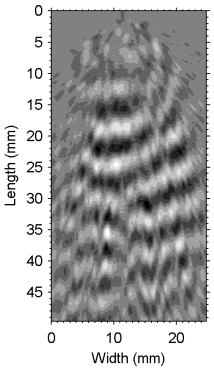

(f) Side Ligaments: $f = 1625$ Hz

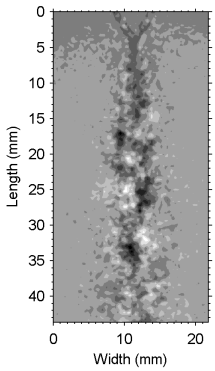

(g) Front Composite

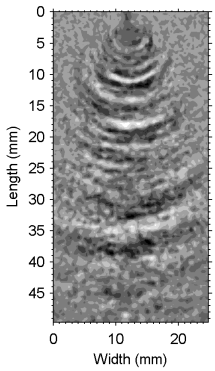

(h) Side Composite

Figure 5.15: Like-Doublet DMD Modes: $v_j = 10$ $^m/_s$

the mean shape of the sheet is once again similar to a leaf. This shape is similar to the mean shape of the $v_j = 5\ ^m/_s$ set point and the shape of a sheet for the closed-rim spray pattern. However, no snapshot of the spray assumes this shape due to the impingement process of two turbulent jets and the distorting and destructive nature of impact waves.

Figure 5.15(b) and (e), displays the sheet modes. In Figure 5.15(e), strong wave structure with a bowed shape emanates from the impingement point and travels down the length of the sheet. The strength of this mode quickly weakens when it reaches the ligament zone indicating that this mode is an impact wave on the surface of the sheet. The wavelength can be determined by measuring the distance between consecutive dark regions. Figure 5.15(b) displays a sheet mode looking at the edge of the sheet. Wave structure is apparent from the impingement point, down the length of the sheet and into the ligament zone. The two impinging jets also display the same wave structure suggesting that this mode originates from the turbulent jets.

Looking at Figure 5.15(c) and (f) show the shapes of the dynamic modes representing the ligaments shed from the end of the sheet. Figure 5.15(c), shows alternating bands of dark and light regions in the ligament zone with strong intensity. Very little of this mode extends into the flat sheet region clearly demonstrating that this mode characterizes the ligament shedding. Figure 5.15(f) shows the side-view of the ligament modes. This mode displays high intensity bands of bowed ligaments starting from the bottom of the sheet and continuing through the entire ligament zone.

The composite plots are seen in Figure 5.15(g) and (h). The front-view shows the two turbulent jets impinging and forming a very sinuous flat sheet. The isolated dark region below the sheet represents a shed ligament. The side-view displays a flat sheet distorted by large impact waves of varying wavelengths. Downstream of the sheet, separated dark regions represent the bowed ligaments shed from the end of the sheet. The composite plots were able to construct an image that is very similar to a still image of the spray from both camera angles.

Once again, a comparison is made between the temporal DMD analysis of the side-view video file with the FFT of the pixel intensity fluctuations for two pixel locations. The pixel locations are chosen so one resides within the flat sheet and the other within the ligament zone. Figure 5.16(a) shows the locations of the two pixels analyzed, where pixel 1 is the sheet pixel and pixel 2 is the ligament pixel. Figure 5.16(b) and (c) display the FFTs of the sheet and ligament zones respectively. The amplitude of the FFT is the power spectrum and is equal to the root mean square (rms) value of the pixel intensity fluctuations squared.

The FFT of the sheet pixel, Figure 5.16(b), shows a cluster of high amplitude frequency content between roughly 1,800 Hz and 4,800 Hz. Likewise, the DMD analysis displayed large amplitude modes at 1,800 Hz, 2,800 Hz, and 6,000 Hz, see Figure 5.14(b). The lower frequency 1,800 Hz peak corresponds well with the upper limit of the ligament shedding frequency while the cluster of frequencies between 2,000 Hz and 5,000 Hz correspond with the range of impact wave frequencies present on the surface of the sheet as determined by the DMD analysis.

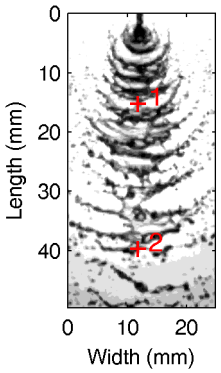

(a) Pixel Locations

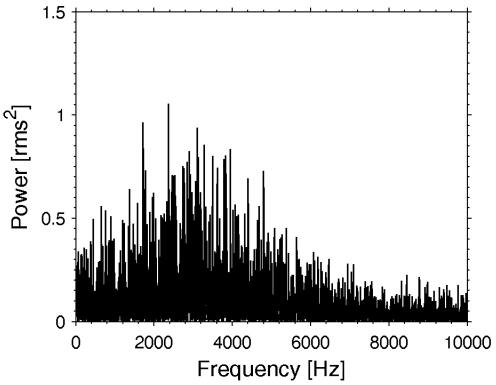

(b) Pixel 1: Sheet Region

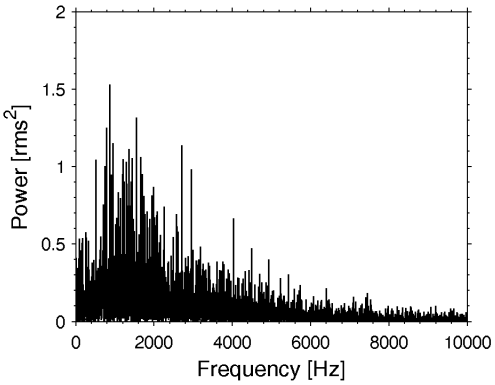

(c) Pixel 2: Ligament Region

Figure 5.16: Pixel FFT: $v_j = 10\ ^m/_s$

The FFT of the ligament pixel, Figure 5.16(c), shows the bulk of the fluctuations occur at frequencies below 3,000 *Hz*. The largest amplitudes are in a frequency range between 800 and 2,800 *Hz*. This range is similar with the range of ligament shedding frequencies determined by both the DMD analysis and ligament wavelength measurements described in Chapter 4. The average frequency of this cluster is about 1,400 *Hz* which is about equal to the mean ligament shedding frequency determined from the ligament wavelength measurements.

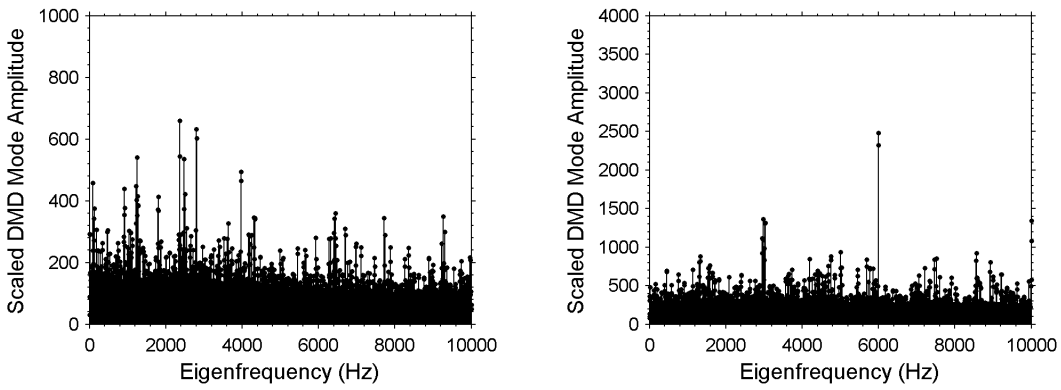

(a) Front View **(b) Side View**

Figure 5.17: Scaled Amplitude Plots: Like-Doublet, $v_j = 20$ $^m/_s$

The frequency ranges of both the impact waves and ligaments were very similar between the results of the DMD analysis and FFT analysis. In addition, the mean ligament shedding frequency was found to be equal with the frequency determined by the ligament wavelength measurements. This increases confidence in the results as three different techniques arrived at similar conclusions.

5.2.2.3 Like-Doublet: $v_j = 20$ $^m/_s$

This subsection will describe the results of the temporal Dynamic Mode Decomposition analysis of the $v_j = 20$ $^m/_s$ test condition. Figure 5.17 displays plots all of the scaled DMD mode amplitudes as a function of the mode frequency for both the front-view and side-view data sets. The amplitude of the 0 Hz mean flow mode is off the scale and not visible.

From the amplitude plots, it is seen that hundreds of low amplitudes dynamic modes span the entire frequency range, from 0 Hz to the Nyquist frequency of

10,000 *Hz* while a relatively few high amplitude modes are dispersed over a wide frequency range. The side-view plot displays two major mode regions, a group of high amplitude modes clustered around 3,000 *Hz* and a couple of large modes at about 6,000 *Hz*. From studying the contour plots of the high amplitude dynamic modes, it was found that the modes above approximately 4,500 *Hz* represent the variety of impact wave frequencies that are formed from the impingement of two turbulent jets. Likewise, the modes with frequencies below 4,500 *Hz* represent the variation of ligament shedding frequency. The single jet at this velocity also displayed high-amplitude dynamic modes in this frequency range with the two largest at about 5,300 and 3,200 *Hz*. This similarity suggests that dynamic content of the like-doublet spray is greatly influenced by the dynamic content within the two impinging jets.

From the results discussed in Chapter 4, it was found that the mean ligament shedding frequency for $v_j = 20$ $^m/_s$, was about 3,000 *Hz* with a standard deviation of about 720 *Hz*. The ligament shedding frequency with the largest amplitude is selected from both the front-view and side-view results to represent the ligament modes. Likewise, the largest mode above 4,500 *Hz* is selected from both views to represent the impact waves on the surface of the sheet. Additionally, the 0 *Hz* mean flow mode is selected. See Table 5.6 for the scaled amplitude, frequency, and growth rate of the selected dynamic modes for each camera view.

Table 5.6: Temporal DMD Results: Like-Doublet, $v_j = 20$ $^m/_s$

Camera View	Mode Type	Scaled Amplitude	Frequency (Hz)	Growth Rate ($^1/_s$)
Front	Mean Flow	12818	0	0.16
	Sheet	359	6446	-106.47
	Ligaments	632	2803	-187.86
Side	Mean Flow	19753	0	0.21
	Sheet	2479	5994	-24.10
	Ligaments	1363	2984	-38.68

See Figure 5.18 for the contour plots of the three selected individual dynamic modes plus a composite of all the modes where each individual mode is weighted by its scaled amplitude for both camera angles. These contour plots give the spatial information of each selected mode to complement the calculated temporal information given in Table 5.6. From these plots, information of how each mode forms and evolves spatially can be observed.

The mean flow mode can be seen in Figure 5.18(a) and (d) for the front and side-view data sets. The front-view displays two smooth jets of constant diameter impinging at a 60° angle producing a flat sheet with the edge of the sheet facing the camera. The length of the flat sheet is shorter when compared with the $v_j = 5$ $^m/_s$ and 10 $^m/_s$ cases, agreeing with the sheet breakup length results described in Chapter 4. The ligament zone resides in the light gray regions below 25 mm. From the side-view, the mean shape of the sheet is once again leaf-like similar to the lower jet velocity results. However, the shape is broader which takes into account both the increased

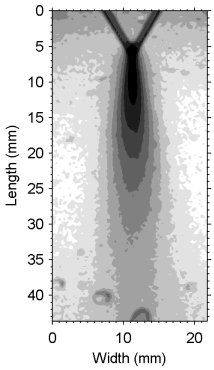

(a) Front Mean Flow: $f = 0$ Hz

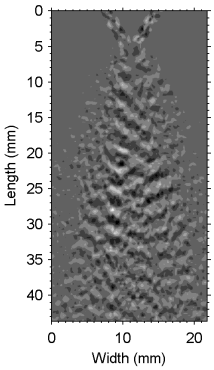

(b) Front Sheet Waves: $f = 6446$ Hz

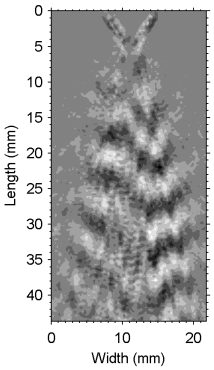

(c) Front Ligaments: $f = 2803$ Hz

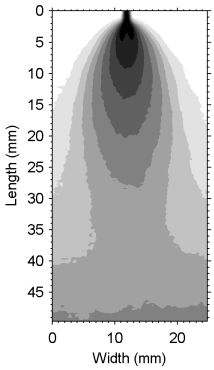

(d) Side Mean Flow: $f = 0$ Hz

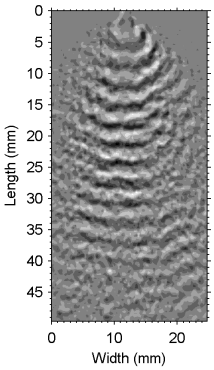

(e) Side Sheet Waves: $f = 5994$ Hz

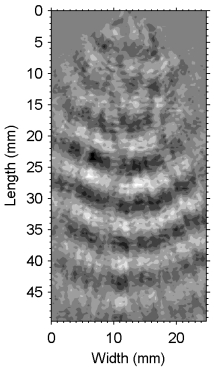

(f) Side Ligaments: $f = 2984$ Hz

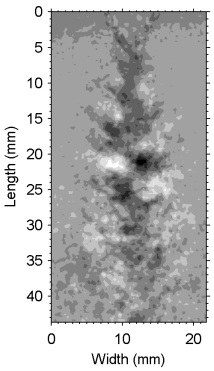

(g) Front Composite

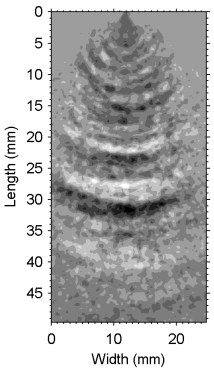

(h) Side Composite

Figure 5.18: Like-Doublet DMD Modes: $v_j = 20$ $^m/_s$

width of the sheet and the increased numbers of droplets shed from the periphery of the sheet. At any one instant of time, the spray does not assume a leaf shape due to the violent impingement process of two turbulent jets and the destructive nature of impact waves.

The spatial sheet modes are displayed in Figure 5.18(b) and (e). In Figure 5.18(e), strong wave structure with a bowed shape emanates from the impingement point and travels down the length of the sheet. The strength of this mode quickly weakens when it reaches the ligament zone indicating that this mode describes a distinct impact wave on the surface of the sheet. Figure 5.18(b) displays a sheet mode looking at the edge of the sheet. Wave structure is apparent from the impingement point, down the length of the sheet and into the ligament zone where it quickly weakens. This mode is also present on the two impinging jets, indicating that impact waves are formed by the disturbances and distortions of the two jets.

The dynamic modes representing the ligaments are seen in Figure 5.18(c) and (f). Figure 5.18(f), shows strong structure from the bottom region of the sheet through the end of the image. This mode has only weak wave structure in the flat sheet region clearly demonstrating that this mode characterizes the bowed ligament shed from the bottom of the sheet. Figure 5.18(c) shows the front-view of the ligament mode. This mode also displays high intensity bands of ligaments starting near the bottom of the sheet and propagating through the entire ligament zone. Weak wave structure is seen in the upper half of the sheet and very little structure is seen on the jets.

The composite plots are seen in Figure 5.18(g) and (h). The front-view plot shows two turbulent jets impinging and forming a sinuous flat sheet. The isolated dark regions below the sheet represents the shed ligaments. The side-view plot displays a flat sheet distorted by large impact waves of varying wavelengths. Downstream of the breakup length of the sheet, separated bands of bowed ligaments are visible. From these two composite plots, it is apparent that DMD has the ability to determine a finite number of dynamic modes that characterize the shape and breakup process of like-doublet impinging injectors.

Finally, a FFT of the pixel intensity fluctuations for two pixel locations are calculated and compared with results of the DMD analysis of the side-view video file. The pixel locations are chosen to reside in either the flat sheet or ligament zone. Figure 5.19(a) shows the locations of the two pixels analyzed, where pixel 1 is the sheet pixel and pixel 2 is the ligament pixel. Figure 5.19(b) and (c) display the FFTs of the sheet and ligament zones respectively. The amplitude of the FFT corresponds with the power spectrum and is equal to the root mean square (rms) value of the pixel intensity fluctuations squared.

The FFT of the sheet pixel, Figure 5.19(b), shows a broad range of high amplitude frequency content between roughly 3,800 Hz and 9,000 Hz. The DMD analysis displayed a large amplitude mode at 3,000 Hz and 6,000 Hz, see Figure 5.17(b). The 3,000 Hz mode in the DMD analysis corresponded with the ligaments while the 6,000 Hz peak was an impact wave mode. The range of high frequency content in the FFT is indicative of the range of impact wave frequencies that exist on the flat sheet. The average frequency of the high amplitude peaks is

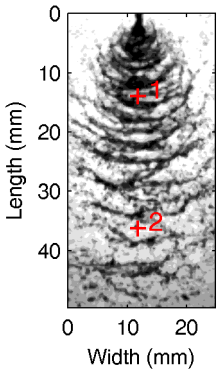

(a) Pixel Locations

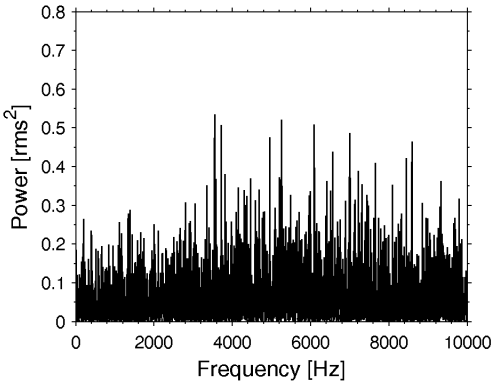

(b) Pixel 1: Sheet Region

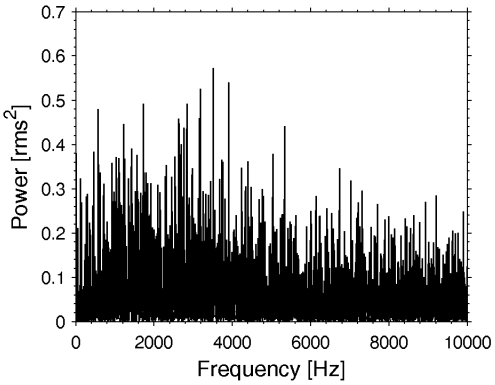

(c) Pixel 2: Ligament Region

Figure 5.19: Pixel FFT: $v_j = 20\ ^m/_s$

5,100 *Hz* which is near the frequency of the sheet mode determined from the DMD analysis.

The FFT of the ligament pixel, Figure 5.19(c), shows the largest dynamic content to be shifted to frequencies below 4,500 *Hz*. The largest amplitudes are in a frequency range between 1,800 and 4,000 *Hz*. This is the expected range of ligament shedding frequencies. The mean frequency of this cluster is approximately 3,000 *Hz*. This result is equal to the frequency of the dominant ligament mode found with

the DMD analysis and with the shedding frequency determined by measuring the ligament wavelengths as described in Chapter 4.

The frequency distributions for the impact waves and ligaments were found to be reproducible between the DMD analysis and FFT analysis. This result demonstrates that the FFT was able to pick-up the range of impact wave frequencies present on the sheet and the average value is similar with the dominant DMD sheet mode frequency. Also, the similar mean ligament shedding frequencies were determined from the FFT spectrum, DMD analysis and the wavelength measurements demonstrating that all three analysis techniques converged to a common result.

5.2.3 Feed System Coupling

Similar with the single jet experiments, the like-doublet tests exhibited feedline oscillations with peak frequencies at 3,200 *Hz* and 3,700 *Hz*, refer to Figure 5.6. These fluctuations are small for the $v_j = 5\ {}^{m}/_{s}$ case and increase in amplitude proportionally with the increase of jet velocity. As determined by Section 5.1.3, the detected oscillations are caused by a resonant standing wave within the feedline between the injector entrance and the opening of the transducer cross as well as a second standing wave within the injector tube itself. Feed system coupling was shown to exist between the liquid jet and the feed system resonances.

Likewise, an analysis of the DMD results will help determine if feed system coupling affects the like-doublet spray. Studying Figure 5.11 shows that a cluster of dynamic modes exist in the range between 3,000 and 4,000 *Hz*. These modes present themselves on the surface of the sheet highlighting that feed system coupling produces

disturbances on the two jets which translates into impact waves on the sheet. The feed system coupling modes do not have the greatest affect on the spray due to the relatively low amplitudes of the acoustic resonances at $v_j = 5\ {}^{m}/_{s}$.

For the $v_j = 10\ {}^{m}/_{s}$ cases, high amplitude dynamic modes are seen in the range between 2,800 and 4,000 Hz in Figure 5.14. These modes are close to the frequency range expected from feed system coupling. In addition, these modes are some of the dominant dynamic modes and present themselves on the surface of the sheet. This is similar with the single jet condition where the dominant modes on the jet were caused by feed system coupling. This provides additional evidence that the impact waves formed on the flat sheet are caused by the disturbances present on the two impinging jets.

Finally, Figure 5.17 shows that high amplitude modes exist in the $v_j = 20\ {}^{m}/_{s}$ spray in the frequency range expected for feed system coupling. However, the modes at this frequency range happen to coincide with the range of shedding frequencies for the ligaments detached from the end of the sheet. This is an interesting result as it could be reasoned that the ligaments would shed from the sheet in periodic intervals with a smaller standard deviation when the feed system coupling frequency coincides with the natural range of ligament shedding frequencies. However, the results presented in Chapter 4 demonstrate that the mean ligament wavelength is equal for all jet velocities and impingement angles tested. The standard deviation of the measured ligament wavelengths did not reduce when $v_j = 20\ {}^{m}/_{s}$, see Table B.1, Table B.2, and Table B.3 located in Appendix B. Therefore from these results, feed system coupling doesn't seem to have an influence on the shed ligaments and is limited

to distorting the flat sheet as part of the wide range of impact waves on the surface of the sheet.

The result of feed system coupling affecting the dynamics of the jet and sheet is similar with the experience of Ramamurthi et al. [68]. Their research tested like-doublet injectors in both non-cavitating and cavitating flow conditions and measured the frequency content of the spray with a microphone. Their results showed that the higher frequency content in the spray was caused by resonant standing waves in the feed system. The peak frequency in both the feed system and spray did not change with the range of Reynolds numbers tested similar with the results described in this section.

CHAPTER 6

CONCLUSION

6.1 Summary of Results

A set of cold flow injector spray experiments were conducted to study the primary atomization characteristics of like-doublet impinging jet injectors. The research program was split into two parts. The first part studied how varying the jet breakup length to impingement distance ratio affects the primary atomization characteristics of like-doublets. The second part conducted an analysis of the impingement process and primary atomization zone of the like-doublet injector spray using Dynamic Mode Decomposition (DMD). A more in-depth summary of the results are given in the following subsections.

6.1.1 Part 1: The Effects of Varying the Impingement Distance for Like-Doublet Injectors

Part 1 of the research program systematically investigated the primary atomization characteristics of like-doublet impinging injectors when the jet breakup length to impingement distance ratio (l_b/l_i) is varied. The impingement distance was varied to test the injector at four different l_b/l_i ratios: $l_b/l_i = 2$, $l_b/l_i = 1.5$, $l_b/l_i = 1$,

and $l_b/l_i = 0.5$. Each l_b/l_i ratio was tested with four jet velocities (5 m/s, 10 m/s, 15 m/s, and 20 m/s) and three impingement angles (30°, 60°, and 90°).

The single jet test series was used to determine the jet breakup length as a function of jet velocity. The experiment found that the average breakup length of the jet increased with jet velocity and the breakup characteristics followed the turbulent primary breakup process. The turbulent jet was characterized by a mix of serpentine and axisymmetric disturbances caused by the motion of the turbulent eddies within the jet and surface tension which initiated the breakup process. Droplets were formed from these disturbances by surface tension and were shed from the end of the jet. The results were found to agree with the existing empirical turbulent jet breakup length correlations of Grant and Middleman [45] as well as Wu and Faeth [41].

For the like-doublet test series, it was found that the l_b/l_i ratio had a large effect upon the resulting spray characteristics. For $l_b/l_i \geq 1.5$, the impingement process produced a flat sheet distorted by impact waves that disintegrated into waves of ligaments and droplets. Two distinct breakup modes were detected. At low to moderate jet Weber numbers, the sheet disintegrated into ligaments and droplets in a ruffled-sheet breakup mode where the sheet breakup length increased with jet Weber number up to a transition point. Beyond the transition point, the breakup mode became fully-developed and the breakup length decreased with further increases of jet Weber number. The transition Weber number was solely a function of the impingement angle. The sheet breakup length and breakup characteristics were unaffected by the l_b/l_i ratio when $l_b/l_i \geq 1.5$. New empirical sheet breakup correlations were developed for this configuration.

The results show that the l_b/l_i ratio has a profound effect on the primary atomization process when the breakup lengths of the impinging jets are about equal to the impingement distance and when the jet breakup length is shorter than the impingement distance. When the impingement distance was increased so that $l_b/l_i = 1$, an unsteady flat sheet arose which formed and then intermittently segmented when one or both of the impinging jets disintegrated prior to reaching the impingement point. The same two breakup modes described for ratios greater than 1.5 were observed and separate empirical sheet breakup length correlations were developed. The presence of an unsteady flat sheet and impingement process could result in a spray that is particularly sensitive to combustion chamber disturbances, leading to atomization and heat release characteristics that fluctuate and/or respond to these disturbances. This process can make an engine susceptible to combustion instability as suggested by Chehroudi [36].

For $l_b/l_i < 1$, no flat sheet was formed. Instead the vast majority of the large droplets detached from the ends of the impinging jets passed through the impingement point. Intermittent droplet collisions did occur at the impingement point, which produced a shower of small droplets down the centerline of the spray. Injectors operating under this type of condition in a rocket engine will likely have poor atomization and mixing characteristics.

The mean wavelength between the ligaments shed from the end of the sheet were found to be nearly constant at about six orifice diameters for all jet velocities and impingement angles when $l_b/l_i \geq 1$. However, the waves of ligaments and droplets were shed at a range of wavelengths about a constant mean value. The mean ligament

shedding frequency was proportional to jet velocity and was shown to be near to and parallel with the threshold of the Hewitt stability correlation. This suggests that the primary atomization process and the ligament shedding frequency might be an important mechanism in the excitation of combustion instability. This observation calls for a more detailed investigation to validate the link.

Mean droplet diameters and droplet diameter distributions were dependent upon impingement angle and jet Weber number. In general, larger impingement angles and Weber numbers corresponded with smaller mean droplet diameters as well as reduced spray polydispersity. The mean droplet diameter was found to be independent of the l_b/l_i ratio when $l_b/l_i \geq 1$. An empirical numerical mean droplet diameter correlation was developed from the collected data. The combination of smaller droplets and reduced spray polydispersity as the Weber number and impingement angle is increased can result in the heat release due to combustion to be concentrated near the injector face which can lead to cooling problems and an engine more susceptible to combustion instability [4].

6.1.2 Part 2: A Visual and DMD Analysis of the Turbulent Jet and Like-Doublet Spray

Part 2 of the research program analyzed the turbulent jets and the primary atomization zone of like-doublet injector sprays using Dynamic Mode Decomposition (DMD). Similar to Part 1, the experiment was divided into single jet and like-doublet test programs. For the single jet and like-doublet tests, the injector was operated at

three jet velocities: 5, 10, and 20 $^{m}/_{s}$. The like-doublet injector had a set impingement angle of 60° and was operated at a constant $^{l_b}/_{l_i}$ ratio of two.

DMD analysis of the turbulent jets showed that the dynamics of the jet were characterized by a few high amplitude modes embedded within a broad spectrum of low amplitude modes that spanned the entire frequency range considered. Most of these high amplitude modes formed axisymmetric disturbances down the length of the jet. A few however, formed sinuous disturbances that gradually evolved into axisymmetric disturbances as surface tension became more dominate in the breakup process down the length of the jet. Also, the jets contained dynamic modes with frequencies equal to the resonant frequencies of the injector and feedline demonstrating that feed system coupling can influence the dynamics of the liquid jet.

The like-doublet primary atomization process was characterized by the use of front-view and side-view camera angles. The side-view configuration had the camera looking directly at the face of the sheet. The videos showed a flat sheet formed by jet impingement that was distorted by impact waves of varying wavelengths. Droplets were shed from the periphery of the sheet while waves of bowed ligaments are shed from the bottom of the sheet. The ligaments were shed at varying wavelengths and subsequently disintegrated into droplets downstream. The front-view configuration had the camera looking at the edge of the sheet and observed both impinging jets. The videos showed the two turbulent jets forming a serpentine-like flat sheet that disintegrated into ligaments and droplets.

Impact waves were observed to form from the local momentum imbalance between the two impinging jets at the impingement point. Jet momentum is not

constant along the length of a turbulent jet as the jet is characterized by many protuberances and bulges causing the jet to have slight variability of mass along its length. Impact waves form when the momentum of the two jets towards each other is not canceled, causing the sheet to distort in the direction of travel of the jet with the greater momentum. Surface tension of the liquid holds the sheet together for a brief period of time before the sheet disintegrates into ligaments and droplets.

The DMD analysis of the spray showed that the spray was characterized by a relatively few high amplitude modes embedded within hundreds of broadband low amplitude modes that spanned the entire frequency range. The high amplitude modes were spread over a wide range of frequencies. From the contour plots of the dynamic modes, it was determined that the higher frequency modes correspond with the impact waves on the surface of the sheet while the lower frequency modes correspond with the range of ligament shedding frequencies.

The DMD modes corresponding with the impact waves exhibited modal structure on both the sheet and the two impinging jets lending further evidence to the source of impact waves originating with the two turbulent jets. The combined observational evidence and DMD results provide a compelling argument that impact waves are a purely hydrodynamic phenomenon caused by the local momentum imbalance between the two jets at the impingement point. Also, the frequency of several DMD modes at each test condition were found to equal the resonant frequency of the injector and feedline demonstrating that feed system coupling can propagate to the jet and sheet.

In addition, the scaled dynamic mode amplitude plots showed a clustering of modes in the frequency range of the measured ligament shedding frequency determined in Part 1 of the research program. Contour plots of these modes displayed strong wave structure extending from the bottom of the sheet through the ligament zone. This demonstrated that DMD is able to determine where both impact waves and ligaments form within the spray.

Composite contour plots of all the calculated dynamic modes weighted by their scaled amplitudes were created. These composite plots presented a contour of the spray pattern that was remarkably similar to a high-speed photograph of the spray. This exemplified the power that DMD has in being able to extract a finite number of dynamic modes that characterize the complex impingement and breakup process of the like-doublet spray.

Finally, an FFT analysis of two pixel locations was conducted for the side-view video files. The pixels were located along the centerline of the spray with one at the midpoint of the sheet and the other within the ligament zone. The sheet FFTs displayed a range of high-amplitude frequency content that was similar with the impact wave modes determined from the DMD analysis. The ligament FFTs displayed a cluster of frequencies that spanned the range of ligament shedding frequencies determined by both the DMD analysis and the calculated frequencies from the ligament wavelength measurements described in Part 1 of the research project. The similarity of the results from all three techniques increases the confidence that the primary atomization characteristics were captured with the DMD technique.

6.2 Future Work

The cold-flow experiments described in this dissertation tested the injector at atmospheric pressure using water as the propellant simulant. The physical properties varied in the experiment were the impingement angle, impingement distance, and jet velocity. The orifice diameter of the injector remained constant for all of the experiments.

Therefore, follow on work should test the like-doublet injector at the same jet Weber numbers but with different orifice diameters and with different liquids. This would help determine the effect the injector diameter has on the sheet breakup length, ligament wavelengths, and mean droplet diameter. In addition, experimenting with various fluids will aid in determining which fluid properties (viscosity, surface tension, etc.) are most important in the atomization behavior of impinging jet injectors. This could lead to empirical correlations that are accurate for a wide range of injector designs and propellant options.

Also, liquid rocket engines operate at high pressures with some operating in the supercritical regime. Future research should test the injector at elevated pressures and compare the results with those found at atmospheric pressure. It would be particularly interesting to see how the breakup characteristics change when the operating conditions transition from subcritical to the supercritical regime.

Finally, rocket engines using impinging injectors have been susceptible to combustion instability. It is still an open question how the spray responds to acoustic waves and/or mechanical excitation particularly when the jet breakup length

approaches the impingement distance. Therefore, cold-flow experiments that excite the spray with standing transverse acoustic waves and/or mechanically vibrate the injector assembly over a range of frequencies similar to those encountered in liquid rocket engines can be beneficial in determining how the injector responds and the spray pattern changes when exposed to these types of disturbances.

APPENDICES

APPENDIX A

TEST CONDITIONS

A.1 Part 1: The Effects of Varying the Impingement Distance for Like-Doublet Injectors

A.1.1 Single Jet Experiments

Table A.1: Single Jet Test Conditions, Orifice 1

Set Point	v_j (m/s)	$\dot{m}$ (g/s)	ΔP_{inj} (bar)	T_{liq} (K)	Re –	We –
1	5.2	4.2	1.14	292	5012	380
2	10.0	8.1	3.65	292	9626	1403
3	15.1	12.2	7.51	292	14458	3151
4	20.1	16.3	12.68	292	19317	5609

Table A.2: Single Jet Test Conditions, Orifice 2

Set Point	v_j (m/s)	$\dot{m}$ (g/s)	ΔP_{inj} (bar)	T_{liq} (K)	Re –	We –
1	5.0	4.1	1.05	292	4812	350
2	10.1	8.2	3.68	291	9569	1421
3	15.0	12.1	7.57	291	14033	3125
4	20.0	16.2	12.75	290	18574	5563

A.1.2 Like-Doublet Experiments

Table A.3: Like-Doublet Test Conditions for Each Orifice, $l_b/l_i = 2$

2θ (deg)	Set Point	v_j (m/s)	$\dot{m}$ (g/s)	ΔP_{inj} (bar)	T_{liq} (K)	Re –	We –
30°	1	5.17	4.19	1.11	293	5081	373
	2	10.02	8.11	3.61	292	9635	1398
	3	15.05	12.18	7.53	292	14702	3152
	4	19.97	16.17	12.60	291	18786	5538
60°	5	5.31	4.30	1.16	294	5402	394
	6	10.10	8.17	3.66	292	9696	1417
	7	14.99	12.14	7.47	291	14235	3123
	8	20.01	16.20	12.65	291	18807	5558
90°	9	5.04	4.08	1.10	288	4395	351
	10	10.02	8.11	3.61	292	9615	1395
	11	15.09	12.21	7.61	291	14312	3163
	12	19.89	16.10	12.56	291	18710	5491

Table A.4: Like-Doublet Test Conditions for Each Orifice, $l_b/l_i = 1.5$

2θ (deg)	Set Point	v_j (m/s)	$\dot{m}$ (g/s)	ΔP_{inj} (bar)	T_{liq} (K)	Re –	We –
30°	13	4.97	4.02	1.03	292	4814	343
	14	10.23	8.28	3.77	291	9735	1455
	15	14.96	12.11	7.49	291	14093	3109
	16	20.02	16.21	12.73	291	18685	5560
60°	17	4.95	4.01	1.03	292	4806	341
	18	10.09	8.17	3.69	291	9617	1415
	19	14.98	12.13	7.50	291	14112	3116
	20	19.95	16.15	12.62	291	18651	5524
90°	21	5.05	4.09	1.07	292	4883	355
	22	10.04	8.13	3.63	291	9564	1401
	23	14.93	12.09	7.48	291	14048	3096
	24	20.01	16.20	12.67	291	18709	5557

Table A.5: Like-Doublet Test Conditions for Each Orifice, $l_b/l_i = 1$

2θ (deg)	Set Point	v_j (m/s)	$\dot{m}$ (g/s)	ΔP_{inj} (bar)	T_{liq} (K)	Re –	We –
30°	25	4.99	4.04	1.04	292	4857	347
	26	10.02	8.10	3.55	295	10413	1403
	27	14.96	12.11	7.49	291	14216	3110
	28	20.08	16.27	12.94	286	16804	5553
60°	29	5.07	4.11	1.08	292	4938	358
	30	9.98	8.08	3.61	292	9590	1386
	31	15.18	12.29	7.66	291	14412	3202
	32	19.92	16.13	12.61	291	18736	5512
90°	33	5.10	4.13	1.09	292	4965	363
	34	10.21	8.26	3.69	295	10527	1458
	35	15.13	12.25	7.65	291	14374	3182
	36	19.95	16.15	12.60	291	18754	5525

Table A.6: Like-Doublet Test Conditions for Each Orifice, $l_b/l_i = 0.5$

2θ (deg)	Set Point	v_j (m/s)	$\dot{m}$ (g/s)	ΔP_{inj} (bar)	T_{liq} (K)	Re –	We –
30°	37	5.19	4.20	1.15	287	4454	371
	38	10.29	8.34	3.88	288	8921	1463
	39	15.24	12.34	7.48	288	13350	3208
	40	19.98	16.18	13.00	286	16708	5495
60°	41	5.01	4.06	1.08	287	4308	347
	42	9.97	8.08	3.70	287	8577	1372
	43	15.91	12.89	7.64	288	13941	3498
	44	19.87	16.10	12.84	286	16593	5436
90°	45	4.99	4.04	1.08	287	4270	344
	46	10.33	8.37	3.94	287	8750	1471
	47	15.07	12.20	7.57	292	14727	3163
	48	19.86	16.09	12.71	286	16423	5429

A.2 Part 2: A Dynamic Mode Decomposition Analysis of the Like-Doublet Spray

A.2.1 Single Jet Experiments

Table A.7: Single Jet Test Conditions (DMD Experiment)

Set Point	v_j $(^m/_s)$	$\dot{m}$ $(^g/_s)$	ΔP_{inj} (bar)	T_{liq} (K)	Re –	We –
1	4.90	3.97	1.02	290	4467	332
2	10.00	8.10	3.64	289	8985	1383
3	20.01	16.21	12.86	288	17549	5533

A.2.2 Like-Doublet Experiments

Table A.8: Like-Doublet Test Conditions for Each Orifice, Side View (DMD Experiment)

2θ (deg)	Set Point	v_j $(^m/_s)$	$\dot{m}$ $(^g/_s)$	ΔP_{inj} (bar)	T_{liq} (K)	Re –	We –
60°	1	5.21	4.22	1.16	290	4740	376
	2	10.04	8.13	3.70	289	9005	1396
	3	20.01	16.20	12.91	288	17487	5528

Table A.9: Like-Doublet Test Conditions for Each Orifice, Front View (DMD Experiment)

2θ (deg)	Set Point	v_j $(^m/_s)$	$\dot{m}$ $(^g/_s)$	ΔP_{inj} (bar)	T_{liq} (K)	Re –	We –
60°	4	5.05	4.09	1.08	290	4608	353
	5	9.87	7.99	3.56	290	8985	1350
	6	20.07	16.25	12.91	289	17830	5569

APPENDIX B

LIKE-DOUBLET SHEET BREAKUP LENGTH & LIGAMENT WAVELENGTH RESULTS

Table B.1: Breakup Length & Wavelength Results, $l_b/l_i = 2$

2θ (deg)	Set Point	v_j (m/s)	v_{ax} (m/s)	l_s/d_o –	λ_l/d_o –	F_{atom} (Hz)
30°	1	5.17	5.2 ± 1.3	23.1 ± 3.4	5.84 ± 1.15	870 ± 179
	2	10.02	9.6 ± 1.3	32.1 ± 5.3	6.57 ± 1.65	1434 ± 385
	3	15.05	13.9 ± 1.4	37.9 ± 5.0	6.15 ± 1.24	2222 ± 469
	4	19.97	18.5 ± 1.8	40.3 ± 4.8	5.59 ± 1.04	3257 ± 627
60°	5	5.31	4.8 ± 1.2	16.4 ± 3.3	5.94 ± 1.29	795 ± 181
	6	10.10	8.6 ± 1.7	24.3 ± 3.7	6.06 ± 1.30	1397 ± 314
	7	14.99	12.6 ± 2.0	24.5 ± 3.3	6.18 ± 1.54	2000 ± 532
	8	20.01	17.0 ± 2.4	22.0 ± 2.6	5.61 ± 1.42	2989 ± 811
90°	9	5.04	4.4 ± 0.7	14.4 ± 3.0	5.51 ± 1.39	793 ± 213
	10	10.02	7.4 ± 1.7	17.6 ± 2.7	5.91 ± 1.88	1230 ± 435
	11	15.09	12.5 ± 1.7	15.5 ± 2.7	6.18 ± 1.69	1985 ± 585
	12	19.89	16.6 ± 2.1	12.5 ± 2.8	5.93 ± 1.46	2752 ± 719

Table B.2: Breakup Length & Wavelength Results, $l_b/l_i = 1.5$

2θ (deg)	Set Point	v_j (m/s)	v_{ax} (m/s)	l_s/d_o –	λ_l/d_o –	F_{atom} (Hz)
30°	13	4.97	5.0 ± 1.5	21.9 ± 3.1	5.87 ± 1.07	842 ± 159
	14	10.23	9.7 ± 1.2	31.7 ± 6.9	5.41 ± 1.74	1771 ± 636
	15	14.96	14.0 ± 1.4	35.5 ± 5.8	5.66 ± 1.55	2435 ± 723
	16	20.02	18.6 ± 1.7	40.0 ± 6.6	6.18 ± 1.45	2960 ± 733
60°	17	4.95	4.7 ± 1.1	15.4 ± 3.1	5.75 ± 1.71	795 ± 259
	18	10.09	8.8 ± 1.2	25.0 ± 4.3	6.41 ± 1.67	1346 ± 375
	19	14.98	12.6 ± 0.9	25.3 ± 3.6	5.95 ± 1.67	2091 ± 636
	20	19.95	17.2 ± 2.1	22.4 ± 2.8	6.09 ± 1.43	2779 ± 691
90°	21	5.05	4.1 ± 0.9	13.7 ± 2.7	5.96 ± 1.10	680 ± 130
	22	10.04	8.2 ± 1.1	17.4 ± 2.2	5.63 ± 1.52	1425 ± 416
	23	14.93	12.3 ± 1.7	15.1 ± 2.4	6.41 ± 1.73	1892 ± 552
	24	20.01	16.7 ± 2.1	12.7 ± 2.0	6.43 ± 1.76	2562 ± 759

Table B.3: Breakup Length & Wavelength Results, $l_b/l_i = 1$

2θ (deg)	Set Point	v_j (m/s)	v_{ax} (m/s)	l_s/d_o –	λ_l/d_o –	F_{atom} (Hz)
30°	25	4.99	4.9 ± 1.1	10.6 ± 4.7	5.65 ± 1.23	859 ± 196
	26	10.02	9.4 ± 0.9	20.5 ± 7.1	5.69 ± 1.61	1632 ± 500
	27	14.96	14.0 ± 1.6	27.4 ± 7.7	6.02 ± 1.60	2288 ± 653
	28	20.08	18.5 ± 1.8	30.8 ± 7.5	5.40 ± 1.19	3373 ± 781
60°	29	5.07	4.5 ± 1.1	11.7 ± 3.6	5.57 ± 1.46	802 ± 226
	30	9.98	8.4 ± 1.6	20.2 ± 3.9	5.57 ± 1.31	1489 ± 370
	31	15.18	12.9 ± 1.8	23.6 ± 4.5	6.89 ± 1.61	1846 ± 456
	32	19.92	16.0 ± 3.0	21.3 ± 2.9	5.55 ± 1.15	2830 ± 613
90°	33	5.10	3.7 ± 1.2	13.5 ± 3.8	5.15 ± 0.85	703 ± 119
	34	10.21	8.2 ± 1.1	15.6 ± 3.6	6.00 ± 2.51	1352 ± 688
	35	15.13	10.8 ± 2.7	15.4 ± 2.8	6.19 ± 1.28	1710 ± 370
	36	19.95	16.6 ± 2.2	12.9 ± 2.3	5.47 ± 1.12	2992 ± 641

APPENDIX C

LIKE-DOUBLET DROPLET DISTRIBUTION RESULTS

C.1 Tabulated Results

Table C.1: Droplet Size Results, $l_b/l_i = 2$

2θ (deg)	Set Point	v_j (m/s)	d_{10} (μm)	d_{32} (μm)	$d_{10\%}$ (μm)	$d_{90\%}$ (μm)	Sp –
30°	1	5.17	908	1327	288	1588	1.49
	2	10.02	622	1130	209	1148	1.77
	3	15.05	445	930	198	744	1.45
	4	19.97	327	926	131	538	1.52
60°	5	5.31	818	1303	215	1528	1.73
	6	10.10	477	1085	147	956	2.17
	7	14.99	328	812	146	533	1.42
	8	20.01	258	652	123	419	1.35
90°	9	5.04	578	992	200	1065	1.69
	10	10.02	308	640	120	538	1.59
	11	15.09	230	396	107	387	1.41
	12	19.89	197	327	98	321	1.29

Table C.2: Droplet Size Results, $l_b/l_i = 1.5$

2θ (deg)	Set Point	v_j (m/s)	d_{10} (μm)	d_{32} (μm)	$d_{10\%}$ (μm)	$d_{90\%}$ (μm)	Sp –
30°	13	4.97	907	1291	315	1519	1.37
	14	10.23	607	1082	238	1075	1.67
	15	14.96	441	1011	175	752	1.60
	16	20.02	325	771	144	526	1.39
60°	17	4.95	795	1289	201	1501	1.80
	18	10.09	475	897	217	795	1.42
	19	14.98	325	782	147	525	1.39
	20	19.95	264	528	136	420	1.23
90°	21	5.05	560	967	152	1023	1.72
	22	10.04	324	522	155	537	1.34
	23	14.93	216	376	97	374	1.49
	24	20.01	190	324	96	309	1.27

Table C.3: Droplet Size Results, $l_b/l_i = 1$

2θ (deg)	Set Point	v_j (m/s)	d_{10} (μm)	d_{32} (μm)	$d_{10\%}$ (μm)	$d_{90\%}$ (μm)	Sp –
30°	25	4.99	874	1299	298	1537	1.51
	26	10.02	579	942	256	947	1.32
	27	14.96	411	1043	147	716	1.75
	28	20.08	324	673	174	489	1.13
60°	29	5.07	730	1194	202	1365	1.78
	30	9.98	373	853	126	675	1.78
	31	15.18	283	580	134	467	1.37
	32	19.92	228	483	112	366	1.28
90°	33	5.10	560	1187	96	1190	2.34
	34	10.21	333	550	172	533	1.22
	35	15.13	181	408	78	325	1.67
	36	19.95	203	331	104	328	1.25

C.2 Droplet Diameter Histograms

C.2.1 30° Impingement Angle

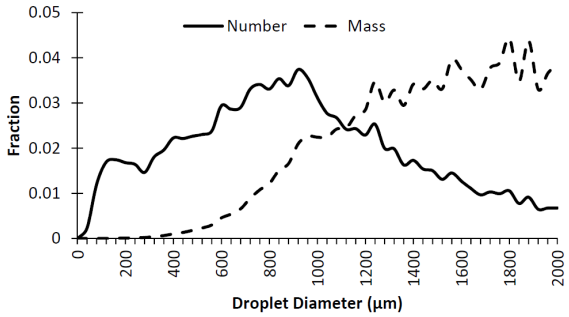

Figure C.1: Droplet Histogram: $2\theta = 30°$, $v_j = 5\ ^m/_s$, $^{l_b}/_{l_i} = 2$

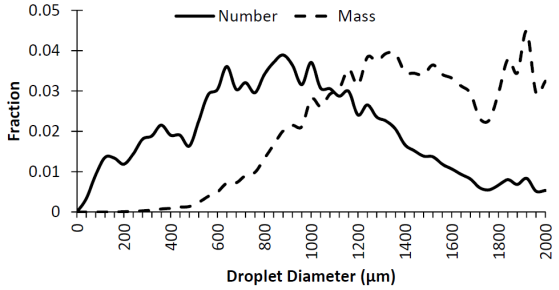

Figure C.2: Droplet Histogram: $2\theta = 30°$, $v_j = 5\ ^m/_s$, $^{l_b}/_{l_i} = 1.5$

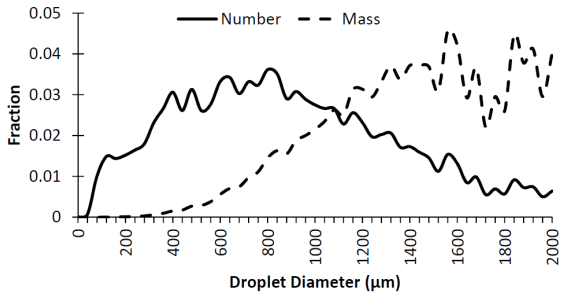

Figure C.3: Droplet Histogram: $2\theta = 30°$, $v_j = 5$ $^m/_s$, $^{l_b}/_{l_i} = 1$

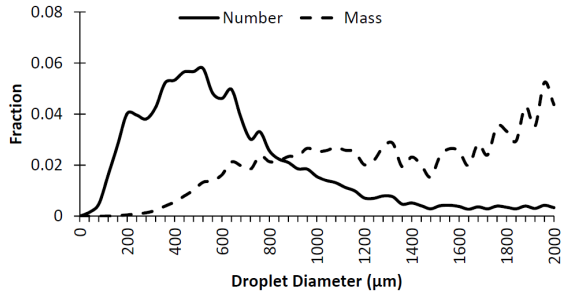

Figure C.4: Droplet Histogram: $2\theta = 30°$, $v_j = 10$ $^m/_s$, $^{l_b}/_{l_i} = 2$

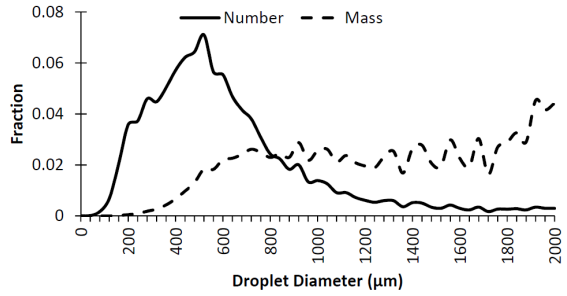

Figure C.5: Droplet Histogram: $2\theta = 30°$, $v_j = 10$ $^m/_s$, $^{l_b}/_{l_i} = 1.5$

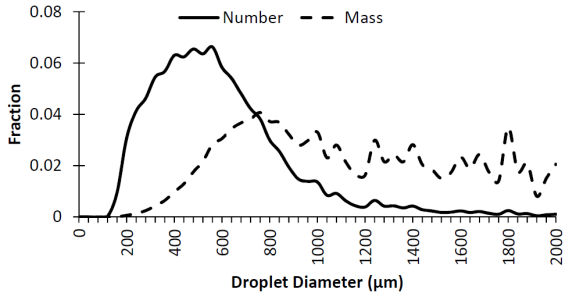

Figure C.6: Droplet Histogram: $2\theta = 30°$, $v_j = 10$ $^m/_s$, $^{l_b}/_{l_i} = 1$

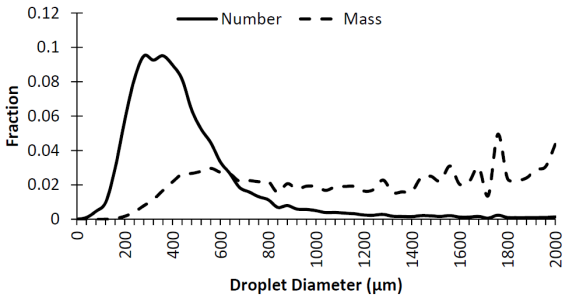

Figure C.7: Droplet Histogram: $2\theta = 30°$, $v_j = 15$ $^m/_s$, $^{l_b}/_{l_i} = 2$

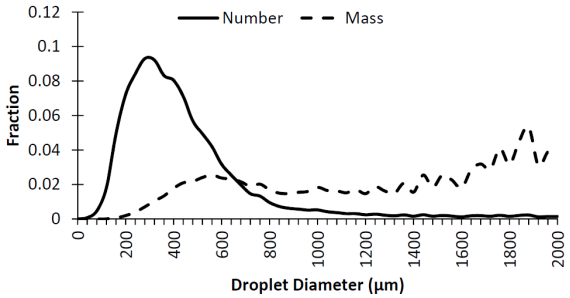

Figure C.8: Droplet Histogram: $2\theta = 30°$, $v_j = 15$ $^m/_s$, $^{l_b}/_{l_i} = 1.5$

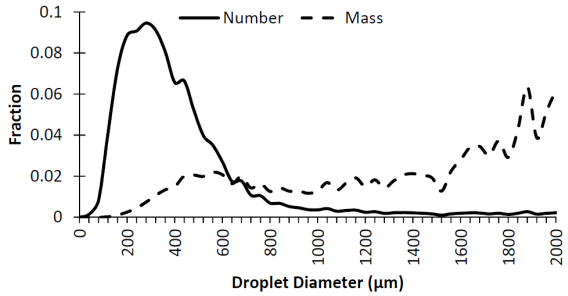

Figure C.9: Droplet Histogram: $2\theta = 30°$, $v_j = 15\ {}^{m}/_{s}$, ${}^{l_b}/_{l_i} = 1$

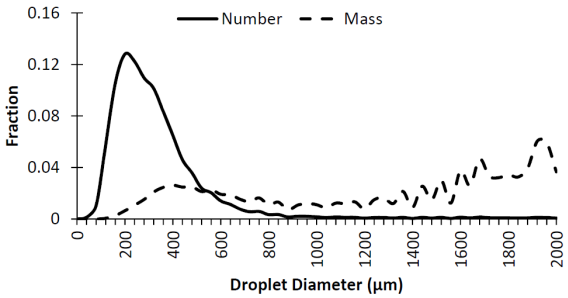

Figure C.10: Droplet Histogram: $2\theta = 30°$, $v_j = 20\ {}^{m}/_{s}$, ${}^{l_b}/_{l_i} = 2$

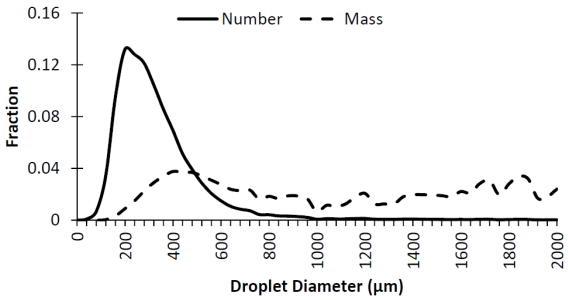

Figure C.11: Droplet Histogram: $2\theta = 30°$, $v_j = 20\ {}^{m}/_{s}$, ${}^{l_b}/_{l_i} = 1.5$

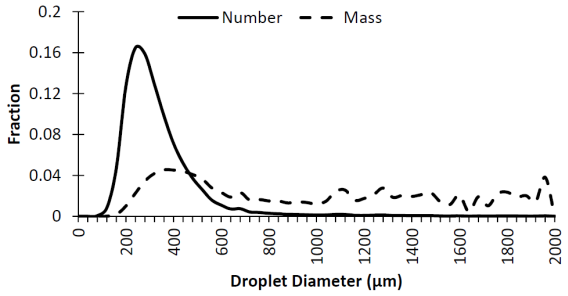

Figure C.12: Droplet Histogram: $2\theta = 30°$, $v_j = 20\ {}^{m}/_{s}$, ${}^{l_b}/_{l_i} = 1$

C.2.2 60° Impingement Angle

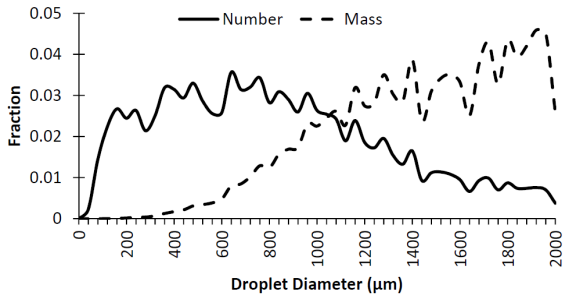

Figure C.13: Droplet Histogram: $2\theta = 60°$, $v_j = 5\ {}^{m}/_{s}$, ${}^{l_b}/_{l_i} = 2$

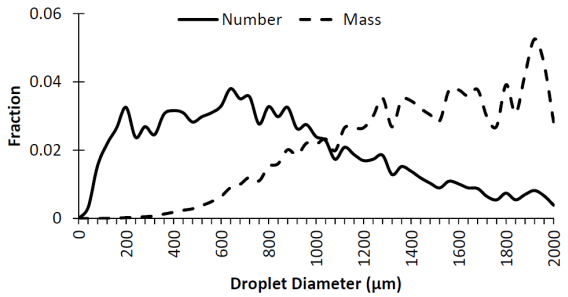

Figure C.14: Droplet Histogram: $2\theta = 60°$, $v_j = 5\ {}^{m}/_{s}$, ${}^{l_b}/_{l_i} = 1.5$

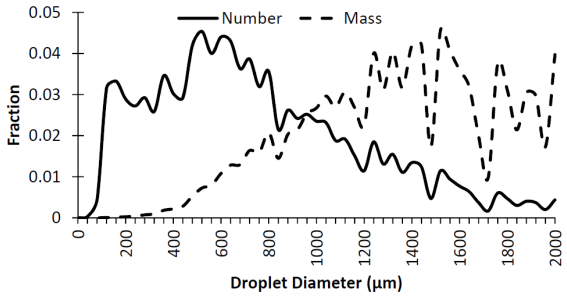

Figure C.15: Droplet Histogram: $2\theta = 60°$, $v_j = 5$ $^m/_s$, $^{l_b}/_{l_i} = 1$

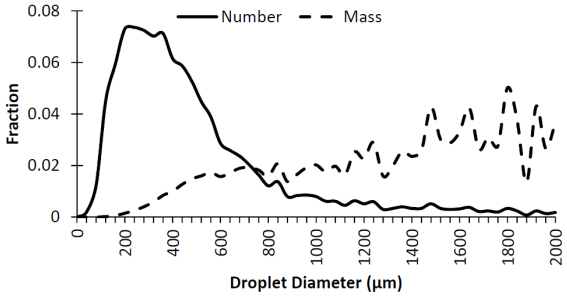

Figure C.16: Droplet Histogram: $2\theta = 60°$, $v_j = 10$ $^m/_s$, $^{l_b}/_{l_i} = 2$

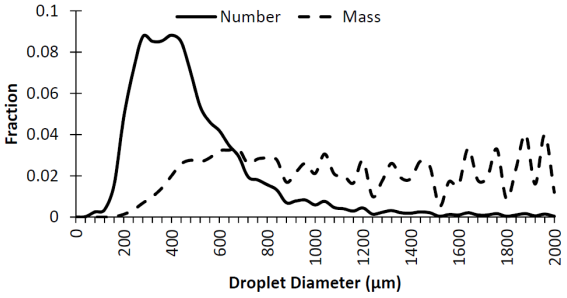

Figure C.17: Droplet Histogram: $2\theta = 60°$, $v_j = 10$ $^m/_s$, $^{l_b}/_{l_i} = 1.5$

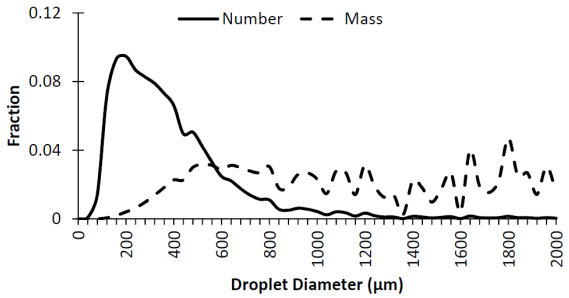

Figure C.18: Droplet Histogram: $2\theta = 60°$, $v_j = 10$ $^m/_s$, $^{l_b}/_{l_i} = 1$

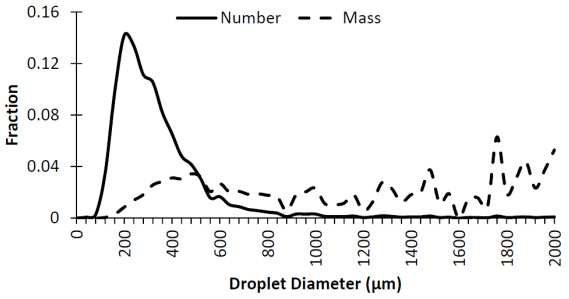

Figure C.19: Droplet Histogram: $2\theta = 60°$, $v_j = 15$ $^m/_s$, $^{l_b}/_{l_i} = 2$

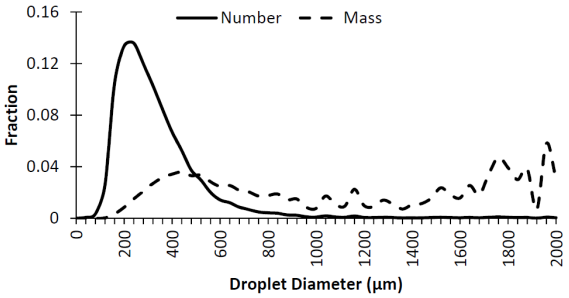

Figure C.20: Droplet Histogram: $2\theta = 60°$, $v_j = 15$ $^m/_s$, $^{l_b}/_{l_i} = 1.5$

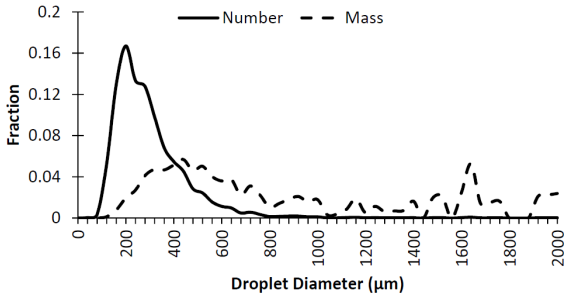

Figure C.21: Droplet Histogram: $2\theta = 60°$, $v_j = 15$ $^m/_s$, $^{l_b}/_{l_i} = 1$

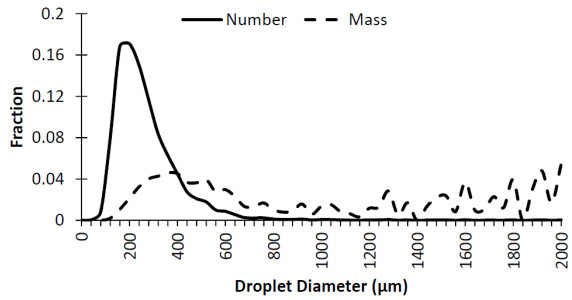

Figure C.22: Droplet Histogram: $2\theta = 60°$, $v_j = 20$ $^m/_s$, $^{l_b}/_{l_i} = 2$

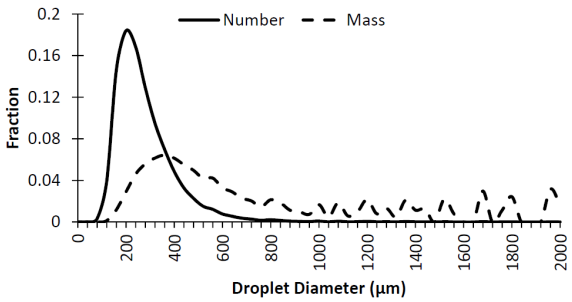

Figure C.23: Droplet Histogram: $2\theta = 60°$, $v_j = 20$ $^m/_s$, $^{l_b}/_{l_i} = 1.5$

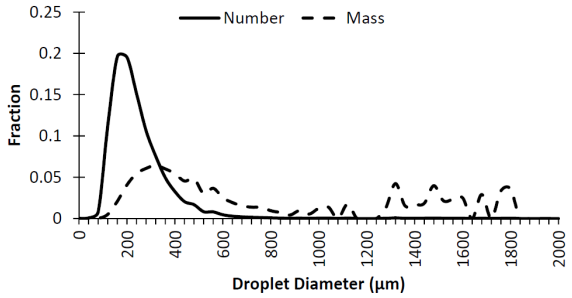

Figure C.24: Droplet Histogram: $2\theta = 60°$, $v_j = 20$ $^m/_s$, $^{l_b}/_{l_i} = 1$

C.2.3 90° Impingement Angle

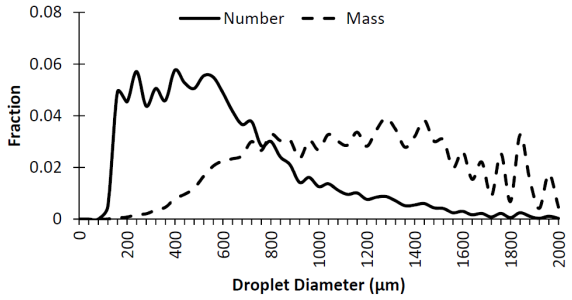

Figure C.25: Droplet Histogram: $2\theta = 90°$, $v_j = 5$ $^m/_s$, $^{l_b}/_{l_i} = 2$

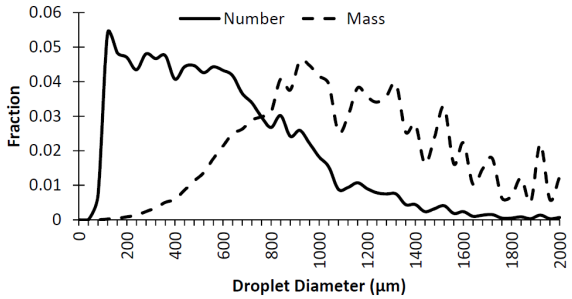

Figure C.26: Droplet Histogram: $2\theta = 90°$, $v_j = 5$ $^m/_s$, $^{l_b}/_{l_i} = 1.5$

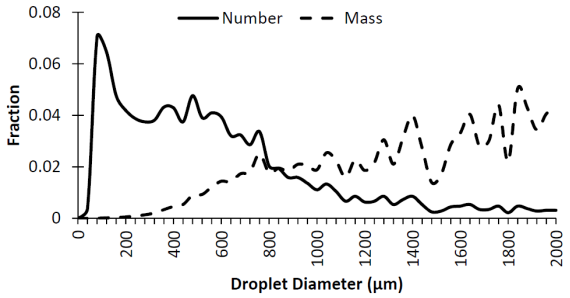

Figure C.27: Droplet Histogram: $2\theta = 90°$, $v_j = 5$ $^m/_s$, $^{l_b}/_{l_i} = 1$

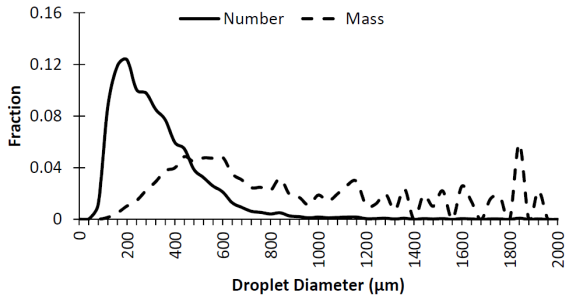

Figure C.28: Droplet Histogram: $2\theta = 90°$, $v_j = 10$ $^m/_s$, $^{l_b}/_{l_i} = 2$

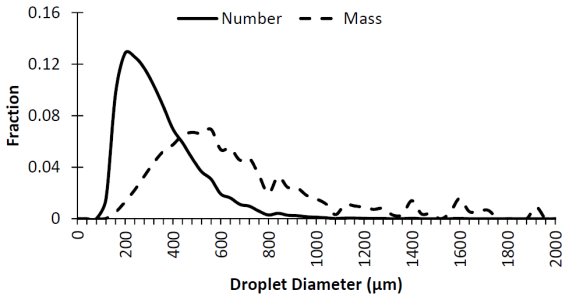

Figure C.29: Droplet Histogram: $2\theta = 90°$, $v_j = 10$ $^m/_s$, $^{l_b}/_{l_i} = 1.5$

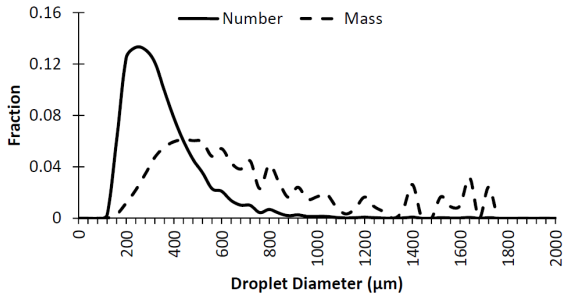

Figure C.30: Droplet Histogram: $2\theta = 90°$, $v_j = 10$ $^m/_s$, $^{l_b}/_{l_i} = 1$

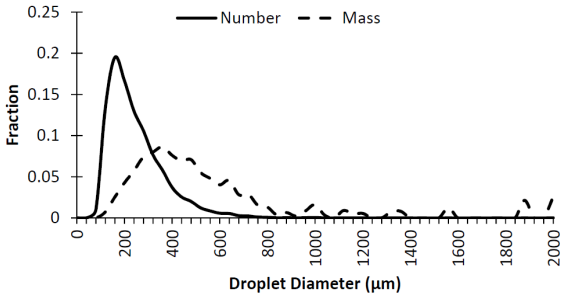

Figure C.31: Droplet Histogram: $2\theta = 90°$, $v_j = 15$ $^m/_s$, $^{l_b}/_{l_i} = 2$

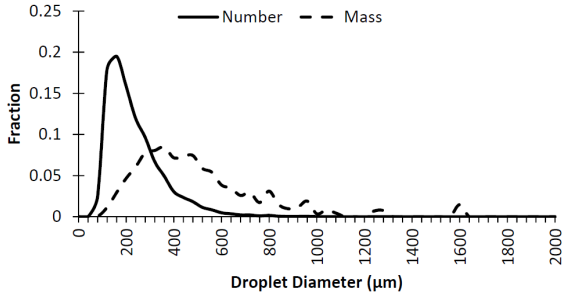

Figure C.32: Droplet Histogram: $2\theta = 90°$, $v_j = 15$ $^m/_s$, $^{l_b}/_{l_i} = 1.5$

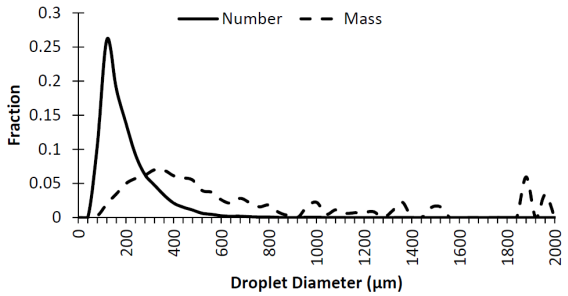

Figure C.33: Droplet Histogram: $2\theta = 90°$, $v_j = 15\ ^m/_s$, $^{l_b}/_{l_i} = 1$

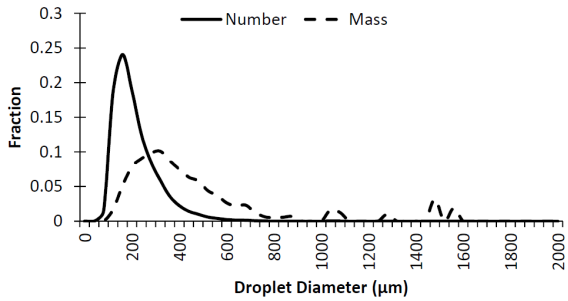

Figure C.34: Droplet Histogram: $2\theta = 90°$, $v_j = 20\ ^m/_s$, $^{l_b}/_{l_i} = 2$

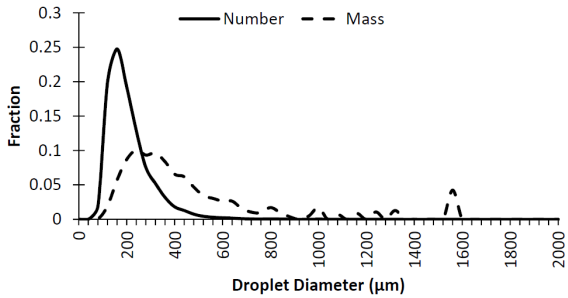

Figure C.35: Droplet Histogram: $2\theta = 90°$, $v_j = 20\ ^m/_s$, $^{l_b}/_{l_i} = 1.5$

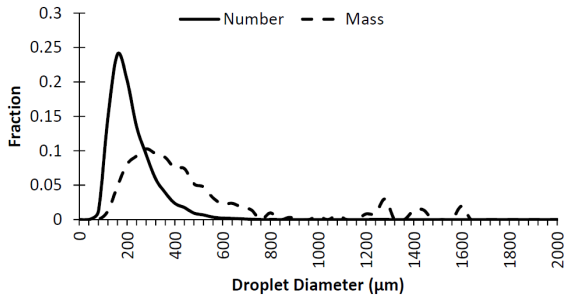

Figure C.36: Droplet Histogram: $2\theta = 90°$, $v_j = 20\ {}^{m}/_{s}$, ${}^{l_b}/_{l_i} = 1$

APPENDIX D

UNCERTAINTY ANALYSIS RESULTS

D.1 Tabulated Uncertainty Results (95% Confidence)

Table D.1: Single Jet Uncertainty Results (%)

Set Point	UT_{liq} (%)	UΔP_{inj} (%)	Uv_j (%)	U$\dot{m}$ (%)	URe (%)	UWe (%)	UOh (%)
1	0.87	8.47	10.34	10.73	12.31	20.25	5.14
2	0.88	5.33	3.03	4.04	7.24	6.23	6.39
3	0.88	2.64	1.56	3.12	6.85	3.60	5.09
4	0.89	1.55	1.00	2.86	6.86	2.74	6.33

Table D.2: Like-Doublet Uncertainty Results (%), $l_b/l_i = 2$

2θ (deg)	Set Point	UT_{liq} (%)	UΔP_{inj} (%)	Uv_j (%)	U$\dot{m}$ (%)	URe (%)	UWe (%)	UOh (%)
30°	1	0.96	16.21	8.99	9.31	11.43	17.56	7.89
	2	0.82	4.98	2.74	3.82	6.90	5.72	5.15
	3	0.86	2.32	1.40	3.04	6.60	3.35	5.24
	4	0.83	1.39	0.90	2.85	6.49	2.63	5.05
60°	5	0.99	15.55	8.48	8.96	10.99	16.77	5.45
	6	0.82	4.91	2.77	3.79	6.89	5.72	5.15
	7	0.82	2.41	1.40	3.01	6.53	3.35	5.09
	8	0.83	1.42	0.95	2.90	6.48	2.68	5.05
90°	9	0.94	17.75	10.02	10.29	12.54	20.09	7.04
	10	0.82	4.99	2.80	3.82	6.85	5.77	5.15
	11	0.82	2.37	1.39	3.03	6.49	3.32	5.09
	12	0.83	1.39	0.93	2.86	6.46	2.67	5.05

Table D.3: Like-Doublet Uncertainty Results (%), $l_b/l_i = 1.5$

2θ (deg)	Set Point	UT_{liq} (%)	UΔP_{inj} (%)	Uv_j (%)	U$\dot{m}$ (%)	URe (%)	UWe (%)	UOh (%)
30°	13	0.82	17.02	9.56	9.82	11.29	18.64	5.20
	14	0.82	4.77	2.69	3.86	6.84	5.67	5.10
	15	0.82	2.40	1.40	3.05	6.58	3.38	5.05
	16	0.83	1.41	0.92	2.87	6.47	2.66	5.01
60°	17	0.82	17.48	9.59	9.98	11.45	18.75	5.20
	18	0.82	4.74	2.73	3.86	6.82	5.83	5.11
	19	0.82	2.40	1.40	3.05	6.52	3.39	5.06
	20	0.83	1.43	0.95	2.85	6.54	2.65	5.02
90°	21	0.82	16.78	9.21	9.54	11.04	18.31	5.18
	22	0.82	4.96	2.79	3.94	6.81	5.82	5.11
	23	0.86	2.41	1.44	3.06	6.69	3.44	5.05
	24	0.83	1.42	0.95	2.90	6.56	2.71	5.02

Table D.4: Like-Doublet Uncertainty Results (%), $l_b/l_i = 1$

2θ (deg)	Set Point	UT_{liq} (%)	UΔP_{inj} (%)	Uv_j (%)	U$\dot{m}$ (%)	URe (%)	UWe (%)	UOh (%)
30°	25	0.82	17.24	9.52	9.90	11.29	18.75	5.22
	26	0.98	5.07	2.80	3.83	7.48	5.77	5.56
	27	0.82	2.40	1.44	3.06	6.52	3.42	5.10
	28	1.22	1.62	1.05	2.92	9.87	2.87	9.02
60°	29	0.82	16.66	9.26	9.50	11.13	18.14	5.22
	30	0.82	4.99	2.80	3.96	6.95	5.88	5.15
	31	0.82	2.35	1.38	3.01	6.43	3.31	5.09
	32	0.86	1.43	0.95	2.85	6.59	2.69	5.05
90°	33	0.82	16.49	9.11	9.56	10.90	18.06	5.21
	34	0.95	4.87	2.64	3.81	7.47	5.59	5.51
	35	0.82	2.35	1.39	3.06	6.41	3.38	5.10
	36	0.83	1.43	0.95	2.85	6.45	2.65	5.05

Table D.5: Like-Doublet Uncertainty Results (%), $l_b/l_i = 0.5$

2θ (deg)	Set Point	UT_{liq} (%)	UΔP_{inj} (%)	Uv_j (%)	U$\dot{m}$ (%)	URe (%)	UWe (%)	UOh (%)
30°	37	0.97	18.28	10.22	10.59	13.00	20.47	6.94
	38	1.22	5.15	2.96	4.08	9.98	6.26	9.33
	39	0.87	2.61	1.41	3.08	7.03	3.38	7.07
	40	1.22	1.62	1.05	2.94	9.90	2.92	9.02
60°	41	0.97	19.43	10.97	11.33	13.50	21.92	6.94
	42	1.18	5.54	3.16	4.21	9.99	6.67	9.26
	43	0.87	2.75	1.51	3.06	7.04	3.52	7.07
	44	1.01	1.52	1.01	2.98	8.26	2.88	6.75
90°	45	0.97	19.03	11.02	11.37	13.43	22.11	6.91
	46	1.01	5.20	3.00	4.12	8.49	6.36	6.84
	47	0.86	2.38	1.39	3.03	6.67	3.37	5.27
	48	1.01	1.49	0.98	2.89	8.27	2.76	6.69

D.2 Uncertainty Plots (95% Confidence)

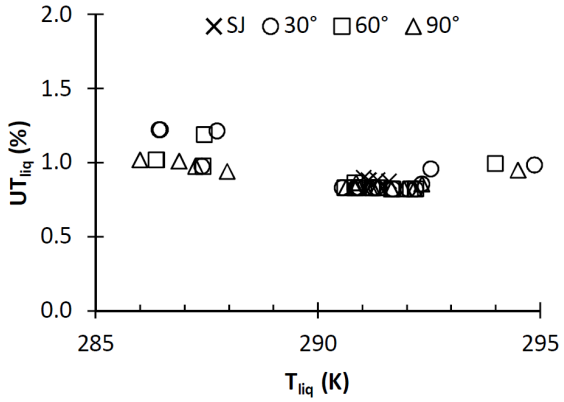

Figure D.1: Uncertainty: Water Temperature

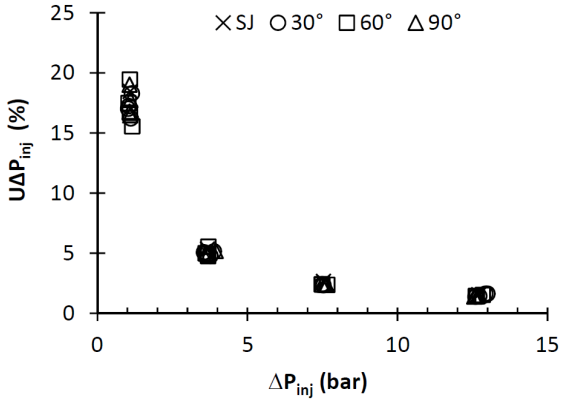

Figure D.2: Uncertainty: Injector Pressure Drop

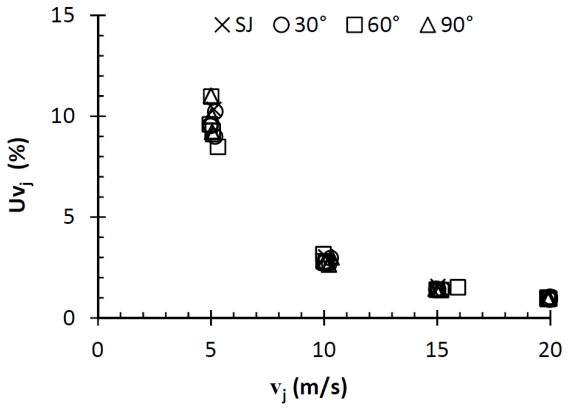

Figure D.3: Uncertainty: Jet Velocity

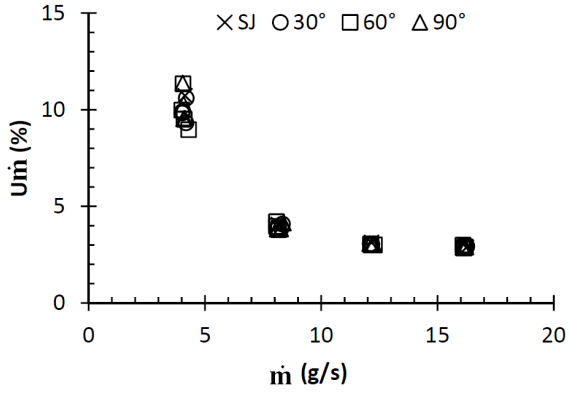

Figure D.4: Uncertainty: Mass Flowrate

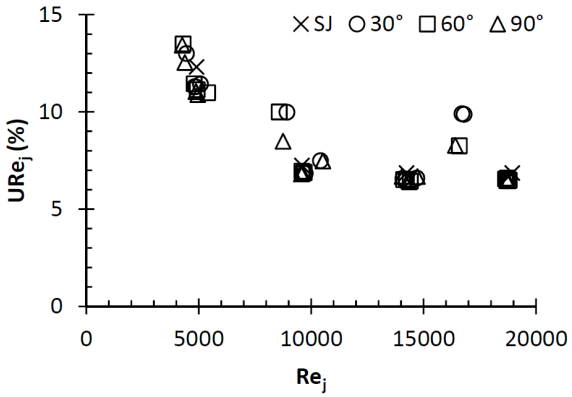

Figure D.5: Uncertainty: Jet Reynolds Number

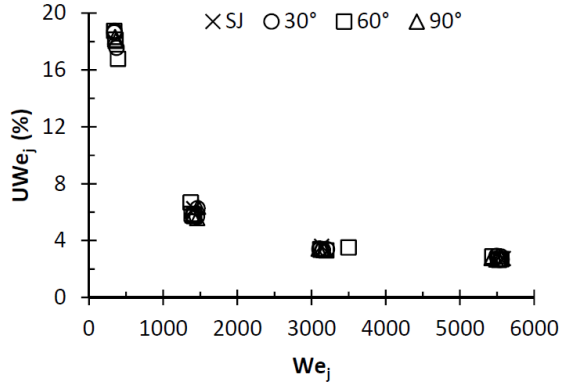

Figure D.6: Uncertainty: Jet Weber Number

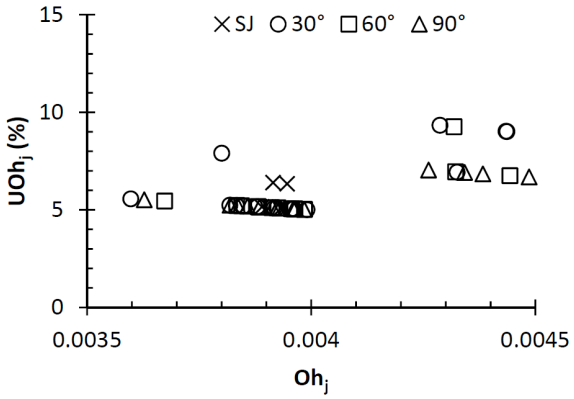

Figure D.7: Uncertainty: Jet Ohnesorge Number

REFERENCES

[1] Humble, R. W., Henry, G. N., and Larson, W. J., *Space Propulsion Analysis and Design*, McGraw-Hill, New York, revised ed., 1995.

[2] Sutton, G. P. and Biblarz, O., *Rocket Propulsion Elements*, John Wiley and Sons, New York, 7th ed., 2001.

[3] Harrje, D. T. and Reardon, F. H., "Liquid Propellant Rocket Combustion Instability," Tech. Rep. SP-194, NASA, 1972.

[4] Muss, J. A., "Instability Phenomena in Liquid Oxygen/Hydrocarbon Rocket Engines," *Liquid Rocket Engine Combustion Instability*, edited by V. Yang and W. E. Anderson, Vol. 169 of *Progress in Astronautics and Aeronautics*, American Institute of Aeronautics and Astronautics, Washington D.C., 1994, pp. 73–88.

[5] "Liquid Rocket Engine Injectors," Space Vehicle Design Criteria: Chemical Propulsion, Tech. Rep. SP-8089, NASA, 1976.

[6] Kendrick, D., Herding, G., Scouflaire, P., Rolon, C., and Candel, S., "Effects of a Recess on Cryogenic Flame Stabilization," *Combustion and Flame*, Vol. 118, 1999, pp. 327–339.

[7] Lightfoot, M. D. A., Danczyk, S. A., and Talley, D. G., "Atomization Rate of Gas-Centered Swirl-Coaxial Injectors," *21st Annual Conference on Liquid Atomization and Spray Systems*, Orlando, FL, 2008.

[8] "SpaceX Falcon Heavy Merlin Engines," http://www.spacex.com/news/2013/04/12/falcon-heavy-merlin-engines, 2013.

[9] Culick, F. E. C., "Unsteady Motions in Combustion Chambers for Propulsion Systems," RTO AGARDograph AG-AVT-039, North Atlantic Treaty Organization, 2006.

[10] Oefelein, J. C. and Yang, V., "Comprehensive Review of Liquid-Propellant Combustion Instabilities in F-1 Engines," *Journal of Propulsion and Power*, Vol. 9, No. 5, Sept.-Oct. 1993, pp. 657–677.

[11] Souchier, A., Rothmund, C., Leven, P., and Hagberg, J., "The Development of the Viking Engine," *35th AIAA/ASME/SAE/ASEE Joint Propulsion Conference and Exhibit*, Los Angeles, CA, 1999, AIAA 99-2902.

[12] http://airandspace.si.edu/collections/artifact.cfm?id=A20060085000, 2013.

[13] Dranovsky, M. L., *Combustion Instabilities in Liquid Rocket Engines: Testing and Development Practices in Russia*, Vol. 221 of *Progress in Astronautics and Aeronautics*, American Institute of Aeronautics and Astronautics, Reston, VA, 2007.

[14] Culick, F. E. C. and Yang, V., "Overview of Combustion Instabilities in Liquid-Propellant Rocket Engines," *Liquid Rocket Engine Combustion Instability*, edited by V. Yang and W. E. Anderson, Vol. 169 of *Progress in Astronautics and Aeronautics*, American Institute of Aeronautics and Astronautics, Washington D.C., 1995, pp. 3–37.

[15] Sliphorst, M., Knapp, B., Groening, S., and Oschwald, M., "Combustion Instability-Coupling Mechanisms Between Liquid Oxygen/Methane Spray Flames and Acoustics," *Journal of Propulsion and Power*, Vol. 28, No. 6, Nov.-Dec. 2012, pp. 1339–1350.

[16] Durox, D., Schuller, T., Noiray, N., Birbaud, A. L., and Candel, S., "Rayleigh Criterion and Acoustic Energy Balance in Unconfined Self-Sustained Oscillating Flames," *Combustion and Flame*, Vol. 156, 2009, pp. 106–119.

[17] Bazarov, V. G. and Yang, V., "Liquid-Propellant Rocket Engine Injector Dynamics," *Journal of Propulsion and Power*, Vol. 14, No. 5, Sept.-Oct. 1998, pp. 797–806.

[18] Kim, J. S. and Williams, F. A., "Acoustic-Instability Boundaries in Liquid-Propellant Rockets: Theoretical Explanation of Empirical Correlation," *Journal of Propulsion and Power*, Vol. 12, No. 3, May-Jun. 1996, pp. 621–624.

[19] Hutt, J. J. and Rocker, M., "High-Frequency Injection-Coupled Combustion Instability," *Liquid Rocket Engine Combustion Instability*, edited by V. Yang and W. E. Anderson, Vol. 169 of *Progress in Astronautics and Aeronautics*, American Institute of Aeronautics and Astronautics, Washington D.C., 1995, pp. 345–355.

[20] Sirignano, W. A., Delplanque, J. P., Chiang, C. H., and Bhatia, R., "Liquid-Propellant Droplet Vaporization: A Rate-Controlling Process for Combustion Instability," *Liquid Rocket Engine Combustion Instability*, edited by V. Yang and W. E. Anderson, Vol. 169 of *Progress in Astronautics and Aeronautics*, American Institute of Aeronautics and Astronautics, Washington D.C., 1994, pp. 307–343.

[21] Anderson, W. E., Ryan, H. M., Pal, S., and Santoro, R. J., "Spray Formation Processes of Impinging Jet Injectors," *NASA Propulsion Engineering Research Center*, Vol. 2, 1993, pp. 69–74, N94-23042.

[22] Miller, K., Sisco, J., Nugent, N., and Anderson, W., "Experimental Study of Combustion Instabilities in a Single-Element Coaxial Swirl Injector," *41st AIAA/ASME/SAE/ASEE Joint Propulsion Conference and Exhibit*, Tucson, AZ, 2005, AIAA 2005-4298.

[23] Davis, D. and Chehroudi, B., "The Effects of Pressure and Acoustic Field on a Cryogenic Coaxial Jet," *42nd AIAA Aerospace Sciences Meeting and Exhibit*, Reno, NV, 2004, AIAA 2004-1330.

[24] "Liquid Rocket Engine Combustion Stabilization Devices," Space Vehicle Design Criteria: Chemical Propulsion, Tech. Rep. SP-8113, NASA, 1974.

[25] You, D., Ku, D. D., and Yang, V., "Acoustic Waves in Baffled Combustion Chamber with Radial and Circumferential Blades," *Journal of Propulsion and Power*, 2013, pp. pp. 657–677, AIAA Early Edition.

[26] Sohn, C. H. and Park, J. H., "A Comparative Study on Acoustic Damping Induced by Half-Wave, Quarter-Wave, and Helmholtz Resonators," *Aerospace Science and Technology*, Vol. 15, No. 8, Dec. 2011, pp. 606–614.

[27] Cavitt, R. C., *Experimental Methodology for Measuring Combustion and Injector Coupled Responses*, Master's thesis, University of Alabama in Huntsville, Huntsville, AL, 2007.

[28] Conrad, T., Bibik, A., Shcherbik, D., Lubarsky, E., and Zinn, B. T., "Control of the Stability Margin in a Liquid Fueled Combustor Using a "Smart" Fuel Injector," *42nd AIAA/ASME/SAE/ASEE Joint Propulsion Conference and Exhibit*, Sacramento, CA, 2006, AIAA 2006-4797.

[29] Munson, B. R., Young, D. F., and Okiishi, T. H., *Fundamentals of Fluid Mechanics*, John Wiley and Sons, New York, 4th ed., 2002.

[30] Lefebvre, A. H., *Atomization and Sprays*, Combustion: An International Series, Hemisphere Publishing Company, New York, 1989.

[31] Bayvel, L. and Orzechowski, Z., *Liquid Atomization*, Combustion: An International Series, Taylor and Francis, New York, 1993.

[32] Vennard, J. K. and Street, R. L., *Elementary Fluid Mechanics*, John Wiley and Sons, New York, 5th ed., 1975.

[33] Wu, P. K., Hsiang, L. P., and Faeth, G. M., "Aerodynamic Effects on Primary and Secondary Spray Breakup," *Liquid Rocket Engine Combustion Instability*, edited by V. Yang and W. E. Anderson, Vol. 169 of *Progress in Astronautics and Aeronautics*, American Institute of Aeronautics and Astronautics, Washington D.C., 1994, pp. 247–279.

[34] Hiroyasu, H., Arai, M., and Shimizu, M., "Effect of Internal Flow Conditions Inside Injector Nozzles on Jet Breakup Processes," *Recent Advances in Spray Combustion: Spray Atomization and Drop Burning Phenomena – Volume 1*, edited by K. K. Kuo, Vol. 166 of *Progress in Astronautics and Aeronautics*, American Institute of Aeronautics and Astronautics, Reston, VA, 1995, pp. 173–184.

[35] Pope, S. B., *Turbulent Flows*, Cambridge University Press, Cambridge, UK, 2000.

[36] Chehroudi, B., "Physical Hypothesis for the Combustion Instability in Cryogenic Liquid Rocket Engines," *Journal of Propulsion and Power*, Vol. 26, No. 6, Nov.-Dec. 2010, pp. 1153–1160.

[37] Chigier, N. and Reitz, R. D., "Regimes of Jet Breakup and Breakup Mechanisms: Physical Aspects," *Recent Advances in Spray Combustion: Spray Atomization and Drop Burning Phenomena – Volume 1*, edited by K. K. Kuo, Vol. 166 of *Progress in Astronautics and Aeronautics*, American Institute of Aeronautics and Astronautics, Reston, VA, 1995, pp. 109–135.

[38] Vingert, L., Gicquel, P., Lourme, D., and Menoret, L., "Coaxial Injector Atomization," *Liquid Rocket Engine Combustion Instability*, edited by V. Yang and W. E. Anderson, Vol. 169 of *Progress in Astronautics and Aeronautics*, American Institute of Aeronautics and Astronautics, Washington D.C., 1995, pp. 145–189.

[39] Tseng, L. K., Ruff, G. A., Wu, P. K., and Faeth, G. M., "Continuous- and Dispersed-Phase Structure of Pressure-Atomized Sprays," *Recent Advances in Spray Combustion: Spray Combustion Measurements and Model Simulation – Volume 2*, edited by K. K. Kuo, Vol. 171 of *Progress in Astronautics and Aeronautics*, American Institute of Aeronautics and Astronautics, Reston, VA, 1995, pp. 3–30.

[40] Sirignano, W. A. and Mehring, C., "Distortion and Disintegration of Liquid Streams," *Liquid Rocket Thrust Chambers: Aspects of Modeling, Analysis, and Design*, edited by V. Yang, M. Habiballah, J. Hulka, and M. Popp, Vol. 200 of *Progress in Astronautics and Aeronautics*, American Institute of Aeronautics and Astronautics, Reston, VA, 2004, pp. 167–249.

[41] Wu, P. K. and Faeth, G. M., "Onset and End of Drop Formation Along the Surface of Turbulent Liquid Jets in Still Gases," *Physics of Fluids*, Vol. 7, No. 11, 1995, pp. 2915– 2917.

[42] Sallam, K. A., Dai, Z., and Faeth, G. M., "Breakup of Turbulent Liquid Jets in Still Gases," *30^{th} AIAA Fluid Dynamics Conference*, Norfolk, VA, 1999, AIAA 99-3759.

[43] Ruff, G. A., Sagar, A. D., and Faeth, G. M., "Structure and Mixing Properties of Pressure-Atomized Sprays," *AIAA Journal*, Vol. 27, No. 7, 1989, pp. 901–908.

[44] Phinney, R. E., "The Breakup of a Turbulent Liquid Jet in a Gaseous Atmosphere," *Journal of Fluid Mechanics*, Vol. 60, No. 4, 1973, pp. 689–701.

[45] Grant, R. P. and Middleman, S., "Newtonian Jet Stability," *AIChE Journal*, Vol. 12, No. 4, 1966, pp. 669–678.

[46] Jung, K., Khil, T., and Yoon, Y., "Effects of Orifice Internal Flow on Breakup Characteristics of Like-Doublet Injectors," *Journal of Propulsion and Power*, Vol. 22, No. 3, May-Jun. 2006, pp. 653–660.

[47] Nurick, W. H., "Orifice Cavitation and its Effects on Spray Mixing," *Journal of Fluids Engineering*, Vol. 98, No. 4, Dec. 1976, pp. 681– 687.

[48] Pal, S., Ryan, H., Hoover, D., and Santoro, R. J., "Pressure Oscillation Effects on Jet Breakup," *Recent Advances in Spray Combustion: Spray Combustion Measurements and Model Simulation – Volume 2*, edited by K. K. Kuo, Vol. 171 of *Progress in Astronautics and Aeronautics*, American Institute of Aeronautics and Astronautics, Reston, VA, 1996, pp. 233–259.

[49] Carpentier, J. B., Baillot, F., Blaisot, J. B., and Dumouchel, C., "Behavior of Cylindrical Liquid Jets Evolving in a Transverse Acoustic Field," *Physics of Fluids*, Vol. 21, No. 2, 2009, pp. 1–15.

[50] Baillot, F., Blaisot, J. B., Boisdron, G., and Dumouchel, C., "Behavior of an Air-Assisted Jet Submitted to a Transverse High-Frequency Acoustic Field," *Journal of Fluid Mechanics*, Vol. 640, 2009, pp. 305–342.

[51] Anderson, W. E., Ryan, H. M., and Santoro, R. J., "Impinging Jet Injector Atomization," *Liquid Rocket Engine Combustion Instability*, edited by V. Yang and W. E. Anderson, Vol. 169 of *Progress in Astronautics and Aeronautics*, American Institute of Aeronautics and Astronautics, Washington D.C., 1995, pp. 215–246.

[52] Strakey, P. A. and Talley, D. G., "Spray Characteristics of Impinging Jet Injectors at High Back-Pressure," *8^{th} International Conference on Liquid Atomization and Spray Systems*, Pasadena, CA, 2000.

[53] Anderson, W. E., Ryan, H. M., and Santoro, R. J., "Combustion Instability Mechanisms in Liquid Rocket Engines Using Impinging Jet Injectors," *31^{st} AIAA/ASME/SAE/ASEE Joint Propulsion Conference and Exhibit*, San Diego, CA, 1995, AIAA 95-2357.

[54] Lourme, D., "Like-on-Like Injector Spray Characterization for the Ariane Viking Engine," *22^{nd} AIAA/ASME/SAE/ASEE Joint Propulsion Conference and Exhibit*, Huntsville, AL, 1986, AIAA 86-1444.

[55] Santoro, R. J. and Anderson, W. E., "Combustion Instability Phenomena of Importance to Liquid Propellant Engines," *The Pennsylvania State University*, 1993, Annual Report to Air Force Office of Scientific Research.

[56] Leyva, I. A., Chehroudi, B., and Talley, D., "Dark Core Analysis of Coaxial Injectors at Sub-, Near-, and Supercritical Pressures in a Transverse Acoustic Field," *43rd AIAA/ASME/SAE/ASEE Joint Propulsion Conference and Exhibit*, Cincinnati, OH, 2007, AIAA 2007-5456.

[57] Smith, J. J., Bechle, M., Suslov, D., Oschwald, M., Haidn, O. J., and Schneider, G. M., "High Pressure LOX/H_2 Combustion and Flame Dynamics: Preliminary Results," *40th AIAA/ASME/SAE/ASEE Joint Propulsion Conference and Exhibit*, Ft. Lauderdale, FL, 2004, AIAA 2004-3376.

[58] Rhys, N. O., *Acoustic Excitation and Destruction of Liquid Sheets*, Ph.D. thesis, University of Alabama in Huntsville, Huntsville, AL, 1999.

[59] Mulmule, A. S., Tirumkudulu, M. S., Ananthkrishnan, N., and Ramamurthy, K., "Liquid Sheet Instability in the Presence of Acoustic Forcing," *43rd AIAA/ASME/SAE/ASEE Joint Propulsion Conference and Exhibit*, Cincinnati, OH, 2007, AIAA 2007-5688.

[60] Heidmann, M. F., Priem, R. J., and Humphrey, J. C., "A Study of Sprays Formed by Two Impinging Jets," Tech. Rep. NACA TN-3835, National Advisory Committee for Aeronautics, 1957.

[61] Bremond, N. and Villermaux, E., "Atomization by Jet Impact," *Journal of Fluid Mechanics*, Vol. 549, 2006, pp. 273–306.

[62] Dombrowski, N. and Hooper, P. C., "A Study of the Sprays Formed by Impinging Jets in Laminar and Turbulent Flow," *Journal of Fluid Mechanics*, Vol. 18, No. 3, 1964, pp. 392–400.

[63] Bailardi, G., Negri, M., and Ciezki, H. K., "Several Aspects of the Atomization Behavior of Various Newtonian Fluids with a Like-on-Like Impinging Jet Injector," *23rd Annual Conference on Liquid Atomization and Spray Systems*, Brno, Czech Republic, 2010, ILASS - Europe.

[64] Chen, X., Ma, D., and Yang, V., "Mechanism Study of Impact Wave in Impinging Jets Atomization," *50th AIAA Aerospace Sciences Meeting*, Nashville, TN, 2012, AIAA 2012-1089.

[65] Zheng, G., Nie, W., Feng, A., and Wu, G., "Numerical Simulation of the Atomization Process of a Like-Doublet Impinging Rocket Injector," *Procedia Engineering*, Vol. 99, 2015, pp. 930–938.

[66] Ryan, H. M., Anderson, W. E., Pal, S., and Santoro, R. J., "Atomization Characteristics of Impinging Liquid Jets," *Journal of Propulsion and Power*, Vol. 11, No. 1, Jan.-Feb. 1995, pp. 135–145.

[67] Anderson, W. E., Miller, K. L., Ryan, H. M., Pal, S., Santoro, R. J., and Dressler, J. L., "Effects of Periodic Atomization on Combustion Instability in Liquid-Fueled Propulsion Systems," *Journal of Propulsion and Power*, Vol. 14, No. 5, Sep.-Oct. 1998, pp. 818–825.

[68] Ramamurthi, K., Nandakumar, K., and Patnaik, R. K., "Characteristics of Sprays Formed by Impingement of a Pair of Liquid Jets," *Journal of Propulsion and Power*, Vol. 20, No. 1, Jan.-Feb. 2004, pp. 76–82.

[69] Choo, Y.-J. and Kang, B.-S., "The Velocity Distribution of the Liquid Sheet Formed by Two Low-Speed Impinging Jets," *Physics of Fluids*, Vol. 14, No. 2, Feb. 2002, pp. 622–627.

[70] Hautman, D. J., "Spray Characterization of Like-on-Like Doublet Impinging Rocket Injectors," *29th Aerospace Sciences Meeting*, Reno, NV, 1991, AIAA 91-0687.

[71] Anon., "National Instruments LabView System Design Software," http://www.ni.com/labview/, 2015.

[72] TSI, *Phase Doppler Particle Analyzer (PDPA)/Laser Doppler Velocimeter (LDV) Operations Manual*, revision F ed., 2008.

[73] Anon., "Omega Engineering Super Omegaclad Thermocouple Probes," http://www.omega.com, 2015.

[74] Anon., "Omega Engineering High Performance Pressure Transducer: 0 to 5 Vdc Output," http://www.omega.com/pptst/PX309-5V.html, 2015.

[75] PCB Piezotronics, *Model 106B ICP Pressure Sensor Installation and Operating Manual*, 2010.

[76] Vision Research, *Phantom One Megapixel v-Series Cameras*, 2014, http://www.visionresearch.com/Products/High-Speed-Cameras/v711/.

[77] Anon., "Nikon Micro-Nikkor 105mm f/2.8 Lens," 2015, URL:http://www.nikonusa.com/en/Nikon-Products/Product/Camera-Lenses/Micro-NIKKOR-105mm-f%252F2.8.html.

[78] Anon., "Nikon AF Micro-Nikkor 200mm f/4D IF-ED Lens," 2015, URL:http://www.nikonusa.com/en/Nikon-Products/Product/Camera-Lenses/AF-Micro-Nikkor-200mm-f%252F4D-IF-ED.html.

[79] Anon., "Nikon AF Micro-Nikkor 60mm f/2.8D Lens," 2016, URL:http://www.nikonusa.com/en/nikon-products/product/camera-lenses/af-micro-nikkor-60mm-f%252f2.8d.html#tab-ProductDetail-ProductTabs-TechSpecs.

[80] Anon., "Nikon AF Nikkor 28mm f/2.8D Lens," 2016, URL:http://www.nikonusa.com/en/nikon-products/product/camera-lenses/af-nikkor-28mm-f%252f2.8d.html#tab-ProductDetail-ProductTabs-TechSpecs.

[81] Ofner, B., "Phase Doppler Anemometry (PDA)," *Optical Measurements: Techniques and Applications*, edited by F. Mayinger and O. Feldman, Heat and Mass Transfer, Springer Berlin Heidelberg, Berlin, Germany, 2nd ed., 2001, pp. 139–152.

[82] Jackson, T., "Droplet Sizing Interferometry," *Liquid Particle Size Measurement Techniques: 2nd Volume*, Vol. STP 1083.

[83] National Instruments, *Particle Measurements*, 2010 (accessed Oct. 29, 2015), http://zone.ni.com/reference/en-XX/help/372916J-01/nivisionconcepts/particle_measurements/.

[84] Coleman, H. W. and Steele, W. G., *Experimentation, Validation, and Uncertainty Analysis for Engineers*, John Wiley and Sons, Hoboken, NJ, 3rd ed., 2009.

[85] Berkooz, G., Holmes, P., and Lumley, J. L., "The Proper Orthogonal Decomposition in the Analysis of Turbulent Flows," *Annual Review of Fluid Mechanics*, Vol. 25, 1993, pp. 539–575.

[86] Arienti, M. and Soteriou, M. C., "Time-Resolved Proper Orthogonal Decomposition of Liquid Jet Dynamics," *Physics of Fluids*, Vol. 21, No. 11, Dec. 2009, pp. 1–15.

[87] Schmid, P. J., "Dynamic Mode Decomposition of Numerical and Experimental Data," *Journal of Fluid Mechanics*, Vol. 656, 2010, pp. 5–28.

[88] Schmid, P. J., "Application of the Dynamic Mode Decomposition to Experimental Data," *Experiments in Fluids*, Vol. 50, 2011, pp. 1123–1130.

[89] Tu, J., Rowley, C. W., and Luchtenburg, D. M., "On Dynamic Mode Decomposition: Theory and Applications," *Journal of Computational Dynamics*, Vol. 1, No. 2, Dec. 2014, pp. 391–421.

[90] Tu, J. H., *Dynamic Mode Decomposition: Theory and Applications*, Ph.D. thesis, Princeton University, Princeton, NJ, Sep. 2013.

[91] Smith, M., "Sumary Statistics for Skewed Distributions," 2012 (accessed Mar. 15, 2016), URL:https://www.ma.utexas.edu/users/mks/statmistakes/skeweddistributions.html/.

[92] Horiba Scientific, *A Guidebook to Particle Size Analysis*, 2012.

[93] Blackstock, D. T., *Fundamentals of Physical Acoustics*, John Wiley and Sons, New York, 2000.